Optical Variability in Compact Sources

Optical Variability in Compact Sources

Optische Variabiliteit in Compacte Bronnen
(met een samenvatting in het Nederlands)

Academisch Proefschrift

ter verkrijging van de graad van doctor
aan de Universiteit van Amsterdam,
op gezag van de Rector Magnificus prof.dr. J.J.M. Franse,
ter overstaan van een door het college van promoties
ingestelde commissie in het openbaar te verdedigen
in de Aula der Universiteit,
op 7 december 1999, te 13:00 uur

door

Paul Joseph Groot

geboren te Amsterdam

Sterrenkundig Instituut ‘Anton Pannekoek’

Promotiecommissie:

Promotor:	prof.dr. J.A. van Paradijs
Co-promotor:	dr. R.G.M. Rutten (ING Group of Telescopes, La Palma)
Overige Leden:	prof.dr. E.P.J. van den Heuvel
	prof.dr. M.B.M. van der Klis
	prof.dr. L.B.F.M. Waters
	prof.dr. J.J.M. Franse
	prof.dr. Ch. van Weert
	prof.dr. F. Verbunt (Universiteit Utrecht)
	dr. C. Kouveliotou (Marshall Space Flight Center, NASA)
	dr. J. Heise (Stichting Ruimteonderzoek Nederland)

Sterrenkundig Instituut 'Anton Pannekoek'
Faculteit der Wiskunde, Informatica, Natuur- en Sterrenkunde
Universiteit van Amsterdam

Cover illustration: The diamond ring after a solar eclipse, caused by the Earth, as photographed by the Apollo 12 crew on their return from the Moon. Copyright NASA

Aan de eeuwig schijnende ster

To the ever shining star

Contents

1

Introduction

1.1 Gamma-Ray Bursts

1.1.1 Hot Bursts in Cool Times

The discovery of gamma-ray bursts is a scientific fringe benefit of the Cold War. If it weren't for the Vela espionage satellites it might have taken years longer to find Gamma-Ray Bursts (GRBs). Designed to detect bursts of γ rays originating in clandestine Soviet nuclear tests outside the Earth atmosphere, the Vela satellites detected sixteen flashes of γ rays in the years between 1967 and 1973 of which, by means of triangulation[1], it was determined that their origin was not terrestrial or Solar (Klebesabel, Strong and Olson, 1973). This was the birth of the question that now, almost thirty years later, has still not been answered: what is the origin of γ-ray bursts? Steady progress has been made over the years and an explosion of discoveries have made γ-ray bursts one of the 'hot' topics of astronomy today. Much of the recent development has been fueled by the discovery of counterparts to γ-ray bursts in all parts of the electromagnetic spectrum, especially in the optical. After the first of these optical counterparts (Chapter 2), more were soon to follow (Chapter 4 and the thesis of Titus Galama), although not every hunt was succesfull (Chapter 3). To understand the importance of these discoveries we have to look at the state of knowledge on γ-ray bursts in, say, the beginning of 1996.

1.1.2 Fashion and Models

After the first detections with the Vela satellites, small γ-ray burst detectors were flown 'piggy-back' on many of the deep-space planetary missions, such as the Soviet Venera satellites to Venus and the American Pioneer and Voyager satellites to the outer planets. These small detectors revealed one of the basic characteristics of γ-ray bursts: their rapid time variability. Changes in the γ-ray flux of GRBs on time scales shorter than a millisecond were observed. A well known astronomical estimate tells us that everything that

[1]Triangulation is especially well-suited for finding relative positions and was therefore one of the main methods of 17th century Dutch cartographers to map the Netherlands. In the flat, church-rich Dutch landscape the relative positions of Dutch cities were determined with high accuracy.

changes on a certain time scale, must be smaller than the distance that electromagnetic radiation can travel over that same time. If the brightness of a source varies on a time scale of a millisecond, then the source of that variable intensity cannot be much larger than a *light*millisecond, or in normal units, $\sim$300 km. There are only a few astronomical objects that are as small as that. Only comets, asteroids, neutron stars and black holes are of the required size. The fact that, in the mean time, no trace of the bursts or their remnants had been found in other parts of the electromagnetic spectrum, showed that they are highly energetic phenomena.

Since the start of X-ray astronomy in the early 1960's it had been recognized that much of the violence and turbulence seen in the X-ray sky was caused by neutron stars, and their more heavy brethren the black holes, in mass-transferring close-binary systems (see Sect. 1.2). Until the end of the 1980's neutron stars in our own Galaxy were therefore the favorite culprits for the origin of γ-ray bursts, either through neutron star quakes or by collisions of neutron stars with other objects, such as rogue comets.

However, some had proposed a GRB origin at completely different distances, in particular a 'cosmological' Gigaparsec distance scale (e.g., Pacźynski 1986). At this distance scale two neutron stars would collide and the ensuing fireworks would show up as a GRB. Not only would these GRBs have to be much more luminous than GRBs that originated in our own Galaxy, but also much rarer.

The extreme difference in distance between an origin in the Galaxy or the outer realms of the Universe, implied extreme differences (typically a factor $\sim 10^{10}$) in the energy that would be needed to observe the phenomena at the brightness seen from Earth. The cause for this uncertainty was that the γ-ray observations themselves did not allow for a firm exclusion of one or the other origin. Neither the known distribution of GRBs on the sky nor the intensity distribution of GRBs gave conclusive evidence for a particular origin and without knowing the cause of a GRB its distance cannot be determined on the basis of the γ-rays alone.

1.1.3 In Touch with the Universe

Much changed in the view on GRBs in the early 1990's as the result of the launch of the Burst and Transient Source Experiment (BATSE) on board the American *Compton Gamma-Ray Observatory* (see Fig. 1.1). BATSE provided a major improvement in sensitivity over the existing γ-ray detectors and its lay-out of eight detectors on the eight corners of *CGRO* gave it an almost all-sky view. Number statistics on GRBs were soon large enough to show that the distribution of GRBs on the sky is isotropic (Meegan et al., 1992, see Figure 1.2) and that the distribution of burst strengths does not follow the prediction of a uniform space density. Too few weak bursts are detected, which implies that there has to be an edge to the distribution. One could say that we are at the center of the GRB Universe, of which the edge is in view.

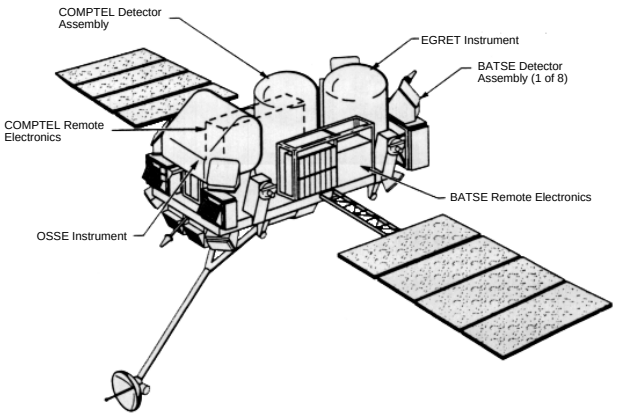

Figure 1.1. Schematic view of the *Compton Gamma-Ray Observatory*. The detectors on the eight corners of the spacecraft together constitute the Burst and Transient Source Experiment.

The combination of these two observational results, an isotropic sky distribution and an inhomogeneous space distribution, clearly favours the cosmological explanation. The isotropy is easy to understand, since on a very large scale (Gigaparsecs) the distribution of matter in the Universe is isotropic. The inhomogeneity can then be explained by the effect of cosmological redshift. The cosmological redshift causes two effects that both cause a decrease of the number of weak bursts that are detected. First the GRB rate is redshifted by $(1+z)^{-1}$, where z is the cosmological redshift. Second, the photon energy and the times of their arrival are both redshifted by a factor $(1+z)$.

The Galactic neutron star model, which was favoured until the BATSE results, is much harder, but not impossible, to reconcile with the isotropy and inhomogeneity. The inhomogeneity is easiest to explain because anything connected with the Galaxy will occupy a limited volume, since the Galaxy itself occupies a limited volume. To satisfy the criterium of isotropy the distribution of galactic GRBs has to be in a sphere that is large enough not to show the offset of the Sun with respect to the Galactic Center. However, the GRB sphere can also not be too large because it would then intersect with a similar sphere which is expected to surround our neighbouring galaxy, the Andromeda Nebula. If the two spheres overlap it will lead to an increased detection probability towards Andromeda, and the distribution on the sky would not be isotropic anymore. This makes the galactic model rather ‘constructed’. It has to be of exactly the right size for isotropy to hold.

Although the BATSE results *favoured* the cosmological origin of GRBs, they did not *prove* that they were cosmological. The reason for this was that the γ-ray observations themselves do not allow a distance determination for a GRB. To determine the distances

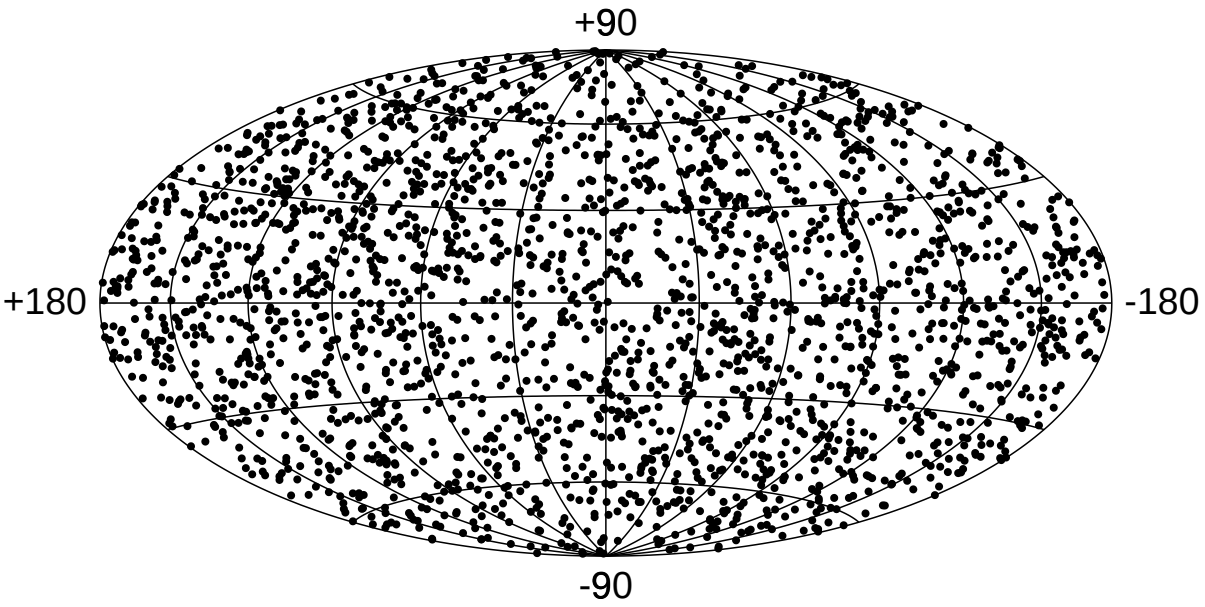

Figure 1.2. Distribution on the sky of the 2408 bursts detected with BATSE up to August 1999. The sky projection is in galactic coordinates, with the galactic plane running along the equator, and the Galactic North and South Pole on top and bottom respectively. If GRBs were connected to the Galaxy, they would show a concentration towards the galactic plane. The observed distribution is, however, completely isotropic. (A band of lower GRB density running roughly from bottom left to top right is caused by a non-uniform sky exposure.)

to GRBs they would have to be connected to known astrophysical objects for which the distance can be determined. Considering the vast difference in possible distances already a loose association with a known astrophysical object would suffice to determine a typical distance scale to GRBs. Prime candidates for such an association would, of course, be stars (for galactic models) or galaxies (for cosmological models). Both of these, however, are only small objects on the sky and in an area as large as the full Moon (used here for easy instructional comparison with GRB error boxes), many hundreds of stars and galaxies can be found if we observe down to a magnitude limit of 20th magnitude. It was expected that any phenomena connected to GRBs would be as dim as this, since the transient phenomena in the sky with a brightness a few magnitudes brighter than this are reasonably well known, and no trace had ever been found of a GRB afterglow in this brightness range. To associate GRBs with known phenomena it would not only be necessary to pinpoint the location of a GRB with high precision, but do it quickly as well. Depending on the energy in the blast wave that was expected to follow a GRB, any afterglow was expected to fade on typical time scales of days to months depending on the wavelength of observation and the energetics of the γ-ray burst.

The positional accuracy of γ-ray detectors is rather poor (a few times the full Moon at best), which made searching for X-ray, optical or radio counterparts a quest for the needle in a Universal haystack. Despite extensive efforts (e.g., Hudec, 1995; Galama et al., 1997a), none were found. The size of the initial γ-ray position would have to be brought down to an area much smaller than a full Moon to make a fast follow-up feasible.

1.1.4 And Let there be Light...

This improvement in positional accuracy came with the launch of the Italian-Dutch X-ray satellite *BeppoSAX* in April 1996. Apart from having an onboard Gamma-Ray Burst Detector, it carries two Wide Field Cameras (WFCs), which continuously monitor $40^\circ \times 40^\circ$ of the sky in X rays, and can detect sources with a positional accuracy of $\sim 3'$ in radius (in area $\sim$1/25th of the size of the full Moon). Since the distribution of GRBs on the sky is isotropic and their occurence is random in time and position, it will happen about once a month that a GRB goes off in the $40^\circ \times 40^\circ$ field-of-view of one of the WFCs and, if the GRB is bright enough in the 2-24 keV energy band, the WFC detects it. The first of these detections occured on July 20, 1996, when the satellite was still in its test phase. The second followed on January 11, 1997. Follow-up observations in the optical (Gorosabel et al., 1998) and radio (Galama et al., 1997b; Frail et al. 1998) did not find anything unusual in the WFC error box. The third of these WFC detections occured in the early hours of February 28, 1997 and an accurate position was available late in the European afternoon of February 28. In a fortunate circumstance service observations on the optical 4.2m William Herschel Telescope (WHT) at La Palma were to be taken of the position of the January 11 burst for the group in Amsterdam. Just before the position of the February 28 burst disappeared below the horizon, the WHT could be targeted to this new position and 21 hours after the GRB deep optical observations were taken: faster and deeper than ever before. Comparison of this exposure with observations taken a few days later revealed the presence of a source that had disappeared in the days in between (Groot et al., 1997a, Van Paradijs et al., 1997). This fading optical source was found to coincide with a fading X-ray source in the WFC error box which, in the mean time, had been found with follow-up X-ray observations of the GRB made with the Narrow Field Instruments on *BeppoSAX* (Costa et al., 1997), and also with a faint, blue galaxy (Groot et al.,1997b, Sahu et al., 1997): the first optical counterpart to a GRB was found (see Fig. 1.3) and its connection with a galaxy provided the long sought for association with a known astrophysical object, although a few percent chance did exist that the superposition was coincidental. With the measurement of the redshift of the optical afterglow of GRB 970508 (Metzger et al., 1997), the conclusion to the debate on the distance scale of GRBs was unambiguous: γ-ray bursts are cosmological in origin (Chapter 2). GRB 970228 was the first of almost a dozen GRBs that have been identified in the optical (e.g., Chapter 4).

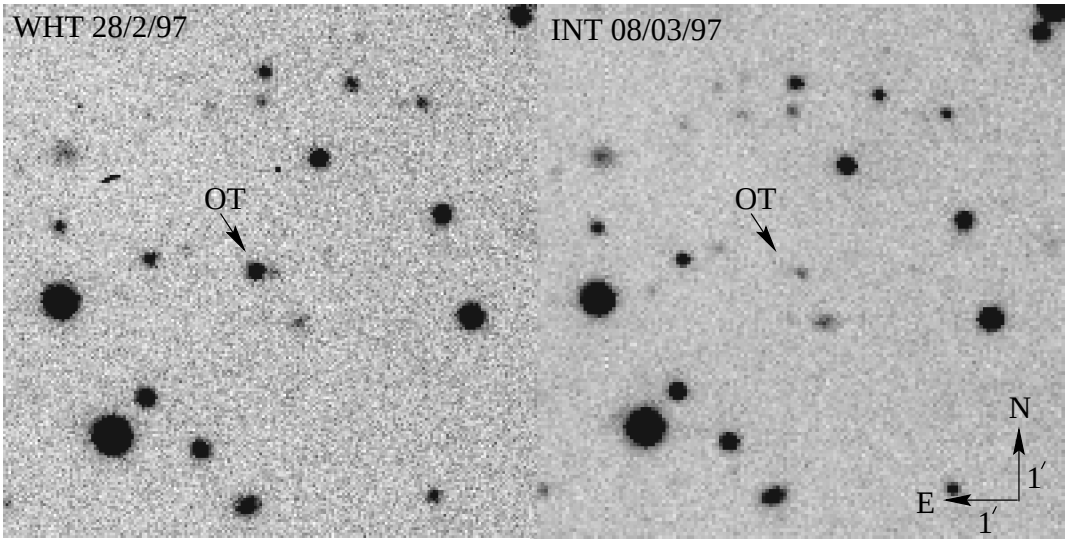

Figure 1.3. The first optical counterpart to a γ-ray burst; GRB 970228. It was discovered by comparison between a WHT-image taken on February 28 (left) and an INT-image taken on March 8 (Groot et al., 1997a; Van Paradijs et al., 1997). It was later found to be coincident with a faint blue galaxy (Groot et al., 1997b; Sahu et al., 1997), which is now known to have a redshift of 0.695 (Djorgovski et al., 1999)

1.1.5 ...But Darkness Still Enshrouds the Origin

The detection of afterglows of GRBs in all parts of the electromagnetic spectrum over the last 2.5 years has expanded our knowledge of the birthplace and energetics of GRBs enormously. The connection with galaxies is quite secure (Hogg and Fruchter, 1999), but what causes the extremely rare event that leads to a GRB is still unknown. There is evidence that they originate in star-forming regions, but this may be the result of an observational selection effect, since the expected brightness of low-energy afterglows depends on the density of the environment in which the GRB occurs (Sari, Piran and Narayan, 1998; Wijers and Galama, 1999). GRB afterglows in dense environments such as star-forming regions will be more luminous than those that occur in intergalactic space. For some GRBs no low-energy afterglows have been detected, which can be due to either a very low or a very high density of the circumburster environment (Chapter 3), or due to very rapid declines which cause the burst to fade before we have a chance to identify an afterglow (Chapter 4). Evidence has been found that beaming of the γ-rays is important to understand their implied energies (e.g., for GRB 990123 by Kulkarni et al., 1999 and Fruchter et al., 1999 and for GRB 980510 by Stanek et al., 1999 and Harrison et al., 1999) and a connection with a rare type of supernova has been implied in some cases (see Galama et al., 1998 for GRB 980425/SN1998bw, Bloom et al., 1999 for GRB 980326 and Reichart, 1999; Galama et al., 1999 for GRB 970228). However, the key that will reveal the GRB origin has not come to light yet.

1.2 Accretion disks

1.2.1 A Powerhouse

Accretion is the Universe's powerhouse. After the recognition of nuclear fusion as the energy source of the Sun and all the other stars, it was thought that fusion is as efficient an energy generator as you can get in nature. During nuclear fusion about 0.7% of the rest mass ($E = mc^2$) is converted into energy, which is used to maintain the stellar pressure equilibrium. However, at the end of the life of a massive star ($M_* > 8$ $M_\odot$) the ensuing supernova explosion liberates, in a second or less, an amount of energy that is equal to or even more than the total amount of energy the star has produced during its entire life by nuclear fusion. The energy to power a supernova explosion comes from the liberation of potential energy as matter falls into a deep gravity well. This process of energy generation is known as accretion.

If we drop a mass, m, that is initially at rest at a very large distance, into a gravity well that is caused by an object of mass, M, and radius R, then the total amount of potential energy, $E_{\rm acc}$, that can be gained by the mass, m is equal to:

$$E_{\rm acc} = GMm/R, \tag{1.1}$$

where G is the gravitational constant. It is the ratio (M/R), which we will call the compactness of an object, that determines if accretion is an efficient powerhouse. For the Sun, the ratio of M/R is very low. The Sun is too large and too light to make accretion onto it a very energetic phenomenon. You would need to dump matter at a rate of 3×10^{-8} $M_\odot$/yr onto the Sun to obtain an accretion luminosity that is equal to its nuclear luminosity for which it needs to fuse only 10^{-11} $M_\odot$/yr.

For accretion to become more efficient than fusion, we have to increase the compactness of an object. In white dwarfs, with $R_{\rm WD}$ = 0.01$R_\odot$ and M $\sim M_\odot$, accretion is already $\sim$100 times more efficient than for the Sun. Even better is accretion onto neutron stars and black holes, with M $\geq M_\odot$ and $R_{\rm NS/BH}$ $\leq$ 10 km ($\leq$ 1/70 000 $R_\odot$). In objects with a compactness as high as this, accretion is about 20 times more efficient in converting mass into energy than nuclear fusion. It is for this reason that most of the high-energy phenomena in our Universe, such as supernovae, quasars, active galactic nuclei, X-ray binaries and probably also γ-ray bursts, involve very compact objects and are ultimately powered by accretion. To understand how these sources are fueled is to understand how accretion works.

1.2.2 Disks, Spins and Binaries

The occurence of accretion is often accompanied by a phenomenon called an accretion disk. The formation of an accretion disk is best illustrated in a class of sources called close

binaries. With the advance of X-ray astronomy in the beginning of the 1960's, some very bright X-ray sources were found that could not be immediately identified in the optical. The optical counterparts to these very luminous X-ray sources were only found after deep searches and it was recognized that some sources that are among the brightest in the X-ray sky are only very dim in the optical. The X rays come from accretion onto a very compact object: a neutron star or a black hole. As we have seen in the previous paragraph, they are very efficient powerhouses and much of that power is radiated in X-rays. After studies of the X-ray and optical behaviour of these sources (e.g. Cyg X-1 where there is a 8th magnitude star in the error box, which is a binary with (plausibly) a black hole as a companion, and Cen X-3, which was found to be an eclipsing X-ray pulsar with the Uhuru satellite) it became clear that they are binary stars: the X-ray binaries, whose apparently puzzling evolutionary history was first explained by Van den Heuvel and Heise (1972).
In an X-ray binary a neutron star or black hole is accompagnied by a normal star, that can either be very massive ($M_* > 8$ $M_\odot$, the High-Mass X-ray Binaries), or very light ($M_* < 1$ $M_\odot$; the Low-Mass X-ray Binaries, LMXB). Through the course of stellar evolution the companion star in an LMXB has come into contact with its Roche-lobe[2]. This is the maximum volume that a star in a binary system can occupy before the gravitational attraction of the other star in the system becomes so large that mass is transferred from one star to the other. Fig. 1.4 shows a graphical representation of the potential in a close binary system. Both stars cause a gravity well, which is connected in the middle by a saddle point: the inner Lagrange point[3], denoted with L_1. At this point the effective gravity in the system is zero and gas will be free to move from one potential well to the other. A contour plot of the potential in the L_1 point shows a very characteristic 'figure-of-eight' shape (as shown by the thick line in the contour projection in Fig. 1.4), which represents the maximum volume any of two stars can fill before overflow through the L_1 point to the other component occurs.

If the companion star fills its Roche-lobe, gas in the outer regions of the atmosphere, close to the L_1 point, will feel almost zero-gravity and random, kinetic motion of the gas will cause an overflow from the companion to the compact object. If the two stars did not revolve around their center-of-mass, the gass would fall directly onto the central object. However, since the system is rotating, the gas overflowing through the L_1 point will have angular momentum, that prevents if from falling onto the central object directly. Instead, it will follow a path that leads it away from the straight trajectory to the central object and, depending on the size of the central object, it will either hit the central object off-center, or miss it completely. In the case of compact objects (including white dwarfs) it will miss

[2]Edouard Roche, 19th century French mathematician, who first calculated the shape of equipotential surfaces in the framework of a synchronously rotating two-body system.

[3]Joseph Louis Comte de Lagrange (1736-1813), French, Turin born, mathematician, who first calculated where in a synchronously rotating two-body system, the points with zero derivitave of the potential lie. These points (five in total) are called the Lagrange points (L_1-L_5).

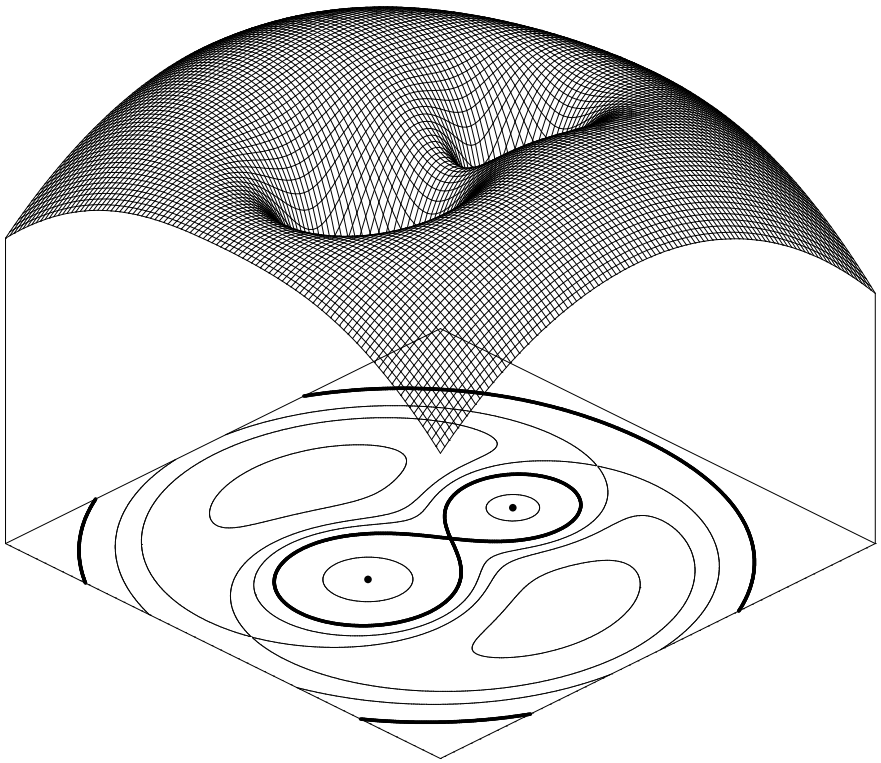

Figure 1.4. A graphical representation of the gravitational potential in a close binary system, with the two stars located in the center of the gravity wells. The slope of the curved upper surface is a measure for the gravity in the system. Points with no slope are locations without a net gravitational pull. There are five of these in total (the Lagrange points). The saddle point between the two stars is the inner Lagrange point, through which mass transfer will ensue if either one of the stars fills the volume available inside this point. The equipotential curve through the inner Lagrange point forms the 'figure-of-eight' shown in the projection by the thick line and is called the Roche-lobe and delimits the maximum volume either of the stars can obtain before mass transfer starts. *Credit Martin Heemskerk.*

the central object and circle around it and hit the stream coming from the secondary. If there were no interaction between the atoms the matter would settle in a ring around the compact object at a distance called the circulisation radius, where the amount of angular momentum in the rotating gas is equal to that of the gas leaving the secondary. This is required since angular momentum must be preserved (see Fig. 1.5).

1.2.3 Friction and Viscosity

In the situation of such a friction-free accretion ring, no matter would ever be accreted onto the compact object. However, we see powerful X-ray sources that are fueled by gas crashing into the surface. So, somehow, the material must lose its angular momentum.

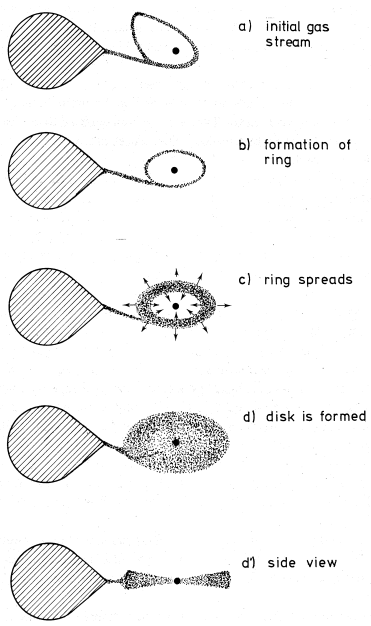

Figure 1.5. The initial formation stages of an accretion disk in a close binary system. The gas stream that initially leaves the mass-losing secondary, will miss the compact object and swing around it. After it collides with itself, the gas will settle in an accretion ring at the circulisation radius, where the angular momentum of the material orbiting the compact object is the same as the angular momentum of the matter leaving the secondary. Through processes that are not well understood, but most likely including magnetic field effects, the interactions between the particles in the accretion ring will cause an exchange of angular momentum. Most particles will lose angular momentum and fall inwards and some will gain angular momentum and spread outwards. At a distance of some 70% between the compact object and the inner Lagrange point, tidal forces will remove the angular momentum again from the individual particles and feed it back into the orbit. From Verbunt (1982).

If it does so, it will find a new orbit closer to the compact object. If it continues to lose angular momentum it will ultimately fall onto the compact object. However, the total amount of angular momentum must be conserved, so if most of the gas is falling inwards, some of it must move outwards, and we see that the accretion ring must spread into an accretion disk. The exchange of angular momentum between the atoms in the accretion ring/disk is caused by the viscosity of the accretion disk. The nature of the viscosity is not well known and a major unsolved question in accretion disk physics, although a magnetic hydrodynamic instability originally discovered by Velikovsky and by Chandrasekhar, and rediscovered by Balbus and Hawley appears to produce the required viscosity. For an excellent overview of accretion power in astrophysics see Frank, King and Raine (1992).

1.2.4 Accretion Overload and Powerhouse Burn-out

Although the ultimate effects of accretion are best seen in supernovae, γ-ray bursts and X-ray binaries, they are actually not the best places to study the physics of accretion disks. The reason for this is that accretion in these systems either occurs too fast (supernovae and γ-ray bursts) or is too powerful (X-ray binaries). In supernovae and γ-ray bursts the

whole event of accretion takes place on a time scale of minutes or less and is hidden from view by the outer layers of the star in a core-collapse supernova.

In X-ray binaries the gas that accretes onto the compact object is already heated up to very high temperatures ($>$ MK) and shines brightly in X rays. These X rays are partly intercepted by the cooler parts of the surrounding accretion disk, and thereby heat the outer parts to temperatures that would not be reached without the X rays. This process is called X-ray heating and is seen in many systems. The occurrence of this X-ray heating not only distorts the accretion disk structure, but also plays an important role in its dynamics (Van Paradijs, 1996). This shows that accretion disks in X-ray binaries are not the best place to study the physics of accretion disks.

1.2.5 A Cataclysmic Substitution

An almost ideal environment for the study of accretion disks is offered by the Cataclysmic Variables (CVs; see Warner 1995 for a monograph). These are identical to LMXBs, except for the fact that the neutron star is replaced by a white dwarf as the compact object. We have seen in Sect. 1.2.1 that white dwarfs are almost a factor 1 000 less efficient in generating accretion energy than neutron stars and are therefore less luminous than X-ray binaries, but the advantage is that the accretion disk is not disturbed by X-ray heating, since most of the light is emitted as UV or optical radiation.

There are several reasons why CVs are such ideal laboratories for accretion disk studies. We have already seen that the accretion energy is not enough to generate a large amount of X rays, and the disks in CVs are therefore relatively undisturbed. Many of the CVs, of the sub-class 'dwarf nova' show brightenings of several magnitudes with inter-outburst times of weeks to decades. These dwarf-nova outbursts are the result of an instability occurring in the accretion disk, when the surface density becomes too high, which causes the viscosity to change. The higher mass transfer rate through the disk causes much of the mass that has slowly been stored in the accretion disk to accrete on the white dwarf and the potential energy that is liberated in the process is partly radiated away. These outbursts give a unique opportunity to study the time-dependence of an accretion disk.

In contrast to other systems (X-ray binaries, AGNs and quasars) CVs are relatively close-by and bright. This allows for studies with high signal-to-noise ratios. Most of the CV light is emitted in the UV and optical regions. Orbital periods in CVs are of the order of a few hours. This is an ideal stretch of time to study the source during one or more nights on a telescope. This is in contrast to, e.g., AGNs and quasars where the intrinsic periods of variation are usually of the order of weeks to months.

The light that we receive from CVs is mainly emitted by the accretion disk itself, with only minor contributions from the white and red dwarfs in the system. Especially in eclipsing

systems this is a very useful feature, since the eclipse profile in the light curve is mainly caused by the light distribution on the accretion disk itself.

CVs show a whole range in mass transfer rates from the secondary to the white dwarf. When the accetion rate is low, we see the systems as the dwarf nova systems described above. If the mass-accretion rate from the secondary is high, the disks become stable. They do not show the dwarf-novae outbursts anymore, but appear to be in a permanent state of outburst. These systems are the novalike variables and their disks are supposed to be in a steady state: the mass transfer rate from the secondary and the mass accretion rate on to the white dwarf are in equilibrium. Current accretion disk theory predicts that the effective temperature of the disk ($T_{\rm d}$) should depend on distance to the white-dwarf ($r_{\rm d}$) as:

$$T_{\rm d} \propto r_{\rm d}^{-3/4}. \tag{1.2}$$

1.2.6 Resolving a Pinpoint

A fundamental difficulty in studying accretion disks in close binaries and AGNs is that none of these systems can be directly resolved with today's telescopes. The total size of a CV is of the order of the radius of the Sun: 700 000 km. At a typical distance of 100 pc this will subtend and angle on the sky of 5×10^{-5} arcseconds. The sharpest images now avaliable with optical telescopes are $>5\times10^{-2}$ arcseconds. We have to resort to different techniques if we want to determine any spatial structure on something we don't see spatially resolved.

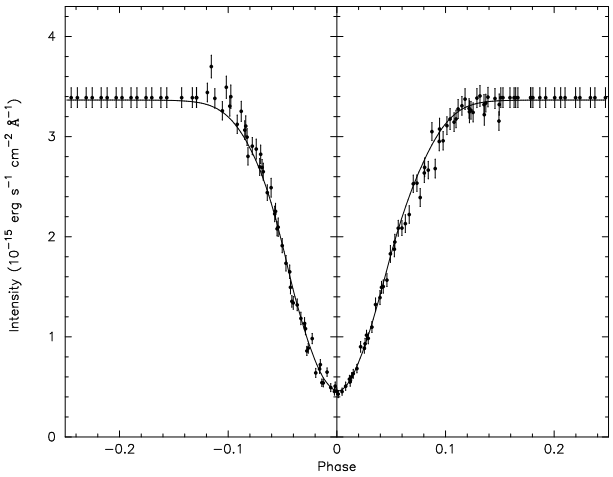

Figure 1.6. The amount of light received on Earth versus (part of) the orbital period of an eclipsing cataclysmic variable. The V-shaped drop in the ligthcurves is caused by the secondary star that eclipses the bright accretion disk. Using the eclipse mapping technique we can deduce the most-likely light distribution on the accretion disk from the shape of this eclipse profile.

One such a technique is eclipse mapping. Initially proposed by Horne (1985) it uses the information on the brightness distribution of the accretion disk that is contained in the eclipse profile. If the inclination of a CV is high enough that we see the secondary star pass in front of (part of) the accretion disk and we can resolve the passage in time, then the light curve of such a CV will look like that shown in Fig. 1.6. The amount of light sharply drops, reaches a minimum and rises again to its normal level. At each step in time, the amount of light that (dis)appears can be projected on a strip of the accretion disk, that is eclipsed in that time step. Since the angles at which we see the shadow of the secondary cross over the accretion disk vary slightly between ingress and egress, we can better determine the position of the (dis)appearing light on the accretion disk (see Fig. 1.7). The result of this technique is a 'picture' of the accretion disk, which shows the brightness distribution over the disk for the wavelength band in which the observations were taken.

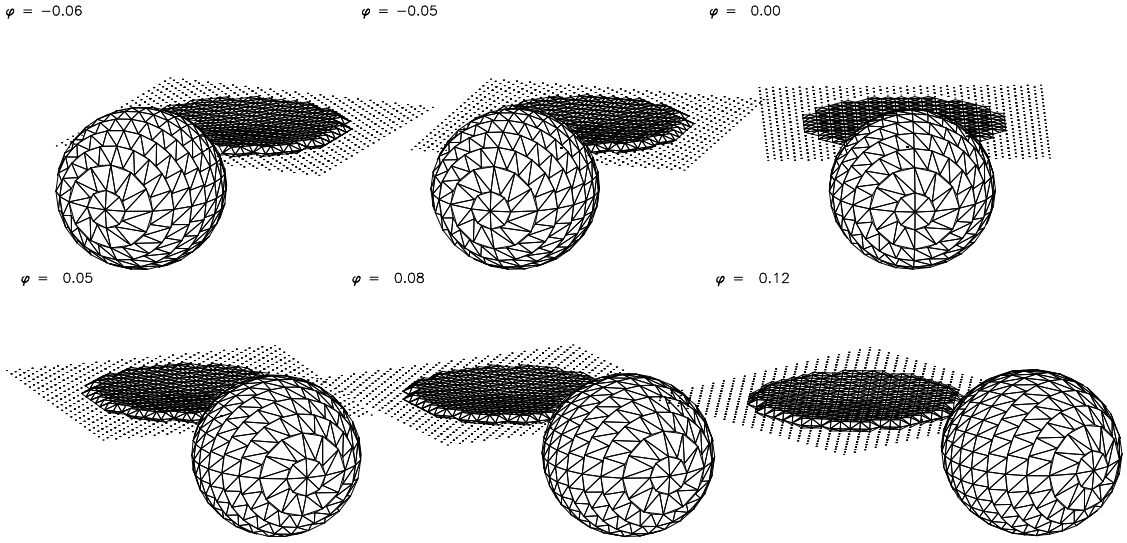

Figure 1.7. Series of graphical illustrations of an eclipsing CV at six phases during its orbital period. We see that the occultation of the accretion disk by the secondary is different for the same phases before and after mid-eclipse. This helps to constrain the emission site in the eclipse mapping reconstruction technique.

If we extend the eclipse mapping technique to multiple wavelength bins we can reconstruct the brightness distribution over the accretion disks at multiple wavelengths. We call this technique spectral eclipse mapping (see Chapters 6, 7 and 8). Rutten et al. (1994) were able to show for the nova-like UX UMa that the temperature dependence on radial distance from the white dwarf was indeed as predicted by Eq. 1.2. However, a sub-class of the nova-like systems, the SW Sex stars, do not show this temperature dependence, but one that is much flatter. In Chapter 6 we investigate what the possible causes for this are and we conclude that a mass-loss from the system in the form of a wind, that originates at

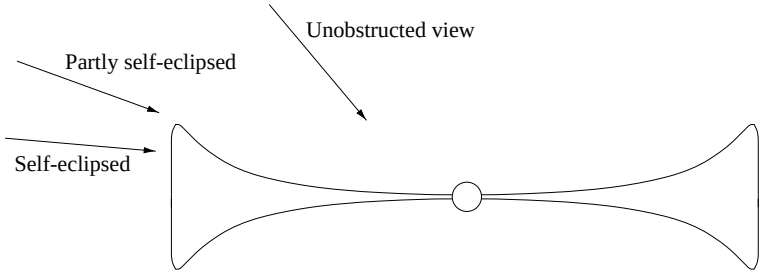

Figure 1.8. A cross-cut through a flared accretion disk. If our line of sight is almost parallel to the plane of the disk, the flared outside of the disk can prevent a direct view of the inner parts of the disk.

a position about half-way in the disk disturbs the inner disk and prevents it from obtaining the temperature dependence given above.
In Chapter 7 we discuss the system RW Tri, which has been classified as a system like UX UMa. We find, however, in our current study that it shows some characteristics that are attributed to the SW Sex stars. Apparently the spectroscopic appearence of a no-valike systems can change with its brightness, which is most likely correlated with the mass-accretion rate from the secondary. Instead of classifying RW Tri as a SW Sex star, we propose to abandon the division into two classes (the UX UMa and SW Sex stars) altogether since there appears to be no physical distinction between the two.

Even when the disk in a NL is in a steady-state, as is the case for UX Uma, it does not mean that it is stationary. The luminosity and size of the accretion disk will change when the mass transfer rate from the secondary changes. Because these changes occur on a much longer timescale (weeks to years) than are normally spent on observing a CV (days to weeks) it has only fairly recently become clear that the mass-transfer rate of secondaries themselves can vary. Studying how the mass transfer rate changes and how the accretion disk reacts to this, will allow us to gain more information on the physics of accretion disks. One system that shows these long-term changes and which is particularly interesting is GS Pavonis (Chapter 5). This is a system that not only eclipses once every orbital period, but that eclipses totally (the accretion disk is completely obscured by the secondary in mid-eclipse) when it is in a low brightness state, and eclipses partially when it is brighter, and may even show self-eclipses of the accretion disk. Self-eclipses occur when the outer parts of the accretion disk shield inner parts of the disk from our line of sight. This can only occur when the disk is flared (i.e. the height increases non-linearly with distance to the white dwarf), which is theoretically predicted to be the shape of accretion disks (see Fig. 1.8).

Although the disk shape in NL-CVs can normally be well approximated by a two dimensional disk, since no strong effect of the three dimensionality of the disk is visible, this assumption cannot be made for disks in the dwarf nova systems. Here the mass transfer rate from the secondary is much lower, which not only leads to the disk instabilities

that cause the dwarf novae outbursts, but also causes the place of impact of the accretion stream on the accretion disk, the hot spot, to contribute a significant amount of light. This contribution of the hot spot is not only seen as an extra ingress and egress step during the eclipse of the accretion disk, but also as a very broad, and possibly very pronounced, hump on the light curve outside eclipse (see Fig. 1.9). The fact that this contribution of the hot spot is not constant with orbital phase shows that the hot spot 'comes into view' at a certain phase and 'disappears from view' half an orbit later. This shows that the disk in some dwarf novae systems has to be treated as a three dimensional object. Early attempts at reconstructing the accretion disk brightness distribution of dwarf nova disks have used a decomposition technique, in which the contribution of the white dwarf, hot spot and accretion disk are subtracted separately from the total light curve, after which the light curve for the accretion disk is used for an eclipse mapping reconstruction (Wood et al., 1989). Although this method works well, it is only suited for systems where the three different components (accretion disk, white dwarf and hot spot) can be well separated. In practice this means that it is only usable with high time resolution data of systems where the ingress and egress of the hot spot and the white dwarf are well separated in time.

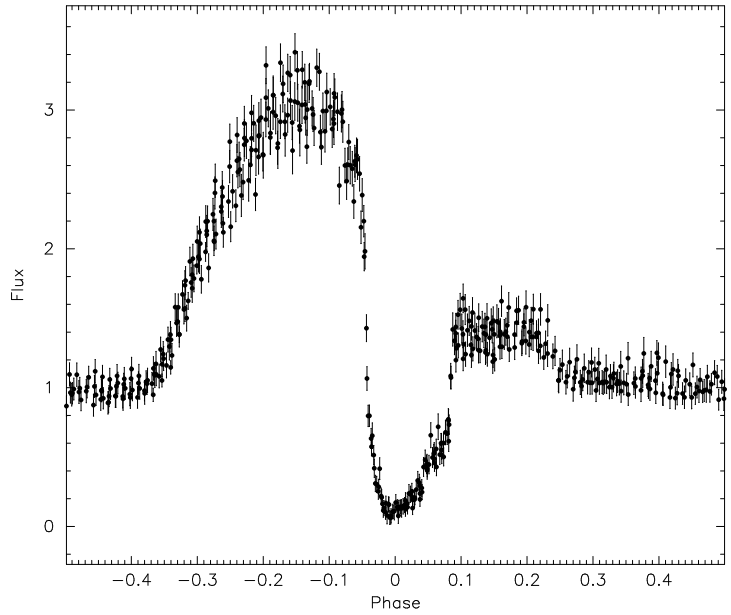

Figure 1.9. The light curve of the dwarf nova cataclysmic variable IP Peg. The broad hump visible before eclipse is caused by the hot-spot region, where the accretion stream hits the accretion disk, and shows the three-dimensionality of the disks in these systems. The gradual increase and decrease of this broad hump suggest a bright region on a disk-rim, that comes into view and fades from view again half an orbit later.

To make the eclipse mapping method applicable to more general cases Rutten (1999) has made a generalisation of the two-dimensional eclipse mapping method to three di-

mensions, in which the disk can be given an arbitrary three-dimensional shape and the Roche-lobe filling secondary star can be included in the light curve fitting routine. Although this 3-D eclipse mapping has the potential of being applicable to many different systems, it has the disadvantage of many degrees of freedom. The shape of the accretion disk is arbitrary and has to be pre-defined by the user. The eclipse mapping technique will then try to find the most-likely distribution of light on this predefined grid. Careful testing of the assumptions that are made about the shape of the disk is of crucial importance to understand the results of 3-D eclipse mapping.
In Chapter 8 we apply, for the first time, this 3-D technique to spectrally reconstruct the accretion disk brightness distribution of the disk in IP Peg, a well known and well studied cataclysmic variable of the dwarf-nova sub-class. From the phasing and brightness of the hot-spot we have been able to deduce that the flaring of the disk is less than 2° at the hot-spot position. Using this constraint on the shape of the disk, we derive that the outer parts of the accretion disk in IP Peg are cold enough for TiO molecules to form.

1.3 The Faint and The Variable

1.3.1 To Boldly Go...

The brightest of the optical counterparts to γ-ray bursts so far known had a brightness of 18th magnitude after a few hours (here we do not discuss GRB 990123 for which prompt emission was discovered at V$\sim$9; Akerlof et al. 1999). Their fast decay of, intially, 1-2 mags/day allows an easy identification of these counterparts. If the beaming mentioned in Sect. 1.1.5 indeed plays an important role, one would expect to find optical counterparts to GRBs, for which we observe no accompanying burst of γ rays. This is caused by the fact that the beaming in γ rays will be larger than the beaming in the optical. For some bursts the Earth will be located outside the beaming cone of the γ rays, but inside the beaming cone of the optical radiation. The expected number of optical GRBs without a burst of γ rays depends on the amount of beaming. If beaming is unimportant (i.e. GRBs explode isotropically) we will never see an optical GRB without a burst of γ rays. Establishing an estimate of, or an upper limit on, the number of optical GRBs will constrain the beaming angle of GRBs and will therefore constrain the problem of energy production in GRBs. If the beaming is large, the total amount of energy that is needed to produce the signal received on Earth is much less than when GRBs explode isotropically.

The variability behaviour of stellar-like objects at magnitudes fainter than 20th magnitude is not well known. Large-scale variability studies are rare because of the large amount of observing time needed to cover an appreciable part of the sky, and studies that reach the faintness where we expect optical counterparts of γ-ray bursts are either limited to specific galactic populations, or probe only a small area on the sky. An example of studies that probe specific stellar populations are the microlensing studies (MACHO, Alcock,

1995; EROS, Beaulieu 1995; OGLE, Udalski, 1992), that are targeted to find transitions of dark-matter objects in front of background stars. To increase the chances of finding these microlenses, these studies are directed at regions that have a very dense stellar sky distribution: the Galactic Bulge, the Large Magellanic Cloud and M31. However, partly due to this high stellar density which causes severe crowding, these studies are limited to relatively shallow depths of 21st magnitude with precisions of 0.5 mag at the faint end. Although sufficient to pick up bright optical counterparts of γ-ray bursts, these studies will not reveal anything that is fainter or less variable.

One of the types of objects that is expected to fall in this last category (faint and variable with amplitudes less than 0.5 mag) is the majority of the Cataclysmic Variables. The sample of CVs with a known orbital period shows a strong bias towards systems with long periods (3-9 hrs) and high luminosity (see e.g. Ritter and Kolb, 1998). This is almost entirely an observational selection effect. These systems are the easiest to find and therefore dominate the sample. Theoretical calculations show that the vast majority of all CVs ($\sim$99%) will have periods below 2 hours and most of these ($\sim$70%) will have very low mass transfer rates ($<10^{-11}$ $M_{\odot}$/yr; Howell, Rappaport and Politano, 1997; Kolb, 1993). These very low mass transfer rates make the accretion disks in these systems intrinsically very dim, which makes them also observationally very faint. Folding of the expected brightness distribution of this theoretical population of CVs with a typical space density shows that most CVs will be fainter than 20th magnitude. Convential ways of finding CVs, such as their detection during dwarf-nova or nova outbursts, or detection based on the very blue colour of the accretion disk, will not work in uncovering this majority of CVs because the inter-outburst times of dwarf-nova outbursts in these systems is of the order of decades or longer. Because of the low mass transfer rates the accretion disks in these systems are not expected to be the dominant source of radiation, and the colours of these system will be a composite of the (red) companion star, the (blueish) accretion disk and the (blue) white dwarf.

All CVs however, show variations in their light curves of a few tenths of magnitudes which is caused by fluctations in the mass transfer stream. This random variation, typically on a timescale of minutes, is referred to as 'flickering'. In the few systems that are suspected to have the low mass transfer rates expected for the majority of all CVs, this flickering is clearly observable. It can, therefore, serve as an identifier of low mass transfer rate CVs.

1.3.2 Large and Sensitive

The observational requirements for the detection of the optical GRBs without a γ-ray burst, as well as the low-luminosity CVs are the same. A large area of the sky needs to be observed much deeper than 20th magnitude, preferably down to 25th magnitude, with precisions that are better than 0.1 mag for the faintest sources and with repeated

observations of the same field over a time period of roughly a week. Over the last few years, technical developments have made the fabrication of large format CCDs (Charged Coupled Devices[4]) possible. Currently the largest CCDs contain 4000×2000 pixels and can be stacked in arrays to make cameras that contain 16 or more of these CCDs.

One of the first of these so-called Wide Field Cameras (WFCs) is the WFC on the 2.5m Isaac Newton Telescope (INT) on the island of La Palma. This camera contains four 4000×2000 pixel CCDs and is able to cover an area on the sky as large as the full Moon ($0\overset{\circ}{.}27$) in one exposure. In the spring of 1997 the Joint Steering Committee of the Isaac Newton Group of Telescopes (to which the INT belongs) decided that a large amount of telescope time with the new WFC was to be made available for large surveys. The 'Faint Sky Variability Survey', which has, among others, the above-mentioned objectives of finding optical GRBs and the majority of the CV population as two of its main targets, was selected as one of three proposals that combined form the INT Wide Field Survey. Observations for the Faint Sky Variability Survey have started in the November 1998 and in Chapter 9 we outline the main goals, the observational strategy and the reduction techniques of this important next step in GRB and CV research.

References

Akerlof, C.W., et al., 1999, Nature 398, 400

Alcock, C., 1997, ApJ 486, 697

Beaulieu, J.P., et al., 1995, A&A 303, 137

Bloom, J., 1999, Nature, *submitted*

Briggs, M.S., et al., 1996, ApJ 459, 40

Costa, E., et al., 1997, Nature 387, 783

Djorgovksi, S.G., et al., 1999, GCN Note # 289

Frail, D.A., Kulkarni, S.R., Shepherd, D.S. and Waxman, E., 1998, ApJ 502, L119

Frank, J., King, A.R. and Raine, D., 1992, *Accretion Power in Astrophysics*, Cambridge Astrophysics Series 21, CUP, Cambridge, UK.

Fruchter, A.S. et al., 1999, ApJL *submitted*

Galama, T.J., et al., 1997a, A&A 321, 229

Galama, T.J., et al., 1997b, ApJ 493, L27

Galama, T.J., et al., 1998, Nature, 395, 670

Galama, T.J., et al., 1999, ApJ, *submitted*

Groot, P.J., et al., 1997a, IAUC 6584

Groot, P.J., et al., 1997b, IAUC 6588

[4]CCDs are commercially used in hand-held compact video and digital cameras. The CCDs in these cameras contain at most $\sim$2 million (1400×1400) pixels

Gorosabel, J., et al., 1998, A&A 339, 719
Hakkila, J., et al., 1994, ApJ 422, 659
Hartmann, D., 1995, Ap&SS 231, 361
Harrison, F.A., et al., 1999, ApJL, *submitted*
Hogg, D. and Fruchter, A.S., 1999, ApJ, *submitted*
Howell, S.B., Rappaport, S. and Politano, M., 1997, MNRAS 287, 929
Hudec, R., 1995, Ap&SS 231, 239
Klebesabel, R.W., Strong, I.B. and Olson, R.A. 1973, ApJ 182, L85
Kolb, U., 1993, A&A 271, 149
Kulkarni, S.R. et al., 1999, Nature, 398, 389
Meegan, C.A., et al., 1992, Nature 381, 49
Paczyński, B., 1986, ApJ 308, L43
Ritter, H. and Kolb, U., 1998, A&AS 129, 83
Sahu, K.C., et al., 1997, Nature 387, 476
Sari, R., Piran, T. and Narayan, R., 1998, ApJ 497, L17
Stanek, K.Z., 1999, ApJL *submitted*
Udalski, A., 1992, AcA 43, 69
Van den Heuvel, E.P.J. and Heise, J., 1972, Nat. Phys. Sci, 239, 67
Van Paradijs, J., 1996, ApJ 464, L139
Van Paradijs, J., Groot, P.J., Galama, T.J., et al., 1997, Nature 386, 686
Verbunt, F., 1982, SSRv 32, 379
Warner, B., 1995, *Cataclysmic Variables*, Cambridge, Astrophysics Series 28, CUP, Cambridge, UK
Wijers, R.A.M.J. and Galama, T.J., 1999, ApJ, *in press*
Wood, J.H., Horne, K., Berriman, G., and Wade, R., 1989, ApJ 341, 974

Part I

Optical Counterparts to Gamma-Ray Bursts

2

Transient optical emission from the error box of the γ-ray burst of 28 February 1997

J. van Paradijs, P.J. Groot, T.J. Galama, C. Kouveliotou, R.G. Strom, J. Telting, R.G.M. Rutten, G.J. Fishman, C.A. Meegan, M. Pettini, N. Tanvir, J. Bloom, H. Pedersen, H.U. Nørgaard-Nielsen, M. Linden-Vørnle, J. Melnick, G. van der Steene, M. Bremer, R. Naber, J. Heise, J. in 't Zand, E. Costa, M. Feroci, L. Piro, F. Frontera, G. Zavattini, L. Nicastro, E. Palazzi, K. Bennet, L. Hanlon & A. Parmar

Nature 386, 686 (1997)

For almost a quarter of a century (Klebesabel, Strong and Olson 1973), the origin of γ-ray bursts –brief, energetic bursts of high-energy photons– has remained unknown. The detection of a counterpart at another wavelength has long been thought to be a key to understanding these bursts (see, for example, Fishman and Meegan 1995), but intensive searches have not revealed such a counterpart. The distribution and properties of the bursts (Meegan et al. 1992) are explained naturally if they lie at cosmological distances (a few Gpc; Paczyński 1986), but there is a countervailing view that they are relatively local objects (Podsialowski, Rees and Ruderman 1995), perhaps distributed in a very large halo around our galaxy. Here we report the detection of a transient and fading optical source in the error box associated with the burst GRB 970228, less than 21 hours after the burst (Groot et al. 1997a, b). The optical transient appears to be associated with a faint galaxy (Groot et al. 1997b; Metzger et al. 1997), suggesting that the burst occured in that galaxy and thus that γ-ray bursts in general lie at cosmological distances.

2.1 GRB 970228

GRB 970228 was detected (Costa et al. 1997) with the Gamma-ray Burst Monitor (Frontera et al. 1991) on board the Italian-Dutch *BeppoSAX* satellite (Piro, Scarsi and Butler 1995) on 1997 February 28, UT $02^{\rm h}58^{\rm m}01^{\rm s}$. The event lasted $\sim$ 80s and reached peak fluxes of $\sim 4\times10^{-6}$, $\sim 6\times10^{-6}$ and 10^{-7} erg cm^{-2} in the 40–600 keV, 40–1 000 keV and 1.5–7.8 keV ranges, respectively (Costa et al. 1997; Palmer et al. 1997). It occured in the field of view of one of the *BeppoSAX* Wide Field Cameras (WFC; Jager et al. 1997). The spectrum of the event is characteristic of classical γ-ray bursts (GRBs; Palmer et al. 1997). Its position (about halfway between α Tauri and γ Orionis) was determined with an accuracy of $3'$ (radius; Costa et al. 1997) at right ascension (RA) $05^{\rm h}01^{\rm m}57^{\rm s}$, declination (dec.) $+11^\circ\ 46\farcm5$. Application of the long-baseline timing technique (Hurley et al. 1996) to the GRB data obtained with the Ulysses spacecraft, and with the *BeppoSAX* and the Wind satellites, respectively, constrained this location to be within each of two parallel annuli, with half-widths (Cline et al. 1997; Hurley et al. 1997) of $31''$ (3σ) and $30''$ (3σ), respectively, which intersect the WFC error circle (Fig. 2.1).

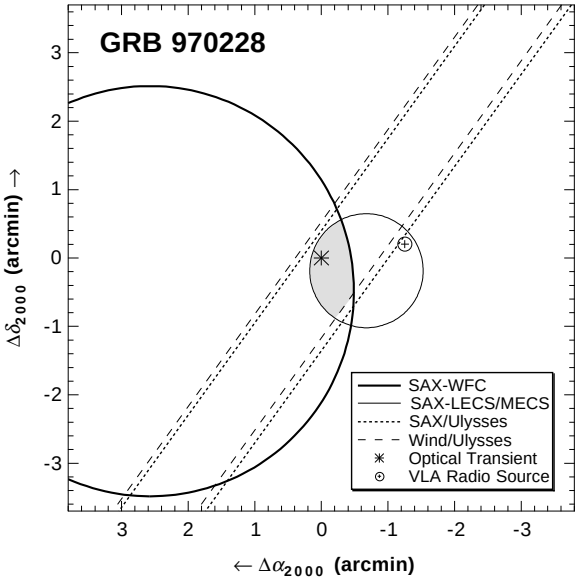

Figure 2.1. The position of the optical transient, indicated with an asterisk, is shown with respect to the $3'$ (radius) WFC location error circle, the $50''$ (radius) error circles of the *BeppoSAX* X-ray transient, and the two annuli obtained from the differences between the times the GRB was detected with *Ulysses*, and with *BeppoSAX* and *Wind*, respectively. The area in common between these error regions is hatched. The coordinates are given in units of arcmin with respect to the position of the optical transient (RA $05^{\rm h}01^{\rm m}46\fs665$, Dec. $+11^\circ\ 46'53\farcs9$, J2000). The position of an unrelated radio source (Frail et al. 1997) in the error circle of the X-ray transient is indicated with the square symbol.

Eight hours after the burst occured, *BeppoSAX* was reoriented so that the GRB position could be observed with the LECS and MECS detectors (Parmar et al. 1997; Bonura et al. 1992). A weak X-ray source was then found (Costa et al. 1997) at RA $05^{\rm h}01^{\rm m}44^{\rm s}$, dec. $+11^\circ\ 46\farcm7$ (error radius $50''$), near the edge of the WFC error circle (Costa et al. 1997; Fig. 2.1). The 2–10 keV (MECS) flux of this source was 2.4×10^{-12} erg cm^{-2} s^{-1}. The LECS instrument measures a 0.1–10 keV source flux of $(2.6 \pm 0.6) \times10^{-12}$ erg cm^{-2} s^{-1}. The source spectrum was consistent with a power-law model with photon index 2.7,

reduced at low energy by a column density $N_{\rm H}$ of 5.6×10^{21} cm^{-2}. During an observation with the same instruments on March 3, $17^{\rm h}37^{\rm m}$ UT this flux had decreased by a factor of 20 (Costa et al. 1997). With *ASCA* the X-ray source was detected (Yoshida et al. 1997) on 7 March at a 2–10 keV flux of $(0.8 \pm 0.2) \times10^{-13}$ erg cm^{-2} s^{-1}.

2.2 Optical observations

On February 28, $23^{\rm h}48^{\rm m}$ UT, 20.8 hours after the GRB occured, before we had any knowledge of the X-ray transient, we obtained a V-band and an I-band image (exposure times 300s each) of the WFC error box with the Prime Focus Camera of the 4.2-m William Herschel Telescope (WHT) on La Palma (Groot et al. 1997c). The 1024×1024 pixel CCD frames (pixel size 24μm, corresponding to $0\farcs421$) cover a $7\farcm2\times7\farcm2$ field, well matched to the size of the GRB error box. The limiting magnitudes of the images are V=23.7 and I = 21.5. We obtained a second I-band image on March 8, $21^{\rm h}12^{\rm m}$ UT with the same instrument on the WHT (exposure time 900s) and a second V-band image on March 8, $20^{\rm h}42^{\rm m}$ UT with the Isaac Newton Telescope (INT) on La Palma (exposure 2500s). Photometric calibration was obtained from images of standard star number 336 in Landolt (1992) field 104. The images were reduced using standard bias subtraction and flatfielding.

A comparison of the two image pairs immediately revealed one object with a large brightness variation (Groot et al. 1997a): it is clearly detected in both the V- and I-band images taken on 28 February, but not in the second pair of images taken on 8 March (see Fig. 2.2). From a comparison with positions of nearby stars that were obtained using the Digitized Sky Survey, we find for its location RA $05^{\rm h}01^{\rm m}46\fs66$, Dec. $+11^\circ\ 46'53\farcs9$ (equinox J2000); this position has an estimated (internal) accuracy of $0\farcs2$. The object is located in the error box defined by the WFC position, the *Ulysses/BeppoSAX/Wind* annuli, and the transient X-ray source position (see Fig. 2.1).

Using aperture photometry software we determined the magnitude of the variable as follows (Groot et al. 1997a): V = 31.2 $\pm$ 0.1, I = 20.6 $\pm$ 0.1 on February 28, and $V > 23.6$, $I > 22.2$ on 8 March. The shape of the source in both the 28 February V- and I-band images is consistent with that of the point-spread function, as determined for 15 stars in the same images.
Close to the optical transient is a star, located $2\farcs85$ away at RA $05^{\rm h}01^{\rm m}46\fs47$, Dec. $+11^\circ\ 46'54\farcs0$, with $V = 23.1$, I = 20.5. A spectrum of this star, taken on March 1, UT $0^{\rm h}$with the ESO 3.6-m telescope using the EFOSC1 spectrograph and the R1000 grating (resolution of 14 Å per pixel), covering the 5600-11000 Å region, reveals the presence of TiO bands, which indicate it is an M-type star. With foreground absorption A_V = 0.4 $\pm$ 0.3 (Hakilla et al. 1997; substantially smaller than the value inferred from the low-energy cutt off in the LECS spectrum), its colour index, $V - I$ = 2.6, corresponds to an M2 star (Johnson 1966). It is most likely to be an M-dwarf at a distance of $\sim$ 3 kpc (an early

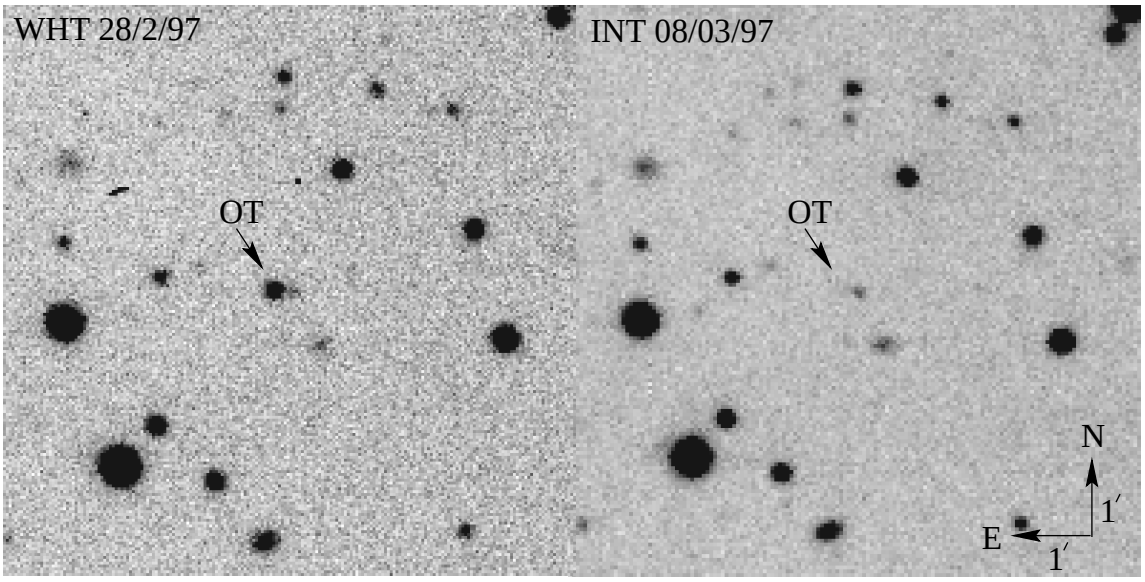

Figure 2.2. V-band images of a $1' \times 1'$ region of the sky containing the position of the optical transient. The left image was obtained with the WHT on 1997, 28 February, UT $23^{\rm h}48^{\rm m}$, the right image with the INT on 8 March, UT $20^{\rm h}42^{\rm m}$. The optical transient is indicated by 'OT'. The M-dwarf, separated from the optical transient by $2\farcs85$, is also indicated.

M-type giant would be located at a distance $\sim$ 0.4 Mpc, which we consider much less likely).

Further images were obtained with the Nordic Optical Telescope (NOT, La Palma) on 4 March, with the INT on 9 March, and with the ESO New Technology Telescope (NTT) on 13 March (see Table 2.1 for a summary). The transient was not detected in these images, which puts a lower limit on its average decay rate (in 4 days) of 0.7 mag per day. The NTT image shows that at the location of the variable object there is an extended object, probably a galaxy (Groot et al. 1997b; Metzger et al. 1997; Fig. 2.3); this object is also seen in the INT B- and R-band images of March 9. From differential astrometry relative to the nearby stars for both the V- and I-band images, we find that the centres of the optical transient and the galaxy have a relative distance ($0\farcs22 \pm 0\farcs12$). (1σ; quadratic addition of the errors in two relative positions). The relative position of the optical transient did nog change by more than $0\farcs2$ between the 28 February V- and I-band images. From the NTT images and the 9 March INT image we measured (Groot et al. 1997b) the galaxy's magnitude to be $R = 23.8 \pm 0.2$ and 24.0 ± 0.2, respectively, consistent with the value of R = 24.0, reported by Metzger et al. (1997), and $B = 25.4 \pm 0.4$ (see Table 2.1).

Table 2.1. Summary of optical observations

Date (1997)	Time (UT)	Telescope	Band	Int. time (s)	Magnitude	Remarks
28 Feb.	23^h48^m	WHT	V	300	V=21.3	Transient
28 Feb.	23^h53^m	WHT	I	300	I=20.6	Transient
04 Mar.	20^h42^m	NOT	V	900	$V > 24.2$	
08 Mar.	20^h42^m	INT	V	2500	$V > 23.6$	
08 Mar.	21^h12^m	WHT	I	300	$I > 22.2$	
09 Mar.	21^h30^m	INT	R	1200	R=24.0	Extended
09 Mar.	20^h30^m	INT	B	2500	B=25.4	Extended
13 Mar.	0^h0^m	NTT	R	3600	R=23.8	Extended

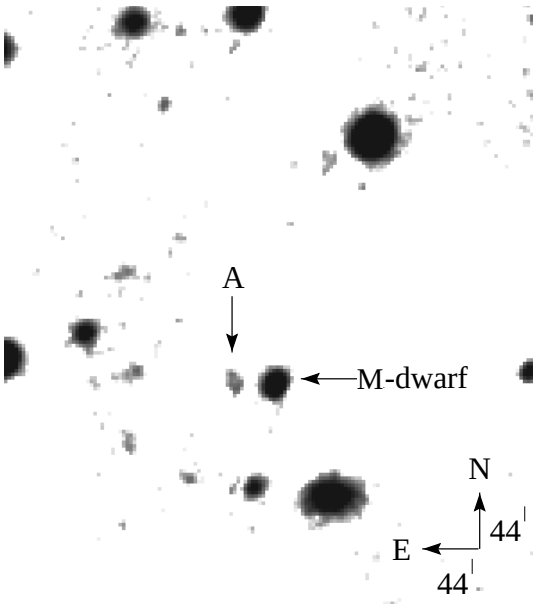

Figure 2.3. R-band image of a $44'' \times 44''$ region of the sky containing the position of the optical transient, obtained with the NTT on 1997 13 March, 0^hUT. The faint galaxy coincident with the optical transient (A) and the M-dwarf are indicated.

2.3 Discussion

Known types of optical transient events (novae, supernovae, dwarf novae, flare stars) are unlikely to account for the optical transient for a variety of reasons, such as the amplitude and short timescale of its variability, its colour index, or its inferred distance. The GRB source is located relatively close to the ecliptic, at latitude -11° , and this raises the possibility that the optical transient is an asteroid. However, on 1 March asteroids in the direction of the GRB have proper motion of at least $0\overset{d}{.}1$ per day (T. Gehrels, private communication), which would have led to easily detectable motion ($>2\overset{''}{.}5$) during the 600-s total exposure time of our two separate images. On the basis of its proper mo-

tion during our two exposures we cannot rule out that the optical transient is a Kuiper Belt object. However, its non-detection on other images taken in the week following the GRB, the low-surface density (one per several hundred square degree at 21st magnitude, T. Gehrels, personal communication) of Kuiper belt objects, and their very red colours (Luu and Jewitt 1996), make such objects a highly unlikely explanation of the optical transient.

The variability of the optical sky above 21st magnitude, on timescales of a few days, has not yet been extensively explored (Paczyński 1997; Trevese et al. 1989), and it is therefore not possible to make a firm estimate of the probability that the optical transient we detected is a faint, strongly variable AGN, unrelated to the GRB, or has another (unknown) origin unrelated to the GRB. Some information is available from the faint-galaxy monitoring program of Kochanski et al. (1996), which covered 2830 galaxies (down to B = 24.8, R = 23.3) in a $16' \times 16'$ field during 10 years. They found that near B = 24 only $\sim 0.5\%$ of these varied by more than 0.03 mag on a timescale of months to years; none varied by more than a magnitude. Variability of blazars on timescales of minutes to hours does not exceed 0.3 mag; day-to-day variations of a factor of two or more have been observed (Miller and Noble 1996).

Although we cannot firmly exclude that the optical transient in the error box of GRB 970228 is caused by some unknown event unrelated to the GRB, the temporal coincidence between the optical and X-ray transients, and their spatial coincidence with the GRB lead us to believe that both the optical transient and the decaying *BeppoSAX* X-ray source are associated with GRB 970228

2.4 Multiwavelength observations

Radio observations (at 6 cm wavelength) of the GRB error box (Groot et al. 1997a) made with the Westerbork Synthesis Radio Telescope on February 28, $23^{\rm h}17^{\rm m}$UT (for 1.2h; 20.4h after the GRB, simultaneous with the WHT observations) and on March 1, $18^{\rm h}$ UT and March 2, $18^{\rm h}$ UT (each lasting 12 hours) show that at the position of the optical transient there is then no radio point source with a flux exceeding 1.0, 0.33 and 0.33 mJy, respectively (2σ upper limit).

Some rough spectral information on the optical/X-ray transient can be obtained if we assume that between the two *BeppoSAX* X-ray observations, made 4 days apart, the X-ray flux of the transient decreased with time since the GRB as a power law. Approximating the spectrum with $F_\nu \propto \nu^\alpha$ we estimate from $F_{\rm X} \simeq 0.04$ μJy (interpolated) and $F_{\rm V} \simeq 10$ μJy, that α = –0.7 $\pm$ 0.1. Extrapolation of this spectrum to the radio region would lead to an expected radio flux density of 10–100 mJy, far exceeding the observed upper limit. This indicates that the X-ray, optical and radio flux densities of the transient cannot be represented by a single power law.

2.5 Positional coincidence with a galaxy

The close position coincidence between the optical transient and the galaxy suggests that the transient may be located in that galaxy. In an effort to quantify this we adopt a bayesian approach. We consider three disjoint and exhaustive hypotheses for the source of the optical transient. The hypotheses are: $H_{\rm c}$, the optical transient is in the centre of a galaxy; $H_{\rm g}$, the optical transient is in a galaxy, but not at its centre; and $H_{\rm n}$, the optical transient is not in a galaxy.

We assume here that there is a single optical transient detected in the field of view of angular area A and that n non-overlapping galaxies are detected in the field. The transient is at distance $r \pm \sigma$ from the nearest galaxy, where the error includes the uncertainty in the positions of the centroids of both the galaxy and the transient. The probability density at r under $H_{\rm c}$ is $P(r|H_{\rm c}) = (2\pi\sigma_r^2 n)^{-1}\exp[-(r^2/2\sigma_r^2)]$. The probability density under $H_{\rm g}$ depends on the size, shape and inclination of the galaxy and the specifics of the model for the distribution of sources in the galaxy. For simplicity, we assume the probability density to be gaussian with width $\sigma_{\rm g}$. Then $P(r|H_{\rm g}) = (2\pi\sigma_g^2 n)^{-1}\exp[-(r^2/2\sigma_g^2)]$. The probability density under $H_{\rm n}$ is uniform over the field of view so $P(r|H_{\rm n}) = A^{-1}$. The posterior probability of each hypothesis H is $P(H|r) = kP(H)P(r|H)$, where $P(H)$ is the prior probability and the normalization constant k is obtained by requirement that $P(H_{\rm c}|r) + P(H_{\rm g}|r) + P(H_{\rm n}|r) = 1$.

For the NTT observation we find seven galaxies in A = (44″)^2 field, that is, n = 13 per arcmin^2, r = 0.″22, σ = 0.″12. A reasonable estimate for the galaxy width is $\sigma_{\rm g}$ = 1″. With these values the probability densities at r are $P(r|H_{\rm c})$ = 0.294, $P(r|H_{\rm g})$ = 0.022 and $P(r|H_{\rm n})$ = 0.0005, all in units of arcsec^{-2}. Assuming equal priors $P(H_{\rm c})$ = $P(H_{\rm g})$ = $P(H_{\rm n})$ = 1/3, the posterior probabilities are $P(H_{\rm c}|r)$ = 0.928, $P(H_{\rm g}|r) = 0.070$ and $P(H_{\rm n}|r)$ = 0.0016. The posterior probability for $H_{\rm g}$ depends sensitively on the assumed $\sigma_{\rm g}$. However, the posterior probability, $P(H_{\rm n}|r)$ that the transient is not associated with a galaxy is in the range 0.09–0.18%, for any assumptions about the size of faint galaxies. Within the range of assumed values for σ_r between 0.″08 and 0.″2 the values of $P(H_{\rm n}|r)$ increase by less than a factor of 3.

The above analysis suggests that the optical transient is related to the faint galaxy, which provides support for the cosmological distance scale for GRBs. A rough estimate of the expected redshift, z of the galaxy may be made by assuming that its absolute magnitude is in the range –21 to –16, which covers the bulk of normal galaxies (Schechter 1976). For an assumed Hubble constant of 60 km s^{-1} Mpc^{-1}, this corresponds to z in the range 0.2–2.

The close proximity of the optical transient to the centre of the faint galaxy, and the presence of relatively bright quasars in the 8.′2 error box of GRB 781119 (V = 20; Pedersen et al. 1983; Pedersen and Hansen 1997; Boer et al. 1997), and in the 3′(radius) error box (in 't Zand et al. 1997) of GRB 960720 (R = 18.8; Greiner and Heise, 1997; Piro et al. 1997,

Walsh et al. 1984) raise the possibility that GRBs occur preferentially, or exclusively, in or near galactic nuclei.

2.6 Conclusions

Searches for an optical counterpart to a GRB have been continually attempted for the past 20 years. Recent reviews and descriptions of serendipitous, rapid follow-up, and delayed searches for the optical counterparts of GRBs (Barthelmy et al. 1996; McNamara et al. 1996a, b; Vrba, Hartmann and Jennings 1995; Vrba 1996; Luginbuhl et al. 1996; Castro-Tirado et al. 1994; Klose 1995; Schaefer 1994) show that these previous searches were generally made a week or longer after the GRB, or they were not as deep ($V < 20$) as the images presented here. The most sensitive rapid follow-up observations so far had delay times (δt) and limiting magnitudes (m) as follows: δt = 1.85 d, $m < 23$ (Shaefer et al. 1994), and δt = 4.0d, $m_{\rm B} < 22$ (McNamara et al. 1996a).

It was not until the launch of *BeppoSAX* in 1996 that accurate (several arcmin) locations for GRBs became available within hours of detection, hence facilitating rapid follow-up observations at large ground-based optical telescopes for those bursts which happened to be in the field of the WFC. The continued operation of *BeppoSAX* and the approval of the *High Energy Transient Explorer-2* (HETE-2) mission bode well for great progress in the rapid follow-up observations of GRBs. Also, near-real-time, fully automated optical systems linked to the BATSE-BACODINE (Barthelmy et al. 1996) system are becoming operational, and their sensitivity is continually improving (Park et al. 1997; Lee et al. 1997).

We expect that X-ray and optical transients associated with GRBs will again be seen (though perhaps not in all cases; Castro-Tirado et al. 1997) in the near future. This could be a turning point in GRB astronomy. Detailed studies (light curves and spectra) of such transients can be expected within a year, and we are optimistic that the distance scale as well as the mechanism behind the enigmatic GRBs are now in reach.

Acknowledgments We thank T. Courvoisier, T. Gehrels, J. Hakkila, D. Hartmann, M. Kippen, S. Pehrlmutter, P. Sackett, T. Tyson and M. Urry for their helpfull answers to our many questions. We also thank W. Lewin and M. van der Klis and the referee, F. Vrba, for their critical comments on this Letter.

Note added in proof: After this paper was submitted, an HST observation was made of the optical transient (Sahu et al. 1997). This observation confirms that the transient is associated with an extended emission region, but seems to exclude that the transient is at the centre of that region.

References

Barthelmy, S. et al. 1996, AIP Proc. 384, 580
Boer, M. et al. 1997, ApJ submitted
Bonura, A. et al. 1992, Proc. SPIE 1743, 510
Castro-Tirado, A. et al. 1994, AIP Proc. 307, 404
Castro-Tirado, A. et al. 1997, IAU Circular, No. 6598
Cline, T.L. et al. 1997, IAU Circular, No. 6593
Costa, E. et al. 1997, Nature 387, 783
Fishman, G.J. and Meegan, C.A. 1995, ARA&A 33, 415
Frail, D. et al. 1997, IAU Circular, No. 6576
Frontera, F. et al. 1991, Adv. Space Res. 11, 281
Greiner, J. and Heise, J. 1997, IAU Circular, No. 6570
Groot, P.J. et al. 1997a, IAU Circular, No. 6584
Groot, P.J. et al. 1997b, IAU Circular, No. 6588
Groot, P.J. et al. 1997c, IAU Circular, No. 6574
Hakkila, J. et al. 1997, AJ 114, 2043
Hurley, K. et al. 1996, AIP Proc. 384, 422
Hurley, K. et al. 1997, IAU Circular, No. 6594
Jager, R. et al. 1997, A&AS 125, 557
Johnson, H.L. 1966, ARA&A 4, 191
Klebesabel, R.W., Strong, I.B. and Olson, R.A. 1973, ApJ 182, L85
Klose, S. 1995, ApJ 446, 357
Kochanski, G.P., Tyson, J.A. and Fischer, P. 1996, AJ 111, 1444
Landolt, A. 1992, AJ 104, 340
Lee, B. et al. 1997, ApJL 482, L125
Luginbuhl, C. et al. 1996, AIP Proc. 384, 676
Luu, J. and Jewitt, D. 1996, AJ 112, 2310
McNamara, B. et al. 1996a ApJS 103, 173
McNamara, B. et al. 1996b AIP Proc. 384, 680
Meegan, C.A. et al. 1992 Nature 355, 143
Metzger, M.R. et al. 1997, IAU Circular, No. 6588
Miller, H.R. and Noble, J.C. 1996, ASP Conf. Ser. 110, 17
Paczyński, B. 1986, ApJL 308, L43
Paczyński, B. 1998, in Proc. 12th AIP Colloq., in press
Palmer, D. et al. 1997, IAU Circular, No. 6577
Park, H.S. et al. 1997, ApJ 490, 99
Parmar, A.N. et al. 1997, A&AS 122, 309

Pedersen, H. et al. 1983, ApJL 270, L43
Pedersen, H. and Hansen, J. 1997, ApJ submitted
Piro, L., Scarsi, L. and Butler, R.C. 1995, Proc. SPIE 2517, 169
Piro, L. et al. 1997, IAU Circular, No. 6570
Podsiadlowski, Ph., Rees, M.J. and Ruderman, M. 1995, MNRAS 273, 755
Sahu, K.C. et al. 1997, Nature 387, 476
Schaefer, B. et al. 1994, ApJL 422, L71
Schechter, P. 1976, ApJ 203, 297
Trevese, D. et al. 1989, AJ 98, 108
Vrba, F., Hartmann, D. and Jennings, M. 1995, ApJ 446, 115
Vrba, F. 1996, AIP Proc. 384, 565
Walsh, D. et al. 1984, MNRAS 211, 105
Yoshida, A. et al. 1997, IAU Circular, No. 6576
in ’t Zand et al. 1997, IAU Circular, No. 6969

3

A Search for Optical Afterglow from GRB 970828

P.J. Groot, T.J. Galama, J. van Paradijs, C. Kouveliotou, R.A.M.J. Wijers, J. Bloom, N. Tanvir, R. Vanderspek, J. Greiner, A.J. Castro-Tirado, J. Gorosabel, T. von Hippel, M. Lehnert, K. Kuijken, H. Hoekstra, N. Metcalfe, C. Howk, C. Conselice, J. Telting, R.G.M. Rutten, J. Rhoads, A. Cole, D.J. Pisano, R. Naber, R. Schwarz

Astrophysical Journal Letters, 493, 27 (1998)

We report on the results of R band observations of the error box of the γ-ray burst of August 28, 1997, made between 4 hours and 8 days after this burst occurred. No counterpart was found varying by more than 0.2 magnitudes down to $R = 23.8$. We discuss the consequences of this non-detection for relativistic blast wave models of γ-ray bursts, and the possible effect of redshift on the relation between optical absorption and the low-energy cut off in the X-ray afterglow spectrum.

3.1 Introduction

Since the first discovery of a γ-ray burst (GRB) in 1967 (Klebesabel et al., 1973) these short outbursts of highly energetic photons have formed one of astronomy's most elusive problems. Following the discovery by Meegan et al. (1992) of their isotropic sky distribution and inhomogeneous spatial distribution (which excluded that GRBs originate from a galactic-disk source population) the discussion on the nature of GRB sources focussed on their distances: either of order 10^5 pc ('galactic halo' model), or several Gpc ('cosmological' model). The association of the optical counterpart of GRB 970228 (Groot et al., 1997; Van Paradijs et al., 1997) with what is most likely a galaxy (Groot et al, 1997b; Metzger et al., 1997a; Sahu et al., 1997) and especially the determination of a redshift for

GRB 970508 (Metzger et al., 1997b) have shown that GRBs are located at cosmological distances, and are thereby the most luminous photon sources known in the Universe. The question of what causes GRBs has now become the centerpiece of the discussion, and the detection of more optical counterparts is a key element in determining this cause.

In this Letter we report on our search for a transient optical counterpart for GRB 970828, based on observations made with the 4.2m William Herschel Telescope (WHT) on La Palma, and the 3.5m WIYN Telescope on Kitt Peak. None was detected, down to a magnitude level $R = 23.8$.

GRB 970828 was discovered with the All-Sky Monitor (ASM) on the *Rossi X-ray Timing Explorer (RXTE)* on August 28, 1997, UT $17^{\rm h}44^{\rm m}36^{\rm s}$ from an elliptical region centered at RA=$18^{\rm h}08^{\rm m}29^{\rm s}$, Dec=+59° 18′.0 (J2000), with a major axis of 5′.0, and a minor axis of 2′.0 (Remillard et al. 1997; Smith et al. 1997). Within 3.6 hours the *RXTE/PCA* scanned the region of the sky around the error box of the ASM burst, and detected a weak X-ray source, located in the ASM error box with a 2–10 keV flux of 0.5 mCrab (Marshall et al. 1997). The burst was also detected with the Burst And Transient Source Experiment (BATSE) and the GRB experiment on Ulysses. Its fluence and peak flux were 7×10^{-5} erg cm^{-2}, and 3×10^{-6} erg cm^{-2} s^{-1}, respectively. From the difference between burst arrival times, its position was constrained to lie within a 1.62 arcminute wide annulus, that intersected the RXTE error box (Hurley et al. 1997). In an ASCA observation made between Aug. 29.91 and 30.85 UT, a weak X-ray source was detected at an average flux level of 4×10^{-13} erg cm^{-2} s^{-1} (2–10 keV). The ASCA error box is centered on RA=$18^{\rm h}08^{\rm m}32^{\rm s}.3$, Dec =+59° 18′54″(J2000) and has a 0′.5 radius (Murakami et al. 1997).

3.2 Observations and Data Analysis

We observed the GRB error box with the Prime Focus Camera of the WHT, on 9 nights between August 28, UT $21^{\rm h}47^{\rm m}$, and September 5, UT $22^{\rm h}07^{\rm m}$ (see Table 3.1). The first observation was made just over 4 hours after the γ-ray burst. All observations were made with a Cousins R band filter (Bessell 1979). During the first two nights and the last three nights, we used a LORAL 2048×2048 CCD chip, with 15μ pixels, giving a field of view of 8′.45×8′.45. During the intervening nights we used an EEV CCD chip (2048×4096), windowed at 2048×2400, with 13.5μ pixels giving a 8′.1×9′.5 field of view. On August 30 two R band images were made with the WIYN Telescope. The camera contained a 2048×2048 CCD, giving a field of view of 6′.8×6′.8.

We obtained a photometric calibration of the CCD images from observations of Landolt Selected Area 113, stars 281, 158, 183 and 167 (Landolt 1992), on Aug 31, $0^{\rm h}14^{\rm m}$ UT with the WHT.

A region of 2′×2′ centered on the ASCA position in the bias-subtracted and flatfielded images was analyzed using DoPhot (Schechter et al., 1993), in which astrometric and

Table 3.1. Log of observations GRB 970828

Date	Telescope	UT Start	Exp. time (s)	Seeing
Aug 28	WHT	21:47	900	0.″86
Aug 29	WHT	21:15	900	0.″74
Aug 30	WIYN	05:08	600	0.″8
Aug 30	WIYN	07:38	900	1.″2
Aug 30	WHT	23:22	900	0.″90
Aug 31	WHT	20:54	900	0.″71
Sep 1	WHT	21:16	600	0.″80
Sep 2	WHT	20:53	600	0.″76
Sep 3	WHT	22:44	600	0.″88
Sep 4	WHT	21:53	600	0.″79
Sep 5	WHT	22:07	600	0.″86

photometric information of all objects are determined from bivariate Gaussian function fits to the brightness distribution in their image; the parameters of these fits also tell us whether an object is stellar (i.e., unresolved) or a galaxy. In this region (see Fig. 3.1) we find a total of 63 objects, 36 of which are stellar, and 27 are galaxies, down to R=23.8.
We have searched for variable objects by comparing the magnitudes of each star as determined for each of the images. Comparison of images taken on different nights showed no variation on time scales between a day and a week in excess of 0.2 mag for $R \leq$23.8 (for the last three nights the limit on variability is 0.3 mag for $R \leq$23.8). Comparison of three images taken on the night of August 29 to 30 showed no variations on time scales of several hours in excess of 0.2 mag for $R < 22.5$.

3.3 Discussion

3.3.1 Comparison with afterglows of GRB 970228 and GRB 970508

The large variation in optical response of GRBs (relative to their strength in γ rays) was already clear from a comparison between GRB 970228 and GRB 970111. Within a day after GRB 970228 ocurred it showed an optical afterglow at R = 20.8 (Van Paradijs et al. 1997; Galama et al. 1997a; Pedichini et al. 1997; Guarneri et al. 1997). GRB 970111 was not detected in optical observations made 19 hours after it occurred ($R >$20.8, and $R >$22.6, for variations in excess of 0.2 and 0.5 magnitudes, respectively, Castro-Tirado et al. 1997), in spite of the fact that its γ-ray fluence (Galama et al., 1997b) was five times larger than that of GRB 970228 (Costa et al., 1997). Since only one deep image was made in the week following GRB 970111, its non-detection may have been the result

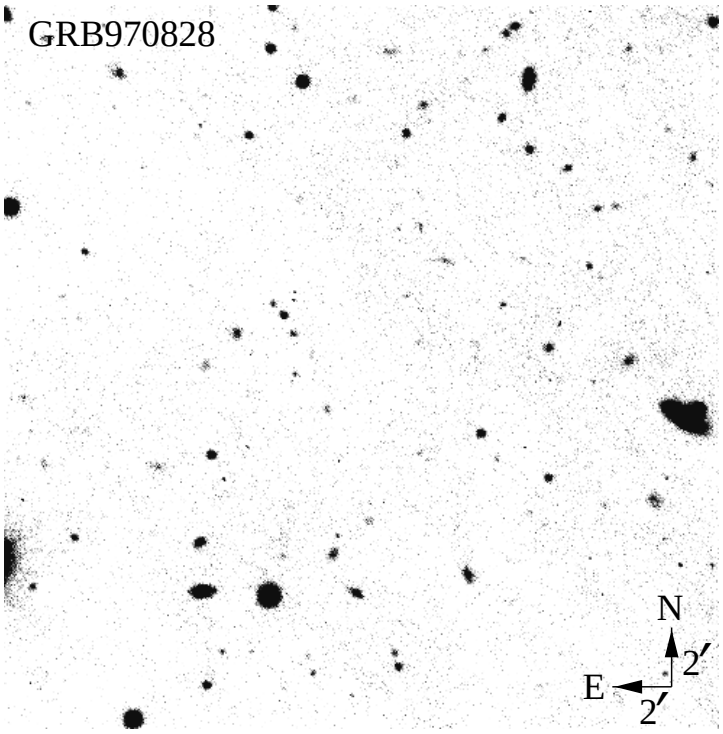

Figure 3.1. $2' \times 2'$ R-band image of the sky region centered on the $0.5'$ radius ASCA error box of GRB 970828, taken at the WHT on Sept 2.

of, e.g., a very rapid decay of any optical afterglow, or a very slow rise thereof (like for GRB 970508, see Bond 1997; Djorgovski et al. 1997; Sahu et al. 1997b; Galama et al. 1998).

The non-detection ($R >$23.8 for variations in excess of 0.2 magnitudes) of GRB 970828 during our optical observations, which covered the time interval between 4 hours and 8 days after the burst at intervals of a day, show the very large range in optical responses of GRBs in an even more striking fashion. We have used the fluence, $E_{\rm GRB}$ (in ergs cm^{-2}), as a measure of the GRB strength, and compared the ratio of the optical peak flux to the GRB fluence of GRB 970828 with that of GRB 970508. The latter had a peak magnitude $R =$19.8 (Mignoli et al., 1997), therefore the difference in optical peak luminosities between GRB 970508 and GRB 970228 is more than 4 magnitudes. The ratio of their fluences, $E_{\rm GRB}$(970828)/$E_{\rm GRB}$(970508)=24 (Kouveliotou et al. 1997a,b). Thus, we find that the optical peak response of GRB 970828, with respect to its γ-ray fluence, is a factor $\sim 10^3$ smaller than that of GRB 970508. (Compared to GRB 970228 the difference is a factor $>10^2$.)

We have made a similar comparison with published X-ray afterglow fluxes ($F_{\rm X}$) for the two GRBs with optical afterglow. Most of these refer to the energy range 2–10 keV.

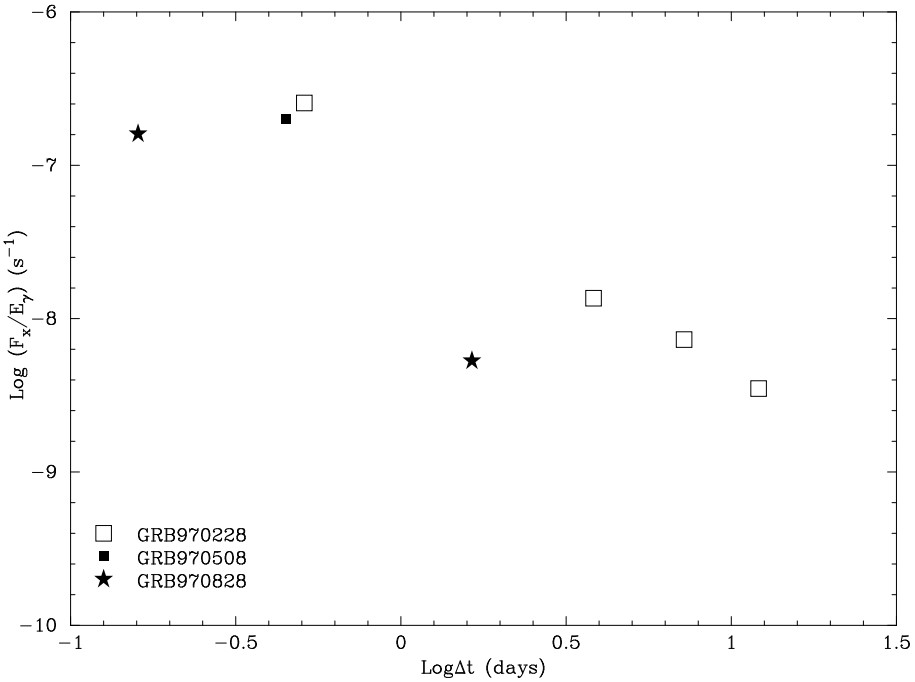

Figure 3.2. Variation of the ratio $R_{\rm X}$ of the afterglow (2-10 keV) X-ray flux (see text) to the fluence in the γ-ray burst as function of time in days. GRB fluences were obtained from the following sources. GRB 970228: Costa et al. (1997); GRB 970508: Kouveliotou et al. (1997a); GRB 970828: Kouveliotou et al. (1997b). The X-ray fluxes were obtained from the following sources: GRB 970228: Costa et al. (1997), Yoshida et al. (1997), Frontera et al. (1997); GRB 970508: Piro et al. (1997); GRB 970828: Marshall et al. (1997), Murakami et al. (1997b).

Only the ROSAT fluxes had to be transformed to this range; in doing this we assumed a power law X-ray spectrum with photon index in the range –1.4 to –2.0 (Costa et al. 1997; Yoshida et al. 1997). This range leads to an uncertainty in the transformed ROSAT flux of less than a factor 2. The results, in the form of the ratio $\mathcal{R}_{\rm X} = F_{\rm X}/E_{\rm GRB}$, are summarized in Fig. 3.2, which shows the variation of this quantity as a function of the time interval since the burst, for four bursts with published X-ray afterglow information. This figure shows that the differences in $\mathcal{R}_{\rm X}$ between these bursts are moderate (less than an order of magnitude). It is noteworthy that the two bursts with optical counterparts also have the highest values of $\mathcal{R}_{\rm X}$ (for a given value of Δt).

We finally compared the peak flux in the R-band afterglows with the brightness of the X-ray afterglow. In view of their rather similar decay rates we used for the latter the 2–10 keV flux as measured 1 day after the GRB occurred, $F_{\rm X}$(1 day). The corresponding ratio $F_{\rm peak}(R_{\rm band})/F_{\rm X}$ (1 day) for GRB 970828 differs by a factor $>$150 from that for GRB 970508, and a factor $>$10 from that for GRB 970228.

3.3.2 Comparison with Relativistic Blast Wave Models

A relatively succesful way of explaining the existence of GRB afterglows (at all wavelengths) has been the so-called blastwave or fireball models (e.g. Mészáros 1995). These models involve the generation of a massive amount of energy in a very small, compact region, by an unexplained mechanism. The result of this dumping of energy is a relativistically expanding fireball (blastwave), that collides with the interstellar or circumstellar medium and generates shocks that emit the synchrotron radiation that is observed as the afterglow.

Figure 3.3 shows the available data for GRB 970828 in γ-rays, X-rays, B, and R, plus simple blastwave model fits, which are normalized to agree with the X-ray data. If we compare this with the data available for GRB 970228 (Wijers , Rees and Mészáros, 1997), it is striking that the decay part of the X-ray curves are virtually the same for these two bursts (i.e. in slope *and* offset). But whereas the first stages of the optical decay for GRB 970228 are in good agreement with the afterglow prediction (Wijers, Rees, and Mészáros 1997), the earliest upper limit to the optical brightness of GRB 970828 is 300 times lower than the predicted value.

The simplest spherically symmetric blastwave models for GRB afterglows require that the slope of the spectrum follows from the slope of the temporal decay, once the decay curve is measured in one wavelength band and is found to be a pure power law. From that, the offset in brightness at any other waveband is fixed and the predicted flux at that waveband is hard to change. Mészáros, Rees and Wijers (1998) showed that if the blastwave is beamed one can get different relations between spectral and temporal slopes, giving possibly much smaller offsets between the optical and X-ray light curves of the afterglow. As an example, let the energy per unit solid angle, E, vary with angle from the jet axis, θ, as $E \propto \theta^{-4}$ and the Lorentz factor $\Gamma \propto \theta^{-1}$. Then a temporal decay rate $F \propto t^{-1.3}$ as seen here would occur for a spectrum $F_\nu \propto \nu^{0.4}$, i.e. it would rise from optical to X rays and the predicted R band curve would be a factor 24 below the X-ray curve. At the time of our first limit this model would give R =28.4, quite consistent with the data.

3.3.3 Absorption in Redshifted Material

Another explanation, pointed out to us by dr. B. Paczyński, for the non-detection of an optical afterglow could be photoelectric absorption, also visible as a low-energy cut-off in the X-ray spectrum. If we assume a modest hydrogen column density of $N_{\rm H} \sim 10^{21}$ atoms cm^{-2} and make the assumption that the absorbing material is at redshift z=0, this would imply 0.34 magnitudes of extinction in the R band (Gorenstein 1975; Cardelli et al. 1989).

In case the absorption takes place at some redshift z the effect is a bit more complicated.

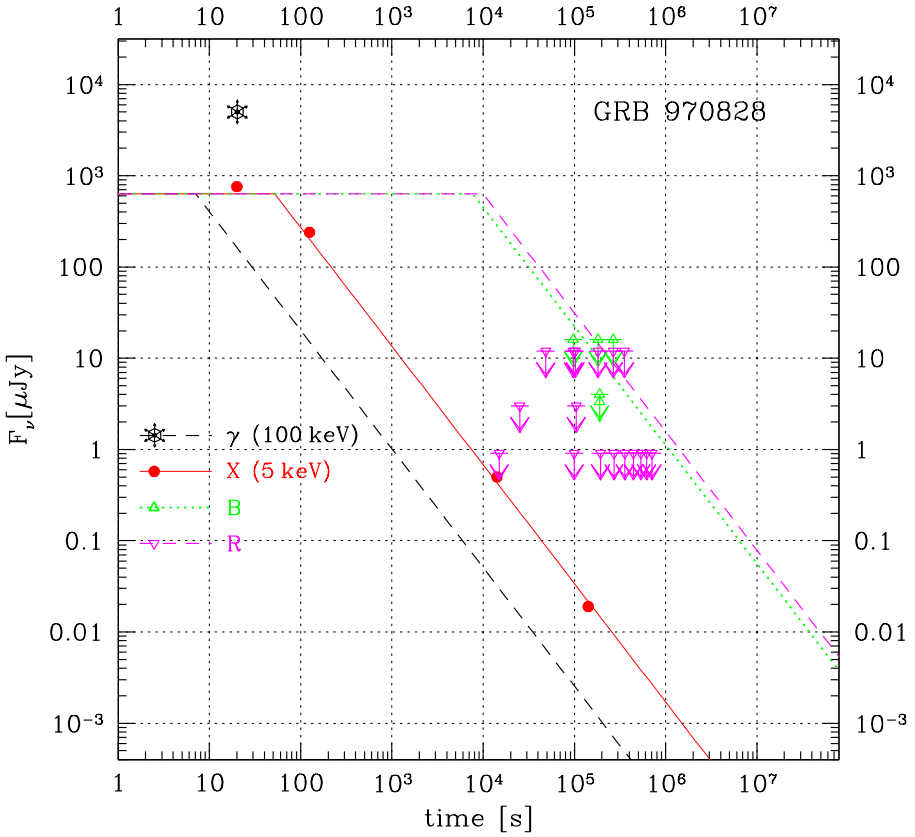

Figure 3.3. Variation of the observed fluxes in γ rays, X rays, and in the B and R bands of GRB 970828, together with simple blast wave model fits as described in Wijers, Rees and Mészáros (1998).

The cross section for photo-electric absorption in the (0.2–5) keV range depends on energy roughly as $E^{-2.6}$ (Morrison and McCammon 1983). Then the factor by which the apparent $N_{\rm H}$, inferred from the low-energy cut-off in the X-ray spectrum, has to be increased is approximately $(1+z)^{2.6}$. If we assume, for example, that the GRB occured at a redshift of z=1, the factor by which the apparent value of $N_{\rm H}$ has to be increased would be $\sim$6. Moreover, the photons in the R band we observe would be at wavelengths near 3200 Å at the source, at which wavelength the interstellar absorption is approximately a factor 2.5 larger than in the R band (Cardelli et al., 1989). These combined effects would lead, for a GRB at z=1 and an apparent, moderate, $N_{\rm H}$=10^{21} atoms cm^{-2} to an R band extinction of $\sim$5 mags.

If absorption is the correct explanation, a substantial fraction of GRB sources (those with a very small optical response) would be located close to where large column densities are available, i.e., in disks of galaxies. This would link GRBs to a population of massive stars. This is expected for the failed-supernova model and for the hypernova model, proposed

by Woosley (1993) and Paczyński (1998), respectively. In view of the large kick velocities imparted on neutron stars at birth (Lyne and Lorimer 1994; Hansen and Phinney 1997; Van den Heuvel and Van Paradijs 1997) it remains to be seen whether a merging neutron star binary model would be consistent with this consequence.

Acknowledgments We thank the *RXTE* ASM and PCA teams for their very fast response to and communications regarding the γ-ray burst of August 28, 1997. We thank B. Paczyński and W. Lewin for enlightening discussions on the importance of redshift for absorption of optical afterglows. TG is supported by NFRA under grant no. 781.76.011. JG and RS are supported by the Deutsche Agentur für Raumfahrtangelegenheiten (DARA) GmbH under contract FKZ 50 QQ 9602 3 and 50 OR 9206 8, respectively.

References

Bessel, M.S., 1979, PASP 91, 589
Bond, H.E. 1997, IAU Circular, No. 6654
Castro-Tirado, A. et al. 1997, IAU Circular, No. 6598
Cardelli, J.A, Clayton, G.C, Mathis, J.S., 1989, ApJ 345, 245
Costa, E. et al. 1997, Nature 387, 783
Djorgovski, S.G. et al. 1997, Nature 387, 876
Frontera, F. et al. 1997, IAU Circular, No. 6637
Galama, T.J. et al. 1997a, Nature 387, 479
Galama, T.J. et al., 1997b, ApJ 486, L5
Galama, T.J. et al. 1998, ApJ 497, L13
Gorenstein, P., 1975, ApJ 198, 95
Groot, P.J. et al., 1997a, IAU Circular, No. 6584
Groot, P.J. et al., 1997b, IAU Circular, No. 6588
Guarneri, A. et al. 1997, private communication
Hansen, B.M.S, and Phinney, E.S., 1997, MNRAS, 291, 569
Hurley, K. et al. 1997, IAU Circular, No. 6728
Klebesabel, R.W., Strong, I.B. and Olson, R.A., 1973, ApJ 182, L85
Kouveliotou, C. et al., 1997a, IAU Circular, No. 6660
Kouveliotou, C. et al., 1997b, private communication
Landolt, A. 1992, AJ 104, 340
Laureijs, R., 1989, PhD thesis, Groningen University
Lyne, A. and Lorimer, D., 1994, Nature 269, 127
Marshall, F.A. et al., 1997, IAU Circular, No. 6727
Meegan, C.A. et al., 1992, Nature 355, 143

Mészáros, P., 1995, Proc. 17th Texas Symp., Annals N.Y. Acad. Sci., 759, 440
Mészáros, P., Rees, M.J. and Wijers, R.A.M.J., 1998, ApJ 499, 301
Metzger, M. et al., 1997a, IAU Circular, No. 6588
Metzger, M. et al., 1997b, Nature 387, 878
Mignoli, M. et al., 1997, IAU Circular, No. 6661
Morrison, R. and McCammon, D., 1983, ApJ 270, 119
Murakami, T. et al., 1997, IAU Circular, No. 6732
Paczyński, B. 1998, ApJ 494, L45
Pedichini et al. 1997, A&A 327, L36
Piro, L. et al. 1997, IAU Circular, No. 6656
Remillard, R.A. et al. 1997, IAU Circular, No. 6726
Sahu, K. et al., 1997a, Nature 387, 476
Sahu, K. et al. 1997b, ApJ 489, L127
Schechter, P.L., Mateo., M., and Saha, A., 1993, PASP 105, 1342
Smith, D. et al. 1997, IAU Circular, No. 6728
Van den Heuvel, E.P.J., Van Paradijs, J., 1997, ApJ 483, 399
Van Paradijs, J. et al. 1997, Nature 386, 686
Wijers, R.A.M.J., Rees, M.J. and Meszaros, P. 1997, MNRAS 288, L51
Woosley, S.E., 1993, ApJ 405, 273
Yoshida, A., et al. 1997, IAU Circular, No. 6593

4

The Rapid Decay of the Optical Emission from GRB 980326 and its Possible Implications

P.J. Groot, T.J. Galama, P.M. Vreeswijk, R.A.M.J. Wijers, E. Pian, E. Palazzi, J. van Paradijs, C. Kouveliotou, J.J.M. in 't Zand, J. Heise, C. Robinson, N. Tanvir, C. Lidman, C. Tinney, M. Keane, M. Briggs, K. Hurley, J.-F. Gonzalez, P. Hall, M.G. Smith, R. Covarrubias, P. Jonker, J. Casares, F. Frontera, M. Feroci, L. Piro, E. Costa, R. Smith, B. Jones, D. Windridge, J. Bland-Hawthorn, S. Veilleux, M. Garcia, W.R. Brown, K.Z. Stanek, A.J. Castro-Tirado, J. Gorosabel, J. Greiner, K. Jäger, A. Böhm, K.J. Fricke

Astrophysical Journal Letters, 502, 123 (1998)

We report the discovery of the optical counterpart to GRB 980326. Its rapid optical decay can be characterized by a power law with exponent –2.10±0.13 and a constant underlying source at R_c=25.5 ±0.5. Its optical colours 2.1 days after the burst imply a spectral slope of –0.66±0.70. The γ-ray spectrum as observed with BATSE shows that it is among the 4% softest bursts ever recorded. We argue that the rapid optical decay may be a reason for the non-detection of some low-energy afterglows of GRBs.

4.1 Introduction

The redshift determinations for GRB 970508 (Metzger et al., 1997) and GRB 971214 (Kulkarni et al., 1998) have demonstrated that GRBs originate at cosmological distances and are therefore the most powerful photon sources in the Universe, with peak luminosities exceeding 10^{52} erg/s, assuming isotropic emission. Afterglow studies of GRB 970228 (Galama et al., 1997, 1998a), GRB 970508 (Galama et al., 1998b, c, d; Pedersen et al.,

1998; Castro-Tirado et al., 1998a), and GRB 971214 (Halpern et al., 1998, Diercks et al., 1998) show a generally good agreement with fireball model predictions (Wijers, Rees and Mészarós, 1997; Sari, Piran and Narayan, 1998, hereafter SPN98).

There are, however, a few marked cases where no X-ray or optical afterglow is seen, most notably GRB 970111 (optical: Castro-Tirado et al., 1997; Gorosabel et al., 1998, X-rays, debated: Feroci et al.,1998), GRB 970828 (optical: Groot et al., 1998a) and GRB 980302 (X-rays). In the last case, *RossiXTE* /PCA scanning, starting only 1.1 hours after the burst, found no X-ray afterglow at a level >1 mCrab. One possible explanation for the lack of optical counterparts is the extinction by large column densities of gas and dust, obscuring the GRB afterglows (Groot et al., 1998a; Halpern et al., 1998). This might indicate an origin in star-forming regions where large quantities of gas and dust are present (e.g. Paczyński, 1998). However, this scenario does not so readily explain the non-detection of an X-ray afterglow.

GRB 980326 was detected (Celidonio et al., 1998) on Mar. 26.888 UT with one of the Wide Field Cameras (WFCs; Jager et al., 1997) and the Gamma Ray Burst Monitor (GRBM; Frontera et al., 1997; Feroci et al., 1997) on board *BeppoSAX* (Piro, Scarsi and Butler, 1995), with *Ulysses* (Hurley et al., 1998) and with the Burst and Transient Source Experiment (BATSE; Briggs et al., 1998) on board the *Compton Gamma-Ray Observatory*. Its best WFC position is RA= $08^{\rm h}36^{\rm m}26^{\rm s}$, Decl = $-18^\circ\ 53'.0$ (J2000), with an $8'$ (radius) accuracy. *RossiXTE* /PCA scanning 8.5 hours after the burst sets an upper limit of 1.6×10^{-12} erg cm^{-2} s^{-1} on the 2–10 keV X-ray afterglow of GRB 980326 (Marshall and Takeshima 1998). Time-of-arrival analysis between the *Ulysses* spacecraft, *BeppoSAX* and BATSE, allows the construction of an Interplanetary Network (IPN) annulus which intersects the *BeppoSAX* WFC camera error box (Hurley et al., 1998). The combined WFC/IPN error box is shown in Fig. 4.1.

In the BATSE energy range (25–1800 keV) the event lasted $\sim$5s, is resolved into three narrow peaks, with a peak flux of 8.8×10^{-7} ergs cm^{-2} s^{-1}, over a 1s timescale. This places it at the knee of the log$N$-log$P$ distribution (Meegan et al. 1996). Its total 25–1800 keV fluence was 1.4×10^{-6} ergs cm^{-2}. The event averaged spectrum has a shape typical of GRBs (photon index $-3.1^{+0.25}_{-0.5}$), but its $E_{\rm peak}$, where the νF_ν spectrum peaks, is unusually low: $E_{\rm peak}$=47$\pm$5 keV. Only 4% of the bursts in the sample of Mallozzi et al. (1998, over 1200 GRBs) have smaller $E_{\rm peak}$ values. However, Mallozzi et al. have also shown that there is a correlation between GRB intensity and spectral hardness (expressed in $E_{\rm peak}$ values). For bursts with similar peak fluxes, the smallest $E_{\rm peak}$ value there is $\sim$ 70 keV (Mallozzi, private communication), which demonstrates the exceptional softness of the integrated spectrum of GRB 980326.

Table 4.1. Log of observations of GRB 980326, supplemented with published observations of the Keck II and KPNO 4-m telescopes.

Date (UT)	Telescope	Integration time (s)	Magnitude OT	Reference
Mar. 27.31	Keck II		R_c=21.19 $\pm$ 0.1	GCN #33
Mar. 27.401	AAT	240	R_c=21.98 $\pm$ 0.16	
Mar. 27.437	AAT	240	R_c=22.18 $\pm$ 0.16	
Mar. 27.84	BO 1.5m	3600	R_c >21.85	GCN # 42
Mar. 27.852	CAHA	3300	R_c >22.0	
Mar. 28.016	ESO NTT	1200	R_c=23.66 $\pm$ 0.12	
Mar. 28.017	ESO 1.5Dan	2700	R_c=23.43 $\pm$ 0.25	
Mar. 28.045	CTIO 4m	600	R_c=23.50 $\pm$ 0.12	
Mar. 28.120	FLW 1.2m	3600	R_c >22.5	
Mar. 28.178	ESO NTT	1200	R_c=23.60 $\pm$ 0.12	
Mar. 28.25	Keck II		R_c=23.69 $\pm$ 0.1	GCN # 32
Mar. 29.09	CTIO 4m	3120	B=25.03$\pm$0.33	
Mar. 29.035	ESO NTT	1800	I_c >22.4	
Mar. 29.008	ESO NTT	1800	V >24.2	
Mar. 29.424	AAT	480	R_c >23.0	
Mar. 30.078	ESO NTT	5400	R_c=$24.88^{+0.32}_{-0.26}$	
Mar. 30.2	Keck II		R_c=25.03 $\pm$ 0.15	GCN #35
Mar. 31.082	ESO NTT	5400	R_c=$25.20^{+0.23}_{-0.20}$	
Apr. 1.080	ESO NTT	5400	R_c >24.9	
Apr. 7.15	KPNO 4m	3300	R_c >24.4	
Apr. 17.3	Keck II		R_c=25.5$\pm$0.5	GCN #57

4.2 The optical counterpart

Optical Cousins R_c-band observations started at the Anglo-Australian Telescope (AAT) on Mar. 27.40 UT, followed by observations at the 3.5m New Technology Telescope (NTT) and the 1.54m Danish telescope (1.5D) at ESO (Chile), the 4m Victor Blanco telescope at CTIO (Chile), the Fred Lawrence Whipple 1.2m (FLW 1.2m; USA) telescope, the 1.5m Bologna University (BO; Italy) telescope and the 2.2m Calar-Alto (CAHA 2.2m; Spain) telescope (see Table 1). All observations were debiased and flatfielded in the standard fashion. Table 2 shows the magnitude of the comparison stars in all photometric bands used. Note that star 2 (see Fig. 4.1) was not detected in the B-band calibration frames.

From a comparison of the first observations at the AAT and ESO/CTIO we discovered one clearly variable object (Groot et al., 1998b). Its location is RA=$08^h36^m34\overset{s}{.}28$, Dec =

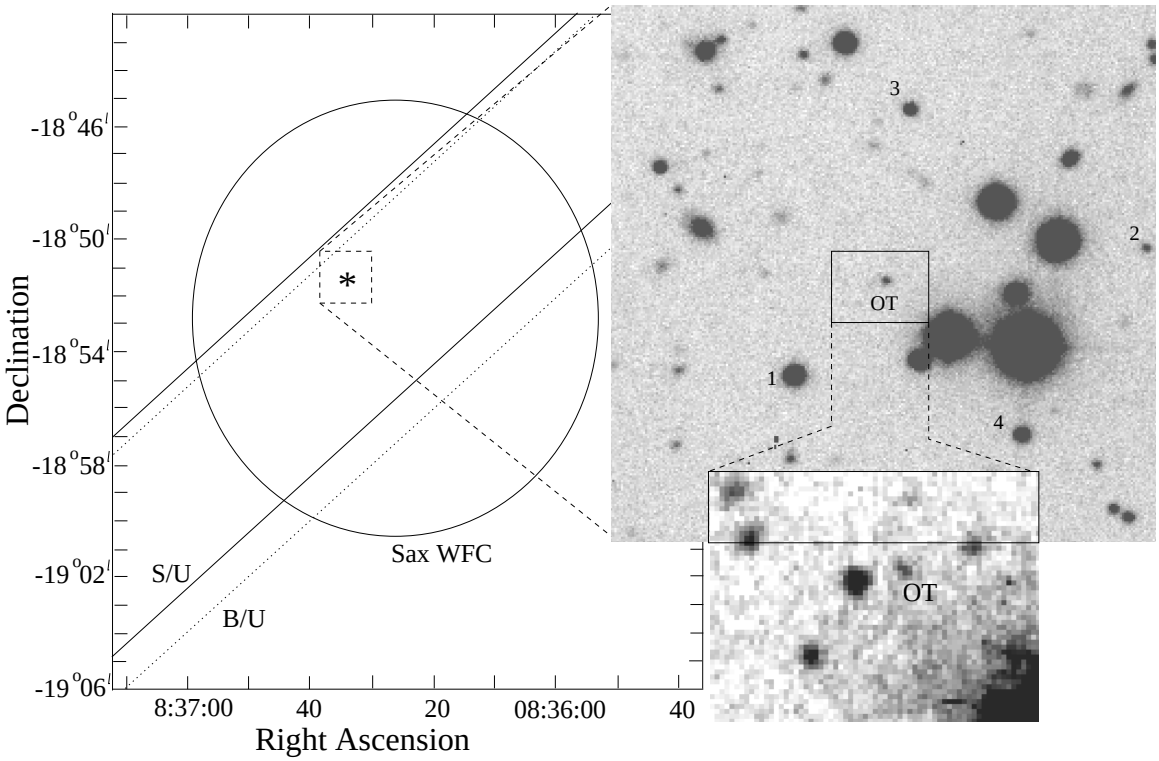

Figure 4.1. The combined *BeppoSAX* WFC and IPN arc error box for GRB 980326, an AAT Mar. 27.4 UT, 1.′6×1.′6 $R_{\rm c}$-band finding chart of the field of the optical transient and a small inset of the immediate surroundings of the OT, made from addition of the last three NTT nights. The solid IPN annulus is the *BeppoSAX* /Ulysses (S/U) annulus, the dotted annulus is the BATSE/Ulysses (B/U) annulus. Local comparison stars are indicated by no. 1–4.

–18° 51′23.″9 (J2000) with an 0.″4 accuracy. Fig. 4.1 shows the region of the OT. Aperture photometry on the combined WFC/IPN error box for the first AAT and CTIO epoch found, apart from asteroid 1998 FO 126 at $R_{\rm c}$=22.7, no other object with a change in magnitude >0.4 mag down to $R_{\rm c}$=23. Although the variability of sources at $R_{\rm c} > 20$ is very poorly known, we conclude that the optical transient is the counterpart to GRB 980326, also considering the exhibited power law decay.

Figure 4.2 shows the $R_{\rm c}$-band light curve of the optical transient. It exhibits a temporal decay which, as applied in previous bursts, can be fitted with a power law and a constant source: $F_\nu \propto t^{-\alpha}$ + C. The power law exponent, α = 2.10±0.13, is by far higher than that of previous afterglows. The light curve exhibits a flattening, with a fitted constant source of 25.5±0.5 (χ^2 for the fit is 10.2/9), such as observed for GRB 970508 (Pedersen et al., 1998; Garcia et al., 1998; Castro-Tirado et al., 1998b), which is possibly the signature of an underlying host galaxy. Grossan et al. (1998) reported an elongation in the NE-SW direction, which is also suggested by visual inspection of the NTT observations taken

Table 4.2. The magnitudes of the four comparison stars used[a]

Star no.	B	V	R_c	I_c
1	20.05±0.10	19.17±0.07	18.51±0.03	18.11±0.02
2	-	23.04±0.15	21.85±0.10	20.74±0.05
3	21.08±0.10	20.76±0.05	20.40±0.05	20.00±0.02
4	20.73±0.10	20.22±0.05	19.78±0.03	19.53±0.02

[a]Photometric calibration of our observations was performed using Landolt (1992) standard fields SA98 and Rubin 149 (R_c-band, taken at the AAT at Mar. 27.4 UT), and PG1047+003 (B, V and I_c-band, taken at ESO at Mar. 30.05 UT).

April 1.08 UT, but S/N levels are too low to draw any conclusion. Visual inspection of the observations reported by Djorgovski et al. (1998) displays an elongation in exactly the perpendicular direction (SE-NW), which may be an effect of fading of the optical transient. This would mean that it is not in the center of an underlying galaxy.

On the night of Mar. 29.0 UT broadband BVI_c measurements of the optical transient were made at the NTT (V and I_c) and at CTIO (B). From the fit to the light curve presented in Fig. 4.2 we deduce an R_c-band value of 24.50 ± 0.10 at Mar 29.0 UT. The colours of the transient at this time were B–R_c = 0.53±0.34, V–R_c > –0.25, R_c–I_c <2.1 (3σ limits on V and I_c). The B–R_c value implies an, uncertain, spectral power law index, $F(\nu) \propto \nu^{-\beta}$, of β =0.66±0.70. One has to realise though, that the underlying source might contribute significantly to the colours, depending on the difference between the afterglow and constant source spectrum.

4.3 Constraints on the electron distribution

Afterglow observations of GRBs over the last year show that a relativistic blast wave, in which the highly relativistic electrons radiate via the synchrotron mechanism, provides a generally good description of the observed properties (Wijers, Rees and Mészáros,1997; SPN98). Here we will discuss briefly the implications of the power-law decay exponent α and the optical spectral slope β for a number of different blast wave models. For an extensive discussion on blast wave models and their application to GRB afterglows we refer the reader to Wijers, Rees and Mészáros (1997), SPN98 and Galama et al. (1998c).

All models have that the flux $F(\nu, t) \propto t^{-\alpha}\nu^{-\beta}$ for a range of frequencies and times which contain no spectral breaks. In each model or spectral state of a model α and β are functions only of p, the power law exponent of the electron Lorentz factor (γ_e) distribution, $N(\gamma_e) \propto \gamma_e^{-p}$. The measurement of either one of α or β therefore fixes p, and predicts the other one.

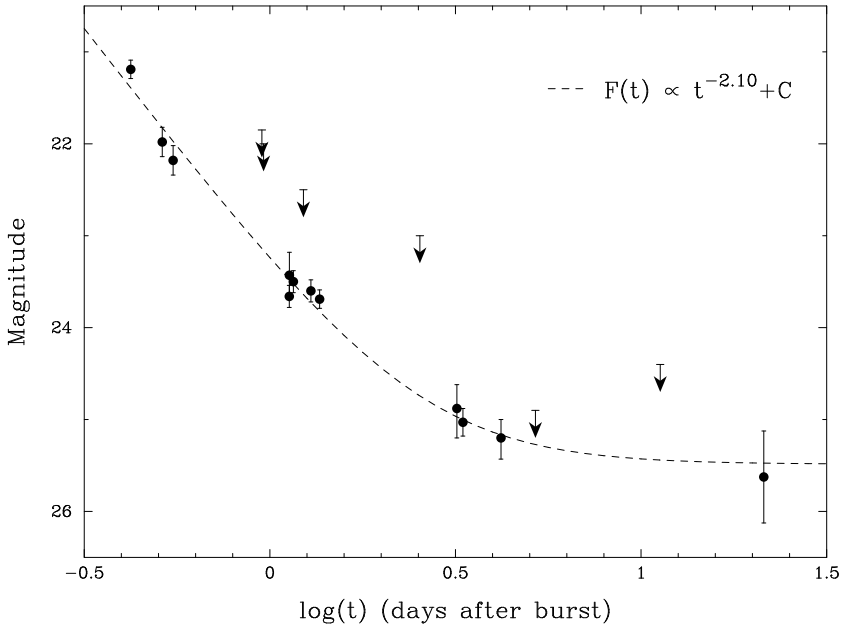

Figure 4.2. R_c-band light curve of GRB 980326. All errors are 1σ, all upper limits are 3σ. The dashed line indicates the power law decay and constant source fit (see Sect. 2).

Given the poor constraint on the spectral slope, we cannot uniquely fit GRB 980326, but we will examine whether its rapid decay requires special circumstances. First we assume that both the peak frequency ν_m and the cooling frequency ν_c (see SPN98 for their definitions) have passed the optical passband at 0.5 days. In this case p=(4α+2)/3=3.5$\pm$0.1, and β=p/2 = 1.75 $\pm$0.06. The second possibility is when ν_m has already passed the optical at 0.5 days, but ν_c not yet at 4.2 days. In this state p = (4α+3)/3 = 3.8$\pm$0.1, and β = –(1–p)/2 = 1.4 $\pm$0.06. Although the latter case agrees slightly better with the measured B–R_c spectral slope, we are hesistant to draw any conclusion from this, considering the uncertainty of the spectral slope. Both, however, imply a much steeper electron spectrum for this burst than the value p =2.2 derived for GRB 970508 (Galama et al. 1998c, d). In case the blast wave is jet-like, the inferred electron spectrum will only be different if the opening angle, θ, of the jet is less than the inverse of the opening angle, here $<7^\circ$, in which case for slowly cooling electrons p=α=2.1, and for rapidly cooling electrons $p = \alpha-1$=1.1 (Rhoads 1998). In both cases β =0.55$\pm$0.05, consistent with the optical colour. Values of p less than 2 are often considered implausible, because they imply a very efficient acceleration mechanism in which the most energetic electrons carry the bulk of the energy.

4.4 The maximum value of p

What is the maximum value of p that can be reached in shock acceleration? In non-relativistic strong shocks it is generally accepted that $p \sim 2$ (Bell, 1978; Blandford and Ostriker, 1978). In ultra-relativistic shocks however, the situation is not so clear (Quenby and Lieu, 1989). Recent calculations show that in this case p will be between 3.2 and 3.8, depending on the morphology of the magnetic field (Gallant and Achterberg, 1999). This is, however, when the electrons do not radiate an appreciable part of their energy during shock acceleration. If the electrons do radiate significantly, as is suggested by GRB 970508 (Galama et al., 1998c,d; SPN98), the electron spectrum will steepen and the distribution of electrons will no longer be a pure power law. In a power-law model fit, measured values exceeding $p \sim 3.8$ are therefore expected and as a consequence, power law decays of afterglows that are even more rapid than the α=2.10 found here are entirely possible.

4.5 Explanations for non-detections: rapid decays and galactic halos

The optical behaviour of bursts like GRB 970828 (Groot et al., 1998a) and GRB 971214 (Halpern et al., 1998) can be explained by extinction due to gas and dust between the observer and the origin of the GRB source. However, extinction will fail to explain the non-existence of an X-ray afterglow above 4–5 keV since at these energies extinction is negligible. The fact that all *BeppoSAX* NFI follow-ups have detected an X-ray afterglow (with the possible exception of GRB 970111, Feroci et al., 1998) and that only two *RossiXTE* /PCA scannings (for GRB 970616 and GRB 970828) have produced X-ray afterglows, makes the question arise what the cause of this difference is.

Suppose we have an X-ray afterglow that decays as a power law with exponent α. What is the X-ray afterglow flux needed shortly ($\sim$ 1 minute) after the burst, as a function of α, if we want to detect the afterglow at a level of $\sim$ 1mCrab after a few hours? The X-ray flux after 1 minute can be estimated by the X-ray emission detected in the burst itself, since this X-ray emission will be a mixture of the X-ray tail of the GRB and the start of the X-ray afterglow. We can therefore derive an estimate of the upper limit to the X-ray afterglow level after a few hours from the prompt X-ray emission.

Figure 4.3 shows the flux needed after 1 minute for a detection after 1, 2 and 5 hours at a level of 1 mCrab as a function of decay rate α. For bursts that have detected X-ray or optical afterglows we have also plotted in Fig. 4.3 the observed total X-ray fluxes during the bursts versus the X-ray power law decay index α. (For GRB 980326 we used the optical α, since no X-ray afterglow decay index is known.) Because of the mixture

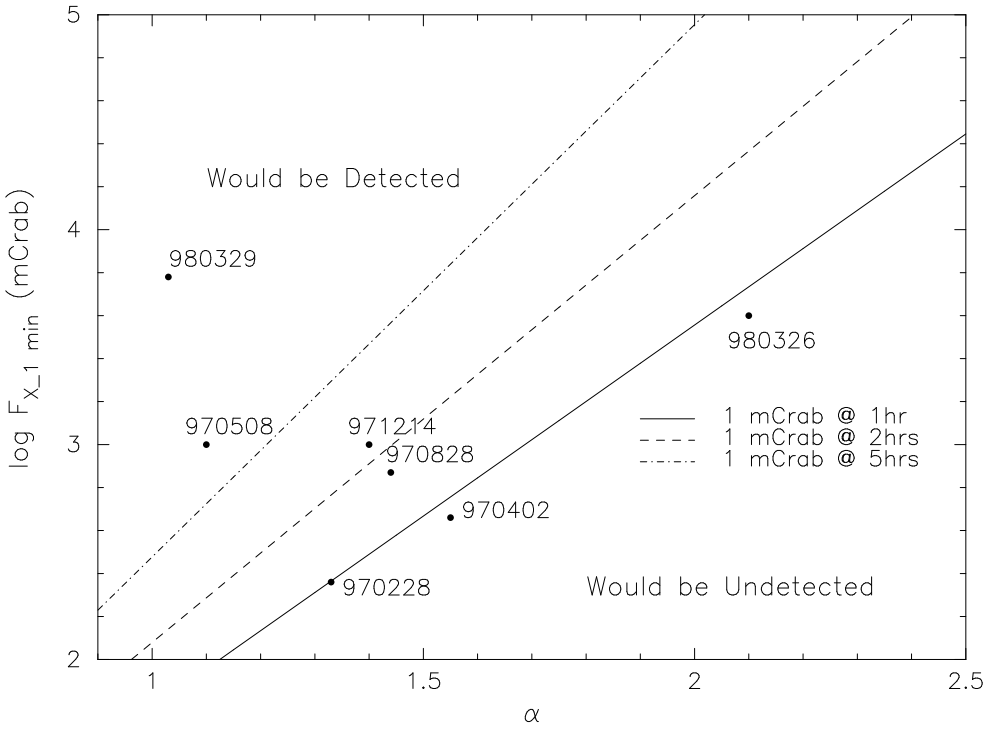

Figure 4.3. The X-ray flux needed after 1 minute to detect a GRB after 1 (solid line) or 2 (dashed line) and 5 (dashed-dotted line) hrs at a level of 1 mCrab as a function of temporal decay power law index α. Indicated for several bursts with measured α is the *total* X-ray flux during the GRB event. References: GRB 970228 Costa et al., 1997; GRB 970402 Nicastro et al., 1997; GRB 970508 Galama et al., 1998a, Sokolov et al., 1998; GRB 970828 Yoshida et al., 1998; GRB 971214 Halpern et al., 1998, Diercks et al., 1998; GRB 980326 this paper; GRB 980329 In 't Zand et al., 1998.

explained above these points actually comprise a set of upper-limits for the flux in the X-ray afterglow after one minute. It is not only clear from Fig. 4.3 that most of the bursts that have been found to exhibit an X-ray afterglow would have been missed by a *RossiXTE* /PCA scan after 2–5 hours, but also that this is particularly the case for bursts with high values of α. A rapid decay is therefore a viable explanation for the non-detection of bursts, even as bright as GRB 980203, by the current *RossiXTE* /PCA follow-up. It has to be noted that the scanning of the *RossiXTE* /PCA is often performed over no more than the 1.5–2σ BATSE errorboxes, and there exists therefore a 5–14% chance of not scanning the GRB.

For bursts that show neither X-ray nor optical afterglows, a different explanation may be found in the fact that all five detected optical afterglows are associated with galaxies. In the merging neutron-star scenario, a substantial fraction of bursts would occur in a galactic halo, where the average density of the interstellar medium is $\sim$1000 times less

than in a disk. Since the afterglow peak flux, $F_{\rm m}$, depends on the square root of the density of the ambient medium, this would mean a reduction of the afterglow peak flux by several magnitudes with respect to bursts that go off in higher density regions (Mészáros and Rees, 1997). Since GRBs are detected by their prompt γ-ray emission, probably produced by internal shocks (Mészáros and Rees, 1997), this would be independent of the density of the ambient medium.

4.6 Conclusions

We have detected the optical counterpart to GRB 980326. Its temporal decay is well represented by a power law with index –2.10, faster than for any previously found GRB afterglow, and a constant contribution at $R_{\rm c}$ = 25.5$\pm$ 0.5, which is most likely caused by an underlying galaxy. Fireball models can give an adequate description of this rapid power law decay of GRB 980326, although its limited optical spectral information makes it hard to distinguish between different models. This emphasizes the need for multi-colour photometry, even when the optical counterpart has not yet been found.

A rapid temporal decay may be a reason for the non-detection of low-energy afterglows of bursts that had X-ray and optical follow-ups. The occurrence of GRBs in galactic halos, in the merging neutron star scenario, may be an alternative explanation for the non-detection of low-energy afterglows. To establish the viability of these explanations for the non-detection of low-energy afterglows, it is of vital importance that more GRB afterglows are found and this is only possible when low-energy follow-up begins as soon as possible ($<$1hr) after the initial GRB event.

Acknowledgments
PJG wishes to thank Bram Achterberg for useful discussions. TJG is supported through a grant from NFRA under contract 781.76.011. RAMJ is supported by a Royal Society URF grant. CK acknowledges support from NASA grant NAG 5-2560.

References

Bell, A.R., 1978, MNRAS 182, 147
Blandford, R.P. and Ostriker, J.P., 1978, ApJ 221, L29
Briggs, M., et al., 1998, IAU Circ No. 6856
Castro-Tirado, A., et al., 1997, IAU Circ No. 6598
Castro-Tirado, A., et al., 1998a, Science 279, 1011
Castro-Tirado, A., et al., 1998b, IAU Circ No. 6848
Celidonio, G., et al., 1998, IAU Circ No. 6851

Costa, E. et al., 1997, Nature 387, 783
Diercks, A., et al., 1998, ApJL 503, 105
Djorgovski, G., et al., 1998, GCN Circular No. 41
Feroci, M., et al., 1997, Proc. SPIE 3114, 186
Feroci, M., et al., 1998, A&A 332, L29
Frontera, F., et al., 1997, A&AS 122, 357
Galama, T.J. et al., 1997, Nature 387, 479
Galama, T.J. et al., 1998a, AIP Proc. 428, 478
Galama, T.J. et al., 1998b, ApJ 497, L13
Galama, T.J., et al., 1998c, ApJ 500, L97
Galama, T.J., et al., 1998d, ApJ 500, L101
Gallant, Y. and Achterberg, A., 1999, MNRAS 305, L6
Garcia, M., et al., 1998, ApJ 500, L105
Gorosabel, J., et al., 1998, A&A 339, 719
Groot, P.J. et al., 1998a, ApJ 493, L27
Groot, P.J. et al., 1998b, IAU Circ No. 6852
Grossan, B., et al., 1998, GCN Circular No. 35
Halpern, J.P. et al. 1998, Nature, 393, 41
Hurley, K., et al., 1998, GCN Circular No. 53
In 't Zand, J.J.M., et al., 1998, ApJ 505, L119
Jager, R., et al., 1997, A&AS 125, 557
Kulkarni, S.R. et al., 1998, Nature 393, 35
Landolt, A.U., 1992, AJ 104, 340
Mallozzi, R.S., et al., AIP Proc. 428, 273
Marshall, F. and Takeshima, T., 1998, GCN Circular No. 58
Meegan, C.A., et al., 1996, ApJS 106, 65
Mészáros, P. and Rees, M.J., 1997, ApJ 476, 232
Metzger, M.R. et al., 1997, Nature 387, 879
Nicastro, L., 1998, A&A 338, L17
Paczyński, B., 1998, ApJ. 494, L45
Pedersen, H., et al., 1998, ApJ 496, 311
Pian, E., et al., 1998, ApJ 493, L103
Piro, L., Scarsi, L., and Butler, R.C., 1995, Proc. SPIE 2517, 169
Quenby, J.J. and Lieu, R., 1989, Nature 342, 654
Rhoads, J.E., 1998, AIP Proc. 428, 699
Rybicki, G.B. and Lightman, A.P., 1979, Radiative Processes in Astrophysics, Wiley, New York, Chapter 6
Sahu, K.C. et al., 1997, Nature 387, 476

Sari, R., Piran, T., and Narayan, R., 1998, ApJ 497, L17
Sokolov, V.V., et al., 1998, A&A 334, 117
Van Paradijs, J. et al., 1997, Nature 368, 686
Wijers, R.A.M., Rees, M.J. and Mészáros, P., 1997, MNRAS 288, L51
Yoshida, A., et al., 1998, AIP Proc. 428, 441

Part II

Accretion Disks in Cataclysmic Variables

5

The Eclipsing Cataclysmic Variable GS Pavonis: Evidence for disk radius changes

P.J. Groot, T. Augusteijn, O. Barziv and J. van Paradijs

Astronomy and Astrophysics Letters 340, L31 (1998)

We have obtained differential time series photometry of the cataclysmic variable GS Pavonis over a timespan of 2 years. These show that this system is deeply eclipsing ($\sim$2–3.5 mag) with an orbital period of 3.72 hr. The eclipse depth and out-of-eclipse light levels are correlated. From this correlation we deduce that the disk radius is changing and that the eclipses in the low state are total. The derived distance to GS Pav is 790$\pm$90 pc, with a height above the galactic plane of 420$\pm$60 pc. We classify GS Pav as a novalike system.

5.1 Introduction

Eclipsing non-magnetic Cataclysmic Variables (CVs) (for a review see Warner 1995, hereafter W95) are of particular interest not only because the masses of both stars can be determined, but especially because studying their eclipses, e.g., by the eclipse mapping method (Horne 1985), gives the opportunity to learn more about the physics of accretion disks. In this *Letter* we report that GS Pav is an eclipsing CV, that shows substantial disk radius changes.

GS Pav was first discovered by Hoffmeister (1963) who denoted it as star S7040 and gave the comment ‘raschwechselnd’ (rapidly varying). It was classified as a dwarf nova type CV in the GCVS and in the catalogue of Downes, Webbink and Shara (1997), who also give a finding chart for the object. It was selected for our observations as a possible

Table 5.1. Log of V-band observations of GS Pav.

Date	Start UT	Integr. Time (s)	No. Obs.
Sept 5, 1993	01^h50^m	120	82
Sept 6, 1993	23^h21^m	120	66
Sept 7, 1993	23^h11^m	120	48
Sept 8, 1993	03^h57^m	120	25
March 22, 1995	08^h06^m	240	25
March 23, 1995	07^h15^m	240	30
June 13, 1995	03^h20^m	240	61
July 11, 1995	05^h40^m	240	65
July 25, 1995	04^h23^m	120	24
Aug 16, 1995	04^h52^m	120	54
Sept 15, 1995	03^h23^m	240	21
Sept 19, 1995	02^h50^m	240	20

member of the halo population (Augusteijn, 1994). Zwitter and Munari (1995) show that it has a normal CV spectrum. We determined its location at RA= $20^h08^m07^s.58$, Dec=–69° 48′58″.1 (J2000), almost identical to that of Downes, Webbink and Shara (1997).

5.2 Observations

Photometric observations were obtained with the Dutch 0.9m telescope at ESO La Silla, Chile. A log of the observations is given in Table 5.1. All observations were made with a 512×512 TEK CCD detector, using a Bessel V filter. Standard flatfielding and debiasing were applied to all observations. A photometric calibration was obtained on September 6, 1993 using the standard star EG 21 (Landolt 1992). Table 5.2 gives the coordinates and magnitudes of the reference stars we have used.

5.3 Photometric ephemeris

Arrival times of mid-eclipse were determined by fitting a Gaussian profile to the eclipses, and by determining the mid-point between the points of steepest ascent and descent. The final arrival times listed in Table 3 were taken as the average of the results from these two methods. We estimate the accuracy of these arrival times to be 5×10^{-4} days, which corresponds to the typical difference between the results from the two methods.
A linear fit to the arrival times listed in Table 3 yields the following ephemeris:

$$\mathrm{HJD}_{\mathrm{min}} = 244\,9711.17388(17) + 0.155269817(87) \cdot N, \tag{5.1}$$

Table 5.2. Reference stars used for the differential photometry of GS Pav.

No.	Name	RA (J2000)	Dec (J2000)	V[a]
1	GAB J200816–6949	$20^h08^m16\overset{s}{.}47$	$-69^\circ\ 49'36\overset{''}{.}0$	17.31(4)
2	GAB J200810–6949	$20^h08^m10\overset{s}{.}49$	$-69^\circ\ 49'34\overset{''}{.}0$	17.41(4)
3	GAB J200804–6949	$20^h08^m04\overset{s}{.}83$	$-69^\circ\ 49'40\overset{''}{.}4$	17.42(4)
4	GAB J200755–6949	$20^h07^m55\overset{s}{.}45$	$-69^\circ\ 49'14\overset{''}{.}4$	17.09(4)
5	GAB J200802–6948	$20^h08^m02\overset{s}{.}49$	$-69^\circ\ 48'57\overset{''}{.}6$	18.54(7)
6	GAB J200800–6948	$20^h08^m00\overset{s}{.}64$	$-69^\circ\ 48'49\overset{''}{.}5$	16.33(3)
7	GAB J200757–6948	$20^h07^m57\overset{s}{.}63$	$-69^\circ\ 48'19\overset{''}{.}6$	17.87(5)
8	GAB J200810–6947	$20^h08^m10\overset{s}{.}41$	$-69^\circ\ 47'55\overset{''}{.}4$	15.45(2)

[a]The quoted errors reflect the internal errors in the brightness measurements of the stars which do not include a 0.1 mag uncertainty in the transformation to standard magnitudes.

Table 5.3. Times of arrival, deduced cycle numbers and the observed minus computed (O–C) residuals for the observations of GS Pav

Cycle No.	HJD_{min}–244 0000	O–C (days)
–3062	9235.7370	-0.70×10^{-3}
–3050	9237.6014	0.46×10^{-3}
–3044	9238.5330	0.44×10^{-3}
–3043	9238.6876	-0.23×10^{-3}
565	9798.9010	-0.32×10^{-3}
571	9799.8340	1.05×10^{-3}
1098	9881.6603	0.16×10^{-3}
1099	9881.8147	-0.71×10^{-3}
1279	9909.7641	0.13×10^{-3}
1280	9909.9191	-0.14×10^{-3}
1369	9923.7376	-0.66×10^{-3}
1511	9945.7857	-0.87×10^{-3}
1704	9975.7542	0.56×10^{-3}
1729	9979.6362	0.82×10^{-3}

with N the cycle number. The error estimates for the parameters are scaled to give a $\chi^2_{\rm red}$ = 1.0. The rms value of the arrival times around the fit is 6.4×10^{-4} days, which is in reasonable agreement with our error estimate.

5.4 Mass ratio, width of the eclipse and inclination

If the secondary follows the lower main-sequence standard mass-period relation (W95):

$$M_2 = 0.065\, P_{\rm orb}^{5/4}({\rm h}) \quad 1.3 \leq\ P_{\rm orb}({\rm h}) \leq 9, \tag{5.2}$$

with M_2 the mass of the secondary, M_2 is ~ 0.34 $M_\odot$. Since the mass ratio, q=M_2/M_1, has to be smaller than 2/3 for stable mass transfer (W95) and the mass of the primary can at most be the Chandrasekhar mass (1.4 $M_\odot$), the mass ratio is limited to the range $0.67 \geq q \geq 0.24$.
Figure 5.1 shows the phase folded eclipse light curves for the 12 epochs listed in Table 2.1. The light curves of June 13 and July 11, 1995 contain two eclipses each.
The width of the eclipse ($\Delta\varphi$) can be estimated by the phases of steepest descent and ascent. For GS Pav we measure a mean $\Delta\varphi$ = 0.064 $\pm$ 0.005, where the error is the scatter on the average of all measurements. From this value and the range in mass ratio's we deduce (Horne 1985) a range in orbital inclination of $74^\circ < i < 83^\circ$.

5.5 Correlation between eclipse depth and out-of-eclipse light

Figure 5.1 shows that GS Pav does not have a constant out-of-eclipse magnitude. In our observations the source varied between V$\sim$14.9 and V$\sim$ 17.1, being mostly at the bright end. Also the eclipse depth is not constant. We have investigated if these two variations are correlated. Since the eclipses are well represented by Gaussian functions, we have taken the zero-level and depth of the Gaussians, used to determine the times of mid-eclipse, as estimates of the depth in magnitudes of mid-eclipse (Δm) and the out-of-eclipse light level (m_V) (Fig. 5.2). The numbers in Fig. 5.2 refer to the eclipses as shown in Fig. 5.1.

In the following we will make a distinction between the observed radius of the accretion disk, which is the size we infer from our observations, and the physical radius of the accretion disk. The difference between these two is determined by the fractions of the optically thick and thin parts of the accretion disk and the brightness distribution across the disk which determines what parts are visible in the chosen passband (here in the V-band). A changing brightness distribution can mimic a change in the physical disk radius, when observed in only one band.

In Fig. 5.2 the straight line labeled 'Line of Totality' shows what the correlation between Δm and $m_{\rm V}$ looks like for a system in which the eclipse is total. A total eclipse means that the observed size of the accretion disk is smaller than the size of the secondary and that at mid-eclipse the amount of observed light from the disk is negligible. In a total eclipse the

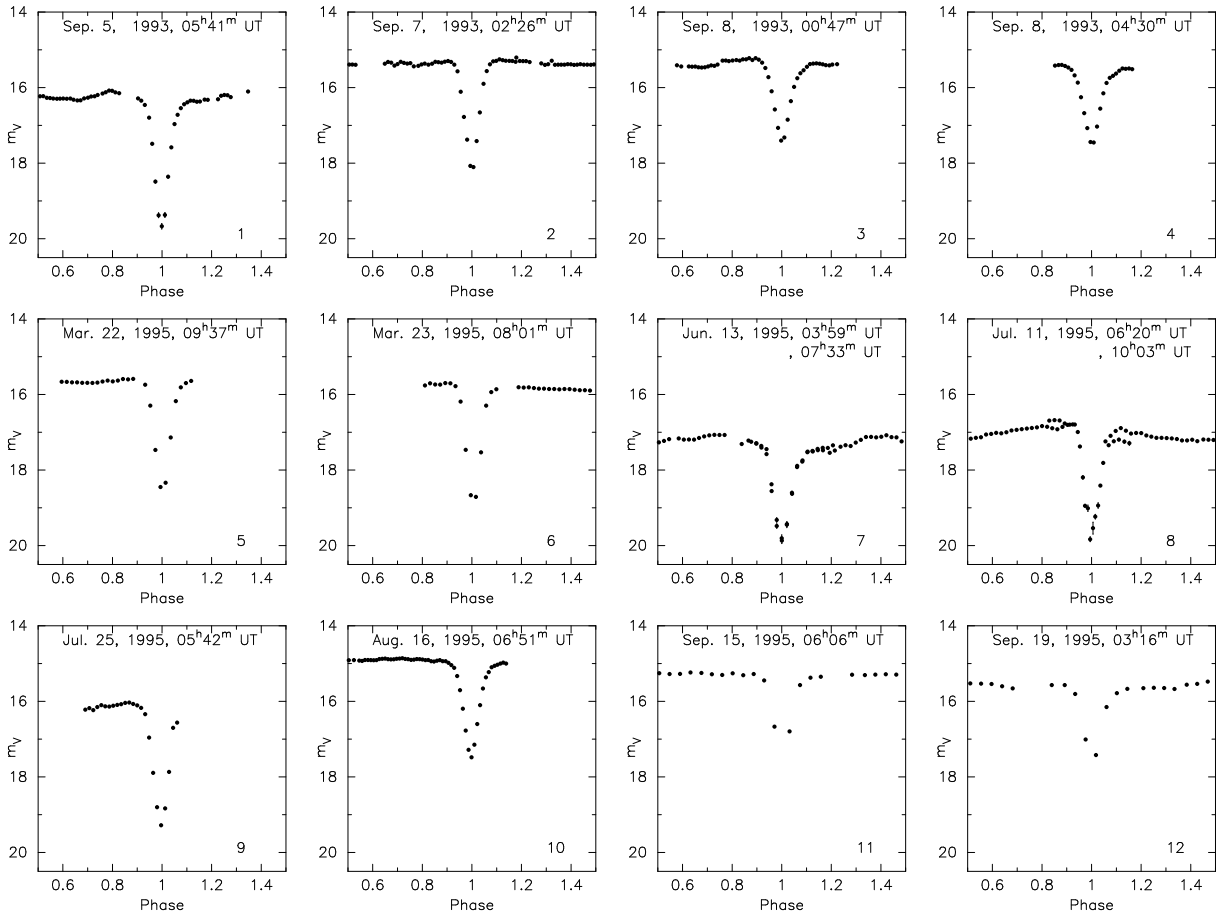

Figure 5.1. The phasefolded V-band eclipse light curves for the 12 epochs. The heliocentric corrected time of mid-eclipse of the observations is given in UT.

mid-eclipse light level will be constant and equal to the brightness of the secondary. Every magnitude of brightening of the disk will cause a magnitude of deepening of the eclipse: the system will follow a straight line, with an angle of 45° , in the Δm-$m_{\rm V}$ diagram. The position of this line in the diagram will be different for each individual system, but can be fixed by determining the brightness of the secondary. If at any time during our observation GS Pas was totally eclipsing, then its mid-eclipse light level will be the brightness of the secondary. The minimum level occured on June 13 and July 11, 1995: V=19.9±0.1. We use this point to fix the position of the 'Line of Totality' in Fig. 5.2. We see that points '7' and '8' (which are from June 13 and July 11, 1995) lie on this line. From the fact that the eclipse depths in point '7' and '8' are different, but the brightness at mid-eclipse is the same, we conclude that at these epochs the eclipse is indeed total. It follows that the observed minimum of V=19.9±0.1 is the brightness of the secondary. The lack of a flat-bottom in the light curves of point '7' and '8' shows that the eclipse is only just total,

although the integration time of 4 minutes may be too long to resolve a flat bottom.

If we now look at the other points in Fig. 5.2 we see that they do not fall on the 'Line of Totality'. With increasing out-of-eclipse light levels, the depth of the eclipse does not increase anymore (as it would have on the Line of Totality), but decreases. Apparently, between point '7' and '1' on the track the observed size of the disk increases to the extent that the eclipse is no longer total, but that part of the accretion disk remains visible in mid-eclipse. With a further increase of the observed accretion disk radius, more and more of the disk is visible at mid-eclipse and the eclipse becomes less and less deep. This behaviour was first found by Walker (1963) in his study of RW Tri, which shows no total eclipses, but does move back and forth on this part of the track. We have therefore labeled this the 'Walker Branch'. Another transition, which to our knowledge has never been noted before, is the one that happens near point '10' in Fig. 5.2. The out-of-eclipse light level reaches a maximum, after which it declines again (the curve bends to the right), but the eclipse depth continues to decrease. We have labeled this part the 'Shallow Branch' because of its decreasing eclipse depth.

If the change in the observed radius is caused by a change in the physical size of the disk (rather than a change in the brightness distribution), then the manifestation of the Shallow Branch may be explained by the effect of self-eclipses. Because the height of the disk is correlated with its physical size (Frank, King and Raine 1985), self-eclipses of the hot, and therefore luminous inner parts of the concave disk by its outer parts, will occur when the physical size of the disk exceeds a critical value and therefore a critical height. The out-of-eclipse light level decreases because the more luminous parts of the accretion disk are self-eclipsed, and at the same time the eclipse depth can continue to decrease if the disk radius continues to increase. To eclipse the inner parts the disk flaring angle must be (90-i)$^\circ$ or higher. In our case this would mean a flaring angle of 7° –16° , similar to what has been found in other CVs (e.g. Robinson et al, 1995).

The variations appear to trace out a unique track over a substantial period of time. Changes from one part of the track to another can occur quite rapidly, e.g. the transition from point '1' to '4' took place within 4 days.

5.6 Distance to the system

With the orbital period of 3.72 hr we can use the $M_{\rm V} - P_{\rm orb}$ relation of W95 to derive a $M_{\rm V}$ = 10.4 with an estimated error of 0.2 magnitudes for the secondary (from Fig. 2.46 in W95). Combined with the apparent magnitude of V=19.9$\pm$0.1, this gives a distance to GS Pav of 790$\pm$90pc. Given its position on the sky, the implied height above the galactic plane is 420$\pm$60 pc. From the distance we can deduce the absolute magnitude of the system out of eclipse, which is dominated by the accretion disk. To obtain an absolute magnitude of the accretion disk, we correct for the inclination of the disk, according to

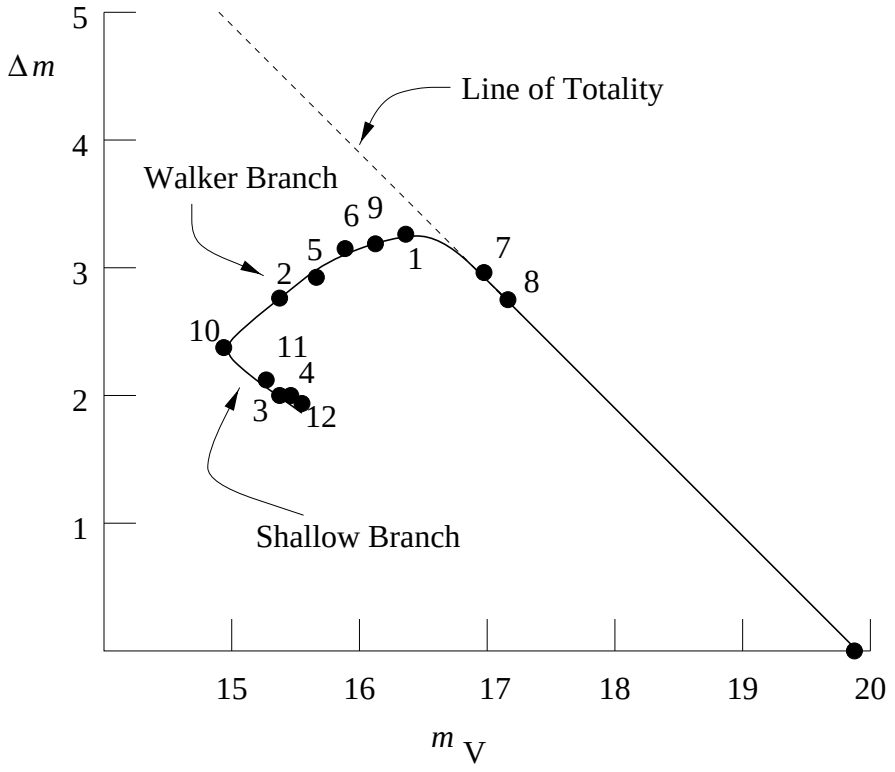

Figure 5.2. The depth of the eclipse in GS Pav as function of the out-of-eclipse light. The numbers correspond to the eclipses in Fig. 5.1.

Eq. 2.63 of W95. This correction varies from 1.0 mag (for i=74°) to 2.1 mag (for i=83°). The absolute magnitude ($M_{\rm V}$) lies therefore between $6.6 \geq M_{\rm V} \geq 4.4$ (for i=74°) and $5.5 \geq M_{\rm V} \geq 3.3$ (for i=83°). Comparison with the mean absolute magnitudes for NLs and DNe (Fig. 4.16 and 3.9 from W95) shows that the derived range is in the normal regime for NLs, but too bright for DN in quiescence.

5.7 Classification as a novalike system

From the shape of the light curve and its absolute magnitude, we conclude that GS Pav is a novalike system, and considering its emission line spectrum (Zwitter and Munari, 1995), that it is of the RW Tri subclass, which is defined as having emission line spectra (W95). According to the definition in W95 of the VY Scl subclass, as NL systems having low states in their long term light curves, and showing no DN outbursts during these low states, we should also classify it as a VY Scl star. This is supported by its orbital period, since almost all known VY Scl stars have periods between 3 and 4 hrs. However, the physical interpretation as outlined in W95 may not apply to GS Pav. In this description a VY Scl system in its low state has a mass-transfer rate $\dot{M}$, that is lower than the critical rate, $\dot{M}_{\rm crit}$,

below which DN outbursts are expected to occur, but it does not show these outbursts. This distinguishes VY Scl systems from Z Cam systems, that do show these outbursts in their low state. In our observations GS Pav at all times seems to have an absolute magnitude which was brighter or equal than that of Z Cam systems during standstill, where $\dot{M}$ is thought to be larger than $\dot{M}_{\rm crit}$. We therefore cannot conclude if GS Pav is a VY Scl system or not. However, it could be that all NL systems with periods between 3 and 4 hours turn out to have low and high states if sufficiently long observed (W95).

An interesting example of a system that may be analogous to GS Pav is VZ Scl for which O'Donoghue, Fairall and Warner (1987) concluded that the size of the accretion disk has changed from one observation to the other. Unfortunately they only observed two eclipses. Since this system, in the low state, is also totally eclipsing, a comparison with GS Pav would be of interest.

5.8 Conclusions

We have shown that GS Pav is a deeply eclipsing cataclysmic variable with a 3.72 hr period. Based on its photometric behaviour, orbital period and absolute magnitude we classify the system as a novalike variable. The depth of the eclipse and the brightness of the system out-of-eclipse are correlated. From this relation we infer that the disk radius changes and that in two of our observations the eclipse is total. Therefore, the apparent visual magnitude of the secondary is V=19.9$\pm$0.1, giving a distance to the system of 790$\pm$90 pc.

References

Augusteijn, T., 1994, PhD thesis, University of Amsterdam

Downes, R, Webbink, R.F and Shara, M.M., 1997, PASP 109, 345

Frank, J., King, A.R. and Raine, D.J., 1985, *Accretion Power in Astrophysics,* Cambridge Astrophysics Series Vol. 21, CUP

Hoffmeister, C., 1963, Veröff. Sternwarte Sonneberg, 6, 1

Horne, K., 1985, MNRAS 213, 129

de Jong, J.A., Van Paradijs, J. and Augusteijn, T., A&A 314, 484

Landolt, A., 1992, AJ 104, 372

O'Donoghue, D., A.P. Fairall and Warner, B., 1987, MNRAS 225, 43

Ritter, H. and Kolb, U., 1998, A&AS 129, 83

Robinson, E.L., Wood, J.H, Bless, R.C. et al., 1995, ApJ 443, 295

Warner, B., 1995, *Cataclysmic Variables,* Cambridge Astrophysics Series Vol. 28, CUP.

Walker, M.F., 1963, ApJ 138, 146

Zwitter, T. and Munari, U., 1995, A&AS 114, 575

6

SW Sextantis in an excited, low state

P.J. Groot, R.G.M. Rutten and J. van Paradijs

Submitted to Astronomy and Astrophysics

We present low-resolution spectrophotometric optical observations of the eclipsing nova-like cataclysmic variable SW Sex, the prototype of the SW Sex stars. We observed the system when it was in an unusual low state. The spectrum is characterized by the presence of strong HeII and CIV emission lines as well as the normal single peaked Balmer emission lines. Through analysis of the eclipse light curves of both the continuum and the emission lines we derive that the characteristics of the SW Sex stars are well explained by the presence of a strong shock that occurs along the accretion stream trajectory, but inside the disk. This shock is the origin of the single peaked emission lines, which are partially emanating from a wind. We speculate that the formation of the shock is the consequence of a relatively high mass-transfer rate from the secondary ($>10^{-9}$ $M_\odot$ yr^{-1}) and a long spin period of the non-magnetic white dwarf.

6.1 Introduction

The SW Sex stars are a subclass of the eclipsing novalike (NL) Cataclysmic Variables (CVs). They are classified on a number of spectroscopic features, mainly the single peaked emission lines, the large shifts between spectroscopic conjunction and photometric mid-eclipse, the transient absorption evident in the emission lines around photometric phase 0.5 and the shallow eclipse of the low excitation lines of HI and He I (see Thorstensen, 1991; Warner 1995). Their unusual spectroscopic behaviour has led to intensive studies, which in turn have led to a number of possible explanations for the SW Sex 'phenomena'. These explanations can be divided in four classes: 'wind' models (Honeycutt, Schlegel and Kaitchuck, 1986), 'overflow' models (Hellier and Robinson, 1994;

Hellier 1996; Hellier 1998), 'magnetic' models (Williams 1989; magnetic accretion and Horne, 1999; magnetic excretion) and 'modified standard' models (Dhillon, Marsh and Jones, 1997, hereafter DMJ97). Although all of these are capable of explaining a subset of the SW Sex phenonema, none show a conclusive case of explaining all of the features listed above.
SW Sex itself is the prototype of the SW Sex stars and has been the topic of many investigations. It was discovered by Green, Schmidt and Liebert (1986) as a UV-excess object with high excitation emission lines (Green et al., 1982). Follow-up photometry showed it to be a deeply eclipsing system with a 3.24 hr orbit (Penning et al., 1984). We refer to DMJ97 for a recent, more detailed, description on the observational history of SW Sex.
From high-speed broad-band photometry Rutten, Van Paradijs en Tinbergen (1992, hereafter RvPT92) derived a radial dependence of the temperature in the accretion disk that is not only much flatter than seen in other systems (see also RvPT92), but also much flatter than predicted by standard accretion disk theory (e.g. Frank, King and Raine, 1992). This result, combined with the unusual behaviour of the emission lines in SW Sex, prompted us to a study of the accretion disk in SW Sex. To this end we obtained time series of low-dispersion spectra of SW Sex with the 2.5m Isaac Newton Telescope on the island of La Palma. These data not only allow us to study the detailed behaviour of the emission lines through the orbit, but also map, spectrally resolved, spatial detail on the accretion disk, using the technique of eclipse mapping (Horne, 1985; Rutten et al., 1993, 1994).

6.2 Data and Reduction

Observations were made on the nights of 25 to 30 March, 1996 using the Intermediate Dispersion Spectrograph (IDS) with the R300V grating and a TEK 1k$\times$1k CCD, giving a dispersion of 3.3Å per pixel over the wavelength range of 3600 Å to 7000 Å. In order to minimize slit-losses and optimize the photometric quality of the data the slit was opened to 2″. This set-up resulted in an effective resolution of 8 Å. A second star (30″ SW of SW Sex) was also placed on the slit to correct for slit-losses. We have made time-series with 90s integration and $\sim$60s dead-time per observation, giving an effective time resolution of $\sim$150s or $\sim$ 1/80th of an orbital period. Throughout the nights CuAr calibration spectra were taken for the wavelength calibration. A total of 282 spectra, covering 9 eclipses, were recorded. An overview of the data is given in Table 6.1.
The data reduction was carried out using the standard ESO-MIDAS reduction package with additionally written software. All the observations were debiased using the mean of the overscan region on each exposure. A run-averaged flatfield was constructed using internal Tungsten lamp flats for the spectral profile and twilight skyflats for the spatial profile. All spectra were optimally extracted (Horne, 1986) and rebinned to a slightly oversampled wavelength-grid with 3Å wide bins. The wavelength calibration was accurate to 0.15 Å. Time and wavelength dependent slit losses were corrected for by applying the

Table 6.1. Overview of SW Sex observations March 1996

Date	Start UT	End UT	No. Exposures
25/3/96	22:17	02:28	62
26/3/96	20:20	01:55	73
28/3/96	23:17	01:55	32
29/3/96	20:21	01:21	70
30/3/96	22:16	02:20	45

variation in the comparison star brightness to SW Sex, while the absolute slit losses were determined from comparing signal strengths of the observations taken with the 2″wide slit with those taken through a wide, 10″, slit. Flux calibration was done by observing the spectrophotometric standard Feige 34 (Massey et al., 1988) through the same set-up with a 10″wide slit. Based on Poisson statistics in the extracted spectrum, each wavelength bin was assigned an error, which is propagated to the flux calibrated spectrum.

6.3 Eclipse timing

A total of nine eclipses were covered during the observing run. Phase-folding, using the ephemeris of DMJ97, gave a phase-offset of minimum light in the photometric light curves of $\sim$0.006 in phase. We redetermined the ephemeris of SW Sex using the eclipse timings as given in DMJ97 and by making Gaussian fits to our own data (see Table 6.2 for all eclipse timings). For the existing data we used an error of 1×10^{-4} days on the time of minimum light. For our own data we used an error of 0.5×10^{-4} days. A linear regression yields the revised orbital ephemeris given in Eq. 6.1.

$$\begin{aligned} HJD_{\rm mid\_eclipse} &= 2\,444\,339.650574(36) \\ &\quad +0.1349384411(10) \times N \end{aligned} \tag{6.1}$$

6.4 Results

6.4.1 Average spectrum

For the spectrophotometry we used seven of nine observed eclipses. The remaining two (of the night of March 28 and the second eclipse of the night of March 30) were not used because the S/N levels of the fainter, secondary star on the slit were too low to make a reliable slit correction. Although the lightcurve at any wavelength was reproduced correctly and therefore used in the above derivation of the ephemeris, the slope of the

Table 6.2. Times of minimum light for SW Sex

HJD (mid-eclipse) (+2 440 000)	Cycle Number (N)	O-C (s)
4339.65087	0	–26.33
4340.73055	8	–33.44
4348.82649	68	–23.50
4631.92758	2166	–42.92
4676.86195	2499	–6.74
4721.79636	2832	–12.73
7566.56813	23914	8.20
7615.41619	24276	13.33
7615.55065	24277	28.26
7616.49516	24284	48.41
7618.51922	24299	61.44
7619.46374	24306	39.39
7620.40856	24313	17.35
7621.48834	24321	10.24
7622.43257	24328	30.38
7921.32167	26543	–13.94
7921.45633	26544	0.98
7950.19842	26757	17.28
7950.33321	26758	32.22
8306.30100	29396	17.89
8306.43599	29397	32.82
10168.452377	43196	–58.15
10168.586651	43197	–43.22
10169.396799	43203	–38.01
10169.531017	43204	–23.07
10171.554764	43219	32.14
10172.364589	43225	37.35
10172.500202	43226	–32.09
10173.443720	43233	72.42
10173.579514	43234	2.98

spectrum was clearly incorrect and not used in any subsequent analysis. This leaves a total of 220 spectra of SW Sex to be used.

Figure 6.1 shows the average spectrum of SW Sex during our run. In many CVs the region where the accretion stream hits the accretion disk (the ‘hot-spot’ region) shows enhanced emission. To illustrate any difference we show the averaged spectrum in three phase-

Table 6.3. SW Sex system parameters as used for the eclipse mapping

Period	11658.67 s
M_{WD}	0.44 $M_\odot$
M_{sec}	0.3 $M_\odot$
Inclination	79°
Distance	290 pc

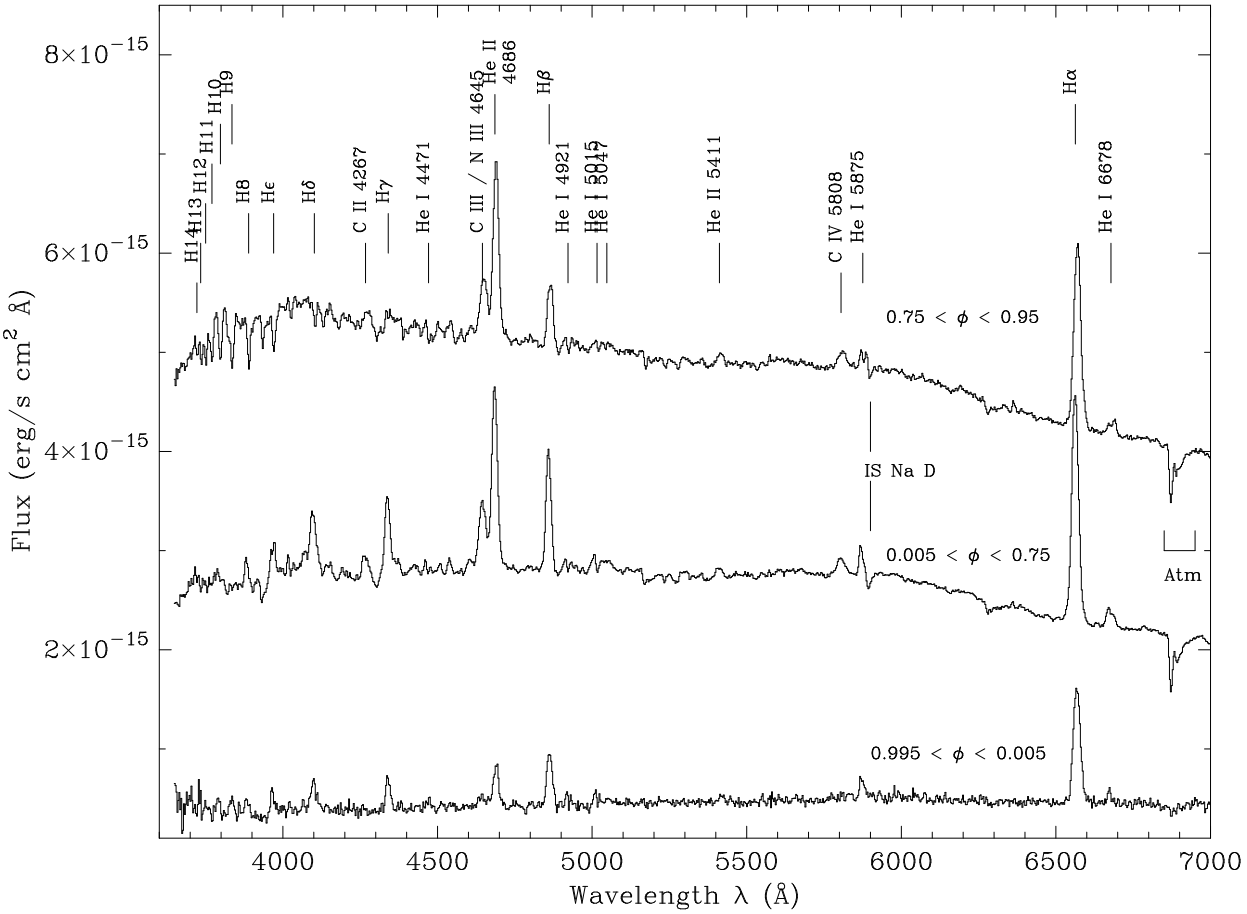

Figure 6.1. The average spectrum of SW Sex at phase intervals $0.995 < \varphi < 0.005$ (bottom), $0.005 < \varphi < 0.75$ (middle) and $0.75 < \varphi < 0.95$ (top, offset by +2.0 10^{-15} erg s^{-1} cm^{-2} $Å^{-1}$). All major lines are indicated.

bins: one that shows the 'normal' spectrum (phases $0.005 < \varphi < 0.75$), one at the phases that enhanced hot-spot emission is visible ($0.75 < \varphi < 0.995$) and one at mid-eclipse ($0.995 < \varphi < 0.005$). The out-of-eclipse shape of the spectrum is reminiscent of other SW Sex stars: strong single peaked Balmer, HeII and NIII and CIII emission. However, the ratio of HeII λ4686 over Hβ is larger than unity in our observations. In previously

published spectroscopic observations of SW Sex (Green et al., 1982; Penning et al., 1984; Williams, 1989 and Dhillon et al., 1997) the flux in HeII λ4686 is less than or equal to that of Hβ, which is typical for all the SW Sex systems. The lines of HeI are weaker than in previous observations, compare e.g. the strength of HeI λ4471, with the spectrum as published in DMJ97. Apparently, a large fraction of the helium that normally causes the HeI emission is now ionized and shows up as HeII λ4686, pointing to a source of high ionization. This is confirmed by the appearance of the CIV λ5805 and HeII λ5411. A strong source of far-UV or soft X-radiation, emitting radiation with energies above $\sim$ 50 eV ($\lambda <$ 250 Å), is needed to observe these lines.
A marked difference with previous observations is the continuum flux level. To be able to compare with previous observations we measure a continuum flux at λ4500 Å of $\sim$2.8$\times10^{-15}$ erg s^{-1} cm^{-2} Å^{-1} (1.9 mJy, AB=15.7) at phases $0.005 < \varphi < 0.75$ and 4×10^{-16} erg s^{-1} cm^{-2} Å^{-1} (0.27 mJy) at phases $0.995 < \varphi < 0.005$. Comparison with observations by Penning et al. (1984), Honeycutt, Schlegel and Kaitchuck (1986) and RvPT92 (who measure AB=14.5 at 4410Å), show the 4500 Å level to be almost $\sim$1.2 mag fainter than in previous observations. The depth of the eclipses (see Sect. 6.7) is not significantly different (1.9-2.0 mag) from previous epochs.

6.4.2 Hot-spot absorption line spectrum

During the phases that a hot-spot may be visible, $0.75< \varphi <0.95$, the blue spectral shape changes dramatically. The higher Balmer lines change from general emission between phases $0.005< \varphi <0.75$ to absorption, visible up to H14, as shown in Fig. 6.2. At the same time, the higher excitation lines of HeII λ4686, CII λ4267 and the CIII/NIII λ4645 complex do *not* change in strength compared to the continuum and each other.
The ensemble of absorption lines as present in the hot-spot spectrum can be identified as those occuring in a B0-type spectrum (e.g. HD77581/Vela X-1; Van Kerkwijk et al., 1996). Typical temperatures in stellar photospheres of B0-type stars range between 19 000 K $< T_{abs} <$ 25 000 K, depending on the local gravity. Since we expect a relatively low local gravity in the hot-spot region ($g \sim 0.1 g_{\odot}$, comparable to a giant's photospheric gravity; Marsh 1988), the temperature will be on the lower end of this range. Deducing a more exact determination of the temperature of this absorption region is compounded by two factors: the low-resolution of the data and the fact that most of the absorption lines that are normally used for spectral classification of OB-type stars (HeI, HeII, CII, CIII) are in emission in SW Sex. However, we can set a lower limit of $\sim$15 000 K (corresponding to a B2 spectral type), from the fact that the SiIV λ4089 Å line is visible and the MgII λ4481 Å line is not visible. We will deduce in the following paragraphs that the hot-spot that comes into view at phases $>$0.75 consists of two components; a part that is optically thick in the continuum and a part that is optically thin in the continuum, but optically thick in the lines. The absorption line spectrum as seen here is formed in an optically thin, chromosphere-like, part of the hot-spot which is located above the plane of the disk

and which causes veiling of continuum radiation from the inner parts of the accretion disk.

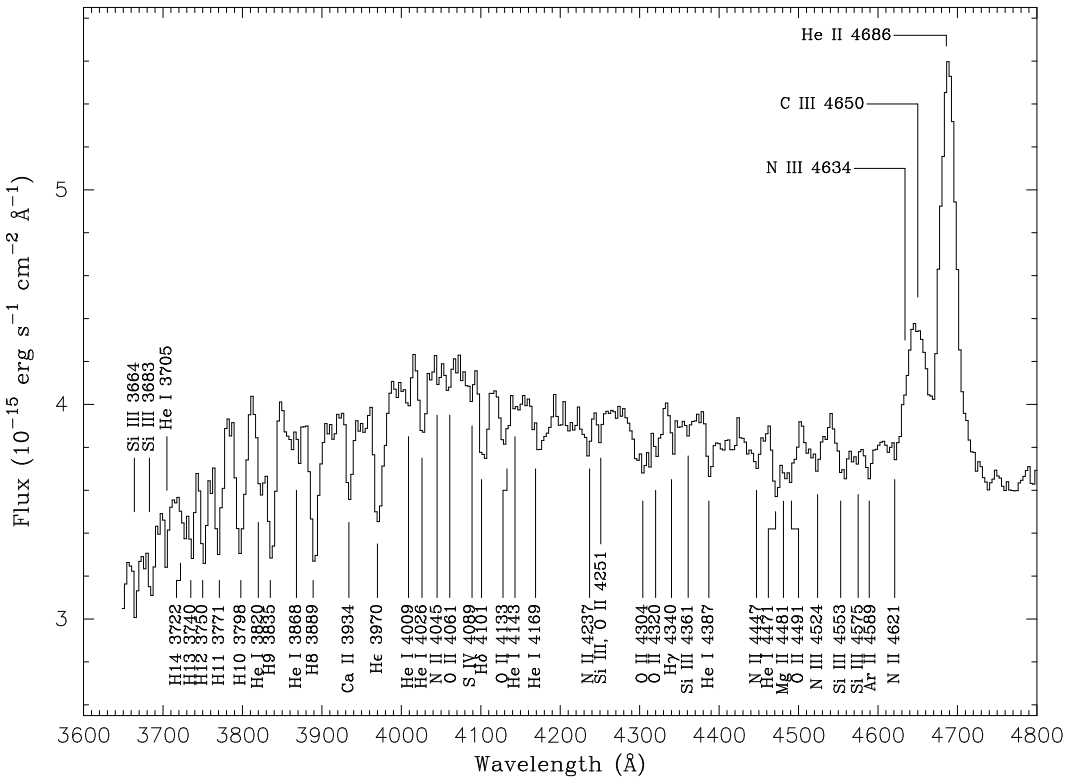

Figure 6.2. The blue part of the average spectrum at $0.75< \varphi <0.95$. The absorption line identifations show the spectrum to be identical to a B0-type spectrum, indicating absorbing material temperatures of 19 000 K $< T_{abs} <$ 25 000 K. Line identifications have been taken from Van Kerkwijk et al. (1996).

6.4.3 Central absorption near φ=0.5?

One of the trademarks of SW Sex systems as described in Sect. 6.1 is transient absorption in the emission lines at phases around 0.5. Since SW Sex does show the other trademarks of SW Sex behaviour in our observations, we investigated whether this transient absorption is present in our current data. Fig. 6.3 shows the blue part of the spectrum between $0.45< \varphi <0.55$ in detail. Although no central absorption is seen, the asymmetric line-profiles of Hγ and Hδ may indicate that it is present at a low level. As we will show in Sect. 6.5 the line flux reaches a local minimum around $\varphi \sim 0.5$, which may be indicative of some absorption. The feature that seems to indicate most clearly the presence of central absorption in Fig. 6.3 is the CII λ4267 line. In Sect. 6.5 we will argue that this is caused by different effects, namely the fact that this line consists of two components

with different phase-dependence of their velocity field, which will cause the line to appear double-lined at certain phases. (The same applies to the HeI $\lambda\lambda$ 6678, 5875 lines.)

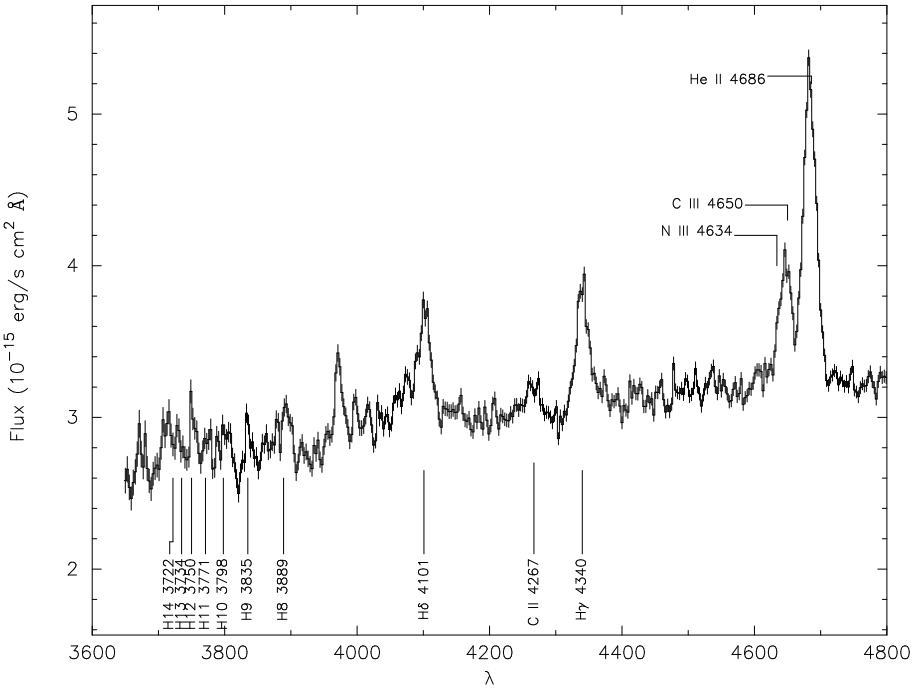

Figure 6.3. The average spectrum of SW Sex between 0.45< φ <0.55. No clear central absorption in any of the emission lines is seen.

6.5 Orbital spectral line variations

6.5.1 Multiple emission components

We have binned the data in 25 phasebins and subtracted the underlying continuum by making a linear fit to surrounding wavelengths. The trailed spectra are shown in Fig. 6.4 for Hα, Hβ, Hγ and Hδ on the top row and HeII λ4686 together with the CIII/NIII complex, the HeI λ6678, the HeI λ5875 together with CIV λ5808, and the CII λ4267 line on the lower panel.

All the lines consist of two components of unequal strength and with a distinct velocity dependence with orbital phase. The two components are most clearly seen in the higher Balmer and the HeI lines. The Hα line most clearly shows a single S-wave, while a low-level second component is barely visible. Going up the Balmer series this second component gains in strength compared with the main component, up to the point where it is of almost equal strength in the Hδ-line.

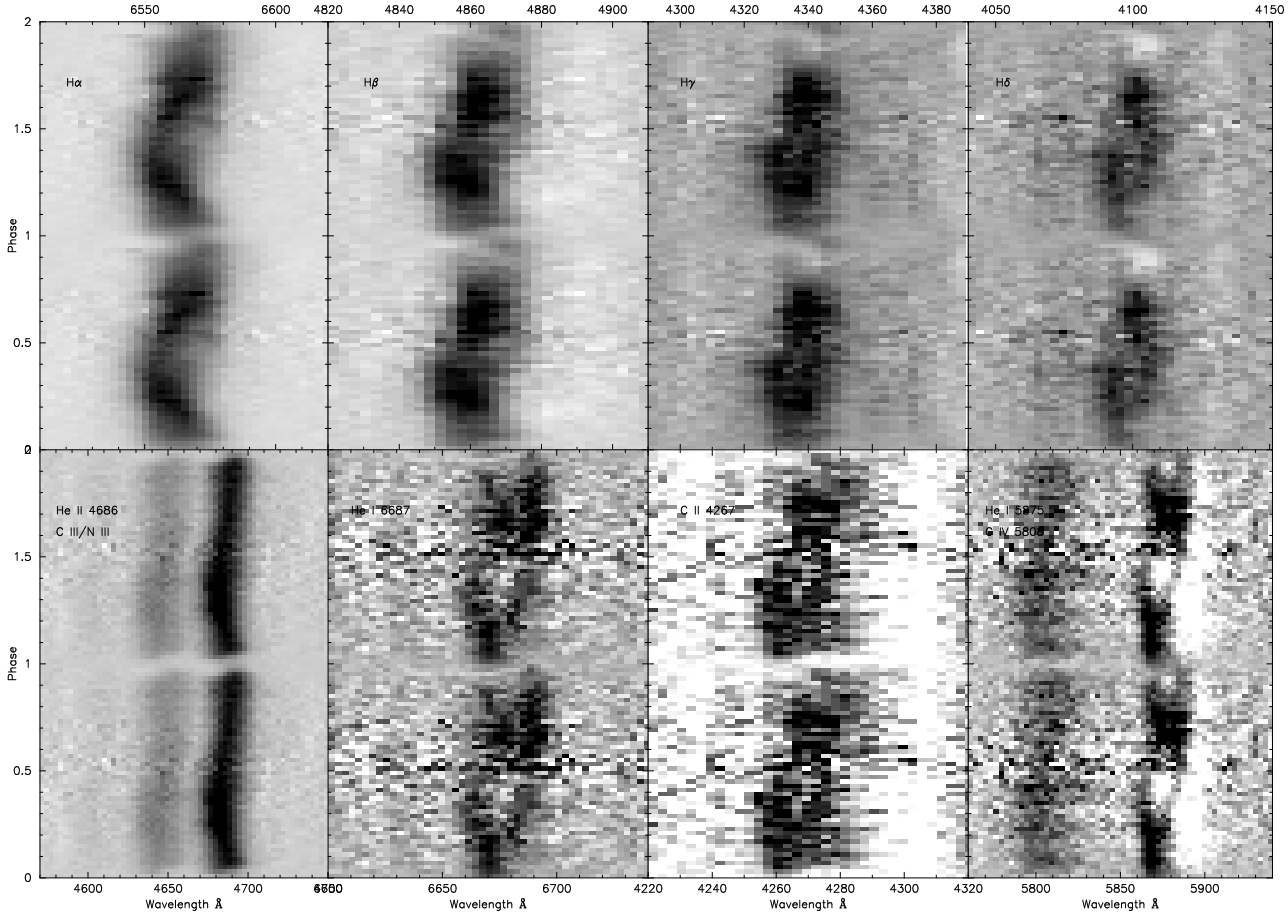

Figure 6.4. Trailed spectra of Hα, Hβ, Hγ and Hδ (top, left to right), and HeII λ4686/ CIII, NIII λ4645, HeI λ6687, CII λ4267 and HeI λ5875 and CIV λ5808 (bottom, left to right). In all spectral lines, but HeII λ4686, to a lesser or stronger degree, two S-wave components are visible, one reaching maximum redshift at $\varphi \sim$0.5, and one reaching maximum redshift at φ 0.9. For the lower Balmer series and the HeII λ4686 line, the latter component dominates. However for the higher Balmer series and the HeI lines the two components are of roughly equal strength. The HeI λ5875 line is badly affected by the NaI doublet next to it.

The fainter component is hardly visible in the HeII λ4686 and in the CIII/NIII blend. It is visible, and most prominently, in the CII λ 4267 and He I lines. Signal-to-noise levels in the CIV λ5805 line are too low to draw any definite conclusion, but it appears to be a single component line, like HeII λ4676 and the CIII/NIII blend.

The existence of two components explains the noted double line feature in the HeI lines and CII λ4267 line in Sect. 6.4.3. The HeI λ5875 is badly affected by the interstellar Na D doublet at λ 5890 Å.

6.5.2 Radial-velocity curves of the main S-wave component

The radial-velocity curves of the main component visible in Hα and HeII λ4686 are shown in Figs. 6.5 and 6.6. These were determined by fitting a single Gaussian to the line profiles at phase intervals of 0.02. The Gaussian fit is effectively determined by the flanks of the emission lines. In both lines the main component has its red-to-blue crossing at $\varphi = 0.09$. This indicates that the emission is not centered on the WD, since in that case the red-to-blue crossing would coincide with superior conjunction of the white dwarf, i.e. at φ=0. This phase lag of the emission lines is a well known phenomena of SW Sex stars (see e.g. Thorstensen 1991, and the review by Dhillon, 1995).

The amplitude of the HeII λ4686 is slightly lower than that of the Hα line. However, judging from the residuals to the HeII λ4686 line just before and after eclipse, there is a hint that the amplitude may have been slightly underestimated, in which case the amplitude of both lines are identical. If we take the average of the two measured values as the total velocity of the emitting material and correct for the orbital inclination (i=79°), we get $v_{\rm res}$ = 230 km/s for the emitting material. The phase-lags are in good agreement with the results from DMJ97, who find almost identical values.

Both radial velocity curves show a rotational disturbance around mid-eclipse. This rotational disturbance is caused during ingress because the blue-shifted part of the accretion disk is eclipsed first and during egress because the red-shifted part of the disk is revealed last. The occurence of a rotational disturbance shows that (part of) the emission originates in a rotating disk. Comparison of the magnitude of the disturbance in the two lines shows that the displayed red-shift at ingress is the same for both lines, but that the blue-shift of the Hα line is clearly lower, and of the HeII λ4686 line clearly higher, when compared with the red-shift. For both lines maximum redshift occurs at $\varphi \sim$0.95, which coincides with the moment of ingress of the white dwarf and the hot-spot region. Maximum blue-shift, however, is reached for both lines again at the same phase: $\varphi \sim$0.03. This is too early to be explained by an emission site in the plane of the disk if Roche geometry holds.

What causes the different features as observed in the radial velocity curves? The 0.09 phase-offset indicates that the emission site is not on the line of centers, between the center-of-mass (CoM) and the white-dwarf, but at a slight angle to it. The identical phase-lag and amplitude of the radial velocity curve indicate that both lines originate in the same location.

The Gaussian fit-method is sensitive to the emission that dominates the profile at a certain phase. For almost all phases this is the emission site just mentioned. However, between $0.95 < \varphi < 0.03$, this emission does not dominate, most likely because it is eclipsed by the secondary and we see emission from those parts of the disk that are still visible. The mid-point of the rotational disturbance, which is at $\varphi \sim$0.99, tells that mid-eclipse of the main emission site occurs slightly before that of the white-dwarf. If the emission site is located in the orbital plane it would mean that inferior conjunction of the emission site should occur *before* that of the white-dwarf, whereas we observe that it occurs *after* the

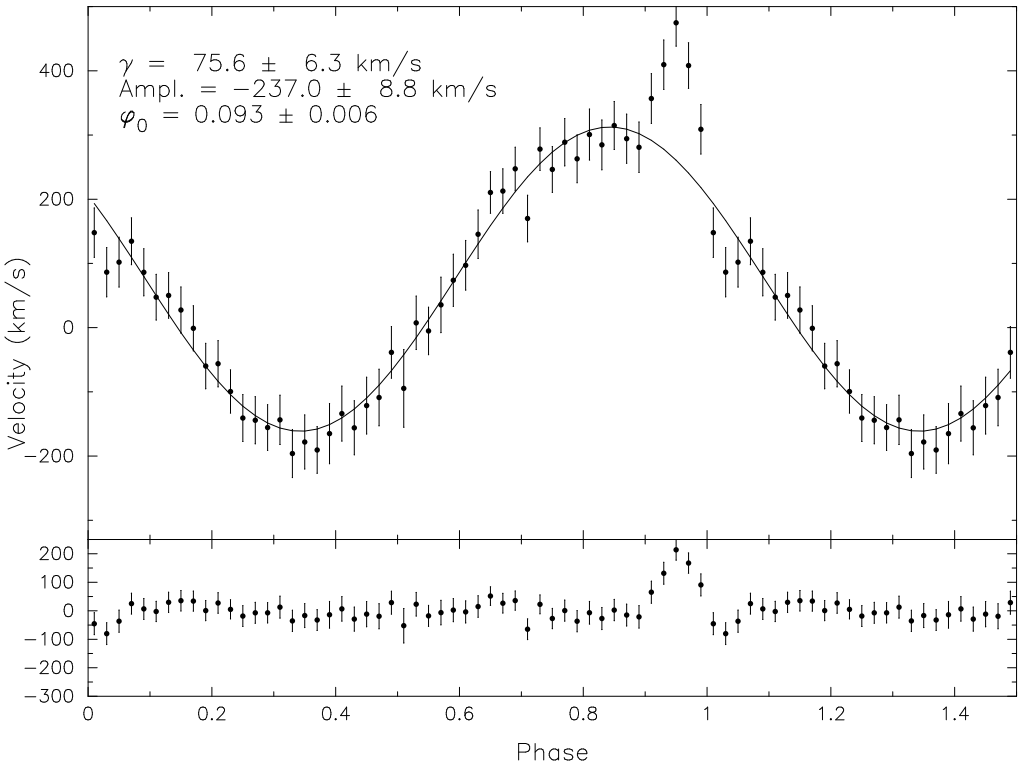

Figure 6.5. Radial velocity curve of Hα , which is dominated by the main S-wave component. The radial velocity curve is lagging the white dwarf (expected red-to-blue crossing at phase 0.) by 0.09 in phase. A fit of form (V(φ) = γ+Ampl$\times$ sin$(\varphi - \varphi_0)$ is fitted to the phaseinterval 0.15 $< \varphi <$0.85. The residuals to the fit are shown in the bottom plot. This clearly show the rotational disturbance around phase zero.

white dwarf ($\Delta\varphi$=0.09). From this we conclude that the emission site is *not* in the plane of the disk, but above it at such an extent that its projection appears to be leading the white dwarf during eclipse, instead of trailing it.

6.6 Transient absorption during the hot-spot phase

One of the most remarkable features in the trailed emission line spectra, shown in Fig. 6.4 is transient absorption that become visible at phases >0.75. Since the absorption is best seen in the higher Balmer lines, let us look at H8 (λ3889 Å). This line was chosen because it is reasonably strong and isolated, allowing for a reliable continuum subtraction. In Fig. 6.7 the trailed spectrum of H8 at phases before and after the eclipse is shown. We see that the absorption feature is only visible between 0.82$< \varphi <$0.94; that it is slightly redshifted, and only weakly (if at all) dependent on phase. No sign is visible of the eclipse (indicated by the dashed line). The line light curve (displayed in the right panel of Fig.

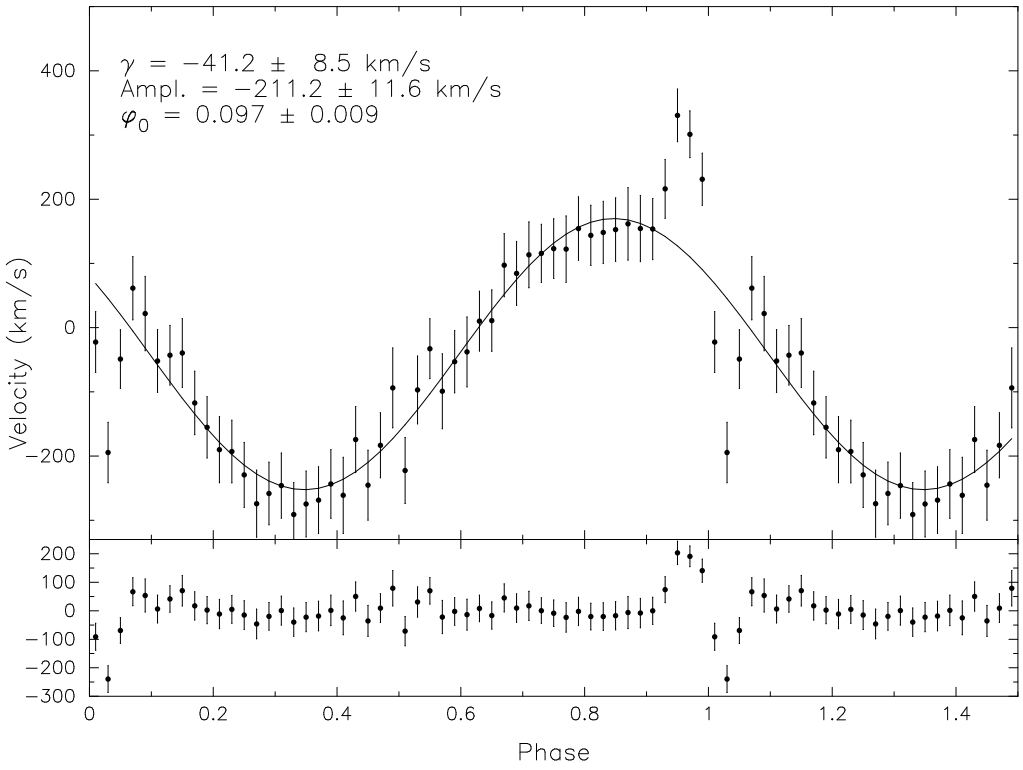

Figure 6.6. Same as Fig. 6.5, but here for the HeII λ4686 line.

6.7), shows that the transient absorption feature is almost U-shaped.

In contrast to the H8 line we also show the same phase interval for the HeII λ4686 line (Fig. 6.8). Here we see no sign of any transient absorption in the phase interval 0.82 $< \varphi <$0.94. The eclipse is prominently visible and the line emission is dominated by the main S-wave component discussed in Sect. 6.5.2.

If we now look at the Hβ or Hα line we can interpret the complex behaviour we see there as the intertwining of three different orbital variations; the eclipse, the main S-wave component and the transient absorption. The absorption spectrum that becomes visible at the 'hot-spot' phase (see Sect. 6.4.2) is identical in behaviour to the H8 line. We have already seen that this material has a temperature of T_{abs}= 19 000-25 000 K. In the following we will argue that it is caused by veiling of the continuum radiation from the inner disk by material that is above the disk in the hot-spot region. The other possibility of the hot-spot region itself being optically thick with a temperature T_{abs} is inconsistent with the continuum lightcurve of the hot-spot as will be presented in Sect. 6.8.

Veiling of radiation occurs when gas that is optically thick at specific wavelengths will absorb radiation from a continuum source located behind the gas and causes absorption features in the received spectrum (the 'reversing layer' model of stellar atmospheres). Spectral analysis will show the temperature of the intervening gas. In our case we can explain

the transient absorption if the white-dwarf and inner disk are the continuum source and gas above the hot-spot region is the intervening material. The absorption will only show up if the white dwarf is directly behind the hot-spot region as seen by the observer. For any likely hot-spot position on the disk, this will occur in the phase-interval $0.8< \varphi <1.0$, and is therefore consistent with the observed interval of $0.82< \varphi <0.94$. Depending on the size of the white-dwarf region and the hot-spot region and the exact geometry, the light curve profile can be U-shaped or V-shaped. If both the WD region and the hot-spot region have a well defined size, the light curve can be U-shaped. If either or both of the regions is extended, has a somewhat 'fuzzy' edge or contains a temperature gradient, the light curve will become more V-shaped. The sudden disappearance of the high excitation lines (as shown in Fig. 6.7) can be explained by the simple fact that by the secondary is eclipsing the hot-spot region. The redshift of the absorption can be explained because at these phases the veiling material will be moving away from the observer, due to a combined motion of gas in the disk and around the center-of-mass. The low resolution of our data and the short phase interval over which the absorption is seen, limits the detectability of any change in the wavelength dependence of the veiling material. The fact that the HeII λ4686 line is not influenced by the transient absorption can in this case be explained by the fact that the optical depth for HeII λ4686 radiation is $\ll 1$ in the veiling material, which is not too suprising because from the absorption spectrum we know that T_{abs} = 19 000-25 000 K, which will in general be too low to contain a considerable fraction of He^{+}.

6.6.1 Line light-curves

Line light-curves for the lines presented in Sec. 6.5 were extracted by summing all data in the relevant wavelength regions and subtracting from these a linear fit to the neighbouring continuum. These light curves are presented in Fig. 6.10. As was already evident in the trailed spectra and is even more evident here, the line light-curves show substantial variations outside eclipse. The distorted profiles are very similar to those that have been seen before in SW Sex (DMJ97). We see that, in contrast to the U-shaped profile of the H8 line presented in the previous paragraph, the lower Balmer line have V-shaped profiles, that reach minimum light progressively earlier if we go up the Balmer series. As explained in the previous paragraph, such a V-shaped profile can be explained by an optically thick hot-spot that partially blocks the continuum emission region. The occurence of minimum light at φ=0.95 can then be explained by a maximal *vertical extension* of an optically thick, but dark, hot-spot. However, this is inconsistent with the continuum light curves which show extra emission at these phases. This problem vanishes when we explain the V-shaped profiles as due to cancellation of the emission line component by a strong, photospheric, absorption component from an optically thick hot-spot region, that does *not* block the continuum light coming from the inner region. We can then explain the occurence of minimum light at φ=0.95 by the maximum *visibility* of the hot-spot, with its

deep photospheric absorption lines. Note that the onset of the absorption and the phase of minimum light for the spectral lines correlate very well with the reconstructed light curve of the hot-spot continuum which peaks at the same phases, as will be shown in the next section. From the similarity between the lightcurves presented here and those presented by DMJ97 we infer that the cause of the early 'ingress' and the rapid egress of the lines is caused by an optically thick hot-spot region. The occurence of deep Balmer absorption lines in the late B-type spectrum of this hot-spot then explains the V-shaped light curves. The fact that these V-shaped light curves appear to be persistent in SW Sex shows that the optically thick hot-spot region is a persistent feature.
The distortion of the lightcurves make that we should be very careful in using the spectral lines in studies that interpret them as coming from the plane of the orbit as is often assumed in e.g. eclipse mapping and Doppler mapping studies. As seen in the previous paragraphs the lines are affected by absorption as early as φ=0.8. Since this variation is not caused by the eclipse of the secondary star, we should be careful in interpreting the results of spectral line eclipse mapping studies.

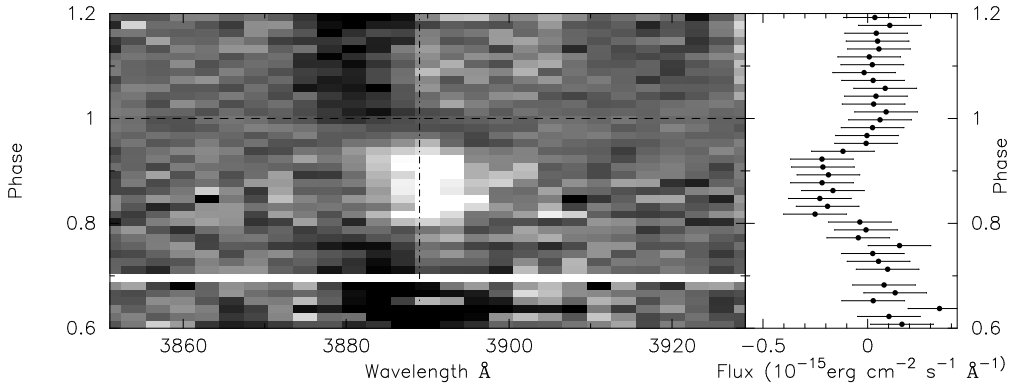

Figure 6.7. Trailed spectrogram of the H8 (λ3889) line (left) and its lightcurve (right) from phase 0.6 to 1.2. The horizontal dashed line shows mid-eclipse according to Eq. 6.1, the vertical dashed line is the central wavelength. The absorption is clearly redshifted and phase-independt.

6.7 Light curves

6.7.1 Continuum light-curves

From the spectrophotometry discussed above, we have extracted light curves at many wavelength regions. Figure 4.2 shows the continuum lightcurves between $\lambda\lambda$ 4200–4240, 5300–5340 and 6720–6760 Å as examples. The most prominent feature in the light curve, except for the eclipse itself, is the presence of a clear orbital hump in the blue part of the

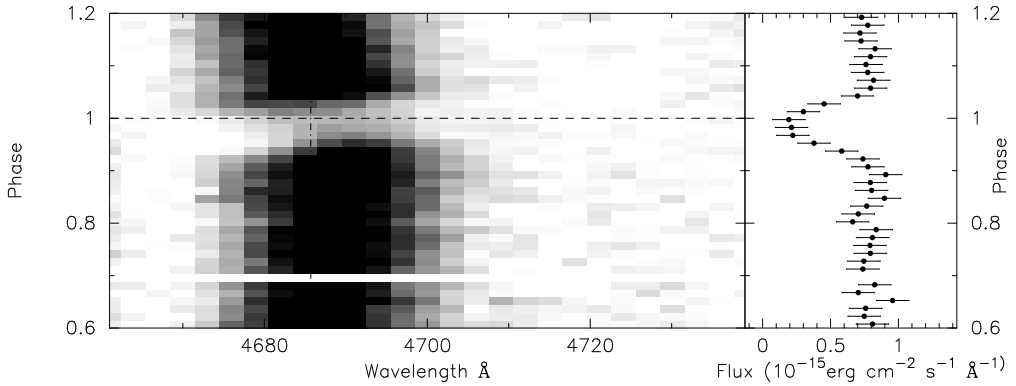

Figure 6.8. As Fig. 6.7, but for HeII λ4686

spectrum, that gradually disappears when going from blue to red and is gone in the red-part of the spectrum.

The flux at mid-eclipse is fairly constant throughout the spectrum, indicating that at mid-eclipse almost no sign of secondary star emission is seen (as also seen in the bottom spectrum of Fig. 6.1).

Comparison of the continuum light curves with previously published data shows a similar amount of asymmetry in the eclipse profile as in DMJ97, Penning et al. (1984) and Ashoka et al. (1984) for the λ 4200–4240 Å light curve. This asymmetry becomes less for the λ 5300–5340 Å light curve and non-existent for the λ 6720–6760 Å light curve. Since all the previous studies have been done in blue or white light, it seems that, as already concluded in the previous paragraph, the presence of a hot-spot region is persistent.

Since the elementary eclipse-mapping program, as will be applied in Sec. 6.9, assumes that all variation in the light curve occurs during eclipse, a correction is required to be able to use the continuum light curves in the eclipse mapping program. We have applied a polynomial fit to the phases smaller than –0.12 and larger than 0.14. Trial fits with different order polynomials showed that a 7th order polynomial returns the smallest residuals, independent of wavelength. The fit to the continuum is also shown in Fig. 6.9.

6.8 The hot spot continuum spectrum

We have seen in Sect. 6.6 that the absorption line spectrum as seen during $0.75 < \varphi < 0.95$ is characterized by a temperature T_{abs}=19 000-25 000 K and is most likely caused by veiling of the continuum radiation from the inner disk by material above the plane of the disk and near the hot-spot region; a hot-spot chromosphere. At the same time we have seen that the decrease in the strength of the lower Balmer lines is best explained by an optically thick hot-spot, that lies in the plane of the disk, and does not block any the light coming from the inner disk. In order to explain the V-shaped Balmer lightcurves

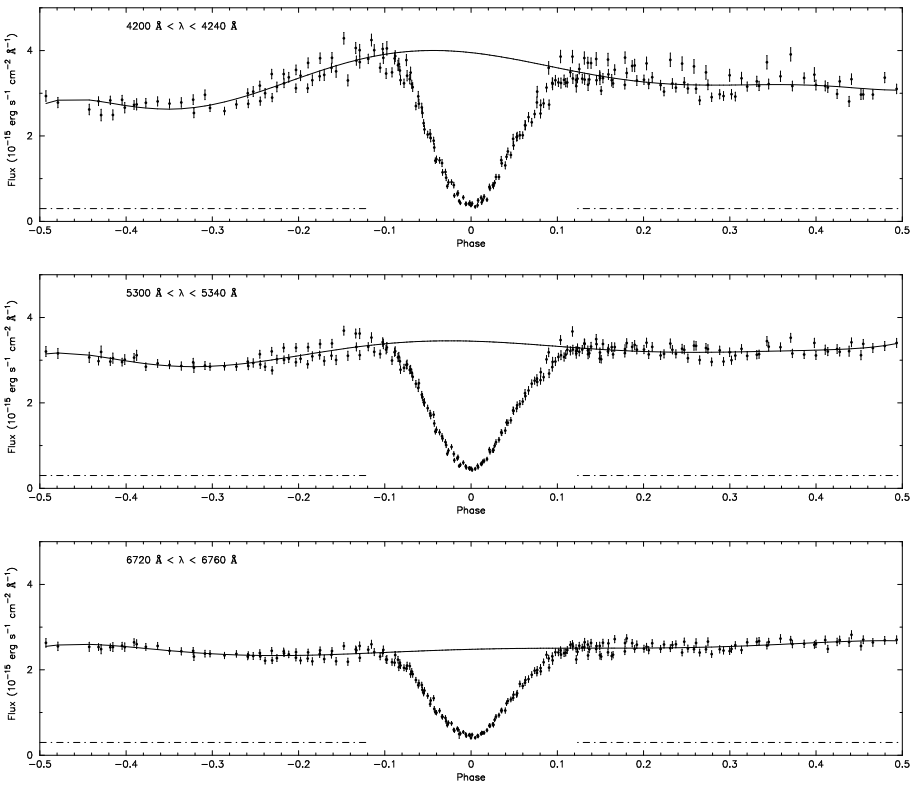

Figure 6.9. The spectrophotometric light curve of SW Sex between 4200Å $< \lambda <$ 4240 Å (top), 5300Å $< \lambda <$ 5340Å (center), and 6720Å $< \lambda <$ 6760 Å (bottom). A pronounced orbital hump is seen in the blue light curve, which gradually diminishes and is gone at the reddest wavelengths. The 7th order polynomial fits to the light curves outside eclipse are shown as the full lines.

this optically thick hot-spot should contain strong Balmer absorption lines. Here we will deduce limits on the temperature of the optically thick hot-spot by a reconstruction of its spectrum at maximum light.

If we assume that the fit to the lightcurve as shown in Fig. 4.2 is an accurate description of the lightcurve of the system if no eclipse were present, we can see that the hot-spot is visible from phases –0.26 to +0.19, with a maximum visibility at phase 0.95. If, for the moment, we assume that the system consists of only two sources of continuum emission: a stationary accretion disk, that does not vary with orbital phase, and a hot-spot that is only visible between phase –0.26 and +0.19, we can in first order reconstruct the spectrum of the hot-spot. From the fits to the lightcurve outside continuum we reconstruct the spectrum as we would have seen it between $0.925 < \varphi < 0.975$ if no eclipse were present. This spectrum will be the sum of the hot-spot continuum radiation and the non-varying contribution of the accretion disk. We can then compare this with the spectrum at a phase when no hot-spot emission is seen; here $0.3 < \varphi < 0.35$. If we subtract these two spectra we are left with the spectrum of the hot-spot, as shown in Fig. 6.11. The drop below zero

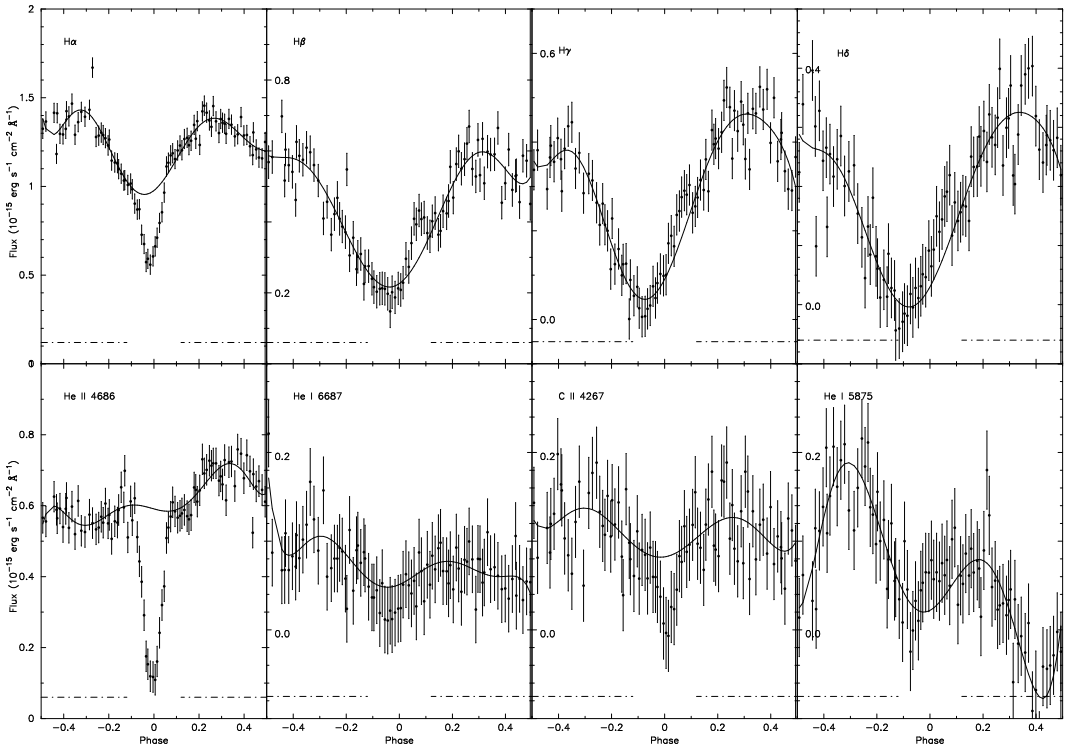

Figure 6.10. The spectrophotometric light curves of the lines presented in Fig. 6.4. Data have been rebinned to 100 phasebins to allow for meaningfull continuum subtraction. The solid line shows the 7th order polynomial fit to the phase intervals outside –0.12 and 0.12 (indicated by the dashed-dotted line). As can clearly be seen, only the He II line and to a lesser extent the Hα and the CII lines show evidence for an eclipse by the secondary.

of the resultant hot-spot spectrum in Fig. 6.11 (bottom line) at wavelengths $>$ 6400 Å, shows that the hot-spot emissivity at wavelengths redwards of this is lower than that of the accretion disk.

We have compared the blue part of the hot-spot spectrum (λ <5000Å), which is most likely to be the closest to the 'real' hot-spot spectrum, with the spectral catalogue of Jacoby and Hunter (1984) to determine the spectral type and therefore the temperature. In this fitting procedure the derived spectrum is most sensitive to the Balmer jump. Best fits were obtained for an B6–B8 spectrum (see Fig. 6.12). As outlined in Marsh (1988) one would expect a giant spectrum to best fit the spectrum because of comparable gravities. However, our reconstructed hot-spot spectrum is of a too low spectral resolution to make this luminosity class distinction. In Fig. 6.12 we compare our hot-spot spectrum (solid line) with the B8 III spectrum of HD28696, rebinned to the same spectral resolution and scaled to the same flux (dashed line). Its shows a fine fit for the Balmer jump and the region blueward of 4300 Å, but an increasingly worse fit for regions redward of 4300Å. This is mainly due to our assumption that the accretion disk and hot-spot due not vary

with phase.

In Fig. 6.12 we also show a B5III and A3III spectrum. The B5III spectrum underestimates the Balmer jump considerably, and hence the hot-spot continuum must be cooler than B5III (T_{spot} <12 000 K). Consequently, the gas, which we see in the absorption line spectrum as presented in Sect. 6.4.2 (the hot-spot chromosphere) is of higher temperature (with a lower limit of T_{abs} >15 000 K) than the gas that emits the enhanced hot-spot continuum radiation (the hot-spot photosphere), for which we can put a very conservative upper limit of T_{spot} <12 000 K. We are therefore dealing with two distinct regions, in temperature, as well as in height.

The strength of photospheric Balmer absorption lines reaches its maximum strength in late B-type and early A-type stars. The evidence shown here that the hot-spot photosphere is of similar temperature as late B-type stars, supports the explanantion for the V-shaped decrease in the Balmer lines as caused by strong photospheric absorption lines that 'cancel-out' the emission components, that are formed at a certain height above the accretion disk.

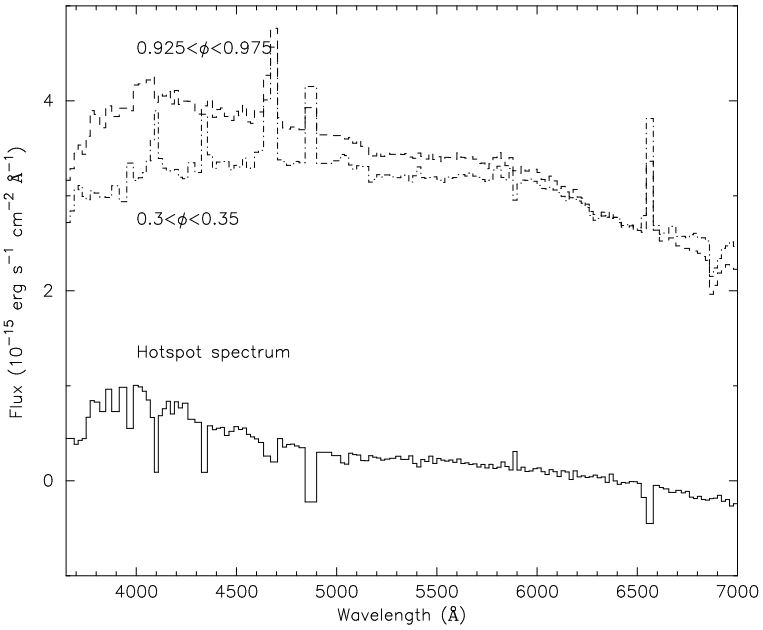

Figure 6.11. The reconstructed spectrum between phases 0.925< φ <0.975 and 0.3< φ <0.35, extracted from the fits to the out-of-eclipse lightcurve as discussed in Sect. 6.7. Under the assumption that the total emission is caused by two components (a phase-indepent emission and a hot-spot spectrum), the difference between these to spectra is the hot-spot spectrum (bottom curve).

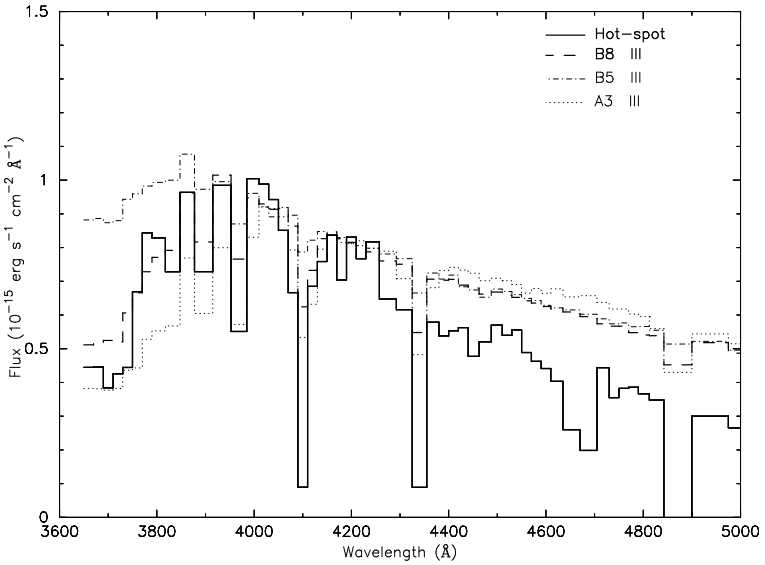

Figure 6.12. The reconstructed hot-spot spectrum (thick line), compared with three standard star spectra (B8III, dashed thick line; B5III, dot-dashed line; and A5III, dotted line) from Jacoby and Hunter (1984). The discrepancy between all three fitted spectra and the reconstructed hot-spot spectrum redward of 4200 Å, shows the limitation of the 'accretion disk plus hot-spot' assumption. The B5III spectrum shows the conservative upper limit on the spectrum of the hot-spot region.

6.9 Spectral Eclipse Mapping

Eclipse mapping uses the information contained in the shape of the eclipse light curve to reconstruct the light distribution on the accretion disk. For a general description of the method we refer to Horne (1985). We have used the same program as was used by Rutten et al., (1994) for the analysis of UX Uma, which uses a maximum-entropy based optimization routine, as described in Horne (1985). The maximum entropy optimization was done with the MEMSYS package, kindly provided by drs. Gull and Skilling. For the reconstruction of the accretion disk in SW Sex we used the basic, thin, flat disk approach, as was also used in RvPT92, who also show that the flat temperature distrubution profile they find for SW Sex from broad-band photometry is not due to the assumptions about the shape or thickness of the disk. No correction for interstellar extinction was deemed necessary since IUE spectra show no presence of the 2200 Å bump (RvPT92).

6.9.1 Light curve selection and preparation

We have split the total wavelength range covered by our spectra (3650–7000 Å) in 40 Å wide bands, with the exception of the spectral lines that are taken as one bin. We have chosen not to subdivide the emission lines in sub-bands because we doubt the applicability of the eclipse-mapping method to the emission lines in SW Sex on the basis of the spectral

line behaviour discussed in the previous paragraphs. A total of 79 wavelength bins were selected in this way. The choice for 40 Å wide bins was made as an optimum between S/N and the number of bins. For the eclipse mapping procedure the light curve outside the eclipse phase interval is set to the average out-of-eclipse level in order to minimize the impact of variations on the data outside eclipse (e.g. flickering).
The errors which were assigned to each spectral bin on the basis of Poisson statistics were propagated to the light curves and used as errors on the phase-points in the light curves. No scaling or offset has been applied to the data to produce the light curves as shown in Fig. 4.2. This shows that SW Sex was very stable during the six nights of our observations. The small amount of variation that is present is either caused by intrinsic flickering in the source (irregularities in the mass-transfer), or small residual imperfections in the slit-loss correction procedure. This variation is clearly seen in the blue part of the spectrum, and diminishes to the red part of the spectrum, and is therefore most likely dominated by intrinsic flickering. This intrinsic flickering will cause the χ^2-based eclipse mapping routine to reconstruct spurious fine structure in the resulting map. To avoid this we have increased the formal errors by up to 40% for the bluest wavelengths. In the red part of the spectrum this adjustment was not more than 10%.
For the reconstructions as presented here, we used a 51×51 pixel map, with the phase interval $-0.20 < \varphi < 0.20$ as input. Considering the large size of the accretion disk of SW Sex as found by RvPT92 we have set no *a priori* limit to the size of the accretion disk, other than that it fits in the Roche-lobe. The light curve zero-point was taken as a free parameter in the fit to to account for any uneclipsed light (RvPT92).

6.9.2 Reconstructed intensity distribution

In Figs. 6.13,6.14 and 6.15 we show the resulting eclipse maps in three different wavelength regions from the blue, middle and red part of our spectrum. The disks show a clear dominance of the white dwarf and surroundings, which is reconstructed as the bright region in the middle. On the scale used here the size of the WD corresponds to $\sim \frac{1}{4}$ pixel. We see that the emission is dominated by the WD and surroundings, with a clear hot-spot contribution in the blue maps, which diminishes towards the red.

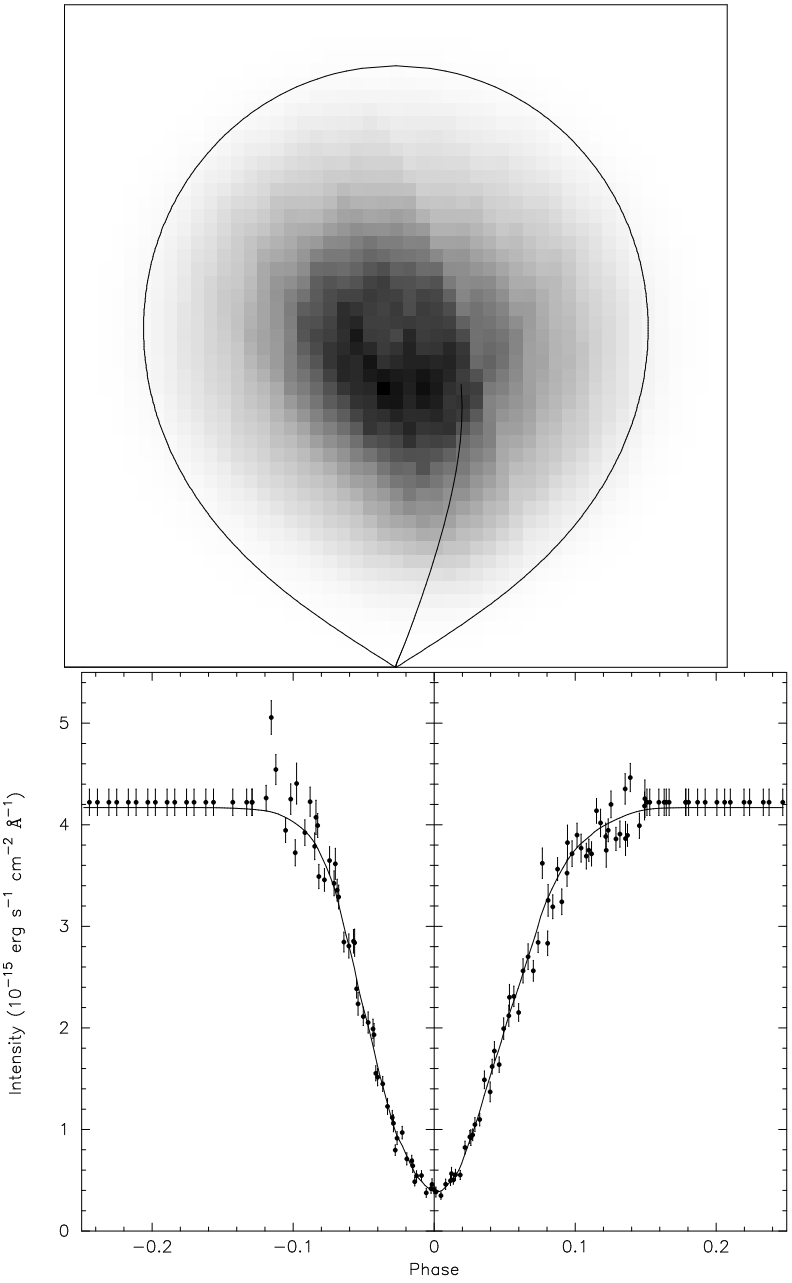

Figure 6.13. The reconstructed accretion disk for the wavelength region between 4040 Å and 4080 Å (top). The bottom panel shows the input (dots) and reconstructed (line) lightcurves. A clear hot-spot contribution is visible.

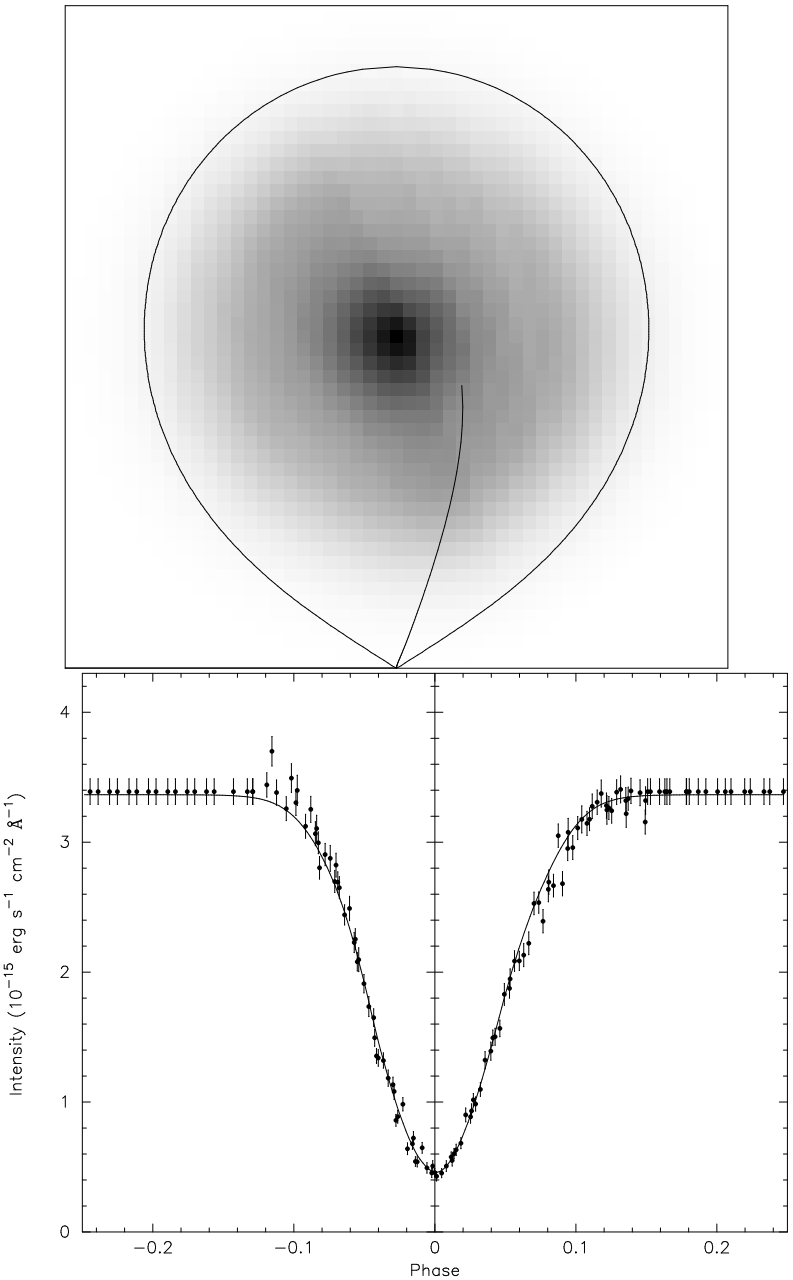

Figure 6.14. The reconstructed accretion disk for the wavelength region between 5490 Å and 5530 Å (top). The bottom panel shows the input (dots) and reconstructed (line) lightcurves.

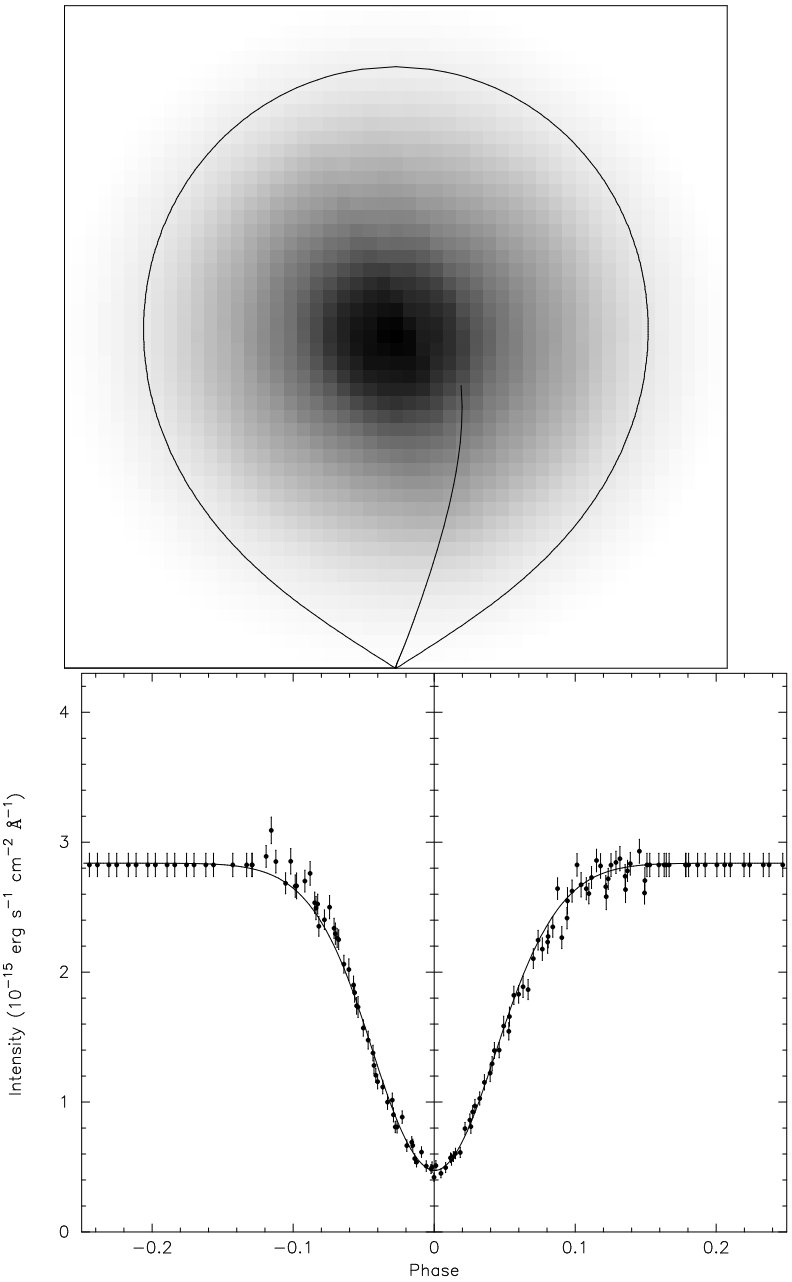

Figure 6.15. The reconstructed accretion disk for the wavelength region between 6330 Å and 6370 Å (top). The bottom panel shows the input (dots) and reconstructed (line) lightcurves.

6.9.3 Size of the accretion disk

To measure the size of the accretion disk we use the same measure as in RvPT92, namely the point where the intensity has fallen to 10% of the central intensity. At 4060 Å we measure $R_d \simeq 0.7\ R_{L_1}$, where R_{L_1} is the distance between the inner Lagrangian point (L_1) and the white dwarf. At azimuth angles that are pointing towards the hot-spot region the apparent size of the disk reaches up to 0.9 R_{L_1}. At 5510 Å the disk reaches up to 0.65-0.7 R_{L_1}, slightly depending on azimuth angle, and at 6350 Å the 10% level is reached at 0.75 R_{L_1}, independent of azimuth angle. The azimuth dependence with wavelength reflects the diminishing influence of the hot-spot in SW Sex. The disk radii measured here are slightly larger than measured by RvPT92. We would like to remind the reader that, although the 10% the criterium is reliably measurable from the eclipse maps, it depends very much on the radial intensity distribution. In contrast with standard accretion disk theory where the radial intensity distribution is sharply peaked to the center, in SW Sex, both in the current study as well as in RvPT92, the intensity profile is rather flat, which automatically pushes the 10% intensity level to larger radii.

6.9.4 Position of the hot-spot

To determine the position of the hot-spot we have added up the eclipse maps between 3800Å and 4140Å, where we have seen in Sect 6.8 that the hot-spot continuum spectrum is the brightest. This sum map is then divided by a map at red wavelengths (for this we took the 6350Å map presented above), to obtain the ratio of the two. This ratio map is shown in Fig. 6.16 and shows clearly that the maximum of the hot-spot is located between 0.4-0.6 R_{L_1} and extents in azimuth from $0.93 < \varphi < 1.0$. The azimuthal extent is somewhat uncertain because of the smearing in the azimuthal direction as applied in the eclipse mapping method.

6.9.5 Emission site velocities

With the localization of the hot spot from the eclipse mapping and the radial velocity curve we can reconstruct the velocity vector of the material in the hot spot region. In Fig. 6.17 we show a schematic picture of the white dwarf Roche lobe with the velocity vectors included. The orbital velocity ($v_{\rm orb}$) at the position of the hot spot and using the system parameters of SW Sex as listed in Table. 6.3 is 60 km/s. We see that the resultant velocity vector as measured from the radial velocity curves is directed in almost the same direction as the orbital velocity, but has a much higher velocity. Combined we deduce that the flow velocity of the material in the hot-spot is of the order of 170 km/s and is directed almost in the same direction as the orbital velocity. If the gas in the emission site is connected to the gas flow in the accretion disk, we would have expected a more or less Keplerian flow with a velocity of the order of $\sim$500 km/s. We can see in Fig. 6.17 that both the direction

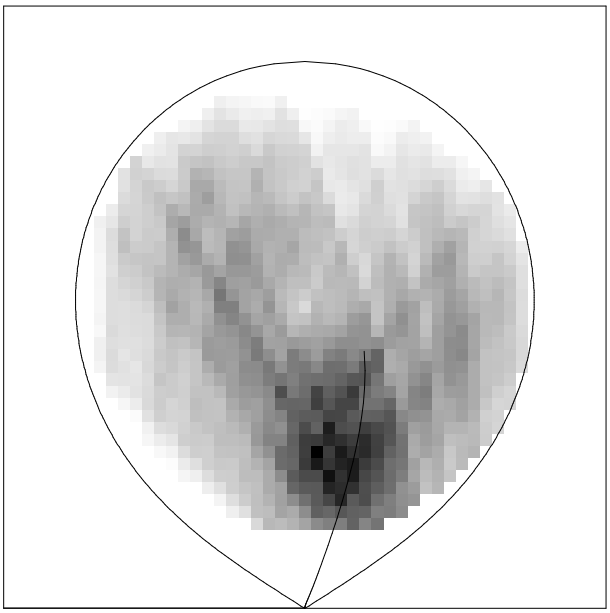

Figure 6.16. The reconstructed hot-spot map between 3800Å and 4140Å. The map was made by summing the maps in this wavelength region and dividing it by the map at 6350Å to obtain solely the hot-spot part. The map shows that the hot-spot is located at 0.4-0.6 R_{L_1}, and has azimuthal extent of $0.93 < \varphi < 1.0$ in phase.

and the magnitude of the Keplerian velocity vector are very different from those observed. We therefore conclude that the gas at the emission site is decoupled from the gas in the accretion disk. To explain the large magnitude of the velocity vector with respect to the orbital velocity a rather large component, directed out of the plane of the disk is needed.

6.9.6 Accretion disk spectrum

The reconstructed intensity maps allow us to deduce the spectrum at any given point in the disk. Since the eclipse-mapping procedure smooths the disk in the azimuthal direction and since we are mainly concerned with the radial profile of the disk, we have used a set of concentric rings (shown in Fig. 6.18) and a selected hot-spot region. The reconstructed spectra are shown in Fig. 6.19. We see that there is some spectral evolution in the radial direction, going from a relatively blue spectrum in the middle of the disk to a redder spectrum near the edges of the disk. The hot-spot region ('G') is clearly much bluer than the other section of the outer ring ('F'). Comparing the spectral evolution seen here with the one that was found in UX Uma by Rutten et al. (1994), we see that the changes in SW Sex are much more moderate and less pronounced than in UX Uma, which was in good agreement with theory (see e.g. Frank, King and Raine 1992).

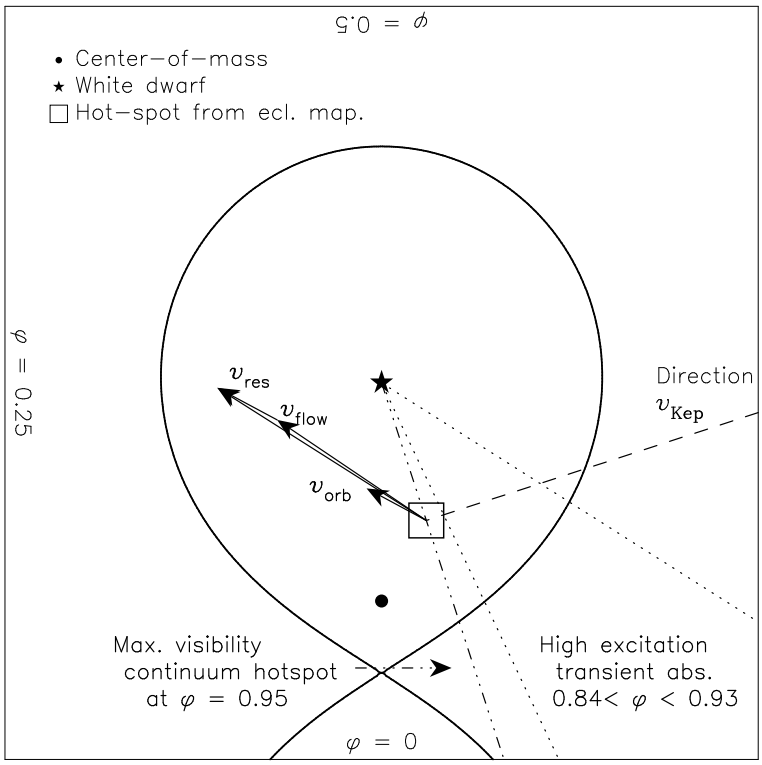

Figure 6.17. A schematic view of the Roche lobe of the white dwarf in SW Sex. The orbital velocity, $v_{\rm orb}$, at the hot spot and the observed velocity vector, $v_{\rm res}$, are almost parallel. The gas flow velocity vector $v_{\rm flow}$, deduced from this is $\sim$170 km/s. This vector is at large angles with the Keplerian velocity vector, which would be expected for the gas flow vector and this indicates that the gas at the emission site is decoupled from the velocity field of the accretion disk.

6.9.7 The uneclipsed light

Any uneclipsed component to the light curve could produce spurious results in the final eclipse map (see RvPT92). For that reason an additional free parameter was included in the code to fit the light curve to allow for any uneclipsed light. The spectrum of this uneclipsed component is shown in Fig. 6.20. We see that the amount of uneclipsed light is very low in the blue (the level $<$4200 Å is noise), but rises significantly to the red. It also prominently shows the Balmer series in emission. A well known feature of SW Sex systems is the partial eclipse of the Balmer lines and the occurence of these lines in emission in the offset pixel is therefore consistent. The uneclipsed light is most likely to emanate from either the secondary star or from outside the orbital plane. The secondary star has not been detected before. The slope of the offset spectrum as reconstructed here is indicative of a very late M-type secondary ($>$M5), which suggests that the light can come from the secondary. The emission lines are unlikely to be attributed to the secondary (unless it is magnetically very active), but could originate at a certain height above the

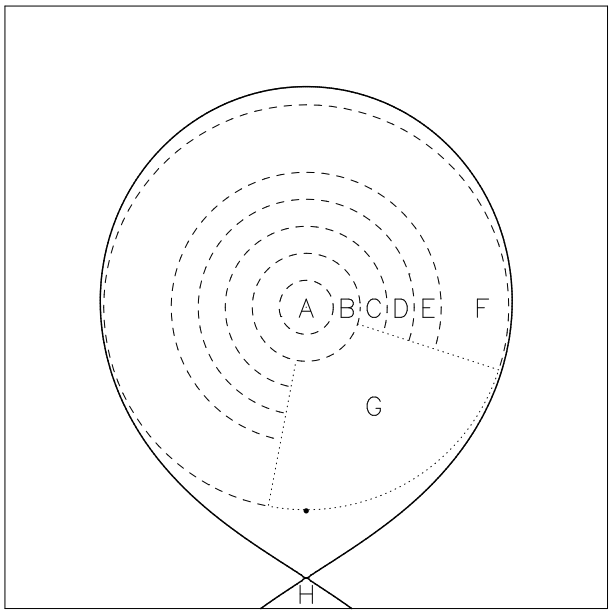

Figure 6.18. To reconstruct the accretion disk spectrum the WD Roche-lobe has been divided in 7 segments, labeled 'A' through 'G' and located, respectively, between 0-0.1, 0.1-0.2, 0.3-0.4, 0.4-0.5, 0.5-0.75 *R_{L_1}. This segments further out than $0.2R_{L_1}$ are split up between the part between phase 0.03 and 0.8 (section 'F') and the hot-spot part between phase 0.8 and 0.03 (section 'G'). The component of uneclipsed light is represented by segment 'H', here tentatively located at the secondary.

accretion disk, which is again consistent with our findings in Sect. 6.5.

6.10 The accretion disk temperature distribution

Using the intensity maps at all wavelengths as obtained from the spectral eclipse mapping, we can construct a temperature distribution on the accretion disk, by making Planck curve fits to the spectrum at each pixel on the disk, assuming the complete disk is optically thick and radiating like a blackbody. We can then write the flux received on earth as:

$$f = \frac{NA\cos i \sum_{j=1}^{N} \sigma T_j^4}{4\pi d^2}, \tag{6.2}$$

with N the number of pixels on the disk, $A\cos i$, the projected size of each pixel, T_j the temperature of each pixel and d the distance to the source.
The distance to SW Sex is not well known. An uncertain value of 250 pc is quoted by Patterson (1984), derived from the Hβ equivalent width and the continuum shape. RvPT92 derived 450 pc from blackbody fits to the inner accretion disk in their four colour photometry and the absence of any feature of the secondary. Including the distance as a free

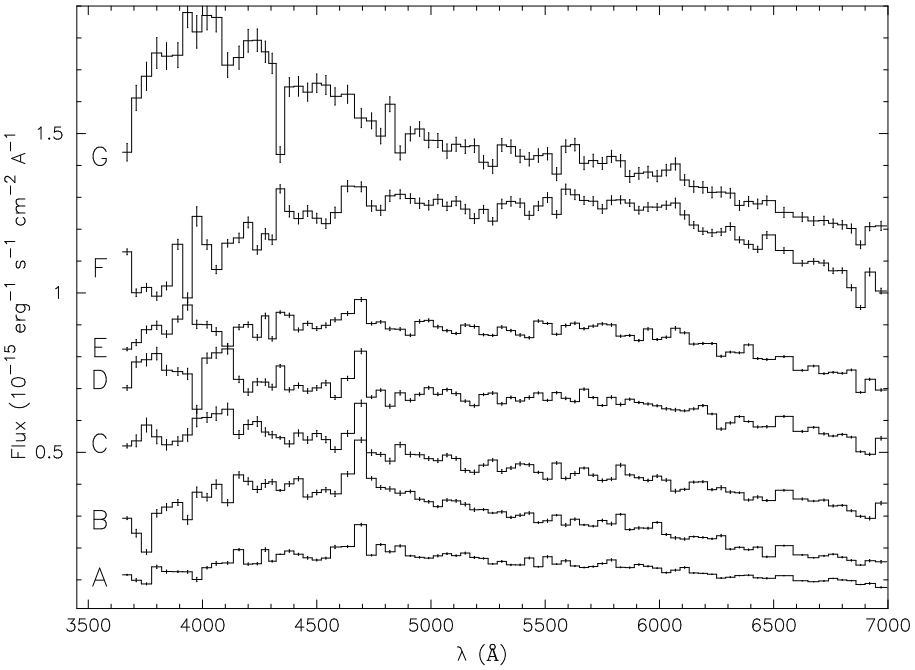

Figure 6.19. Reconstructed accretion disk spectrum in the regions A through G as indicated in Fig. 6.18. To seperate the spectra from each other shifts have been applied of respectively – 0.1, 0.05, 0.25, 0.46, 0.55, 0.85 for the regions A through G. Fluxes have been calculated as the summed flux in each segment.

parameter in our blackbody fits, we derive a distance to SW Sex of 290 pc. Using the value of 450 pc as found by RvPT92 gave clearly incorrect blackbody fits at all points in the disk. This argues for a low value of the distance. However, as remarked by RvPT92, the large distance of SW Sex is not only the consequence of Planck-fits to the reconstructed disk spectrum, but also because no trace is seen of the secondary. What distance is implied by this absence of secondary star features? The orbital period-mass relation of Warner (1995) would imply a secondary for SW Sex of late M-type, similar to the secondary of e.g. IP Peg. Because of the small disk in IP Peg we can measure the flux from its secondary directly. At the 6500 Å bump, which shows up as a plateau underlying the Hα line, the secondary of IP Peg as a flux of $\sim$1 mJy (Groot, Rutten and Van Paradijs, 1999) at a distance of 150 pc (Wood et al., 1986). We can place limits on the strength of IP Peg by estimating the flux that would be needed to detect the secondary in mid-eclipse. If we assume that we are still able to detect the secondary at mid-eclipse if it contributed 10% or more of the observed light, we can place a limit of 0.027 mJy on the flux of the secondary. Comparing this with the 1 mJy at 150 pc for IP Peg sets a lower limit to the distance of $>$900 pc for SW Sex. This is clearly inconsistent with both the values of 290 pc derived as well as the 450 pc derived by RvPT92. It is clear that the distance to SW Sex is not known with any uncertainty.

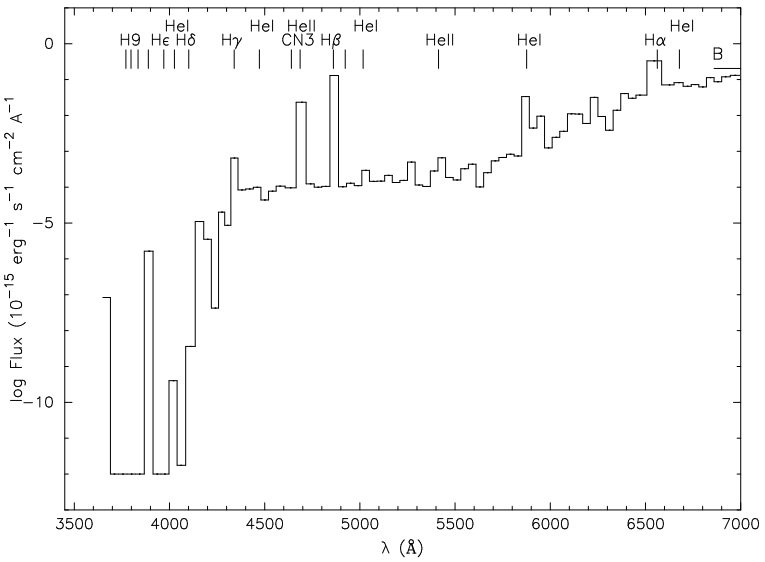

Figure 6.20. The reconstructed spectrum of the uneclipsed light component.

When the distance is determined from Eq. 6.2 an under- or over-estimation of the true radiating surface, e.g. by not including the effect of flaring or a disk rim, will also lead to an over- or under-estimation of the distance to the source.
For the moment we will use the value of 290 pc for the distance, obtained from the black-body fits to the accretion disk spectrum. With this we obtain a temperature map of the accretion disk of SW Sex, of which the radial cut is shown in Fig. 6.21. We are currently primarily concerned with the shape of this profile. The uncertain distance mainly affects the level of the profile, but not its shape.

6.11 The mass-transfer rate through the disk

Using the temperature profile as derived in the last section we can derive a mass-transfer rate through the disk and compare this with previous measurements and the theoretical predictions of steady state, optically thick disks. We show the derived mass-transfer rate profile in Fig. 6.21. The slope of this profile is very similar to the one found in RvPT92, the only other eclipse mapping study of SW Sex. They also showed that the slope does not follow the standard, steady state prediction, but deviates at radii $<0.5\mathrm{R}_{\mathrm{L}_1}$. There are however, also some marked difference between the current study and the one presented by RvPT92. In their study the hot-spot contribution is much more visible in the mass-transfer profile. This is not surprising because comparing the lightcurves of RvPT92 with ours, we immediately see that the light curves of RvPT92 are less symmetric than in our study. The hot-spot therefore contributed even more to the total light than it does here. Our current lightcurves and the derived mass-transfer profile are more reminiscent

of V1315 Aql, another SW Sex star, as also presented in RvPT92. There the profile is also relatively smooth, and flattening out at smaller radial distances. A comparison between a spectophotometric study of V1315 Aql and SW Sex is highly desirable.

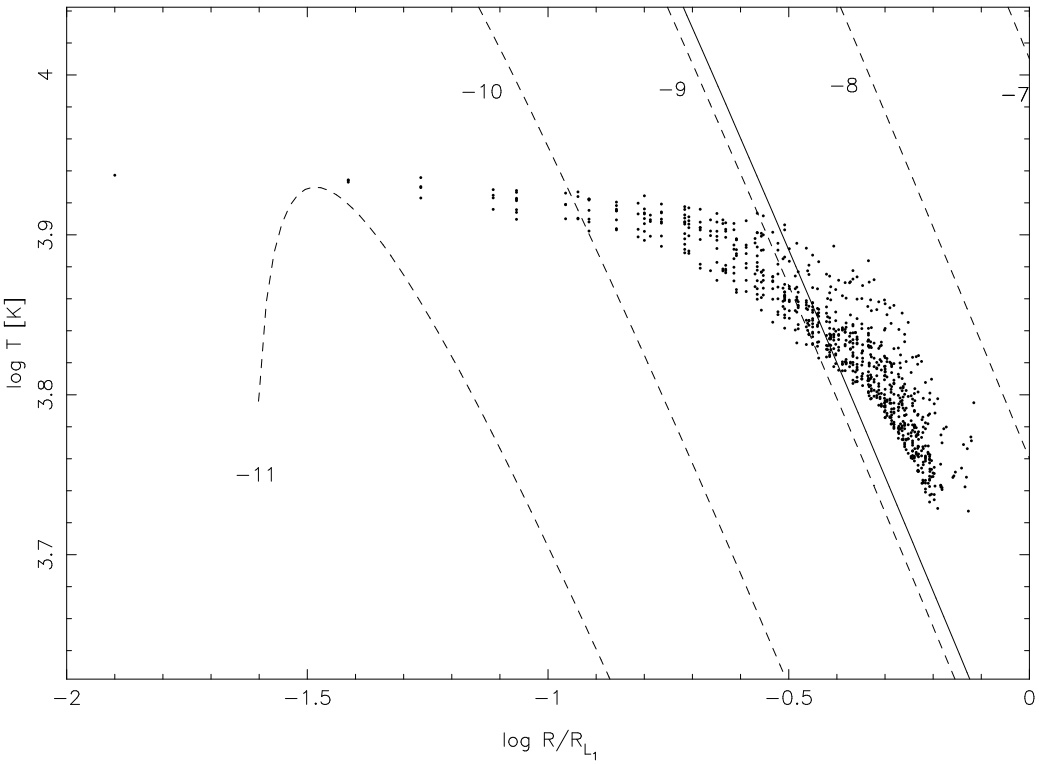

Figure 6.21. The derived $\dot{M}$ profile as function of the radial distance from the white dwarf. The solid line shows the averaged fitted mass-transfer rate. The dashed lines show the expected profile on the basis of standard accretion disk theory in units of 10log of the mass transfer rate (i.e. '–10' is 10^{-10} $M_\odot$ yr^{-1}).

6.12 Discussion

6.12.1 (Dis)appearance of the veiling spectrum

The picture of the hot-spot environment that emerges from the observations shown above is that the hot-spot is optically thick, with a photospheric temperature T_{spot} ∼10 000 K and a 'extended atmosphere' with a temperature T_{abs} ∼19 000-25 000 K. The hot-spot photosphere generates strong Balmer absorption lines which cause the V-shaped light curve profiles (Fig. 6.10) in the lower Balmer lines. The absence of any photospheric HeII λ4686 absorption (which will only show up significantly at $T \gg T_{spot}$) explains the 'undisturbed' HeII λ4686 light curves. The hot-spot region is best seen at φ=0.95 at which

phase both the decrease in the emission strength and the reconstructed hot-spot continuum strength reach their maximum. At phases 0.82 $<\varphi<$0.93 the extended atmosphere is strongly back-lit by the WD-region and the absorption line spectrum as shown in Sect. 6.4.2 appears. The disappearance of the absorption at phase 0.93 can be explained in two ways: either the inner disk is being eclipsed by the hot-spot photosphere, such that the continuum background source disappears from sight and the absorption also disappears, or at φ=0.93 the hot-spot extended atmosphere is eclipsed by the secondary star. Since the former explanation needs a relatively large disk flaring angle of $>11^{\circ}$ at the hot-spot position, we prefer the explanation that the absorption spectrum disappears due to the eclipse by the secondary.

6.13 Radial temperature and $\dot{M}$ profile

In Sect. 6.10 and 6.11 we have seen that the radial temperature profile and inferred mass-transfer rate deviate substantially from a steady state, optically thick accretion disk. In this section we will address the reality of this deviation. It has been shown by e.g. RvPT92 and Rutten et al (1994) that the (spectral) eclipse mapping technique is able to reconstruct the radial temperature profile accurately if the disk is in an optically thick, steady state. On three occasions now, for SW Sex and V1315 Aql by RvPT92 and independently for SW Sex in the current study, it has been shown that the disk in SW Sex stars shows a flat temperature profile.

At the mass-transfer rates expected in novalike systems, the accretion disk should be in a steady state and optically thick. Even at the relatively low $\dot{M}$ of SW Sex here, one would expect the disk to be in a steady state. Smak (1994) argued that the flat temperature profile is due to obscuration of the inner parts of the disk due to a large flaring angle, combined with high inclination. For SW Sex this would mean that the inclination $i \sim 85^{\circ}$, which is excluded by DMJ97. Rutten (1998) has shown that, in contrast with the results of Smak (1994), he finds no substantial flattening of the temperature profile even at large flaring angles when light curves from a 3D accretion disk model are reconstructed using a standard flat disk geometry.

The strongest argument against self-eclipses and strongly flared disks in our observations of SW Sex is the lack at any wavelength of a 'front-back asymmetry', which one would expect from a self-eclipsed disk. In this 'front-back asymmetry', the side of the reconstructed disk furthest away from the L_1 point should be considerably brighter, because of the higher temperatures, than the front side of the disk, where we are looking at the cool rim of the disk. It would require a rather delicate balance of accretion-stream rim-heating, inclination angle and flaring angle to mask this effect and produce eclipse maps that are as symmetric as the ones oberved here in SW Sex.

6.13.1 V Per: a twin to SW Sex?

A very interesting case and a possible twin of SW Sex is the little studied old nova V Per. Shafter and Abbott (1989) have shown that this is an eclipsing CV in the period gap (P_{orb}=2.57 hr), that shows single peaked emission lines, and most interesting, HeII λ4686 (with a strength $>$Hβ), and He II λ5411 in emission; both characteristics as seen in our data of SW Sex. Since, to our knowledge, no phase-resolved spectra of V Per have been obtained nothing is known of the relative phasing of its emission lines with respect to the continuum eclipses. However, Wood, Abbott and Shafter (1992) have shown from broad-band eclipse light curves, that the disk temperature profile is very similar to that found here for SW Sex. Wood et al. explain this behaviour by the absence of the inner part of the accretion disk and speculate that this could be the result of a magnetic field, which would make V Per a possible intermediate polar. A phase-resolved spectroscopic study of this system is required to understand the nature of this system and its relation to the subclass of SW Sex stars. If it is found to show the 'classic' SW Sex phenomena (phase lags, transient absorption), it would extend the orbital range of SW Sex stars considerably downwards, and if V795 Her (Casares et al., 1996) is indeed a SW Sex star, be the second SW Sex star in the period gap.

6.13.2 SW Sex stars are not intermediate polars

It has been suggested that SW Sex stars (and also V Per) are intermediate polars at high inclination. It is clear that we need an additional source of high energy photons in SW Sex. The strength of the HeII λ4686, HeII λ5411 and CIV λ5808 lines, and the absence of the HeI lines normally seen in non-magnetic CVs clearly hint at the presence of a magnetic white-dwarf in SW Sex. However, these are also the *only* suggestions for a magnetic white dwarf. No periodic oscillations, as seen in almost all polars and intermediate polars, are found in the optical in any of the SW Sex stars. Hard X-ray emission is not detected from SW Sex stars, no cyclotron features have been observed and in V1315 Aql no polarization is detected (Dhillon and Rutten, 1995). Of all the SW Sex stars only the aforementioned low-inclination system V795 Her has been detected in the ROSAT PSPC All Sky Survey (Verbunt et al. 1997). Above all, we have seen that the emission site of the HeII λ4686 radiation is *not* connected to the white dwarf, but to the hot-spot region. We can therefore rule out a magnetic white dwarf as the source of high-energy photons.

6.13.3 Shock induced high excitation lines

Since we have shown that the WD cannot be responsible for a radiation field that ionizes the inner disk region, there are only two possible ways of producing the high temperatures that are needed for the formation of the prominent high excitation lines (HeII λ4686, CIV λ5808 and HeII λ5411). Either the inner disk is optically thin and contains temperatures

that are high enough for the production of He^{+} and C^{3+}, or a prominent shock heats the gas to the required temperatures. In the optically thin case there is no reason why the HeII λ4686 and Hα line would have a phase-lag with respect to the white-dwarf. We would expect the line to form more or less uniformly over the inner disk region.
This leaves the shock scenario. We have seen that the formation site of the major emission lines coincides with the hot-spot region, which is located at (φ, r) = (0.95, 0.5). The gas in the accretion disk somehow enters a standing shock region where it is heated to high temperatures. If the gas in the shock region orbits the white-dwarf at a Keplerian velocity, a wind component, originating at the shock region, is also needed to explain the observed velocity vector.
The cause of the shock is yet unclear. The fact that the shock lies along the stream trajectory of the gas as it leaves the secondary clearly shows that the accretion stream is important in the formation of the shock. From the radial mass-transfer rate profile we see that in the region 0.5-0.75 R_{L_1} a more or less steady state optically thick disk is formed. This suggests that the hot-spot is not a classic hot-spot due to the disk-stream interaction, since we would not expect the formation of a disk outside the hot-spot region.
The fact that the hot-spot coincides with the radial distance from the white dwarf where the temperature profile clearly deviates from a steady-state disk prediction suggests that the hot-spot environment dominates the disk behaviour at radial distances closer to the white-dwarf and prevents the inner disk from achieving the temperatures expected by the mass-transfer rate. If the mass-accretion rate onto the white-dwarf is also low, this will prevent the white-dwarf from heating up and showing up as a source of soft X-radiation. This can explain the apparent lack of SW Sex stars in the ROSAT PSPC All Sky Survey results as presented by Verbunt et al. (1997)

6.13.4 Shock generation scenarios

Although a thorough theoretical explanation of the cause of the shock region is outside the scope of this paper we will shortly discuss possible causes for the shock. If accretion stream overflow is important in the disk, one would expect the gas to re-impact on the disk at the circulization radius, $r_{\rm circ}$ (see Frank et al., 1992), which may cause a shock at that radius. However, for the system parameters of SW Sex, the circulisation radius lies at $0.25R_{L_1}$, well inside the radius we deduce for the shock.
For X-ray binaries (Gosh and Lamb, 1978) and T Tauri stars (Shu, 1994) it has been shown, that the co-rotation radius (where the Keplerian rotation rate and the white dwarf rotation rate are equal) is a possible shock formation site, due to an accretion disk - magnetic field interaction, in which case it is also a good place to launch a magnetocentrifugally driven wind. For the corotation radius to be equal to the deduced hot-spot radius, the white dwarf in SW Sex should have a spinrate of $\sim$2 000 s, which is not impossible. However, current theories require the magnetospheric radius to be (almost) equal to the co-rotation radius. This would require a white dwarf magnetic field strength that would

make SW Sex readily observable as an intermediate polar.
In order for the above mechanism to be the cause of the shock in SW Sex stars we will need the possibility of the magnetospheric radius to be much smaller than the co-rotation radius, in which case a weak magnetic field would suffice to generate the shock. It is presently unclear if such a shock could form.

6.13.5 Shock formation as a consequence of high mass-transfer rates

What is so special about the SW Sex stars that a shock only forms in these systems and not in others? We here speculate that the SW Sex phenomenon occurs if the mass-transfer rate through the outer disk is high ($>10^{-9}$ $M_\odot$ yr^{-1}) and the rotation rate of the white dwarf is low. At lower accretion rates a classic hot-spot as seen in dwarf novae will develop. Although these hot-spots are clearly seen in the continuum radiation, no strong wind will occur and the line emission will be dominated by the accretion disk, giving the usual double-peaked line profiles. If the shock generation is caused by a mechanism similar to a magnetocentrofugally driven wind scenario, it will further be required that the rotation rate of the WD is not too high. At fast rotation rates the co-rotation radius will lie closer to the WD, unreachable for the (continuation of the) accretion stream. If in this case a shock does form at the co-rotation radius, the mass flow will not be dominated any more by the accretion stream and a more axisymmetric shock is expected.

6.14 The structure of SW Sex

We have shown in the previous sections that the behaviour of SW Sex in our observations is well explained if the accretion disk in SW Sex is optically thick and in a steady state in its outer regions. (See Fig. 6.22 for a graphical overview.) The inner regions of the disk are however definitely not in the steady state expected from theory on the basis of the mass-transfer rate through the outer disk. We deduce that this is caused by a region near (φ, r) = (0.95, $0.5R_{L_1}$) where a strong shock causes very high temperatures and a possible wind outflow from SW Sex. This high temperature shock region is the emission site of the main emission lines. The hot-spot region itself is optically thick and has a photospheric temperature of T_{spot} = 10 000-12 000 K. The strong Balmer absorption lines that will occur in this photosphere attenuate the strength of the Balmer emission lines and are the cause for the early ($\varphi \sim 0.8$) absorption components in the Balmer lines. The hot-spot photosphere is surrounded by an extended atmosphere with a temperature of T_{abs} = 19 000-25 000 K. When the extended atmosphere is back-lit by the inner parts of the accretion disk, an absorption line spectrum with characteristic temperature T_{abs} becomes visible. The relatively undisturbed light curve of HeII λ4686 is explained by the fact that $T_{spot} < T_{abs} < T_{ionHe^+}$, with T_{ionHe^+} the temperature needed to ionize He.

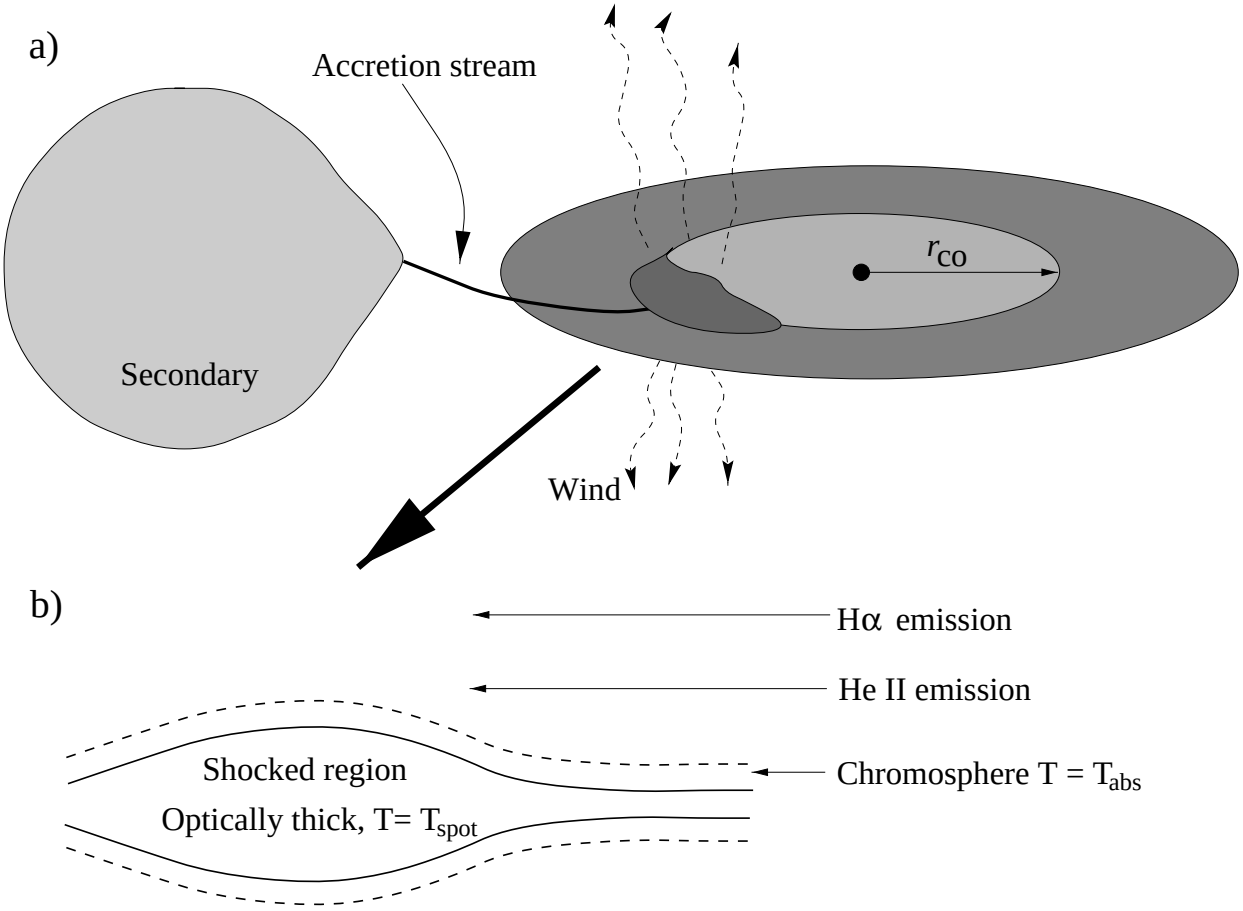

Figure 6.22. Schematic view of SW Sex (top). The major emission lines are formed in a shocked region along the trajectory of the accretion stream that leaves the secondary through the L_1-point. The shock forms at a distance r_{co} from the WD. A close-up view of the shock region is shown in the bottom part. The optically thick shock region as a temperature T_{spot} ∼10,000 K. A extended atmosphere is formed above the shock region. This extended atmosphere with temperature T_{abs} is seen in absorption when back-lit by the inner disk. Above the extended atmosphere the temperature rises further and He II emission occurs. Higher up in the coronal region, at the bottom of a accretion disk wind, the lower excitation lines such as Hα are formed.

6.14.1 The SW Sex phenomena explained (?)

The scenario as sketched above is capable of explaining many of the classical SW Sex phenomena as we will outline here:

- Single peaked emission lines. We have shown that the emission lines are formed in a strong shock at the hot-spot location. Since they are formed in a single region the lines will also be single peaked. Their radial velocity amplitude contains either a strong non-Keplerian gas-flow component, or a rather large vertical compo-

nent, which is also suggested by the results from Doppler mapping studies (DMJ97) where it is shown that the emission line amplitudes in SW Sex are too low to be explained by either disk or accretion stream emission. If a significant vertical component is present in the emission lines, this will render the basic assumption of Doppler mapping, that all velocity vectors are in the plane of the orbit, invalid.

- Large phase shifts. The large phase shifts are naturally explained by the origin of the lines in the hot-spot. The precise location of this hot-spot with respect to the center-of-mass will determine the phase-shift observed in the emission lines, and can in principle change with epoch.

- Phase 0.5 absorption. Although this absorption is not detected in our current observations it is relatively easy to imagine that the absorption is due to back-lighting of material in front of the hot-spot shock by the hot-spot continuum radiation as seen at $\varphi \sim 0.5$. If the mass-transfer rate from the secondary is larger than observed here for SW Sex it is well possible that a larger amount of the mass is transferred to the inner disk which may cause the veiling. Backlighting by the hot-spot continuum radiation certainly explains the phase-dependence of the absorption features which has been shown to have maximum depth around $\varphi \sim 0.45$, exactly when we see the hot-spot region from across the disk (Szkody and Piché, 1990).

- Shallow eclipses of the emission lines. Assuming that the emission lines are formed above the disk, they will show eclipses that are less deep than that of the continuum.

Classically the SW Sex phenomena was constrained to eclipsing systems in the period range between 3 and 4 hours. Over the last few years however, several systems at lower inclination or outside the 3-4 hr orbital period range have been proposed as SW Sex stars, e.g. V795 Her (Casares et al., 1998), LS Pegasi (Martínez-Pais et al., 1999; Taylor et al., 1999), WX Arietis (Hellier et al., 1994), BT Mon (Smith et al., 1998) and V Per (this work). The scenario as given above does not depend on the inclination angle, although we expect that at very low inclination angles the transient absorption will become less strong. At non-eclipsing inclination angles the phase 0.5 absorption will be caused by wind material that is back-lit by either the hot-spot, or the outer disk region behind the hot-spot, closer to the secondary. If the scenario outlined above holds true we expect that the velocities at which the absorption components are found will become larger with lower inclination, simply because we are looking more and more directly into the wind.
The attractiveness of this scenario over the others mentioned in Sect. 6.1 is the fact that it not only able to explain all the observed feature of SW Sex stars, but especially the early decrease of the Balmer emission line strength, which cannot be explained by any of the other models.

Acknowledgements
PJG is partially supported by the NWO Spinoza grant 08-0 to E.P.J. van den Heuvel. PJG wishes to thank the hospitality of Claudio Moreno and the staff of the ING observatory during a number of visits. The INT is operated on the Observatorio del Roque de los Muchachos on the island of La Palma on behalf of the British PPARC and the Dutch NWO.

References

Casares, J., Martínez-Pais, I.G., Marsh, T.R., Charles, P.A. and Lazaro, C., 1996, MNRAS 278, 219

Casares, J., 1999, MNRAS 305, 661

Dhillon, V.S., Marsh, T.R., and Jones, D.H.P., 1997, MNRAS 291, 694

Dhillon, V.S. and Rutten, R.G.M., 1995, MNRAS 277, 770

Frank, J., King, A.R., Raine, 1992, in *Accretion Power in Astrophysics*, Cambridge Astrophysics Series No. 21, CUP, Cambridge UK

Green, R.F., Ferguson, D.H., Liebert, J., Schmidt, M., 1982, PASP 94, 560

Hellier, C. and Robinson, E.L., 1994, ApJ 431, L107

Hellier, C., Ringwald, F.A., and Robinson, E.L., 1994, A&A 289, 184

Hellier, C., 1996, ApJ 471, 949

Hellier, C., 1998, PASP 110, 420

Horne, K., 1986, PASP 98, 609

Horne, K., 1999, astroph-9901007

Honneycutt, R.K., Schlegel, E.M., Kaitchuck, R.H., 1986, ApJ 302, 388

Hunter, and Jacoby, 1984, ApJS 56, 257

Massey, P., Strobel, K., Barnes, J.V., Anderson, E., 1988, ApJ 328, 315

Penning, W.R., Ferguson, D.H., McGraw, J.T., Lienert, J. and Green, R.F., 1984, ApJ 276, 233

Rutten, R.G.M., Van Paradijs, J., and Tinbergen, J., 1992, A&A 260, 213

Rutten, R.G.M., Dhillon, V.S., Horne, K., Kuulkers, E. and Van Paradijs, J., 1993, Nature 362, 518

Rutten, R.G.M., Dhillon, V.S., Horne, K. and Kuulkers, E., 1994, A&A 283, 441

Rutten, R.G.M., 1998, A&ASS 127, 581

Shafter, A.W. and Abbott, T.M.C., 1989, ApJ 339, L75

Szkody, P. and Piché, F., 1990, 361, 235

Smak, J., 1994, Acta Astr., 44, 265

Smith, D.A., Dhillon, V.S. and Marsh, T.R., 1998, MNRAS 296, 465

Taylor, C.J., Thorstensen, J.R., Patterson, J., 1999, PASP 111, 184

Thorstensen, J.R., Ringwald, F.A, Wade, R.A., Schmidt, G.D. and Norsworthy, J.E., 1991, AJ 102, 272

Verbunt, F., Bunk, W.H., Ritter, H. and Pfefferman, E., 1997, A&A 327, 602

Warner, B., 1995, *Cataclysmic Variable Stars*, Cambridge Astrophysics Series 28, CUP, Cambridge, UK

Williams, R.E., 1989, AJ 97, 1752

Wood, J.H, Abbott, T.M.C and Shafter, A.W., 1992, ApJ 393, 729

7

A spectrophotometric study of RW Trianguli

P.J. Groot, R.G.M. Rutten and J. van Paradijs

Submitted to Astronomy and Astrophysics

On the basis of spectrophotometric observations we reconstruct the accretion disk of the eclipsing novalike cataclysmic variable RW Tri in the wavelength region 3600-7000Å. We show that the mass-accretion rate in RW Tri is $(1.0\pm0.1)\times10^{-8}$ $M_\odot$/yr and that the radial temperature profile is consistent with that expected on the basis of the theory of optically thick, steady state accretion disks. We further show that the decrease of the line strength of the Balmer lines, as is often observed in high inclination novalike CVs, is caused by a layer of gas that surrounds the hot-spot and accretion disk region and which is optically thick in the lower Balmer and neutral helium lines: a Balmer Bubble. In our observations RW Tri shows a number of features that are characteristic of the SW Sex sub-class of novalike stars. Instead of classifying RW Tri as 'yet-another' SW Sex star we propose to abandon the division of novalikes in the UX UMa and SW Sex sub-classes altogether since there appears to be no physical distinction between members of these two classes.

7.1 Introduction

Although RW Tri is one of the longest known cataclysmic variables (CVs), discovered by Protitch (1937), and has been studies extensively photometrically, it has been largely neglected in spectroscopic studies. To our knowledge only two extensive optical spectrophotometric studies, by Kaitchuck, Honeycutt and Schlegel (1983) and Still, Dhillon and Jones (1995) have been made of this system. RW Tri is generally assumed to be a

standard novalike CV (see Warner, 1995 for a general overview of CVs), but both spectroscopic studies have shown that the phase depedence and the light curves of the emission lines show features that are difficult to explain in a standard CV picture.

RW Tri was included in the broad-band photometry eclipse mapping studies of Rutten, Van Paradijs and Tinbergen (1992) who showed that its radial temperature profile is consistent with the $T \propto R^{-3/4}$ dependence expected on the basis of accretion disk theory (see e.g. Frank, King and Raine, 1992). RW Tri is in this respect similar to UX UMa (Rutten et al., 1993; 1994) that has been shown spectrophotometrically to follow the same temperature profile.

Apart from the emission line behaviour, RW Tri is also known to undergo irregular variations of up to one magnitude in its out-of-eclipse brightness, as was first shown by Walker (1963) and occasionally increases even to more than three magnitudes from its faint brightness level at AB$\sim$13.5, as was seen in the spectrophotometric study of Still et al. (1995). This irregular behaviour, most likely caused by a variation in the mass-transfer rate from the mass-losing secondary star, is not unique for RW Tri (see e.g. the recent results on GS Pav; Groot et al., 1998), although it is the best documented case.

The radial temperature profile and the peculiar emission line behaviour prompted us to a spectrophotometric study of RW Tri.

7.2 Observations

On the nights of 22-26 October 1994, we have obtained a total of 671 low-resolution spectra using the Intermediate Dispersion Spectrograph with the R300V grating and a 1k$\times$1k Tek CCD. A wide slit (2.″5) and a second star on the slit (48″ NW of RW Tri) were used to obtain differential photometry. An absolute flux calibration was obtained by observing the spectral flux standard BD +28 (Oke, 1990) using a 5″ wide slit for both the spectral flux standard as well as RW Tri and its local comparison star.

All data is reduced in the standard fashion using the ESO-MIDAS package, with additionally written software. All stars were optimally extracted using the technique developed by Horne (1986). All spectra were obtained with a 50s on-target integration time. With a $\sim$60s dead-time for CCD readout and data storage, we obtained an effective time resolution of 110s, or 1/182nd of the orbital period of 5h34m. A total of five eclipses were observed. Throughout the nights CuAr arc spectra were taken for the wavelength calibration.

Based on the colour excess given by Rutten et al., (1992) of $E(B-V)$=0.1 we have dereddened all our spectra using the galactic reddening coeffcients given by Cardelli, Clayton and Mathis (1990), assuming a standard R_V=3.1.

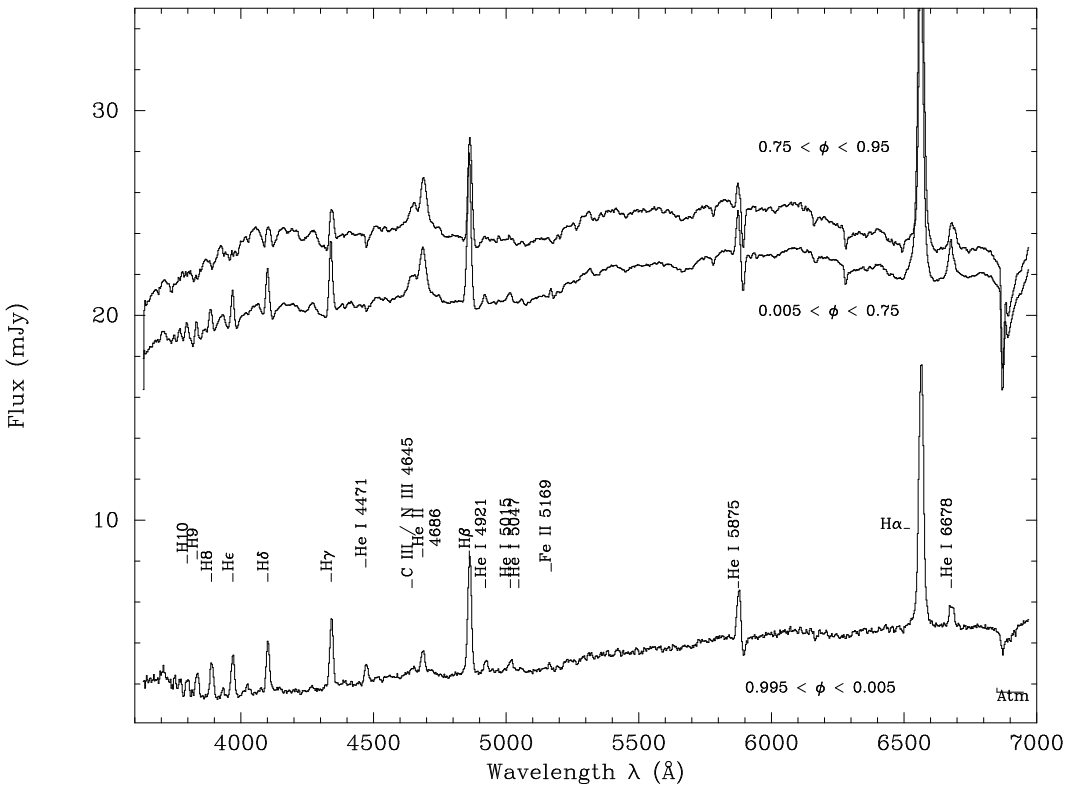

Figure 7.1. The average spectrum of RW Tri, divided in three phase intervals. The bottom curve shows the spectrum in mid-eclipse (0.995< φ <0.005), the middle curve the spectrum outside eclipse and outside the phase interval that a hot-spot can be visible (0.005< φ <0.75) and the top curve shows the spectrum during the hot-spot phase (0.75< φ <0.995). All the emission lines appear single-peaked which can be due to our low-resolution. The Balmer lines remain largely uneclipsed. In the higher Balmer lines strong underlying absorption troughs can be seen. The absorption feature at 6160Åis the strongest absorption line of the CaI triplet between 6100-6160Å. The HeI λ4471 is in absorption during the complete orbit, except the eclipse, where it shows up in emission. The top two curves are displaced by 1 mJy with respect to each other.

7.3 Ephemeris and System Parameters

We have phase folded all spectra using the ephemeris given by Robinson, Shetrone and Africano (1991). Trial eclipse maps using the system parameters given in Table 7.1 showed a phase shift in the phase of minimum light. Shifting the phases by –0.0046 of an orbital period as has been found before by Smak (1995), corrected this. A revised ephemeris is given in Eq. 7.1

$$HJD_{\rm mid\_ecl} = 2\,441\,129.36380(10) + 0.231883297E \qquad (7.1)$$

The system parameters of RW Tri are rather uncertain, especially the (q, i) pair. Values

Table 7.1. System parameters of RW Tri.

Period	20034.717 s
M_{WD}	0.7 $M_{\odot}$
M_{sec}	0.6 $M_{\odot}$
Inclination	75°
Distance	330 pc

for i range between 67° (Kaitchuck, 1983) to as high as 80° (Mason, Drew and Knigge, 1997), with the component masses varying accordingly. It is clear that the mass ratio in RW Tri is rather close to unity, and Smak (1995) even argued that the mass-ratio is larger than unity (e.g. the secondary is more massive than the white dwarf primary). It is, however, unclear if a system with a mass-ratio larger than unity can maintain stable Roche-lobe overflow on a nuclear timescale, as observed in RW Tri. For this reason we have opted to use the values as given in Rutten et al., (1992), with a mass-ratio smaller than unity and, consequently, a relatively high inclination: i=75° . We will comment on the distance choice in Sect. 7.8.3 on on the other system parameters in Sect. 7.9.

7.4 Average Spectrum

In Fig. 7.1 we show the average flux calibrated spectrum of RW Tri during our observations. The spectrum shows the usual emission lines of H, HeI and HeII. We see that the HeII and Bowen blend of NIII and CIII, which are not visible in the spectra of Kaitchuck et al. (1983) and Still et al. (1995), merge together in one broad feature. All lines appear single peaked. Although RW Tri is supposed to have double-peaked emission lines, these will show up as single peaked in our low-resolution spectra. We see that the continuum emission is deeply eclipsed, but that the majority of the emission lines are not so deeply eclipsed, indicating that the emission lines are formed in a different region than the continuum. We see that the spectrum of RW Tri does not change dramatically between phases 0.005$< \varphi <$0.75 and phases 0.75$< \varphi <$0.995 when a hot-spot could be visible and during which interval SW Sex showed deep absorption lines in the blue (Groot, Rutten and Van Paradijs, 1999).
The higher Balmer lines, especially Hϵ and Hδ can be seen to consist of two components in the out-of-eclipse spectra. Underlying the emission lines we see absorption troughs, that are caused by optically thick parts of the disk. They could also be photosperic absorption lines from the white-dwarf, although they appear to be too narrow for that.
It is evident from a comparison of the HeI λ4471 line between the three spectra displayed here, that the behaviour of this line is unusual: almost non-existent in the phase interval 0.005$< \varphi <$0.75, in absorption in the interval 0.75$< \varphi <$0.995, and in emission during mid-eclipse. We will further discuss this line in the next section.

The red part of the spectrum shows the atmospheric features at 6300Å and 6900Å. A clear absorption line is visible at 6160Å, caused by the K7 secondary in RW Tri.

7.5 Trailed spectra

The trailed spectra of the Balmer and He lines as presented by Kaitchuck et al. (1983) and Still et al. (1995) already show that the emission line behaviour in RW Tri is complex. The main emission lines have a relatively low orbital velocity modulation of $<$200 km s^{-1}. In Fig. 7.2 we show the trailed spectra of the, continuum subtracted, main lines in RW Tri and in Fig. 7.3 we show the corresponding light curves. We see from these figures that a total of five components can be identified:

- The strongest component in the lines is an emission component that has a small velocity dependence with phase. This component dominates the main emission in the Balmer lines. We can also see that in the Balmer lines this component decreases in strength between phase 0.75 and phase 0.1. The HeII λ4686 line is unaffected by this decrease in strength.

- The second component has a considerable velocity dependence with phase and is best seen in the HeI λ6678 line. It reaches maximum blueshift around phase 0.25 and maximum redshift around phase 0.75-0.8. In the Balmer lines and HeII λ4686 this component is visible throughout the complete orbit and does not seem to suffer from either the decrease of the main component in the Balmer lines or the primary eclipse by the secondary. It is this same component that we see in absorption during most of the orbit in HeI λ4471 and HeI λ4026. The strength of the absorption in these two HeI lines diminishes between orbital phases $0.15 < \varphi < 0.5$.

- The third component is an emission component that is only visible during mid-eclipse. This component is best seen in He I λ 4471, where the line profile changes from absorption to emission, and in the higher Balmer lines. This clearly indicates that (part of) the emission site of the Balmer lines and the HeI lines is *not* eclipsed. Only the HeII λ4686 line is unaffected by this mid-eclipse emission and shows a strong eclipse, similar to the continuum (see next Section).

- The fourth component are the absorption troughs in the higher Balmer lines, best seen in Hδ and Hϵ. These originate most likely in an optically thick part of the accretion disk.

- The fifth component is the primary eclipse. It is seen as a decrease of the emission strength in HeII λ4686 only. Paradoxically the primary eclipse is seen as an *increase* of the linestrength in most of the other lines.

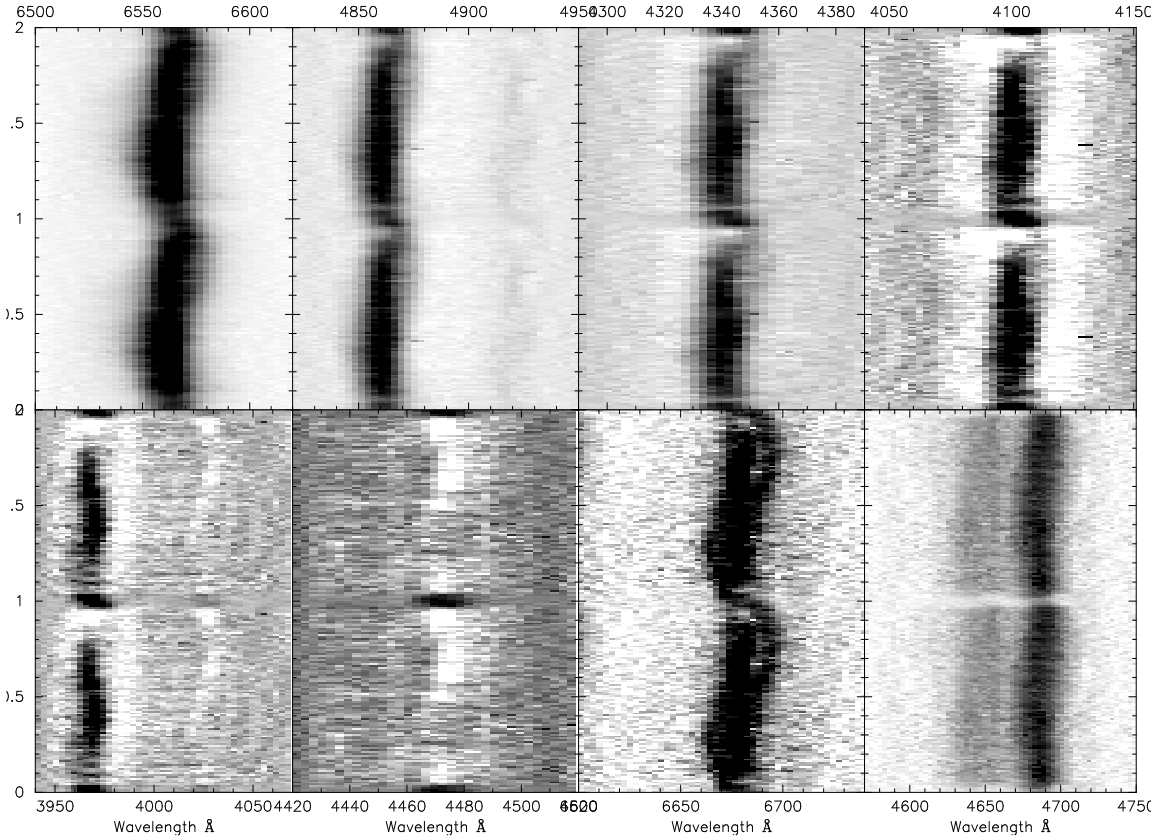

Figure 7.2. The trailed spectra (in bins 0.01 in phase) for Hα , Hβ (plus HeI λ4921, Hγ and Hδ on the top row and Hϵ (plus HeIλ4026), HeI λ4471, HeI 6678, and HeII λ4686 plus CIII/NIII on the bottom row. The Balmer lines, HeII λ4686 and HeI λ6678 consist of (at least) a low-velocity main emission component, and a lower intensity high-velocity component. Note that the HeI $\lambda\lambda$6678, 5875 and 4921 lines are in emission, and the HeI $\lambda\lambda$ 4026 and 4771 lines are in absorption, even though they share the same velocity dependence with phase.

7.5.1 Radial velocity curve of the secondary

The interpretation of the place of origin of these lines is helped by the absorption lines around 6160Å. We can see in Fig. 7.4 that there is more than one absorption line in this region; at $\sim$6160Å the strongest one is visible, at $\sim$6120Å the second is visible and a trace can be seen of a third line around 6100Å. These three wavelengths uniquely identify this set of lines as the CaI triplet at 6102, 6122 and 6162 Å, which are indeed among the strongest lines in a late K-type star. The radial velocity curve of the CaI λ6162 is shown in Fig. 7.5. We see that the phasing of the line coincides with that of the secondary and the derived amplitude is consistent with that derived by Smith et al. (1994). The strength of the absorption lines reaches a minimum between phase $0.45 < \varphi < 0.55$, which indicates that they are influenced by a secondary eclipse.

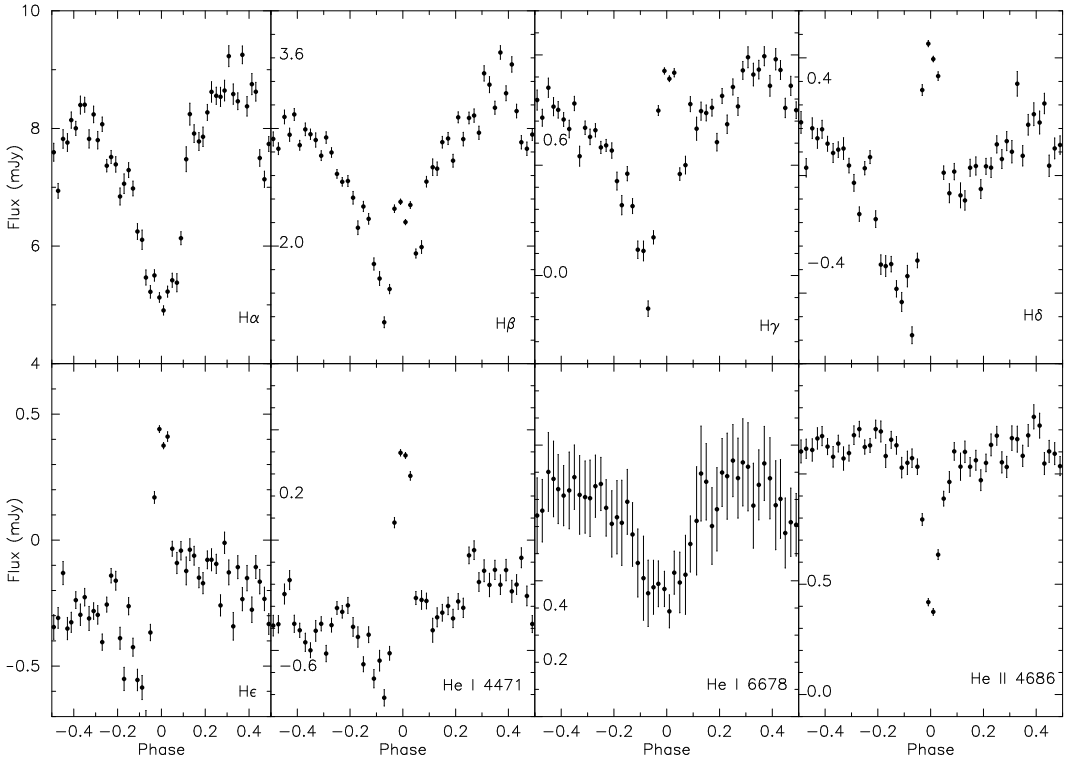

Figure 7.3. The light curves of the same lines as showed in Fig. 7.2. All lines, except HeII λ4686, decrease in their strength at phases φ >0.75. The HeII λ4686 line closely resembles the continuum light curves. Apart from Hα , HeII λ4686 and HeI λ6678, all lines show a significant brightening during mid-eclipse, indicative that a strong emission source is left uneclipsed.

7.5.2 Origin of the emission lines

The main emission component has been attributed to emission from the irradiated inner half of the secondary star by Still et al. (1995). Fig. 7.6 shows the radial velocity curve that has been derived by fitting a single Gaussian, with variable width, to the total line profile. We see that both the phasing as well as the amplitude of the radial velocity curve are in good agreement with those found by Still et al. (1995) and Kaitchuck et al. (1983). We do however, not agree with the conclusion by Still et al. (1995) that the bulk of the emission line originates on the heated side of the secondary. For the system parameters used here, which are identical to the ones used by Still et al. (1995) the center-of-mass of the system lies in the Roche-lobe of the white dwarf, but rather close to the L_1 point. If the inner side of the secondary is the place of origin of the bulk of the Balmer emission, one would expect the radial velocity curve to show a maximum *blueshift* near φ ∼0.75-0.8, and not a maximum *redshift*, as observed. This locates the emission site on the white-dwarf side of the center-of-mass. The same result, but with higher scatter on the radial velocity curve, is obtained when only the core of Hα line is used in the Gaussian fit. We

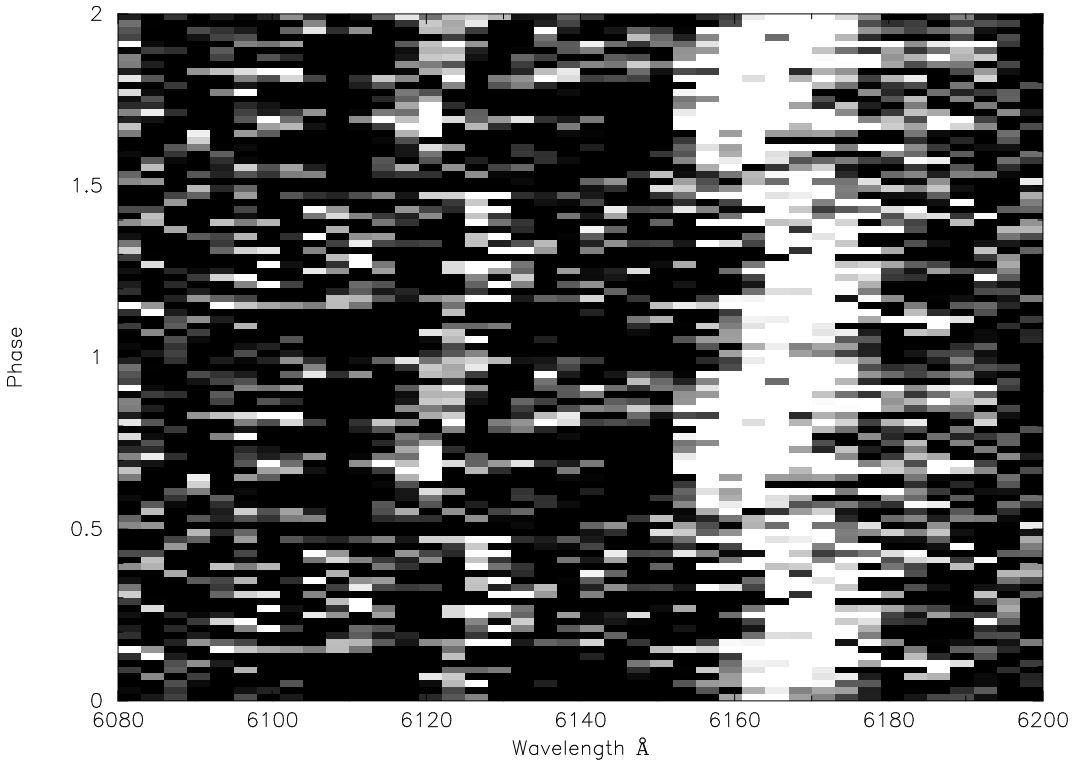

Figure 7.4. Trailed spectrogram of the CaI absorption triplet between 6100-6160Å. The CaI λ6162 is the strongest of the three, and the others are located at λ6121 Åand λ6102 Å. This last one is only slightly visible.

conclude that the bulk of the Balmer emission originates in the accretion disk region.

7.5.3 The behaviour of the HeI lines

It is rather peculiar the we see the high velocity component in emission in the HeI λ5875 and λ6678 lines and in absorption in the λ4026 and λ4471 lines. The trio of lines (λ5875, λ4471, λ4026) belong to the same triplet group of transitions to the 2s ground state, with the λ5875 line coming from the 3d level, the λ4471 line from the 4d and the λ4026 line from the 5d level. In LTE we would expect that all three lines would be either in emission or in absorption, since their common velocity and phasing properties indicate that in RW Tri they originate in the same physical location. An explanation for the emission of the λ5875 line based on either a different geometry for the line formation site, or on a different temperature regime for the line formation sites of the different lines, is therefore not valid.

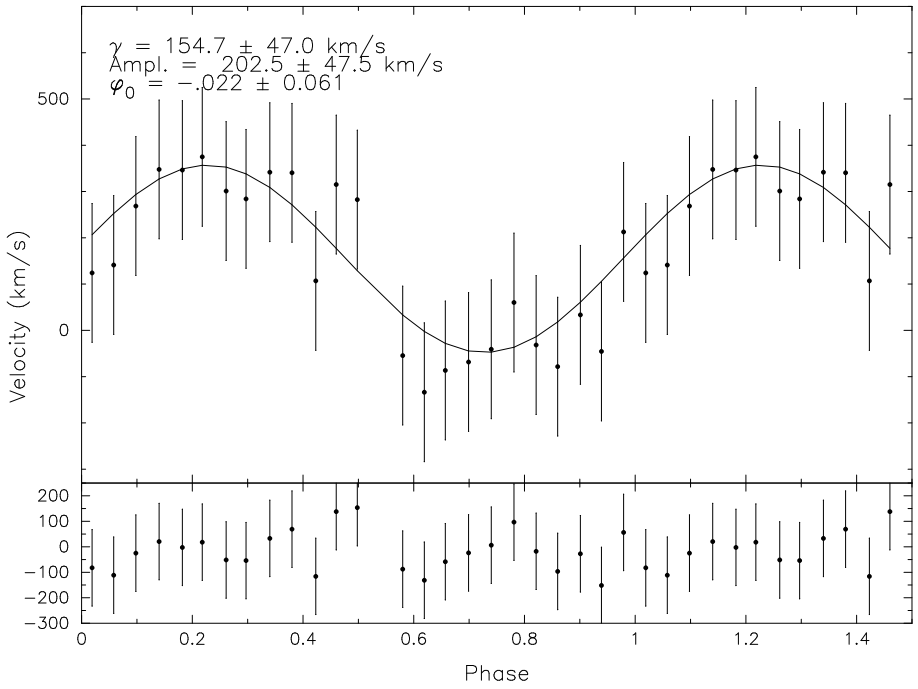

Figure 7.5. The radial velocity curve of the CaI absorption line at 6162Å. The phasing and amplitude of the radial velocity curve correspond well with a place of origin on the secondary star. The decrease of absorption around $\varphi \sim 0.5$ shows that a secondary eclipse affects the absorption line.

7.6 An explanation for the Balmer absorption effects

We have seen in Sect. 7.5 that the main component of the emission lines suffers from a strong decrease in the line strength between $0.75 < \varphi < 0.1$. This feature appears to be a consistent part of high inclination novalike systems and has been seen before in RW Tri in the studies of Still et al. (1995) and Kaitchuck et al. (1983). In Sect. 7.5 we have already concluded that the main emission component does not have its origin on the secondary. The behaviour of the emission line light curve can be explained if we assume that the line emission region is optically thick in the lines, but not in the continuum. This means that in the continuum our line of sight always end on the continuum source, i.e. the accretion disk. In the emission lines, however, the continuum source is not seen, because the lines are optically thick and our line of sight ends at the line emission region. In Fig. 7.7 we show a schematic picture of this geometry. In further we will call the emission site region that is optically thick in the lines, but optically thin in the continuum, the Balmer Bubble. The existence of such a Balmer Bubble causes the total amount of flux that is emitted in the continuum and the lines to be decoupled. If the continuum strength varies, the lines do not have to follow this behaviour. In Fig, 7.8 we show the average flux calibrated spectrum of RW Tri in five phase intervals, ranging from bottom to top: $0.1 < \varphi < 0.2$,

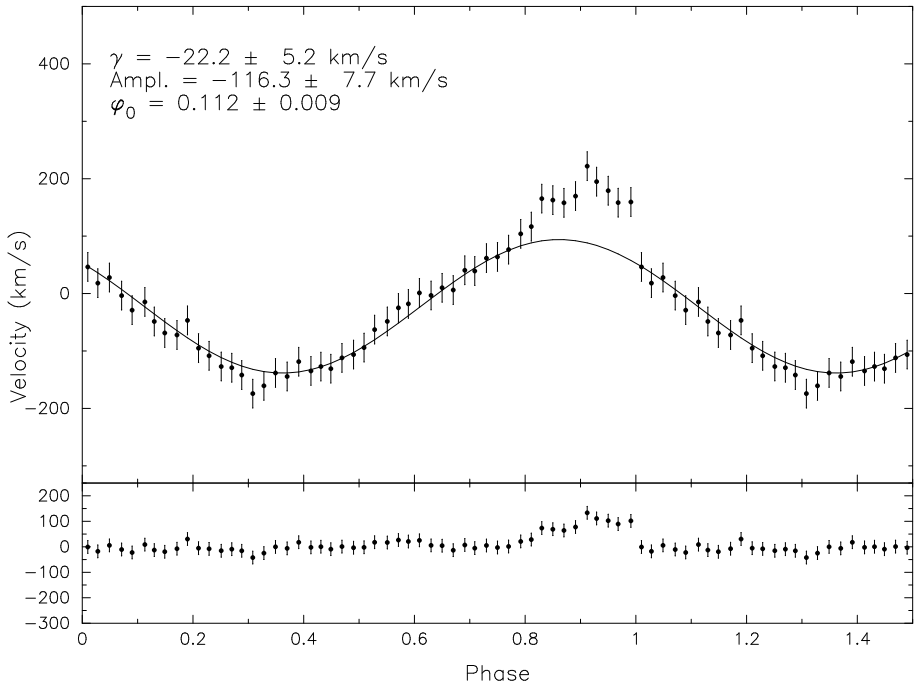

Figure 7.6. The radial velocity curve of Hα , determined by fitting a single Gaussian to the complete profile. The phasing of the curve shows that the main emission site is *inconsistent* with an origin on the heated side of the secondary. Velocities in the phaseinterval $0.8 < \varphi < 0.1$ have not been taken into account for the sinusoidal fit. The errors on the velocities have been set to 25 km/s ($\sim$1/6 of a wavelength bin at Hα).

$0.5< \varphi <0.6$, $0.6< \varphi <0.7$,$0.7< \varphi <0.8$ and $0.8< \varphi <0.9$. A number of important results can be seen from this figure:

- The continuum rises from an almost constant level between $0.1< \varphi <0.6$ to a maximum between $0.8< \varphi <0.9$.
- The Balmer lines from Hβ to Hϵ show a *constant* total flux. Although the continuum is rising, the Balmer lines do not increase in strength.
- The HeII λ4686 and CII λ4267 flux *does* rise simultaneously with the continuum.
- For H8 and higher up the Balmer series the line flux is not constant, but rises together with the continuum.

The rising continuum is caused by the optically thick hot spot coming into view on the optically thick rim of the accretion disk. We can clearly see that a number of photospheric absorption lines of the accretion disk and hot-spot area are present in the spectrum of RW Tri. The aforementioned HeI λ4471 and HeI λ4026 lines are two of them. This rise of the continuum is caused by a temperature difference between the 'hot' hot-spot region and

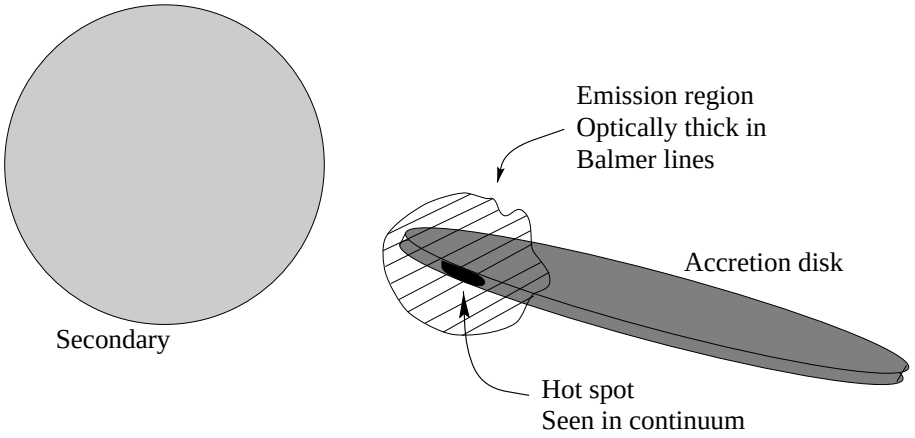

Figure 7.7. Schematic view of the hot-spot region in RW Tri. The hot spot, seen in continuum, is located on the rim of the disk, where the accretion stream (not shown) from the secondary impacts on the disk. This region is surrounded by a gas cloud or 'Balmer Bubble' that is optically thick in the lower Balmer and HeI lines and hides the hot-spot from view in these lines, and is optically thin in the higher Balmer and HeI lines and in the continuum.

the 'cool' remaining part of the accretion disk rim. This can e.g. be seen by the increasing strength of the HeI absorption lines, that increase in strength with increasing temperature. The lower Balmer lines, up to Hϵ, however, do not rise with the continuum, but stay at a constant flux. This means that the continuum radiation from the hot spot that we see rising towards $\varphi \sim$0.8-0.9 at any wavelength other than the Balmer lines is not able to reach us in the Balmer lines. In the Balmer lines the hot-spot region is hidden from our view because an optical depth of unity is reached before the hot spot continuum layer is seen. The fact that there is no variation in the total amount of flux received in the lower emission lines means that the Balmer Bubble must surround the emission site at all sides. It not only intersects our line of sight, which is rather close to the orbital plane, when the hot-spot continuum radiation is in full view, but also half an orbit later. The constancy of the flux in the Balmer lines, independent from the continuum variations, does not allow for a partial coverage of the hot spot region by this layer of gas.

The observed phase lag of the Hα radial velocity curve seems to indicate that the Balmer Bubble does not encompass the complete accretion disk, since in this case we would expect no phase lags with respect to the white dwarf. The Balmer Bubble, which is the line emission region, must be confined to a small part of the accretion disk. The phase lag identifies the hot-spot region as the center of the Balmer Bubble. This means that the radial velocity of the Hα line reflects the orbital motion of the hot-spot region. We will further discuss the consquences of this in Sect. 7.9. The dominance of the hot-spot region in the line emission was already concluded for SW Sex where both the Balmer lines as well as the HeII λ4686 lines are emitted in a region above the hot-spot (Groot et al., 1999).

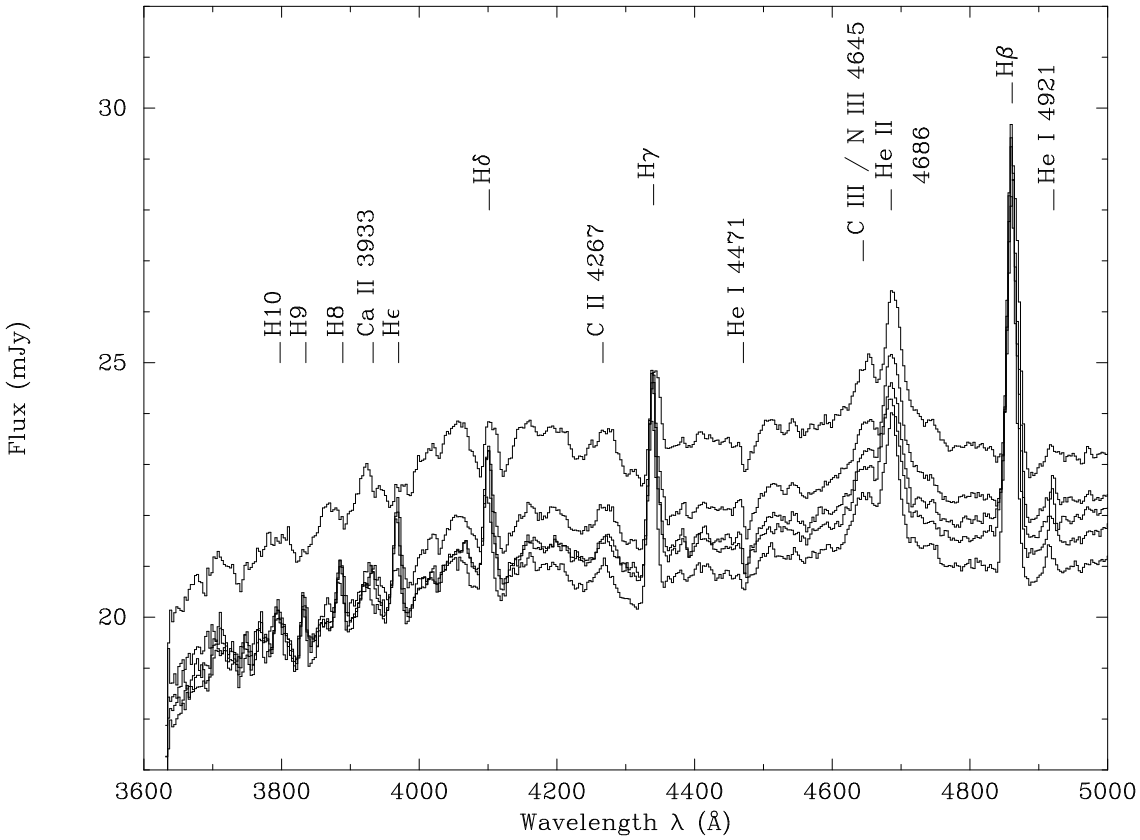

Figure 7.8. The flux calibrated average spectrum of RW Tri in the phase intervals $0.1< \varphi <0.2$, $0.5< \varphi <0.6$, $0.6< \varphi <0.7$, $0.7< \varphi <0.8$ and $0.8 < \varphi <0.9$, running from bottom to top. We see that the continuum rises when the hot spot comes into view, and that the HeII λ4686 and CII λ4267 lines rise with it. The Balmer lines up to Hϵ, however, stay at a constant flux. This indicates that these lines are optically thick and that the hot-spot continuum is hidden from view at these wavelengths. From H8 on the Balmer lines become optically thin.

The fact that the total amount of flux received in the Balmer lines is constant, but that at the same time the surrounding continuum rises in strength because the hot-spot comes into view, explains the, continuum subtracted, line strength behaviour seen in Fig. 7.3.
The HeII λ4686 line does rise together with the continuum, which indicates that the Balmer Bubble is not optically thick in the HeII λ4686 line. This shows that the temperature of the Balmer Bubble is too low to contain an appreciable amount of ionized helium. Since the linestrength is also not rising when the hot-spot comes into view (Fig. 7.3), it means that the emission site of the HeII λ4686 is equally well visible at all phases. The apparent increase in the, continuum subtracted, strength of the emission lines during mid-eclipse indicates that the Balmer Bubble extends to an appreciable height above the accretion disk. The observed origin of the Balmer Bubble at the hot-spot region and the radial velocity curve of the Hα line indicate that the gas in the Balmer Bubble is decoupled

from the gas flow in the disk which is assumed to be Keplerian. Studies of these lines that interpret them as coming from the plane of the disk, e.g. Doppler mapping, will therefore give erroneous results.

7.6.1 Optically thin higher Balmer lines

We have seen in Fig. 7.8 that the Balmer lines of H8 and higher do follow the continuum in its rise towards maximum. From this we can conclude that between Hϵ and H8 the gas layer changes from optically thick to optically thin. In the higher Balmer lines the hot-spot continuum is no longer hidden from view. The reason that the higher Balmer lines are not rising together with the continuum analogous to the HeII λ4686 lines is caused by two secondary effects of the high hot spot temperature and the vertical extension of the emission region. The first of these effects is that the depth of the photospheric Balmer absorption lines, underlying the emission lines, will, at the temperatures encountered in the hot-spot region ($\sim$10 000 K), increase with increasing temperature. The second of these effects is that continuum radiation that originates in the accretion disk as seen to be located *behind* the Balmer Bubble above the hot spot region will scatter out of our line-of-sight due to a non-zero optical depth in the higher Balmer lines. This will lead to an increase of the absorption line depth. These secondary effects will cause an increase of the absorption line depth, which, together with the constant Balmer emission from the Balmer Bubble will cause the higher Balmer lines to go into absorption as seen in Fig. 7.8.

7.6.2 The HeI line appearance

This same optical depth effect can also explain the puzzling behaviour of the HeI lines as described in Sect. 7.5.3. The lower HeI λ6678 and λ5875 lines are optically thick and our line-of-sight ends in a similar 'Helium Bubble' as in the 'Balmer Bubble' for the lower Balmer lines. For the higher helium lines, the optical depth decreases to less than unity. Since we can see that the HeI λ4471 line is almost non-existent in the phase-interval $0.1< \varphi <0.5$, while the HeI λ5875 line is clearly in absorption and the HeI λ4026 clearly in absorption, we can deduce that $\tau_{\rm He} > 1$ for the helium lines >4471Å, $\tau_{\rm He} <1$ for the helium lines <4471Å and $\tau_{\rm He} \sim 1$ for HeI λ4471.

7.7 Continuum light curves

The continuum light curves of RW Tri (Fig. 7.9) show that the system varied from night to night up to $\sim$30% in its out-of-eclipse light level. These short term variations of RW Tri have been long known (Walker 1963, Smak 1995), but are not unique to RW Tri. The novalike system GS Pav has been shown to exhibit similar variations on similar timescales

of days to weeks (Groot et al., 1998). Almost all well studied novalike systems show slow variations in their average out-of-eclipse levels. RW Tri is rather extreme, since it has been shown to vary by more than three magnitudes from the very high state at AB$\sim$10.1 in the observations of Still et al., (1995) to the low states at AB$\sim$13.5 as seen by Walker (1963). In our observations the system varied, at 4500 Å, between AB=13.2 (18.5 mJy) on the night of October 23, to AB=12.9 (23 mJy) on October 26.

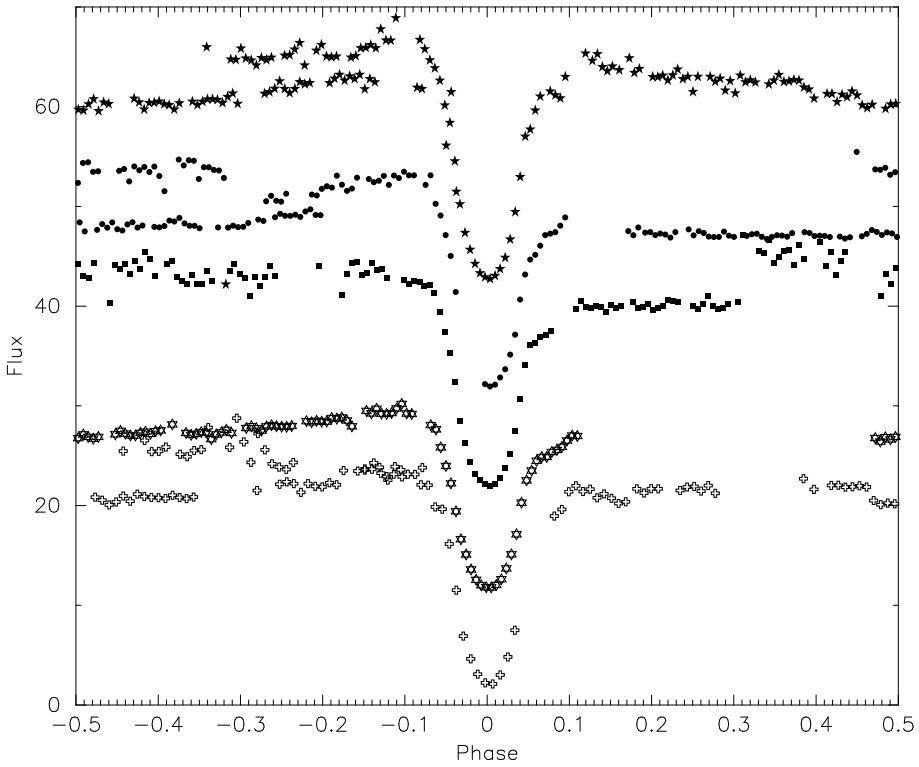

Figure 7.9. The continuum light curves of RW Tri between 4400Å and 4600 Å, from bottom (22 October) to top (26 October). The light curves are offset by steps of 10 mJy per night, with no offset for the bottom curve.

We see from Fig. 7.9 that the light curves show a round bottomed eclipse profile which is intermediate between the V-shaped eclipse profiles seen in many novalike systems, and the U-shaped profiles common to dwarf nova systems. This indicates a strong dominance of the inner accretion disk. A clear egress feature is visible in all the light curves, but no corresponding strong orbital hump is seen just before the onset of the eclipse. This shape of the light curve is not uncommon in novalikes and has been seen before in RW Tri and UX Uma (see Smak, 1995; 1994 and references therein). Smak (1994) has designated the light curves that do show a clear egress delay caused by a hot-spot, but no orbital hump, to be of the *peculiar* type and he argues that the lack of an orbital hump is caused by circumbinary material, which invalidates the use of these light curves for eclipse and

accretion disk analysis. We would like to argue, however, that there is no further support for the presence of circumbinary material, that has to be optically thick in the continuum to affect the continuum light curves. The HeII λ4686 line, which most closely resembles the continuum light curve is not affected by any absorption in the phase interval just before eclipse. If any optically thick circumbinary material is the cause of a lack of an orbital hump, this would most certainly also influence the HeII λ4686 line.

7.8 Spectral Eclipse Mapping

For the eclipse mapping procedure, we used the run-combined light curve to obtain sufficient phase resolution and phase coverage. Analysis of the light curves showed that the profile of eclipse of October 23 deviated in its shape from the rest of the eclipse profiles, especially in the steepness of the egress feature. This eclipse profile has therefore been excluded from the run-combined average which is based on the other four eclipses.
One of the assumptions of the eclipse mapping program is that no variation on the light curve occurs outside eclipse. We have therefore applied a correction to the observed light curves and brought them to a common scale, which was chosen to be the brightness of RW Tri on the first night, which is, at AB=13.0 at 4500Å, average for the four eclipse curves used here. We would like to note that the results from the eclipse maps should be viewed as the *average* state of the accretion disk of RW Tri during our observation. Any information on the time dependence of the accretion disk is lost.

The spectrum of RW Tri has been divided in 80 narrow band light curves, each 40Å wide, except around the spectral lines, which were taken as one bin each. In Fig. 7.10 we show the corrected light curves in three narrow band wavelength regions, distributed over the wavelength range covered. We see that, despite the variation of the out-of-eclipse light, the eclipse profiles do not vary strongly, especially in the blue. We also see that the amount of asymmetry of the light curves, caused by the hot-spot egress feature, diminishes from the blue to the red. The amount of scatter on the narrow-band light curves increases when going to the red. This indicates that it is the cool outer layer of the accretion disk that varies mostly when the out-of-eclipse brightness varies. We can also see that the phasing of the four eclipses used in these lightcurves, is rather unlucky in the sense that they bunch together and do not make a smooth profile. In the eclipse mapping procedure this limits the phase-bin size that can be used in the reconstruction.
For the reconstruction we have used a 51×51 pixel map, phasebins of 0.005 in phase and the system parameters as given in Table 7.1.

7.8.1 Disk size

To measure the size of the accretion disk at different wavelengths we have used the distance ($R_{0.1}$) where the intensity on the disk has fallen to 10% of the central intensity. This

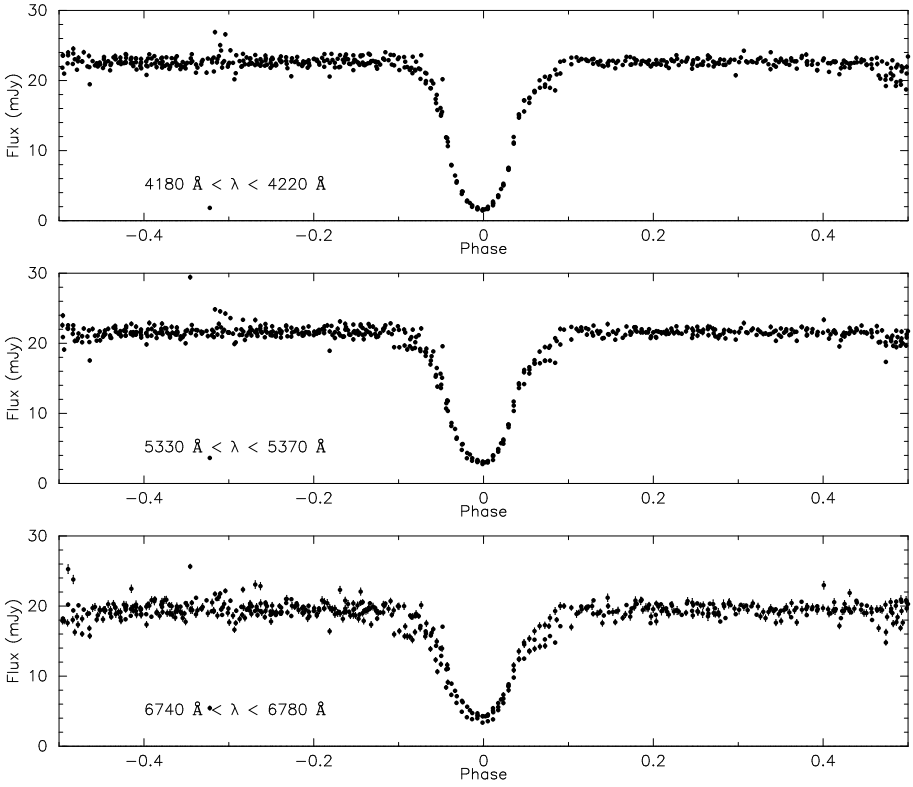

Figure 7.10. The corrected run-combined light curves of RW Tri in three wavelength regions centered on 4200Å, 5350Åand 6760Å. The correction has been applied by spline curve fitting to the phases outside the interval $-0.12 < \varphi < 0.12$.

measure was used by Rutten et al. (1992) to compare the relative sizes of the disks in six different novalike systems. We find from our eclipse maps that $R_{0.1}$ = 0.25±0.10R_{L_1} at 4420Å. The rather large error is caused by a relatively flat run of the reconstructed intensity with radial distance at this wavelength. For 6270Å the disk size has increased to $R_{0.1}$ = 0.45±0.05R_{L_1}. Both values are comparable to the values found by Rutten et al. (1992) at 4410Å ($R_{0.1}$=0.28±0.03R_{L_1}) and 8010Å ($R_{0.1}$=0.43±0.03R_{L_1}).

7.8.2 Accretion disk annuli spectra

We have defined seven regions in the accretion disk of RW Tri, shown in Fig. 7.11, and labeled 'A' through 'H'. The spectra of these regions are shown in Fig. 7.12. We see that there is a strong change in the slope of the spectrum when going from the white dwarf to the outside of the accretion disk. The emission lines are in absorption in the inner disk, and changing to emission when going outwards. Not surprisingly the non-eclipsed light (region H) shows the emission lines strongly in emission on top of a continuum level that strongly rises to the red. This change of the reconstructed accretion disk spectrum is very

similar to that of UX UMa as shown by Rutten et al. (1994).

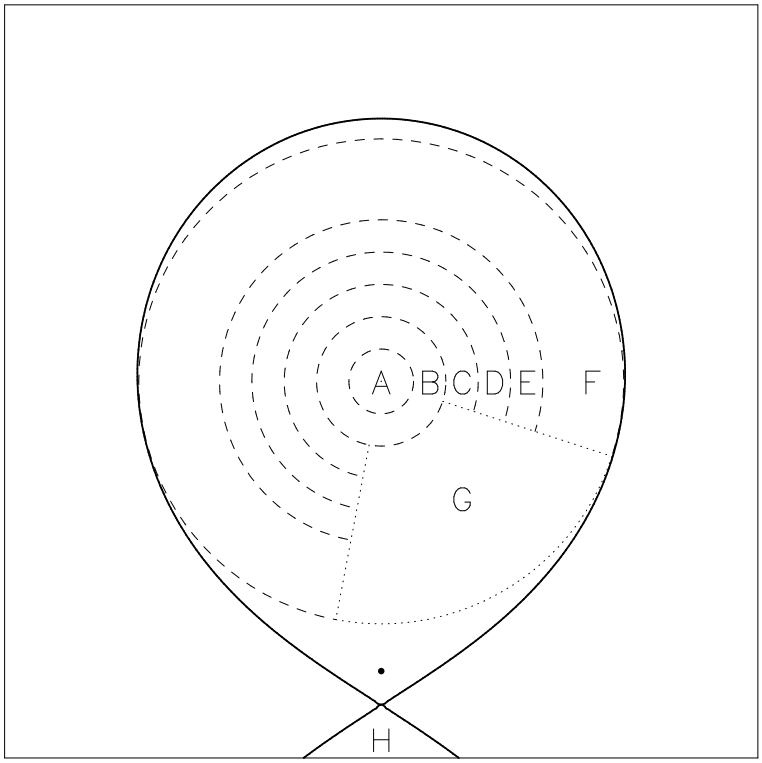

Figure 7.11. Schematic view of the white dwarf Roche lobe, showing the subdivision of the Roche lobe in seven regions, labeled 'A'-'G', which increase outwards in steps of $0.1R_{L_1}$, except region 'G' that covers the annulus from $0.5R_{L_1}$-$0.75R_{L_1}$. The uneclipsed light is denoted by region 'H', tentatively placed on the secondary.

7.8.3 Distance to RW Tri

In order to convert the reconstructed fluxes to specific intensities, from which temperatures can be derived by e.g. blackbody fitting, it is imperative to have a good estimate of the distance to the system. The distance of RW Tri was recently determined by parallax measurements using the HST Fine Guidance Sensor to be 341$\pm$35 pc (McArthur et al., 1999).

The distance of RW Tri can also be estimated by allowing the distance as well as the temperature to vary in blackbody fits to the reconstructed accretion disk spectra. Blackbody fitting in the wavelength region 4000-6200Å gives a distance to RW Tri of 330$\pm$40 pc, in excellent agreement with the parallax measurements and also with the estimate of the fractional contribution of the secondary by Rutten et al. (1992). We refer to McArthur et

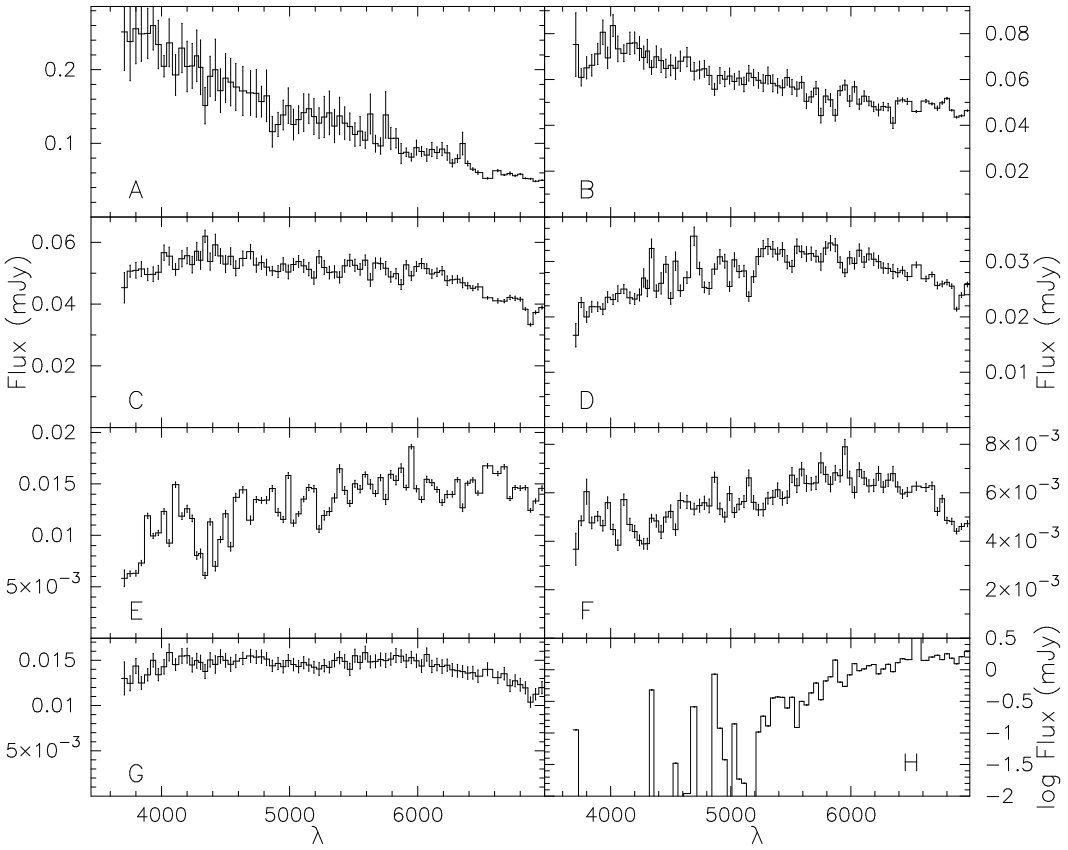

Figure 7.12. The reconstructed spectrum of the accretion disk in RW Tri in the regions defined in Fig. 7.11. Fluxes are in fluxes per surface element. We see that the slope of the spectrum changes dramatically from very blue in the inner parts, to red in the outer parts. The hot-spot area (region 'G') is more blue that the rest of the outer disk. The fluxes of the uneclipsed light component (region 'H') are plotted on a logarithmic scale, all others on a linear scale.

al. (1999) for a comparison with other distance estimates. We will use the value of 330 pc in the further analysis.

7.8.4 The Radial temperature profile

The radial temperature profile of the accretion disk can now be determined. For this we have used the wavelength region of 4000Å-6200Å, from which the emission lines have been omitted. The blue cut-off has been chosen to avoid any influence of the Balmer jump and the red cut-off has been chosen because trial blackbody fits showed that the reconstructed intensities at these wavelengths strongly deviated from the expected values based on the trend in the bluer part of the wavelength which generally agreed well with the blackbody fits. We cannot say whether this is caused by an incorrect flux calibration

in this wavelength region or by a physical reason which causes the accretion disk spectra in this region to deviate from approximately blackbody.
We show the radial temperature profile of the accretion disk in RW Tri in Fig. 7.13, which also shows the theoretical predictions for the radial temperature profile based on optically thick, steady state accretion disks. We see that the reconstructed radial temperature profile follows the theoretical prediction rather well in the radial distance range of 0.55–0.15 R_{L_1}. Inside $0.15R_{L_1}$ the temperature profile flattens with respect to the theoretical prediction. Comparing the temperature profile derived here with those derived by Rutten et al. (1992) on the basis of four-colour photometry and by Horne and Stiening (1985) on the basis of brightness temperature estimates of their B band photometry, we see that our radial temperature profile already levels off at a larger distance from the white dwarf (at $\sim 0.15R_{L_1}$ here and at $\sim 0.06R_{L_1}$ in Rutten et al., 1992 and Horne and Stiening, 1985). The derived mass-transfer rates are almost the same, although the one of Rutten et al. (1992) is somewhat lower, but this will partly be caused by the lower distance (270 pc) used in that study.
Comparing the radial temperature profile of RW Tri as derived here with those of other novalike systems, we see that it most closely resembles the profile of UX Uma as derived by Rutten et al. (1992), but also shows some aspects of the profiles displayed by the SW Sex stars (Rutten et al., 1992 and Groot et al., 1999), especially the flattening of the temperature profile.

7.8.5 Position of the hot-spot

We have seen in Fig. 7.12 that the hot-spot is blue and peaks at $\sim$4000Å. To better determine the position of the hot-spot we have taken the ratio of the continuum intensity maps at 4060Å, at the peak of the hot-spot, and one at 6270Å, where the hot spot influence is much less. We see in Fig. 7.14 that the hot spot peaks at a position (in radial coordinates, r, φ) of ($0.5R_{L_1}$,0.875).

7.9 RW Tri system parameters

We have seen in the previous paragraph that the radial velocity curve of the Balmer lines most likely reflects the orbital motion of the hot-spot: $K_{\rm HS}$ = 120$\pm$15 km s^{-1}after correction for the inclination (i=75°). We have also determined the position of the hot spot at (r, φ) = ($0.5R_{L_1}$, 0.875). Using this position we can now check if the radial velocity derived from the Hα profile is indeed a good reflection of the orbital motion of material at the position of the hot spot, for the parameters we have used for RW Tri (see Table 7.1).
For M_1=0.7 $M_\odot$ and M_2 =0.6 $M_\odot$ and an orbital period of 20034.72 s, the position of the center-of-mass is located just inside the Roche-lobe of the white dwarf at (r, φ) = (0.895,0.). From simple geometry it then follows that the distance of the hot spot from

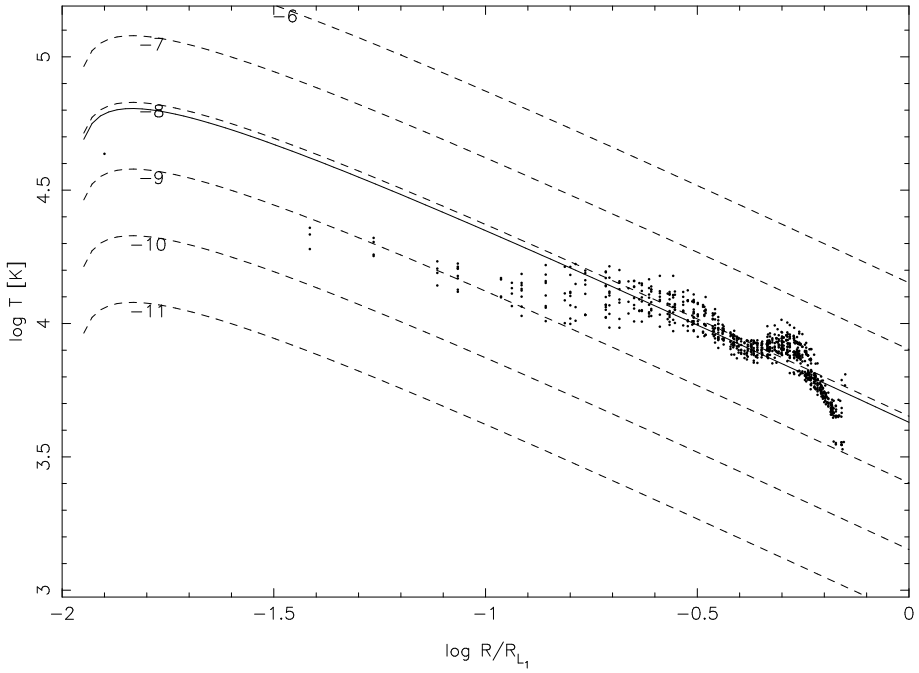

Figure 7.13. The radial temperature profile of RW Tri, as deduced from the spectral eclipse mapping. The average mass-accretion rate in the radial distance range of $0.55R_{L_1} < r < 0.15R_{L_1}$ is $(1.0\pm0.1)\times10^{-8}$ $M_\odot$/yr. The dashed lines show the theoretical prediction of the radial temperature profile based on the theory of optically thick, steady state accretion disks.

the center-of-mass is $0.65R_{L_1}$ and using the orbital period the orbital velocity at this position is $\sim$125 km s^{-1}. This agrees very well with the 120$\pm$15 km s^{-1}as found from the Hα profile. This also shows that the gas causing the Hα emission must be completely decoupled from the velocity field, normally assumed to be Keplerian, in the accretion disk itself.
The velocity expected for the center of the secondary for these system parameters is 225 km s^{-1}, again in excellent agreement with the observed value of 210$\pm$50 km s^{-1}(after correction for the inclination) as found from the rather noisy radial velocity curve of the CaI λ6162 line. Future, higher resolution observations should be able to constrain both values, and therefore the system parameters to higher accuracy.

7.9.1 RW Tri as an SW Sex star?

During our observations RW Tri shows some features that are commonly used as identifiers of the SW Sex sub-class of novalike CVs (see Thorstensen, 1991 and Groot et al., 1999): single-peaked emission lines, low radial velocities, phase lags and shallow eclipses of the Balmer lines, a flat radial temperature profile, HeII λ4686 emission and an apparent decrease in emission line strength before the eclipse in the Balmer lines. It is,

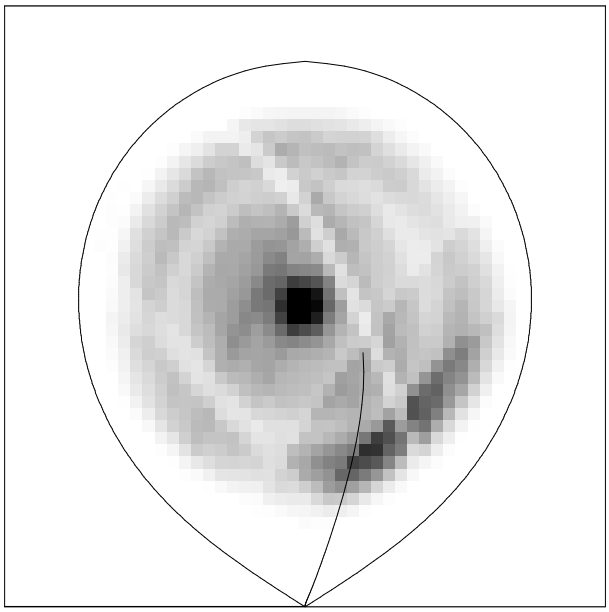

Figure 7.14. The ratio of the eclipse maps at 4060Å and at 6270Å. We can clearly see the location of the white dwarf and the hot spot. The bright arcs are reconstruction artefacts caused by gaps in the eclipse profile.

however, striking to see that the same system did not show a number of these in earlier observations. In the observations presented by Horne and Stiening (1985) and Rutten et al. (1992) the radial temperature profile only flattened at a distance much closer to the white dwarf. In the spectroscopic observations of Still et al. (1995) and Kaitchuck et al. (1983) the HeII λ4686 emission was not seen. It appears that in our observations RW Tri behaved 'SW Sexier' than normal.

On the other hand Groot et al. (1999) showed that in recent observations of SW Sex in a low state, this system behaved less 'SW Sexy' than normal, not showing e.g. the phase 0.5 absorption. Combined with the RW Tri observations presented here it appears that the boundary between UX UMa-like novalikes (such as RW Tri) and SW Sex stars is vague and depends on the brightness of the system at the moment of observation, i.e. it most likely depends on the mass-transfer rate from the secondary. We would therefore like to suggest that there is no clear physical distinction between SW Sex stars and UX UMa stars, and that the behaviour that is 'standard' for the two sub-classes are the extremes of a sliding scale. How we classify a system between these sub-classes depends on the spectroscopic state at the time of a particular observation and can change from epoch to epoch.

We will therefore not classify RW Tri, based on our current observations, as an SW Sex star. We argue that the SW Sex stars are not a different sub-class of the novalikes. The classification suffices to describe, in general terms, the spectroscopic behaviour of a no-

valike system, but should not be used to denote a physically different sub-class.

7.10 The structure of RW Tri

From the evidence given above we conclude that the RW Tri system consists of an $0.7M_{\odot}$ white dwarf and an $0.6M_{\odot}$ late K-type secondary, which is transferring mass to the white dwarf at a rate of $(1.0\pm0.1)\times10^{-8}$ $M_{\odot}$/yr. The accretion disk around the white dwarf is optically thick, as evidenced by the absorption features seen in its spectrum. The radial temperature profile of the accretion disk is consistent with the prediction of steady state accretion disk theory up to a distance of 0.15 R_{L_1} from the white dwarf. Within this distance the radial temperature profile levels off. This radial temperature profile is a case in between the previous observations of RW Tri (Horne and Stiening, 1985; Rutten et al., 1992) and UX UMa (Rutten et al., 1992), where the radial temperature profile continues to follow the theoretical prediction up to distances of $0.06R_{L_1}$ from the white dwarf, and the observations of the SW Sex stars, where the radial profile already flattens at distances $>0.2R_{L_1}$ (Groot et al., 1999; Rutten et al., 1992).
The hot-spot region is a bright region on the rim of the accretion disk. The hot spot region is surrounded by a gas layer, or 'Balmer Bubble' that is optically thick in the lower Balmer and HeI lines, and is the cause of the transient absorption of the Balmer lines, also seen in other novalike systems (e.g. SW Sex, Groot et al., 1999, Dhillon, Marsh and Jones, 1997). The gas seen in the emission lines is decoupled from the velocity field of the accretion disk and we can estimate the orbital velocity of the hot-spot region from the emission line radial velocity curves. Together with the radial velocity curve of the secondary these confirm the system parameters of RW Tri as given above.
RW Tri shows some characteristics that are commonly attributed to SW Sex stars. Instead of classifying RW Tri as 'yet-another' SW Sex star we argue that the whole division of novalike systems into the SW Sex and UX UMa sub-classes should be disregarded and all the systems should be considered as one class: the novalikes. The spectroscopic appearance of an eclipsing novalike depends on brightness of the system at the particular epoch of the observations and further study should clarify why, and how, the accretion disk structure changes with a varying brightness.

Acknowledgements
PJG whishes to thank Alex de Koter for pleasant and enlightening discussions on the line formation mechanisms in non-LTE regimes, and Claudio Moreno and the staff of the ING observatory for their hospitality during numerous visits. PJG is partially supported by NWO Spinoza grant 08-0 to E.P.J. van den Heuvel. The Isaac Newton Telescope is part of the Isaac Newton Group of Telescopes operated on the island of La Palma by the Instítuto de Astrofísica de Canarias on behalf of the British PPARC and the Dutch NWO.

References

Beuermann, K. and Thomas, H.-C., 1990, A&A 230, 326

Cardelli, J.A., Clayton, G.C. and Mathis, J.S., 1990, ApJ 345, 245

Davey, S and Smith, R.C., 1992, MNRAS 257, 476

Dhillon, V.S., Marsh, T.R., and Jones, D.H.P., 1997, MNRAS 291, 694

Frank, J., King, A.R. and Raine, D., 1992, in *Accretion Power in Astrophysics*, Cambridge Astrophysics Series No. 21, CUP, Cambridge, UK

Groot, P.J., et al., 1998, A&A 340, L31 (Chapter 5)

Groot, P.J., Rutten, R.G.M. and Van Paradijs, J., 1999, A&A, *submitted* (Chapter 6)

Kaitchuck, R.H., Honeycutt, R.K. and Schlegel, E.M., 1983, ApJ 267, 239

McArthur, B.E., et al., 1999, ApJ 520, L59

Mason, K.O., Drew, J.E. and Knigge, C., 1997, MNRAS 290, L23

Oke, J.B., 1990, AJ 99, 1621

Protitch, M., 1937, *Bull. Astr. Obs. Belgrade*, 9-10, 38

Robinson, E.L., Shetrone, M.D. and Africano, J.L., 1991, AJ 102, 1176

Rutten, R.G.M., Van Paradijs, J. and Tinbergen, J., 1992, A&A 260, 213

Rutten, R.G.M., et al., 1993, Nature 362, 518

Rutten, R.G.M., Dhillon, V.S., Horne, K. and Kuulkers, E., 1994, A&A 283, 441

Smak, J., 1995, ActA 45, 259

Still, M.D., Dhillon, V.S. and Jones, D.H.P., 1995, MNRAS 273, 849

Thorstensen, J.R., et al., 1991, AJ 102, 272

8

3-D Spectral Eclipse Mapping of the Cataclysmic Variable IP Pegasi

P.J. Groot, R.G.M. Rutten and J. van Paradijs

To be submitted to Astronomy and Astrophysics

In order to study the quiescent accretion disk of IP Pegasi, we have obtained phase-resolved spectrophotometric data in the wavelength region of 3600Å-7000Å, covering 8 eclipses and all orbital phases. The light curve of IP Peg is dominated by a very broad orbital hump, caused by a bright spot at the accretion stream - accretion disk interaction. The bright spot would display a maximum brightness at φ=–0.055 if no secondary were present and extends an angle of 47° along the disk rim. It has a temperature of $\sim$10 000 K and the disk at the position of the bright spot is flared with an opening angle of 1.5° . Transient HeII λ4686 emission is seen, originating at the bright spot. From 3D eclipse mapping of narrow band light curves over the full wavelength region we conclude that the accretion disk in IP Peg in quiescence is cold enough for TiO molecules to form in its outer parts, as evidenced by TiO bands in the reconstructed accretion disk spectrum.

8.1 Introduction

Although found fairly recently (Goranskij et al., 1985), IP Pegasi is one of the best studied Cataclysmic Variables (CV), due to its almost ideal characteristics: it is a deeply eclipsing (i $\sim$80°), long period ($P_{\rm orb}$=3.8hr), bright (V$\sim$14) CV of the dwarf nova (DN) subtype with strong emission lines in its spectrum (see Warner, 1995 for a general overview of CV characteristics). It shows regular dwarf novae outbursts and is as such an excellent system for the study of time-dependent accretion disks in low-mass tranfer rate systems. Most

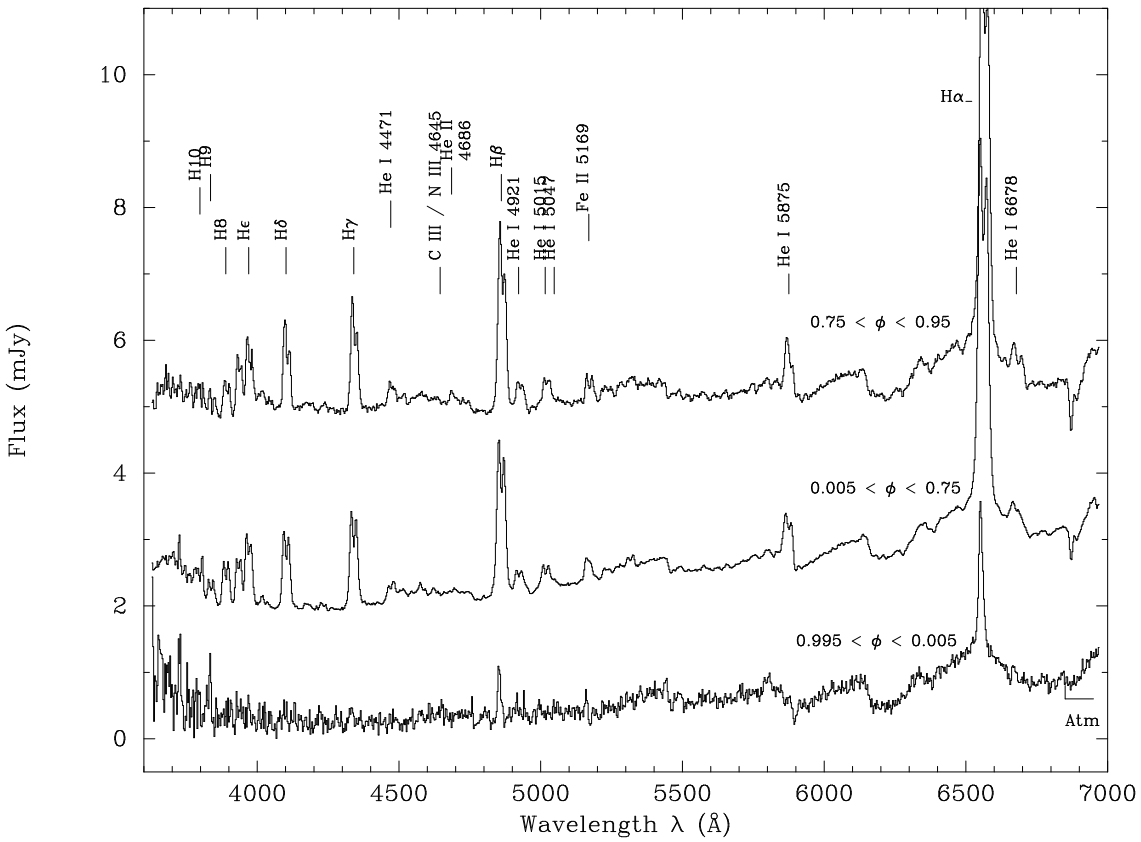

Figure 8.1. The average spectrum of IP Peg in three phase intervals: during the maximum of the orbital hump (top), at mid-eclipse (bottom) and during the rest of the orbit (middle). The major lines are indicated. The TiO bands originate in the secondary.

studies have therefore concentrated on the emission line behaviour during quiescence and during outburst (e.g. Marsh, 1988; Bobinger, 1997; Steeghs et al., 1997). The detection of strong spiral waves in the accretion disk of IP Peg during outburst is the most striking result of these studies (Steeghs et al., 1997).

Studies of the continuum spectrum of IP Peg have mostly been limited to either broad-band photometry (Wood et al., 1986; 1989; Wolf et al., 1993) or outburst epochs (Bobinger et al., 1997). Analysis of the quiescent continuum spectrum of IP Peg has been largely neglected. In order to better understand the quiescent structure of the accretion disk in IP Peg we have included this source in our ongoing investigation to obtain spectrally resolved eclipse maps of accretion disks in Cataclysmic Variables (see Groot, 1999; Groot, Rutten and Van Paradijs, 2000a; b). IP Peg is the first dwarf nova system in this investigation.

Already shortly after its discovery it became clear that the light curve of IP Peg is dominated by the anisotropic emission from the bright spot, where the accretion stream from

the secondary intersects the accretion disk. The resultant orbital hump (see e.g. Fig. 8.7) extends over a major part of the binary orbit. As first recognized by Wood and Crawford (1986) the eclipse ingress of the bright spot and of the white dwarf coincide in phase, although the egress of the two features is clearly seperated. The ingress coincidence makes that a 'disection-approach' as used for Z Cha by Wood et al. (1986) is not possible for IP Peg. Wolf et al. (1998) and Bobinger et al. (1999) have used a combination of eclipse mapping and doppler mapping techniques to obtain insight in the disk structure of IP Peg. Their study, however, is limited to a small wavelength interval around the major emission lines.
Here we use data obtained with the 2.5m Isaac Newton Telescope over the wavelength range of 3600-7000 Å and the 3-D eclipse mapping method developed by Rutten (1998) to gain insight in the disk structure of IP Peg in quiescence.

8.2 Data and Reduction

On the nights of 22-26 October 1994, we obtained a total of 512 low-resolution spectra using the Intermediate Dispersion Spectrograph with the R300V grating and a 1k$\times$1k Tek CCD at the 2.5m Isaac Newton Telescope on the island of La Palma. A wide slit ($2''$) and a second star on the slit ($30''$ SW of IP Peg) were used to obtain differential spectrophotometry. An absolute flux calibration was obtained by observing the spectral flux standard BD +25 3941 (Oke, 1990) using a $10''$ wide slit for both the spectral flux standard as well as IP Peg and its local comparison star.
All data is reduced in the standard fashion using the ESO-MIDAS package, with additionally written software. All stars were optimally extracted (Horne, 1986). All spectra were obtained with a 60s on-target integration time. With a $\sim$60s dead-time for CCD readout and data storage, we obtained an effective time resolution of 120s, or 1/110th of the orbital period of 3h47m. Throughout the nights CuAr arc spectra were taken for wavelength calibration.
A total of 512 spectra were recorded, covering 8 eclipses. An overview of the data is given in Table 8.1. Based on Poisson statistics in the extracted spectrum, each pixel was assigned an error, which is also propagated to the flux calibrated spectrum.

8.3 Average spectrum

The average spectrum of IP Peg in three phase intervals is shown in Fig. 8.1: at the maximum of the orbital hump (top), during mid-eclipse (bottom) and during the rest of the orbit (middle). The spectrum is a hybrid between the blue spectrum of the accretion disk and the red spectrum of the secondary. The spectrum shows the classical double-peaked emission lines (Smak 1969, 1981; Horne and Marsh, 1986) of the Balmer series

Table 8.1. Overview of IP Peg observations August 1995

Date	Start UT	End UT	No. Exposures
11/8/95	01:09	06:00	98
11-12/8/95	23:53	02:17	51
13/8/95	02:05	03:33	31
13-14/8/95	22:35	05:47	95
15/8/95	01:27	05:59	99
15-16/8/95	23:26	05:42	138

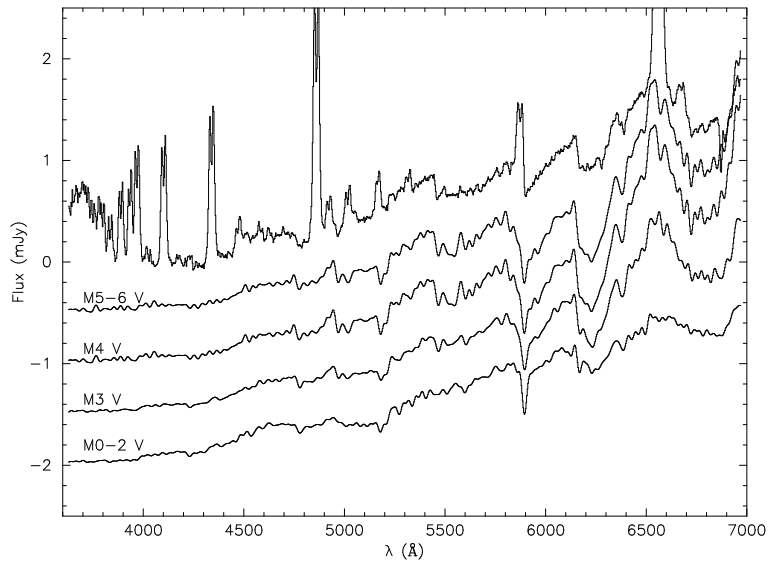

Figure 8.2. The spectrum of IP Peg as observed in the phase interval $0.25< \varphi <0.6$, compared with four spectral standards (taken from Pickles, 1985) in the spectral range M0 – M6 V.

(Hα -H12), He I and Fe II. The fact that all these lines are double-peaked clearly shows their origin in the disk. IP Peg is one of the few CVs were the secondary can be identified in the spectrum, as is seen in Fig. 8.1 by the strong molecular bands redwards of λ5000 Å, which are typical for M-type dwarfs. Also the 'plateau' on which the Hα resides is caused by the secondary star. No absorption wings from the white-dwarf primary are visible. No spectral change occurs when the bright spot comes into view, which indicates that the bright-spot spectrum is rather featureless.

8.4 The Secondary star

The spectral type of the secondary star in SW Sex has been determined to be most likely an M4-M4.5 dwarf on the basis of the ellipsoidal variations of IP Peg (Szkody and Mateo,

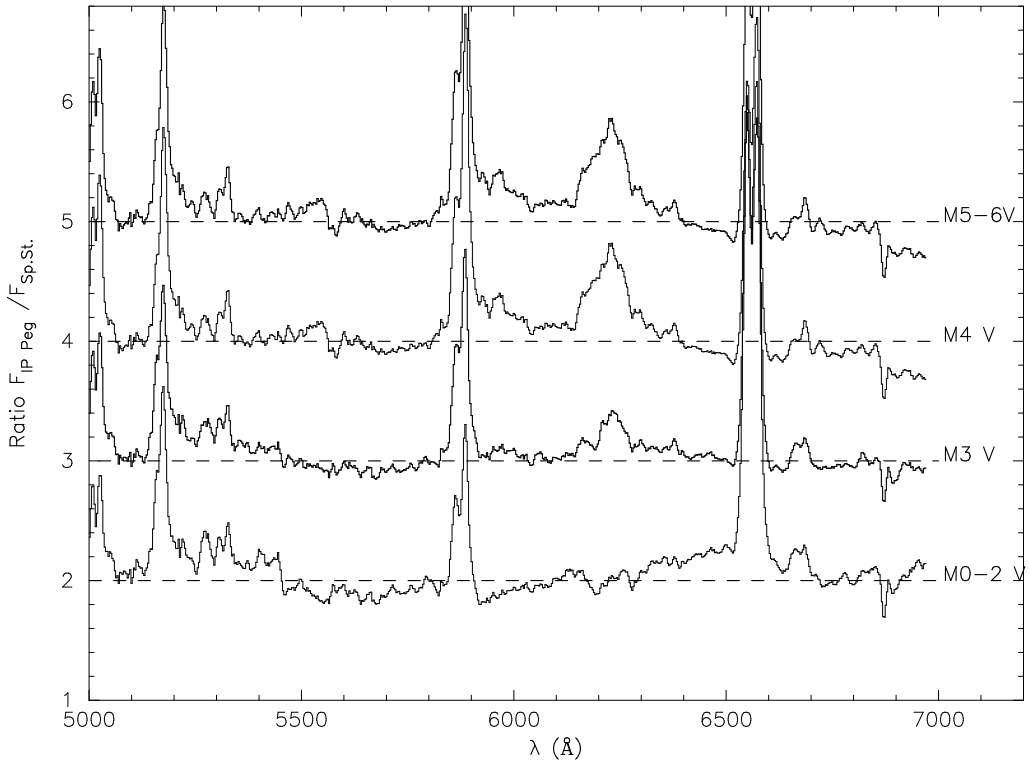

Figure 8.3. The ratio of the observed spectrum of IP Peg between $0.25< \varphi <0.6$, and the spectral standards as shown in Fig. 8.2. The ratio for the M3 V standard is the smoothest of the four. For plotting purposes the ratio's (M0-2 V through M5-6V) have been shifted upwards 1, 2, 3 and 4 units with respect to their real ratio.

1986) and its near-infrared spectrum (Martin et al., 1989). In Fig. 8.2 we show the spectrum as observed between phase $0.25< \varphi <0.6$, and four spectral standards of spectral type M0-2V, M3 V, M4 V and M5-6V from Pickles (1985). To determine the best match to IP Peg we have to subtract the contribution of the accretion disk. To do this we have determined the flux of the system between $4150\text{Å}< \lambda <4300$ Å and assumed that there is no contribution from the secondary in this wavelength region. To subtract the accretion disk spectrum we have extrapolated this flux redwards assuming an accretion disk slope of $\nu^{1/3}$ (see Frank, King and Raine, 1992) and compared the resulting spectrum with the spectral standards. In Fig. 8.3 we show the ratio of the corrected IP Peg spectrum to that of the spectral standards. It is clear from Fig. 8.3 that the slope of the secondary in IP Peg is best reproduced with an M3 V type spectrum, although the strength of the TiO bands, especially the one at λ6150Å is too shallow in IP Peg, indicating an earlier spectral type.

Since our main aim is to correct the spectra of IP Peg for the presence of the secondary for the eclipse mapping procedure that will be discussed in Sect. 8.10 we opt for the best fitting spectral slope and therefore choose the M3 V type spectrum to best fit the observed

spectrum of the secondary in IP Peg. Note that this seems to indicate a spectral type that is somewhat earlier than previously determined, which agrees well with the rather high mass ($0.64 M_{\odot}$) found for the secondary (Marsh 1988).

8.5 Radial velocity curve of the secondary

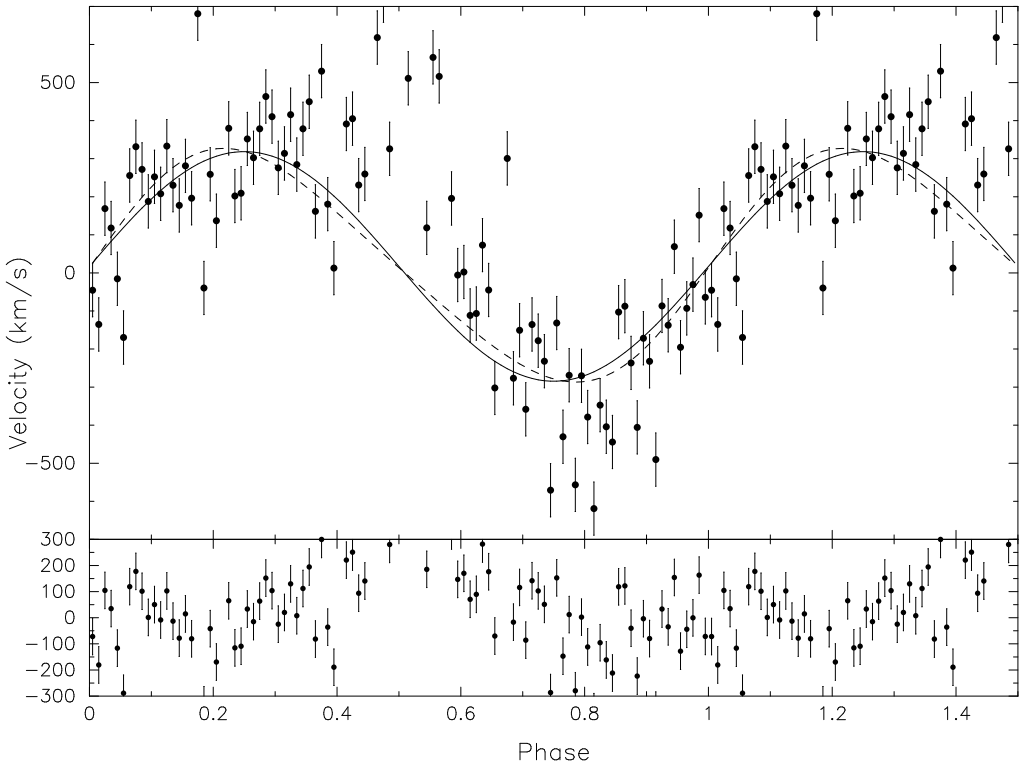

Figure 8.4. The radial velocity curve of the secondary in IP Peg, deduced from the TiO band at 6250Å. The full line is a circular fit to the data outside the phase-interval $0.4 < \varphi < 0.6$. The dashed lines shows the best fit elliptical fit for the same phase-range. Although the ellipticity appears substantial the improvement of the fit is minimal. Residuals to the fit are shown in the bottom panel.

The radial velocity (K_2) of the secondary star in IP Peg has been previously measured by Martin et al (1989) and Marsh (1988) and determined to be 295 ± 15 km s^{-1}. The measurement of K_2 is complicated by irradiation of the secondary by the white dwarf and the accretion disk, which has the effect that the line strength of the M-dwarf features in the near-infrared is weakened (see Wade and Horne, 1988 for Z Cha and Davey and Smith, 1992 for a number of CVs). This change in line strength will distort the radial velocity curve and make it non-sinusoidal. It will also have the effect of amplifying the observed radial velocity $K_{\rm abs}$ to values larger (up to $\sim$15%) than the true velocity K_2.

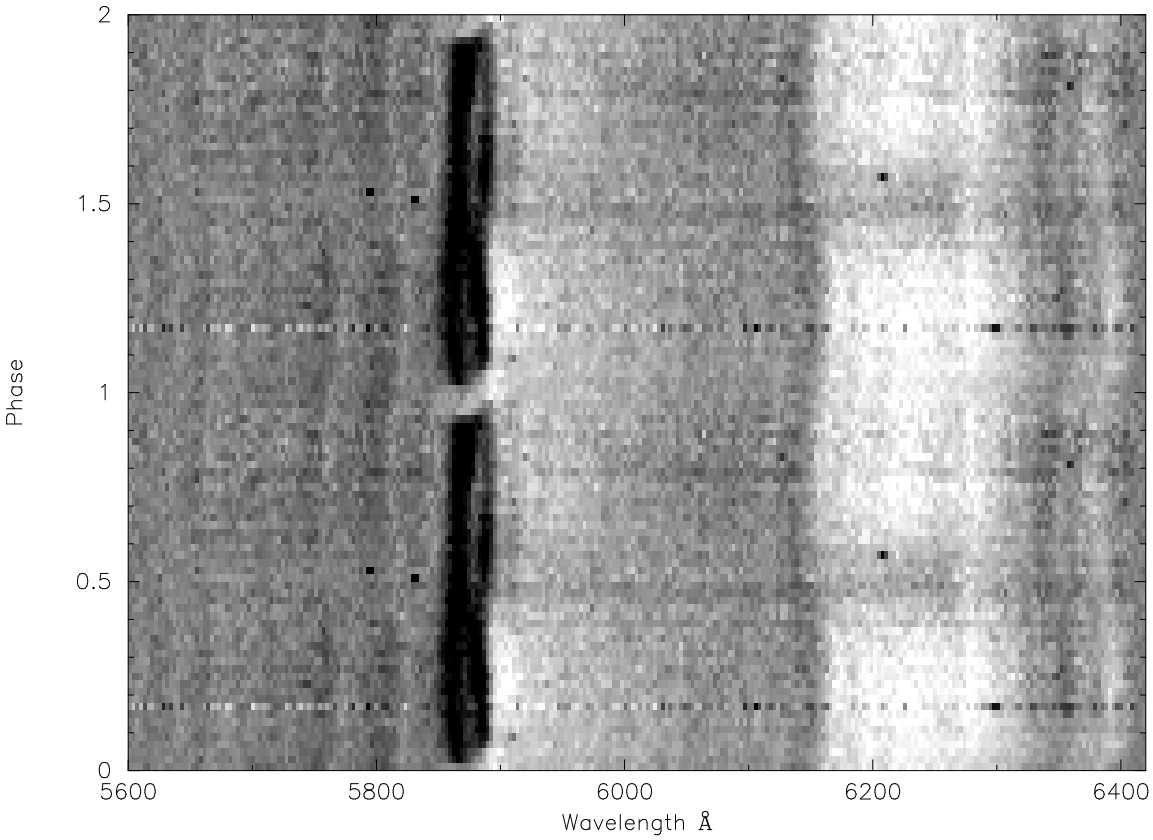

Figure 8.5. The trail spectrum in the wavelength region 5600-6450Å, after a subtraction of the continuum. It can be seen that the strength of the TiO band at 6250Å diminishes around φ=0.5, indicating that heating from the secondary is substantial.

Marsh (1988) has shown that the distortions are smallest when using velocities around mid-eclipse.
We have used a small wavelength region (6100-6200 Å), which is centered on the TiO-band edge at λ6150Å, and which is devoid of any accretion disk emission line contamination, as a probe of the secondary radial velocity curve. The phase-dependent radial velocity (shown in Fig. 8.4) was determined by subtracting the shifted secondary spectrum from the observed spectrum and determining the resultant χ^2 behaviour with respect to a constant as function of the shift. A parabola was fitted to a 1400 km s^{-1}wide range around the χ^2-minimum. With a wavelength bin size of 3 Å as used in our analysis, the 1400 km s^{-1} range is well beyond the expected radial velocity amplitude of $\sim$300 km s^{-1}. A sinusoidal fit, (shown in Fig. 8.4) of the form:

$$V(\varphi) = \gamma + K_{\rm abs}\sin(\varphi), \tag{8.1}$$

with V(φ) the radial velocity at phase φ and γ the systemic velocity over the phase range

0.6< φ <0.4 yeilds values of K_{abs} of 301±11 km s^{-1}and γ= 17±8 km s^{-1}. We have excluded the phase-range of 0.4< φ <0.6 because the TiO edge disappears at these phases. The effect of irradiation can be estimated by making an eccentric, rather than a sinusoidal, fit to the data, as described in Davey and Smith (1992). In our case the eccentric fit does not improve the fit and we will further only consider the circular solution.
When following the suggestion of Marsh (1988) and using only the phases (0.8< φ <0.2) in the fit to the radial velocity curve, we obtain values for $K_{\rm abs}$ that are higher than the ones given above: $K_{\rm abs} \geq 330$ km s^{-1}. The reason for this, as seen in Fig. 8.4, is the large distortion of the radial velocity curve between phases 0.4< φ <0.85. The reason for this distortion is the irradiation from the secondary that causes the strength of the TiO-bands to diminish and even disappear near phases $\varphi \sim$0.55 (see Fig. 8.5). Figure 8.5 also shows that there is substructure in the TiO band at 6200 Å, which is also indicative of an early M-type secondary spectral type, since at M4 or later this substructure disappears.
A detailed analysis of the strength and phase-dependence of the secondary star in IP Peg is outside the scope of this paper. For the current study we suffice by subtracting an orbital-velocity corrected M3V-type star from the spectra of IP Peg to correct for the contribution of the secondary to the total light. In Fig. 8.6 we show the average spectrum of IP Peg after this subtraction.

8.6 Eclipse timing

We have phase folded the spectra using the ephemeris of Wolf et al. (1993) without their second order correction. Analysis of the ingress and egress times of the resulting light curves showed that an extra phasefit of 0.007 needed to be applied to center the white-dwarf mid-eclipse on phase zero. This phase shift results in a slightly altered ephemeris given in Eq. 8.2, which only differs from the one given by Wolf et al. (1993) in the first term and not in the period.

$$T_{\rm mid\_eclipse} = 244\,5616.4147 + 0.15820616 \times N, \tag{8.2}$$

with N the number of cycles.
In our subsequent analysis of the lightcurves of IP Peg we have used the system parameters as derived by Marsh (1988), which we summarize in Table 8.2.

8.7 Continuum light curves

After correction for the secondary star the light curves of IP Peg show the familiar shape that is dominated by the strong orbital hump and the eclipse. In Fig. 8.7 we show the lightcurve of IP Peg in three broad-band regions, that were chosen to be (almost) devoid of spectral lines. From Fig. 8.7 we see that light curve of IP Peg is very similar at the

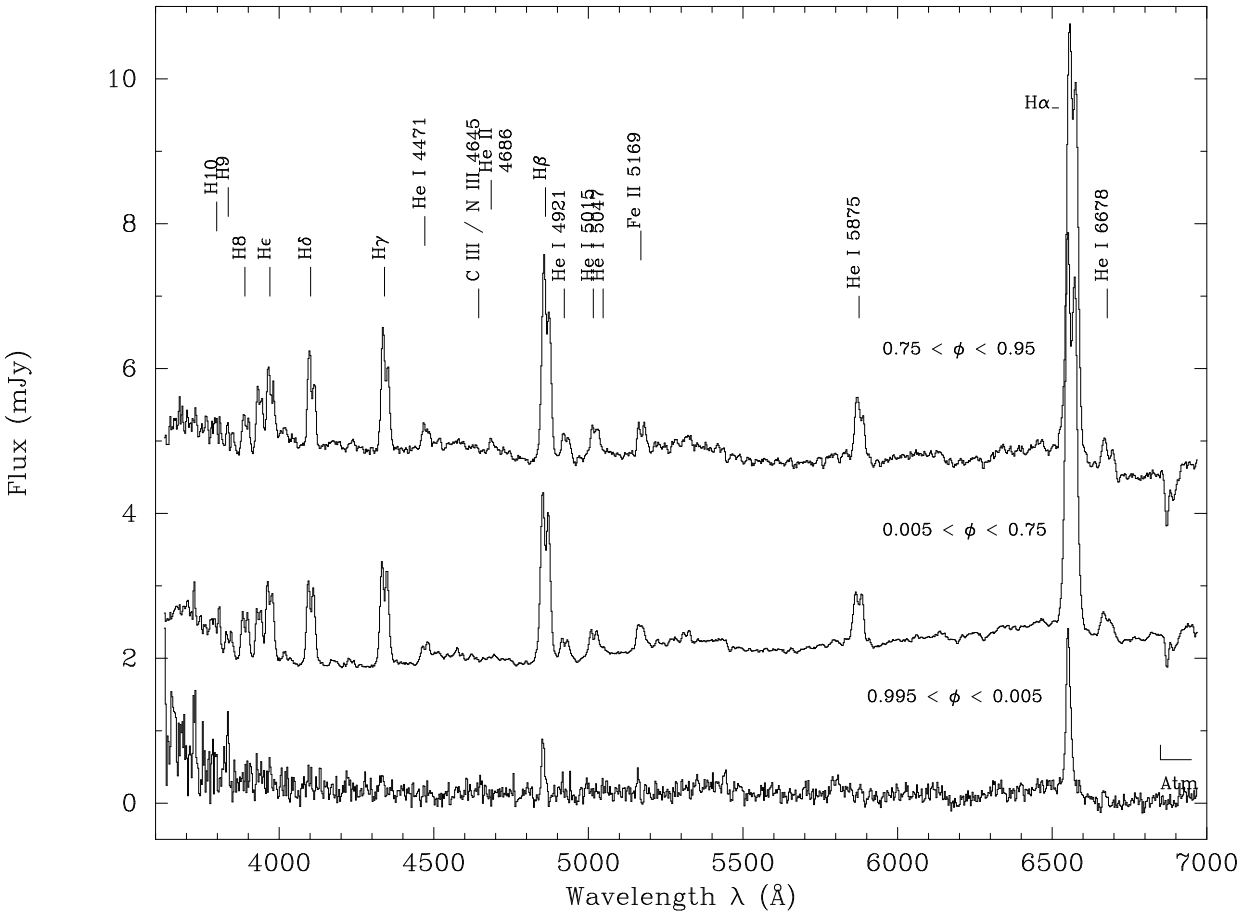

Figure 8.6. The same as Fig. 8.1, but with the contribution of the secondary subtracted

Table 8.2. Overview of system parameters used for IP Peg

M_1	1.09 $M_\odot$
M_2	0.64 $M_\odot$
i	79.3°
P	13669.01224 s
d	150 pc

different wavelengths. We can identify the combined white-dwarf and bright-spot ingress (see Wood et al., 1988) and the white-dwarf egress followed by the bright-spot egress. We can also see an extra 'step' in the lightcurve around phase φ ∼0.23, which will be discussed in Sect. 8.9 We have divided the total wavelength region in 78 bins each 40Å wide, except around the emission lines, which are taken as one wavelength bin. We will use these 78 light curves to reconstruct the brightness distribution and temperature profile of the accretion disk in Sect. 8.10.

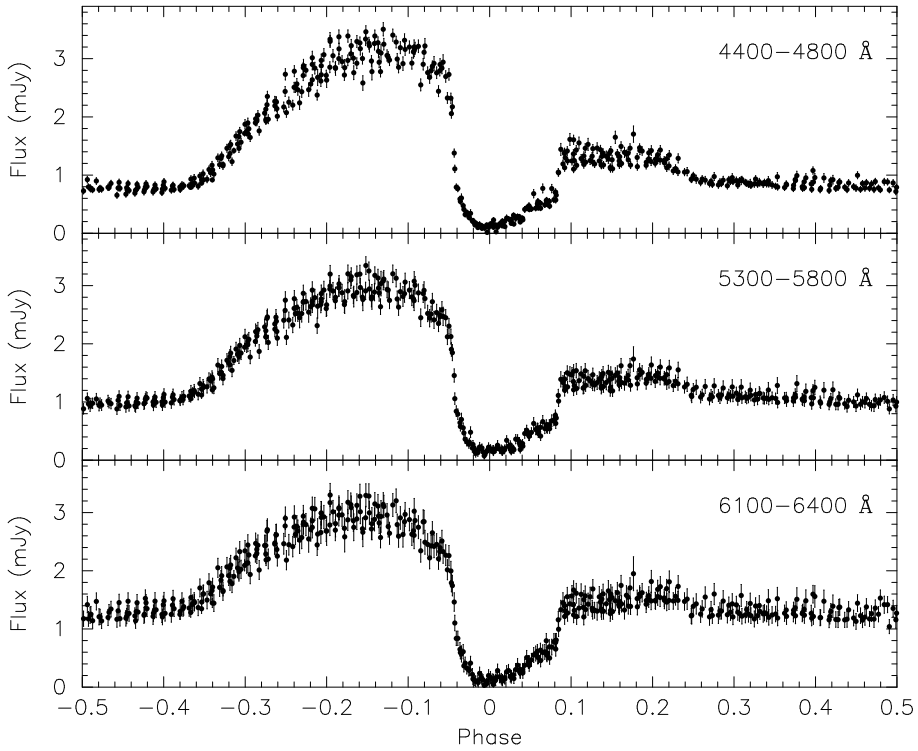

Figure 8.7. Continuum light curves of IP Peg during our observing run in three wavelenth regions: 4400-4800Å (top), 5300-5500 Å (middle) and 6100-6400 Å (bottom). The light curves show the familiar dominance of the orbital hump, peaking at $\varphi \sim 0.85$ and the eclipse caused by the secondary. Also clearly seen is an extra 'step'-like feature at $\varphi \sim 0.23$, which indicated the disappearance from view of the bright-spot region.

8.8 Faint bright spot emission lines

The spectral region between $\lambda\lambda$ 4400-4800 Å appears to contain a number of weak emission lines (see Fig. 8.1). In Figure 8.8 we show the trailed spectrum of this spectral region, normalised by making a linear fit to the regions of $\lambda\lambda$ 4400-4440 Å and 4780-4800 Å. Fig. 8.8 shows that the features in this region are indeed weak emission lines, since throughout the whole spectral region the effect of the eclipse of the lines is clearly seen.
We also see that the HeII λ4686 line is in single-peaked emission during part of the orbit. An arclet is visible, appearing around $\varphi \sim 0.6$ and reaching maximum strength around $\varphi \sim 0.85$. It is eclipsed and re-appears red shifted and is visible until $\varphi \sim 0.25$. After this phase the feature completely disappears for half an orbit. The phasing and radial velocity dependence of the HeII λ4686 line indicate that it originates in the bright spot and is as such reminiscent of the formation of HeII λ4686 in the nova-like SW Sex stars (Groot, Rutten and Van Paradijs, 2000).

Puzzling is the appearance of two weak, single-peaked emission lines in the other emis-

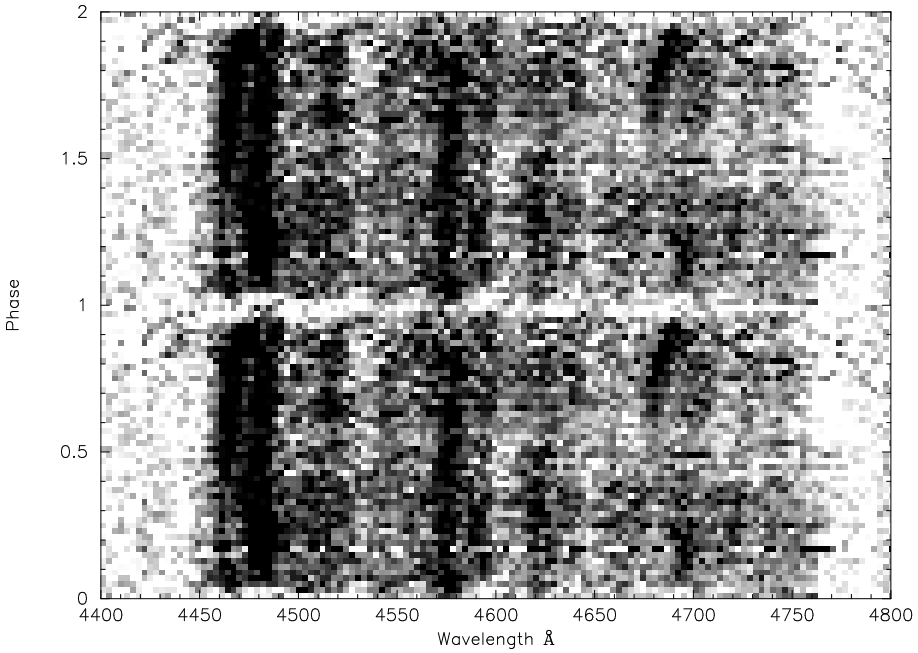

Figure 8.8. The trailed spectrum of the emission line region between $\lambda\lambda$4400-4800 Å. Note that the emission line arc of HeII λ4686 is clearly seen.

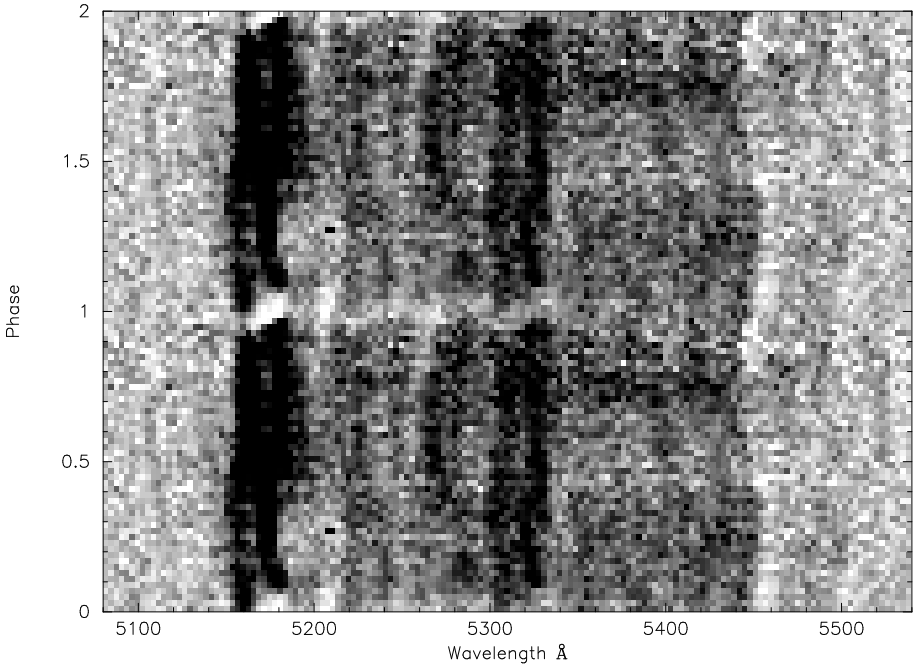

Figure 8.9. The trailed spectrum of the emission line region between 5100-5500 Å. Well visible are the double peaked FeII $\lambda\lambda$ 5169, 5316 Å lines, the secondary TiO-band at λ5450 Åand the unknown line with the phasing of the bright spot at $\lambda \sim$5280Å.

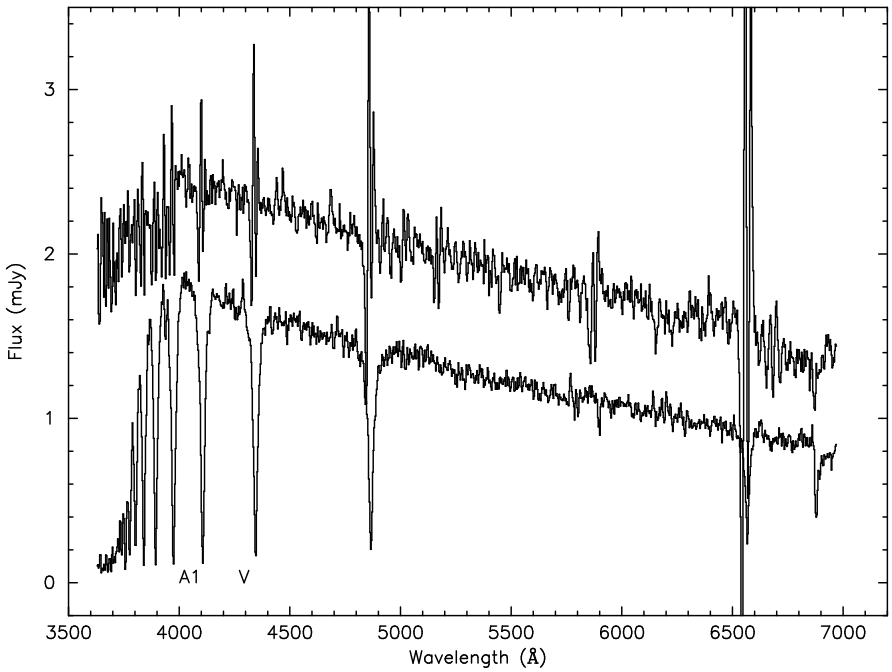

Figure 8.10. The spectrum of the bright spot, reconstructed by subtracting the spectrum when the bright spot is not visible (at φ=0.35) from that at maximum visibility of the bright spot (φ=0.85) (top spectrum), and compared with a A1V spectrum (bottom spectrum).

sion line complex region at $\lambda\lambda$ 5100-5400 Å. In Fig. 8.9 we show a trailed spectrogram of this region. The two main features, at 5169 Å and 5316 Å are both FeII lines. The two single peaked emission lines appear at $\sim$5280Å and $\sim$5230Å, the first being the stronger one. The two lines are visible during almost the complete orbit, show an eclipse and have the same phasing as the HeII λ4686 line, which identifies them as also coming from the bright-spot region. However, since they are visible during the entire orbit without a clear increase in strength near φ=0.85, as the HeII λ4686 line does, this identifies them as originating above or below the bright-spot region, out of the orbital plane. Their identification is unclear. If we assume that they come from the same ions, then only FeI and FeIII have lines at the appropriate wavelengths. All other commonly encountered ions in CV accretion disks (HeI, II, CIII/IV, NIII/IV, FeII) do not have a pair of lines at these wavelengths. Since the accretion disk is already energetic enough to ionize Fe once and the formation site is associated with the bright spot, we consider the FeIII lines more likely than the FeI lines. Higher spectral resolution observations will be needed to securely identify these lines.

8.9 The Bright Spot

We have seen in Fig. 8.7 that the bright spot at its maximum (around φ ∼0.85) is almost twice as bright as the rest of the disk. We can reconstruct the spectrum of the bright spot by subtracting the spectrum at a phase when the bright spot is not visible (say, φ=0.35) from that of the spectrum at maximum visibility of the bright spot (at φ=0.85), as shown in Fig. 8.10. We determine the temperature of this spectrum by comparing its spectral slope with stellar spectra, taken from the catalogue of Jacoby and Hunter (1984). In Fig. 8.10 we show the spectrum of an A1 V star which fits the continuum distribution of the bright spot spectrum best. We see that the Balmer jump (blueward of 4000Å) is much weaker in the bright spot spectrum than in the A1 V spectrum. Part of this is caused by the lower expected gravities in the bright spot region of the accretion disk ($g_{\rm bs}$ ∼$0.1 g_{\odot}$) as was pointed out by Marsh (1988), but the Balmer jump will also be partly filled in by the forest of emission lines in this region, because we see in Fig. 8.1 that the Balmer jump is in emission for the *total* accretion disk. An A1 spectral type corresponds to an effective temperature of ∼9600 K for the bright spot region.
Analogous to Marsh (1988), we now derive the surface area, A, needed at the bright-spot maximum to produce the observed flux of ∼2.3 mJy at 4500 Å with a temperature of 9600 K. Assuming a spot with an isotropic blackbody emission from one side only, we can write the surface area that is needed to produce the observed flux f_ν as:

$$A = \frac{f_\nu d^2}{B_{\nu,T} \sin i}, \tag{8.3}$$

with d the distance to the source, i the inclination and $B_{\nu,T}$ the Planck function at temperature T and frequency ν. This is the same equation as given by Marsh (1988), but in a more basic form. Using the values given above (f_ν = 2.3 mJy at 4500 Å, d=150pc, i=79.3 and T = 9600 K), we derive a surface area of (3.0±0.5)×10^{19} cm^2.
This surface area is consistent with the result derived by Marsh (1988, who found 2.4×10^{19} cm^2). The intensity of the bright spot is slightly lower in our observations (2.3 mJy vs 3.0 mJy), but the derived temperature is also slightly lower (9 600 K vs. 11 200 K). We therefore conclude that the bright spot is of equal size in the two epochs, but slightly cooler in our observations.

8.9.1 The azimuthal extent of the bright spot

We have seen in Sect. 8.7 and Fig. 8.7 that an extra transition in the light curve occurs around φ ∼0.23. If we attribute this extra transition to the bright spot disappearing from view, we can deduce the azimuthal extent of the bright spot on the rim of the disk. As shown in Fig. 8.11 φ=–0.37 is the phase when the bright spot first comes into view and φ=0.26 is the phase when it last disappears from view. Taking these phases and assuming that the bright spot is symmetric, the phase of maximum visibility of the hot spot, in the

absence of the eclipse, would occur at φ=–0.055. The fact that we see the maximum of the orbital hump at φ=–0.15 is caused by the shallow increase of a sinusoidal bright spot light curve around this phase, combined with the eclipse of the outer accretion disk, which sets in around phase φ=–0.12.
The total phase angle over which we see the bright spot is $\Delta\varphi$=0.63, which is obviously larger than half the orbit one would expect for a point source located on the rim. Combined with the phase of maximum visibility for the bright spot, we can calculate from this that the bright spot must extend an azimuthal angle from φ=–0.12 to φ=0.01 over a total angle of $\Delta\varphi_{\rm spot}$ = 0.13 in phase (47°).

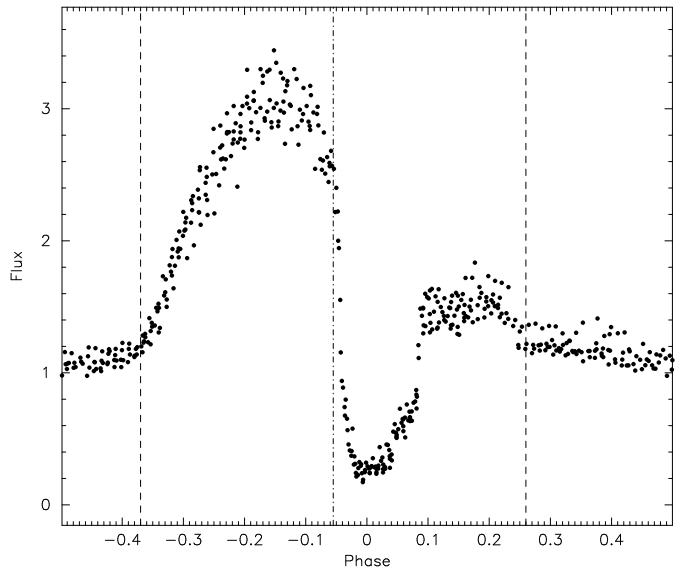

Figure 8.11. The light curve of IP Peg between 5300Åand 5800Å. The two dashed lines show the first and last phase of the bright spot visibility at φ=–0.37 and φ=0.26.

8.9.2 Vertical extent of the bright spot

With the azimuthal extent of the bright spot and the surface area calculated in Sect. 8.9 we can now derive the vertical extent of the bright spot. As we will show in Sec. 8.10 the phasing of the bright spot ingress and egress locates it at a distance of R_d = 0.5R$_{\rm L_1}$ from the white dwarf. If we, for the moment, assume that the disk rim is like a flat ribbon tied around the disk (as in e.g. a bow-tie shaped disk), then the surface of the disk rim, $A_{\rm spot}$, in the phase interval $\Delta\varphi_{\rm spot}$ is simply:

$$A_{\rm spot} = \Delta\varphi_{\rm spot}\, h_{\rm spot}\, R_d, \tag{8.4}$$

as seen in the plane of the orbit (note that we have already corrected for the inclination in the derivation of the surface area), and with $h_{\rm spot}$ the full height of the disk.

However, the projected surface area, $A_{\rm proj}$, as we see it radiating towards us (in the plane of the orbit) is slightly smaller and equal to:

$$A_{\rm proj} = 2\,R_d\,\sin(\frac{\Delta\varphi_{\rm spot}}{2})\,h_{\rm spot} \tag{8.5}$$

Using this last equation, the disk radius R_d=0.5 R_{L_1}, the system parameters as given in Table 8.2 and the surface area calculated in Sect. 8.9, we derive a full vertical extension of the disk at the bright spot of $h_{\rm spot}$ = 1.32$\times 10^9$ cm. Combined with the disk radius (0.5 R_{L_1}, or 2.85$\times 10^{10}$ cm), this gives an opening angle of the disk of 1°.33. This shows that the flare angle of the accretion disk is very moderate, even at the bright spot where we expect the accretion disk to have a maximum flare angle.

8.10 3-D Eclipse mapping

With the results derived above for the azimuthal extent and height of the bright spot we can reconstruct the brightness distribution on the disk using the technique of 3-D eclipse mapping (Rutten 1998). This is a recent extension of the 2-D eclipse mapping (Horne, 1985). One of the important assumptions in standard 2-D eclipse mapping is that the light curve is constant outside the eclipse. We have seen that this does not hold for IP Peg, and more general, for most dwarf novae. One method to still be able to use the 2-D eclipse mapping technique is to decompose the light curve in three components; the white dwarf, the bright spot and the accretion disk light curves, as has been done for Z Cha by Wood et al (1986). However, this method is only applicable to high signal-to-noise data of systems where the ingress and egress features of the white dwarf and the bright spot are well seperated. Because the white-dwarf and bright-spot ingress in IP Peg are coincident, such a decomposition is not applicable to IP Peg.

Rutten (1998) has extended the convential 2-D eclipse mapping to three dimensions. In this method the information in the total lightcurve is used to map the light distribution on both the accretion disk as well as the secondary star. When desired, one of the components can be switched off and the light distribution is reconstructed on the remaining one only. The advantage of using all the information in the light curve and the wider applicability is balanced by the need to supply a pre-defined three dimensional grid geometry to map the light distribution on to. This increases the number of degrees of freedom enormously, since any arbitrary shape is possible. A careful analysis of the choice of geometry is therefore warrented.

We have chosen to use this experimental technique on our current dataset of IP Peg for the following reasons. First, the eclipse shape and the unfortunate coincidence of white-dwarf and bright-spot ingress force us to deal with the light curve in a three dimensional way. Second, the current dataset of IP Peg covers all phases of the orbit and not only the eclipse with relatively high time resolution, which renders the data suitable for 3-D eclipse

mapping, and the system was stable over the observing period (no offsets or scalings have been applied to the lightcurves in Fig. 8.7). Third, in Sect. 8.9 we have been able to derive rather tight constraints on the geometry of the bright-spot region. These constraints can be effectively used in the 3-D eclipse mapping technique to limit the number of possible geometries for the accretion disk.

8.10.1 Accretion disk geometry

In the 3-D eclipse mapping program as developed and described by Rutten (1998), a square tile geometry is used to define the disk shape. Each tile is divided in 4 triangular shaped subtiles, each of which can be given a certain height above the disk. All tiles radiate isotropically and foreshortening factors are taken into account. Currently, no limb darkening is taken into account. The visibility of each tile is calculated for each phase and the sum of the contributions of all tiles as a function of phase produces the light curve. The intensities of all tiles is then adjusted so that the resulting light curve mimics the data to a reduced χ^2 of unity. Maximum entropy is then used to obtain the smoothest solution, analogous to the 2-D eclipse mapping method (Horne, 1985).

To test the technique of 3-D eclipse mapping on IP Peg we have choosen the system parameters as listed in Table 8.2. To decrease the degrees of freedom only the accretion disk was mapped, and we have therefore used the light curves that were already corrected for the contribution of the secondary star as described in Sect. 8.4.

We have derived in Sect. 8.9.2 that the opening angle of the disk is 1-2° at the bright spot. For 3-D eclipse mapping it is nessecary to define a geometry of the disk. This geometry is constrained by the duration of the eclipse, which constrains the disk radius, and the flaring angle derived in Sect. 8.9.2. The two simplest 3-D geometries that satisfy both these constraints are *i)* an axisymmetric pillbox shaped disk, and *ii)* a linearly flaring axisymmetric disk (a bow-tie). Since accretion disk theory predicts that the height of the accretion disk increases with radius from the white dwarf, we choose to use the bow-tie disk for our 3-D eclipse mapping.

The flare angle was set to 2° . This is somewhat larger than the flare angle derived in Sect. 8.9.2, but there we assumed that the disk rim had no radial extent (i.e. a sharp drop). In any realistic accretion disk this will not be the case, and to correct for the loss in projected surface area we have slightly increased the flare angle. Variation of the disk radius showed that a disk with a total size of $0.53R_{L_1}$ gave the best fits to the width of the eclipse. With the specific description of disk height that we have used, this means that maximum height of the disk is reached at $0.5R_{L_1}$, after which the disk height drops to zero at $0.53R_{L_1}$. In the subsequent analysis we have therefore used a disk radius of $0.53R_{L_1}$ and a flare angle of 2° . Together these define the 3-D geometry. In Fig. 8.12 we show the disk geometry as we have used it.

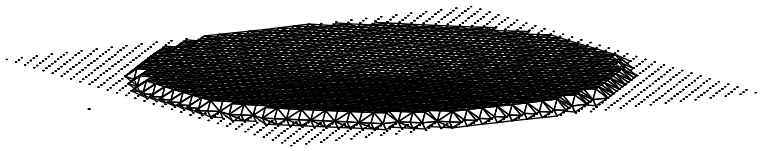

Figure 8.12. The geometry of a axisymmetric linearly flaring disk, with a flaring angle of 2° , seen under an inclination of 79.3° and at $\varphi \sim 0.84$.

8.11 Spectral eclipse mapping

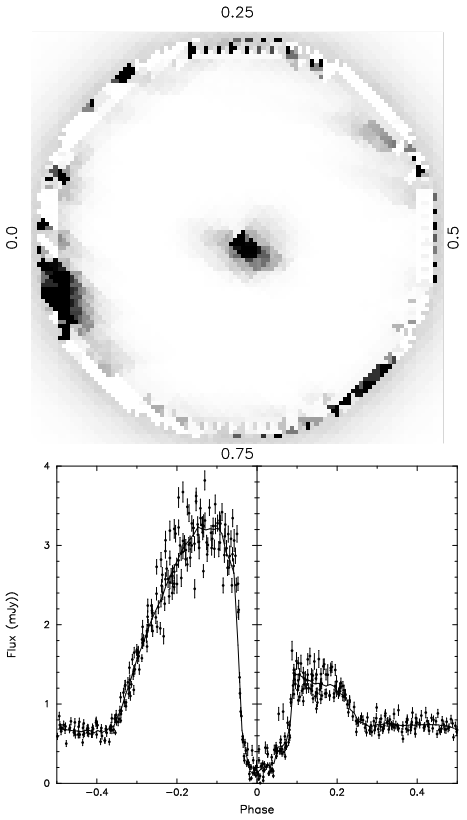

Figure 8.13. The reconstructed accretion disk map in the wavelength region between 4180-4220Å (top) and the corresponding light curve (bottom).

8.11.1 Narrow-band light curves

For the spectral eclipse mapping we have divided the total wavelength range (from 3600Å –7000Å) in 78 narrow band wavelength bins, each 40Å wide, except around the major emission lines, which are taken as one bin each. For the eclipse mapping procedure we have used the disk geometry as outlined above and the system parameters as given in Table. 8.2. A 31×31 tile geometry and a phase resolution of 0.005 in phase were used

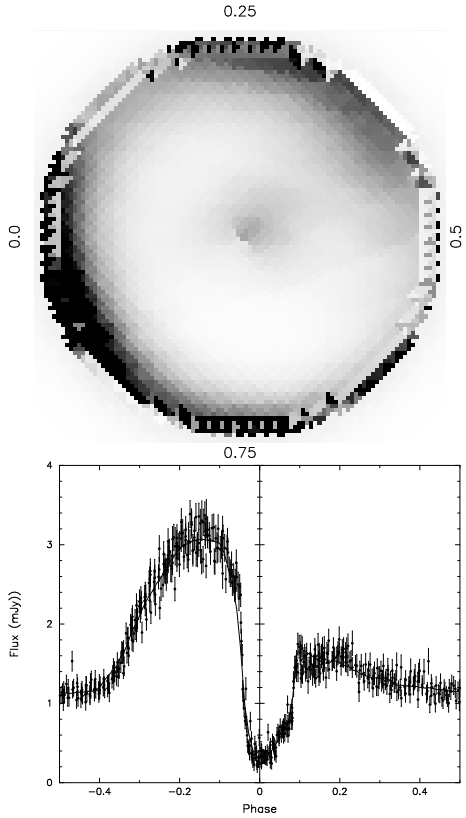

Figure 8.14. The reconstructed accretion disk map in the wavelength region between 5770-5810Å (top) and the corresponding light curve (bottom).

in all the reconstructions. This choice is a balance between spatial (less tiles gives a 'blocky' disk that influences the reconstruction) and temporal (a larger phase binning did not reconstruct the sharp bright spot ingress and egress) resolution, and computing time.

In Fig. 8.13 we show the narrow band light curve of IP Peg in the wavelength interval of 4180–4220Å, and the 3D eclipse mapping reconstruction. We see that the major features of the light curve (the orbital hump, the eclipse and the step at φ $\sim$0.23) are all well reconstructed. The top rim has been folded outwards and surrounds the top surface in Fig. 8.13. In Fig. 8.13 the secondary is located to the left of the figure.

Figs. 8.14 and 8.15 show the reconstructed light curve, using the same geometry, at 5790Åand at 6880Å. We see that in both cases the ligth curves are well reconstructed, although for the long wavelength end, some problems arise in the reconstruction of the bright-spot egress.

From Fig. 8.13, 8.14 and 8.15 we see that the bright-spot maximum is reconstructed at an azimuth angle of ϕ=160° (where 180° points towards the L_1-point). If no secondary were present we would therefore see the maximum of the bright spot at φ=–0.055, exactly at the phase where we decuded that the bright-spot maximum would have to be if the egress

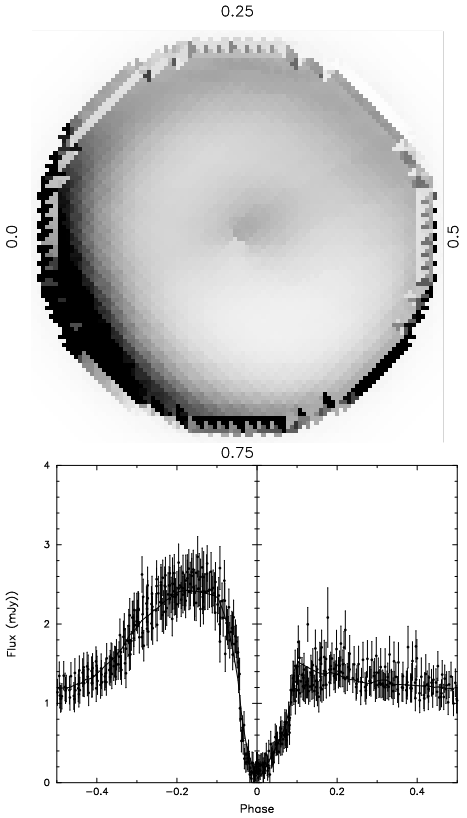

Figure 8.15. The reconstructed accretion disk map in the wavelength region between 6860-6900Å (top) and the corresponding light curve (bottom).

shoulder on the light curve were due to residual emission from the bright spot. Note that the bright spot appears to have a larger azimuthal extent in Fig. 8.14 and Fig. 8.15 with respect to Fig. 8.13 mainly because of a decrease in contrast between the bright spot and the rest of the disk.
The rest of the disk is smooth and shows no strong azimuthal structure. The light stored in the regions outside the accretion disk rim is caused by non-eclipsed light. The current version of the 3-D eclipse mapping program does not included an offset pixel when only the disk is mapped.

8.11.2 Accretion disk spectra

Using the light curves at all wavelengths we can now reconstruct the accretion disk spectrum at an arbitrary point on the disk. Since we are mainly interested in the radial structure of the disk, we have divided the accretion disk in six regions, shown in Fig. 8.16, consisting of concentric annuli around the white dwarf. The outermost annulus is divided in two azimuthal regions; one around the bright spot and the other encompassing the rest of the

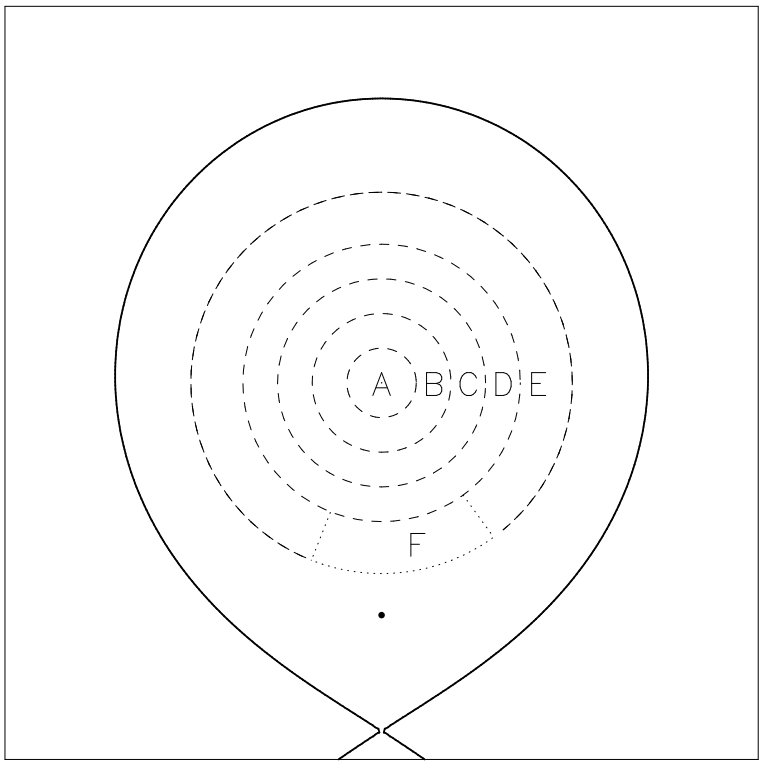

Figure 8.16. The white dwarf Roche lobe in IP Peg and the six regions in which the disk (extending to $0.53R_{L_1}$) has been divided; region A: 0-$0.1R_{L_1}$, region B: 0.1-$0.2R_{L_1}$, region C: 0.2-0.3 R_{L_1}, region D: 0.3-$0.45R_{L_1}$, region E: 0.45-0.55 R_{L_1}, not including the bright spot and region F: 0.45-0.55 R_{L_1}, around the bright spot.

accretion disk rim. In Fig. 8.17 we show the spectra in these regions.
We can see from Fig. 8.17 that the continuum slope changes from blue to red when going from inside to outside. The bright spot is the dominant source of radiation and has a spectrum that is very blue. Comparing the bright-spot spectrum as derived here and as derived in Sect. 8.9, we see that the two slopes agree very well. The bright-spot spectrum does not show any emission lines, which is consistent with the spectrum in Sect. 8.9 and also with the fact that the double-peaked profile of the main emission lines indicate that they are formed over the entire accretion disk, which is also seen in the other annuli that all show the Balmer and HeI lines in emission.

8.11.3 TiO bands in the outer accretion disk spectrum

We can also see in Fig. 8.17 that the outer most ring, excluding the bright-spot region, shows not only a red spectrum, but also features that are easily identified as those of the TiO bands as seen in M-dwarfs. Since the narrow-band light curves, that form the basis

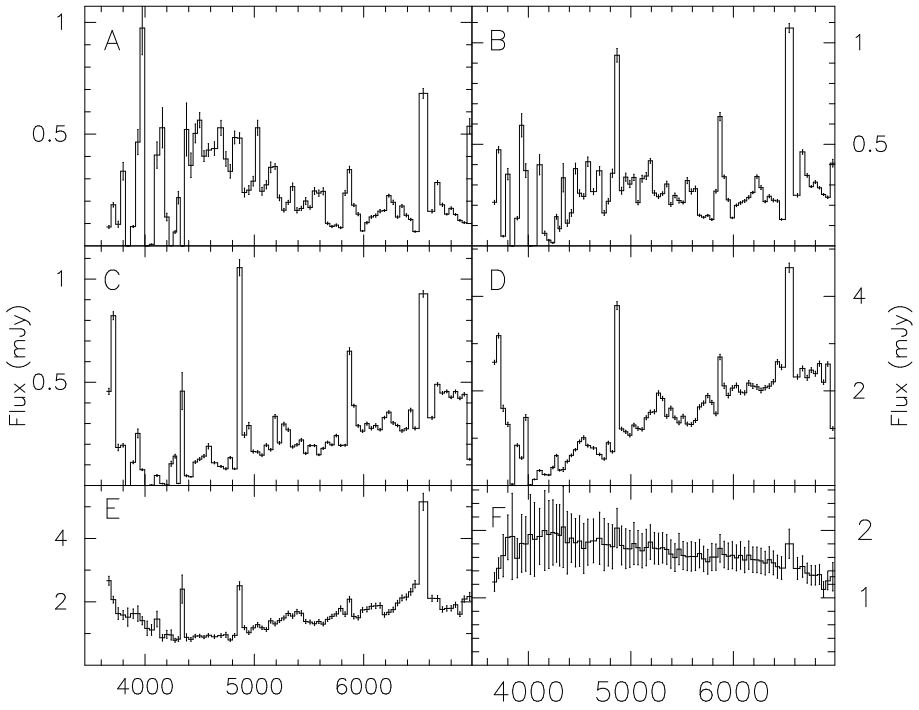

Figure 8.17. The spectrum of the accretion disk in the regions defined in Fig. 8.16. Fluxes are integrated over the region under consideration. Error bars are derived from the scatter on the individual tiles in a selected region.

for the 3D eclipse mapping, have been derived from spectra that were already corrected for the presence of the secondary star, this suggests that the observed spectral features are intrinsic to the disk. Apparently the outer parts of the accretion disk of IP Peg in quiescence are cold enough for molecules to form. In an effort to further quantify the physical conditions in the disk we have reconstructed the spectrum of the accretion disk in a pie-point shaped region located between azimuth angles of $270< \phi <360$, where ϕ=180 points towards the L_1-point. This azimuth interval has been chosen to be 'away' from the bright-spot region, where local heating clearly disrupts the temperature profile of the outer disk.

In Fig. 8.18 we show the spectrum in this pie-point shaped region in the radial region of $0.45R_{L_1} < r < 0.5R_{L_1}$, which is on the inside of the disk and has no rim included and in the radial region $0.5R_{L_1} < r < 0.53R_{L_1}$, which is the outward facing disk rim. Comparing the disk spectrum in Fig. 8.18 with the standard star spectra in Fig. 8.2 we see that the outer disk spectrum is of a late-M spectral type. Especially the TiO band at 5500Å becomes only apparent at a spectral type later than M4.

The disk rim spectrum as shown in the bottom panel of Fig. 8.18 is much bluer than the spectrum just inside the disk rim. This can be the effect of tidal forces which are expected

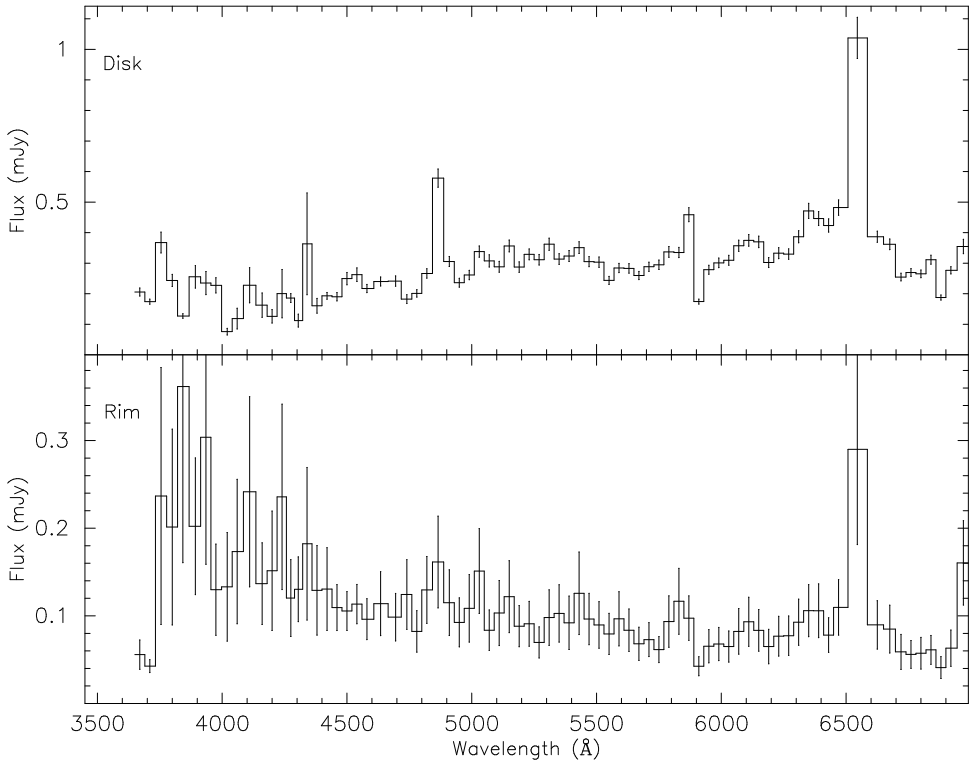

Figure 8.18. The reconstructed accretion disk spectrum in the azimuth range of 270$< \phi <$360 and radial range 0.45$< r <$0.5 (top) and the rim spectrum (0.5$< r <$0.53) in the same azimuth range (bottom).

to dissipate heat at the disk edge, although the disk in our situation is rather small for tidal heating to be very strong. Another possibility is that, if the disk has a vertical temperature profile that decreases from the mid-plane outwards, we are looking at a higher mid-plane temperature, because we effectively look at a cross-cut through the disk.

A legitimate question, that cannot be satisfactorily answered at this point, is, whether the detected accretion disk M-type spectral features are due to a residual from a non-perfect subtraction of the secondary M-dwarf spectrum. We have seen in Fig. 8.3 that there is a discrepancy between the secondary continuum and the strength of its lines. The chosen secondary spectral type (M3V) optimizes the continuum of the secondary but leaves some residual spectral features. However, comparing Fig. 8.3 and Fig. 8.18 we see that the TiO band at 5500 is effectively removed in the secondary star subtraction, and there should therefore be no reason why it should show up in the accretion disk spectrum. Furthermore, we see in Fig. 8.18 that not only the TiO bands resemble a late type spectrum, but also the continuum slope. If the spectral features are solely due to an imperfect secondary star subtraction, we would not expect the continuum slope to match the spectral features observed. We therefore conclude that the TiO band features and continuum slope of the

outer accretion disk are most likely originating in the accretion disk itself and are therefore evidence for a very cool outer disk.

Acknowledgements
PJG is supported by Spinoza grant 08-0 to E.P.J. van den Heuvel. The Isaac Newton Telescope is part of the Isaac Newton Group of Telescopes operated on the island of La Palma by the Instítuto de Astrofísica de Canarias on behalf of de British PPARC and the Dutch NWO.

References

Bobinger, A., Horne, K., Mantel, K.-H., Wolf, S., 1997, A&A 327, 1023

Bobinger, A., Barwig, H., Fiedler, H., Mantel, K.H, Simic, D. and Wolf, S., 1999, A&A 348, 145

Davey, S. and Smith, R.C., 1992, MNRAS 257, 476

Frank, J., King, A.R. and Raine, D., 1992, *Accretion power in Astrophysics*, Cambridge Astrophysics Series 21, CUP Cambridge, UK

Goranskij, V.P., Shugarov, S.Yu., Orlowski, E.I and Rahimov, V.Yu., 1985, *Inf. Bull. Var. Stars*, No 2653

Groot, P.J., 1999, PhD Thesis, University of Amsterdam

Groot, P.J., Rutten, R.G.M. and Van Paradijs, J., 2000a, A&A, *submitted* (Chapter 6).

Groot, P.J., Rutten, R.G.M. and Van Paradijs, J., 2000b, A&A, *submitted* (Chapter 7).

Horne, K., 1985, MNRAS 213, 129

Horne, K., 1986, PASP 98, 609

Horne, K., Marsh, T.R., 1986, MNRAS 218,761

Marsh, T., 1988, MNRAS 231, 1117

Martin, J.S., Jones, D.H.P., Friend, M.T. and Smith, R.C., 1989, MNRAS 240, 519

Oke, J.B., 1990, AJ 99, 1621

Pickles, A.J., 1985, ApJS 59, 33

Rutten, R.G.M., 1998, A&AS, 127, 581

Szkody, P. and Mateo, M., 1986, AJ 92, 483

Smak, J., 1969, Acta Astr 19, 155

Smak, J., 1981, Acta Astr 31, 395

Steeghs, D., Horne, K, Marsh, T.R. and Donati, J.F., 1996, MNRAS 281, 626

Steeghs, D., Harlaftis, E.T. and Horne, K., 1996, MNRAS 290, 28

Wade, R.A. and Horne, K., 1988, APJ 324, 411

Warner, B., 1995, *Cataclysmic Variable Stars*, Cambridge Astrophysics Series 28, CUP, Cambridge, UK

Wolf, S., et al., 1993, A&A 273, 160

Wolf, S., Barwig, H., Bobinger, A., Mantel, K.H. and Simic, D., 1998, A&A 332, 984
Wood, J.H., et al., 1986, MNRAS 219, 629
Wood, J.H. and Crawford C.S., 1986, MNRAS 222, 645
Wood, J.H., Horne, K., Berriman, G and Wade, R.A., 1989, ApJ 341, 974

Part III

The Faint Sky Variability Survey

9

The Faint Sky Variability Survey[1]

P.J. Groot, P.M. Vreeswijk, M. Everett, S.B. Howell, J. van Paradijs, D. Davis, H. Scholl, M. Huber, T. Augusteijn, H. Böhnhardt, P.A. Charles, T.J. Galama, E. Kuulkers, C. Kouveliotou, C. Moreno, G. Nelemans, R. Rebolo, R.G.M. Rutten, J. Storm, N. Tanvir, L.B.F.M. Waters, R.A.M.J. Wijers

To be submitted to the Monthly Notices of the Royal Astronomical Society

The Faint Sky Variability Survey aims at finding variable objects in the brightness range between 17th and 24th magnitude on time scales between tens of minutes and years with precisions ranging from 5 millimagnitudes for the brightest to 0.15 magnitudes for the faintest objects. An area of at least 50 square degrees will be covered using the Wide Field Camera on the 2.5m Isaac Newton Telescope on the island of La Palma. The survey has started in November 1998. Here we describe the main goals of this Survey, the methods used in extracting the relevant information and the future prospects of the survey.

9.1 Introduction

The advance of large format ($>$2k$\times$2k) CCDs with high quantum efficiency has opened up a new area in Galactic and extragalactic astrophysics: the systematic study of astrophysical objects fainter than 20th magnitude. The importance of this brightness regime is nicely illustrated by the current, fast development in the field of γ-ray bursts (GRBs; for recent reviews see Katz, Piran and Sari, 1998; Piran, 1999; and Van Paradijs, Kouveliotou and Wijers, 2000), where the localization of faint variable optical counterparts has led to a large increase in our understanding of the aftermaths of a GRB.

[1]Based on observations with the 2.5m Isaac Newton Telescope at La Palma and part of the INT Wide Field Survey

With the installation of the Wide Field Camera (WFC, see Sect. 9.3) at the 2.5m Isaac Newton Telescope a seperate call for proposals resulted in the INT Wide Field Survey, consisting of three main projects; the INT Wide Angle Survey (McMahon et al., 1999), A Deep UBVRI Imagaing Survey with the INT WFC (Dalton et al., 1999), both aimed at extragalactic research and the Faint Sky Variability Survey (FSVS), described here. The FSVS aims at finding variable objects in the brightness range between 17th and 24th magnitude on time scales between tens of minutes and years. In the following sections we will outline the main goals of the survey (Sect. 9.2), the INT Wide Field Camera (Sect. 9.3), the observing strategy (Sect. 9.4) and field selection (Sect. 9.5). After a short comparison with other, running surveys (Sect. 9.6), we will discuss the data reduction (Sect. 9.7), the final data products (Sec. 9.8), the availability of the data (Sect. 9.9) and a short overview of the current status of the survey (Sect. 9.10). An overview of the first year's results (Everett et al., 1999; hereafter Paper II) and a first report on our search for GRB afterglows without a corresponding GRB (Vreeswijk et al., 1999) in the first year of observations will be given in additional papers.

9.2 Goals of the FSVS

Understanding the variability of stars has often been crucial in the development of astrophysics, with applications ranging from the evolution of stars, to the structure of our Galaxy and the distance scale of the Universe. Variability studies are currently mainly restricted to either bright regimes (brighter than 20th magnitude) or very small areas (e.g. supernovae and GRB searches). In the galactic realm, a deep variability study will not only reveal the characteristics of specific groups of stellar objects, but will also shed light on the outer parts of our Solar System, the direct Solar Neighbourhood, the structure of our Galaxy, and the extent of the Galactic Halo. The FSVS is aimed at observing at least 50 square degrees ($50^{\square}$) down to 25th magnitude. The main targets can be divided in two broad areas of interest: photometrically variable objects and astrometrically variable objects.

9.2.1 Photometrically variable objects

From the large variety of variable stars we here limit ourselves to a few obvious examples.
• **Close Binaries**: Current detections of low-mass close-binary systems (i.e. Cataclysmic Variables, Low-Mass X-ray Binaries, Soft X-ray Transients and AM CVn stars) are strongly biased to small subsets of their populations. Of these systems the Cataclysmic Variables (CVs) form the main subgroup we expect to find. Currently, most CVs are either found as by-products of extragalactic studies such as quasar surveys (e.g. the Palomar-Green survey, Green, Schmidt and Liebert, 1986; the Hamburg/ESO Quasar Survey, Engels et al., 1994; Wisotzki et al., 1996; and the Edingburgh-Cape Survey, Stobie et al., 1988),

or by their outbursts in which the system brightens 3-10 magnitudes due to an disk instability. However, theoretical calculations show that the majority of the CV population has evolved down to mass-transfer rates that are lower than $\sim 10^{-11}$ $M_{\odot}$ yr^{-1} (See e.g. Howell, Rappaport and Politano 1996, Kolb 1993). At these very low-mass transfer rates CVs are expected to be faint (typically V>20), lack a UV-excess, and show outbursts only on time scales of years to decades, and will therefore not show up in conventional searches. However, all CVs show intrinsic variability of the order of tenths of magnitudes or more. This variability is either caused by 'flickering' (mass-transfer instabilities), orbital modulations (hot-spots or eclipses) or long-term mass-transfer fluctuations. Searching for faint variable stars is therefore the best way to disclose the characteristics of the majority of the CV population. This will not only lead to a better understanding of the evolutionary history of CVs, but will also give the possibility of studying accretion disks that are formed in a very-low mass-transfer rate environment. We refer to Warner (1995) for an excellent review of CV properties.

• **RR Lyrae stars:** Due to their standard candle properties and easy recognition by their colour and variability, RR Lyrae stars can be used as excellent tracers of the structure of the galactic halo. A few of these stars have been found at large galactocentric distances (Hawkins, 1984; Ciardullo et al., 1989), but statistics are still poor. Increasing the number of RR Lyraes will enable a more detailed study of the formation history and structure of the outer galactic halo, and by follow-up radial velocity studies to construct a relation between enclosed mass and distance for the Galaxy, which will give insight in the distribution of dark matter around the Galaxy.

• **Optical Transients to Gamma-Ray Bursts** The discovery of optical counterparts to γ-ray bursts (GRBs, e.g. Van Paradijs et al., 1997), and the subsequent findings that GRBs originate at cosmological distances (e.g. Metzger et al., 1997, Kulkarni et al., 1998) have shown that GRBs are among the most energetic phenomena known in the Universe. The high energies implied by observations of GRB afterglows (10^{53-54} erg in γ-rays if isotropy is assumed, Kulkarni et al., 1998; 1999), raises the question whether GRBs are emitting their energy isotropically or in the form of jets. In the latter case the energies involved will be much lower, depending on the amount of beaming. Since the Lorentz factor of the fireball that causes the GRB decreases with time one expects the beaming of the later optical afterglow to be less severe than that of the GRB itself. It is therefore to be expected that GRBs will be missed (observer outside the beam), that will be detectable by their optical afterglows. The statistics on the detections (or non-detections) of such optical transient events will constrain the beaming angles of GRBs. A more thorough discussion and an analysis of the results of the first year of the FSVS will be presented in Vreeswijk et al. (1999).

9.2.2 Astrometrically variable objects

The observing schedule that we have adopted for the FSVS (see Sect. 9.4) also allows for the detection of astrometrically variable objects. These fall in two main categories:
• **Kuiper Belt Objects**: Kuiper Belt Objects (KBOs) are icy bodies revolving around the Sun in orbits that lie outside the orbit of Neptune (which has led to the alternative name of Trans Neptunian Objects; TNOs). Since their discovery in 1993 (Jewitt and Luu, 1993), more than 100 of these objects have been found. Studying their properties will give important insight in the formation of the Solar system and planetary systems in general.
• **Solar Neighbourhood Objects**: The planned re-observations after one year will allow for the detection of high proper-motion objects in the Solar neighbourhood. The MACHO results show that in their 4-year survey of the Large Magellanic Cloud (Alcock et al., 1997) sixteen microlensing events caused by Massive Compact Halo Objects have been seen. This number is higher than would be expected for a standard Galactic halo population model (Griest 1991). The population of objects causing the microlensing events should also pervade the space in the Solar Neighbourhoud and should in principle be detectable in a deep proper-motion study such as the FSVS. Recent results of the re-observation of the Hubble Deep Field (HDF; Williams, 1996) show a small number of blue, faint objects that move up to 25 mas/yr (Ibata et al., 1999). If these are old white-dwarfs of $\sim$0.5 $M_{\odot}$, they could account for a large fraction of the missing mass of the Galaxy. Although objects like those detected in the HDF are too faint for the FSVS, members of this population that are closer-by and therefore brighter should show up in the FSVS observations.

9.3 The INT Wide Field Camera

The Wide Field Camera[2] (WFC) is mounted at the prime focus of the 2.5m Isaac Newton Telescope (INT) on the island of La Palma. The WFC consists of 4 EEV42 chips, each containing 2k$\times$ 4k pixels. They are fitted in a L-shaped pattern, which makes the Camera 6k$\times$6k, minus a 2k$\times$2k corner (see Fig. 9.1). The chips consist of 13.5μ pixels (0.″33 per pixel on the sky), which gives a sky coverage per chip of 22.′8$\times$11.′4. A total of 0.□29 is covered per exposure. With a typical seeing of 1.″0-1.″3 on the INT, point objects are well-sampled, which allows for accurate photometry. The WFC is equipped with a two filter sets, one consisting of B,V and R Harris glass filters and U and I RGO filters and the other with the Sloan filters (Fukugita, 1996). Zeropoints, defined as the magnitude that gives 1 detected e^{-}/s, of the instrument are 25.6 in B,V and R, 23.7 in U and 25.0 in I.

[2]see: http://www.ast.cam.ac.uk/∼mike/casu/WFCsur/WFCsur.html for an extensive description of the WFC

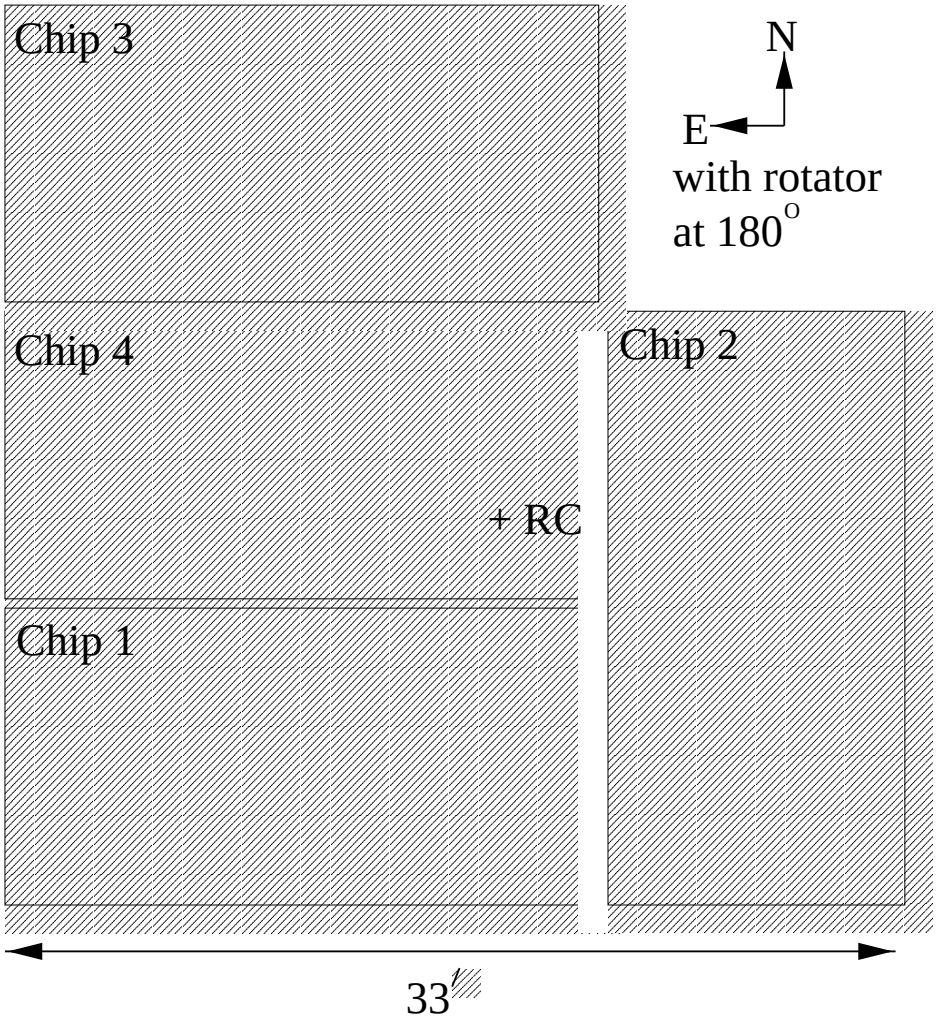

Figure 9.1. The lay-out of the four chips that make up the INT Wide Field Camera. Each chip is 4k×2k, giving a total sky coverage of 0.□29. The rotator center (RC) of the camera is located on Chip 4. An auxiliary autoguider 1k×1K Tek CCD is located on the side below Chip 1 and Chip 2. With a rotator angle of 180° , as was used in our observations, North is up and East to the left.

9.4 Observing strategy

The typical time scales of variability covered by the objects listed above vary from hours (CVs, KBOs, RR Lyraes) to days (OTs) to years (high proper motion stars). To cover all possible time scales of variation we have devised an observing strategy that optimises both the coverage per field as well as the total sky coverage. The variability search is done in the V-band filter. Additionally each field is observed once in B and I to obtain colour information. For the photometric variability we find that at least ten pointings are needed to firmly state that an object is variable and also get an indication of the time scale of its

Table 9.1. The observing schedule shows the sequence of observations for a set of six nights. A total of 18 fields (each 0.27 □) will be covered. The third column shows the observing sequence per night. Observations are grouped in pairs of three to show a 36 min interval. All observations of a set of three fields (e.g. F1F2F3) will be made within a three hours interval (denoted by the comma). F1 means a 10 minute V-band integration of Field 1.

Night	**Fields**	: **Observing sequence**
Night 1	F1-9	: F1F2F3-F1F2F3-F1F2F3-F1F2F3-F1F2F3, F4F5F6-F4F5F6-etc.
Night 2	F10-18	: F10F11F12-F10F11F12-F10F11F12-F10F11F12-F10F11F12, etc.
Night 3	F10-18	: Single BVI exposures + Standards
Night 4	F1-9	: Single BVI exposures + Standards
Night 5	F1-9	: F1F1F1-F1F2F3-F2F2F2-F2F1F3-F3F3F3, F4F4F4-F4F5F6-etc.
Night 6	F10-18	: F10F10F10-F10F11F12-F11F11F11-F11F10F12-F12F12F12,etc.

variability. For the first two years the FSVS has been allocated one week of dark time per semester. Since each observing run consists of six to seven nights of dark time, the ten pointings per field that are required for the variability study, have to be distributed over these nights. One of the criteria for the selection of the fields (see Sect. 9.5) is that they are observable within 30° of the zenith. Per night this gives an effective time-slot of three hours to observe a particular field.

These considerations led us to an observing sequence in which on a given night, a field is observed four times in a row, then with a gap of a few hours once again. On a following night the field is observed only once or twice, then on a third night not at all, on a fourth night four times every 45 minutes and on the fifth night once or twice again. The exact order of observations within the observing period depends on when a photometric night occurs. It is on these nights that the photometric calibration and field observations in B and I are done, along with two observations in V. Integration times are 10 minutes in B and V and 15 minutes in I. Combined with the observing schedule outlined above, this means that per three hour period three different fields can be observed. In a six night run it is possible to observe two sets of fields, that have an intertwining observing schedule (see also Table 9.1). In practice this means that for observations in e.g. November, when nights have 9-10 hours of dark time, we can observe 2 (sets of fields)$\times$3 (observing slots per night)$\times$3 (fields within one slot) = 18 fields in total. As described in Paper II, in November 1998 we were able to cover 18 fields (=5.□22). In May 1999, when observing nights were only 6-7 hours, we covered 12 fields (3.□48). After one year each field is re-observed, enabling the search for long-term photometric variability and high-proper motion objects.

9.5 Field selection

The field selection is governed by the following four criteria (in order of importance), which have been set to ensure maximum quality of the data:

- Fields are located between Galactic latitude $20^\circ < b^{II} < 40^\circ$: to probe the Galactic halo as well as the Galactic disk to considerable depth we target our fields at mid-Galactic latitudes. This also prevents problems with field crowding and interstellar extinction that will be present at lower Galactic latitudes. The field crowding would limit the accuracy of the differential photometry especially for faint objects. The main effect of interstellar extinction would be to limit the distance to which we are able to observe out in to the halo.

- Fields are observed within a zenith distance, z, $<30^\circ$: this criterium has been set to ensure that the effect of variable atmospheric extinction coefficients does not impart on the accuracy with which the differential photometry can be done.

- Fields are near the ecliptic: Almost all of the Kuiper Belt Objects have been found within $\sim 15^\circ$ of the ecliptic, with the majority of these even within 5° . This partly reflects a selection effect (most searches for KBOs have been conducted along the ecliptic) and the scaleheight of KBOs is poorly known. However, the overall trend of solar system objects to be concentrated towards the ecliptica, and in this context especially the short-period comets, does indicate that chances of finding KBOs are largest along the ecliptic.

- Bright stars are avoided: stars brighter than $\sim$10th magnitude will cause large charge overflows and diffraction patterns that limit the area on a chip that can be used for accurate photometry, depending on the placement and brightness of the star. To prevent this from happening the fields are selected to be as devoid as possible of bright stars.

It is clear that not all four criteria can be met at any time of the year. From the northern Hemisphere all four criteria are only satisfied in late November-early December.

9.6 Comparison with other surveys

How does the FSVS compare with other, current surveys that use large-format CCDs? The FSVS is unique in its search for variability on short time scales (hours to days), depth and precision of its differential photometry, although having a rather moderate sky-coverage. The Sloan Digital Sky Survey (SDSS) covers a much larger area of the sky (10 000 $^\square$), but at brighter magnitudes ($14 < g' < 22.5$), and provides almost no variability information. The microlensing studies (e.g. MACHO, Alcock et al., 1997; EROS, Beaulieu et al.,

1995) do obtain variability information, but are targeted at different stellar populations (the Galactic Bulge, the LMC, or M31) and have a limit of V$\sim$21, with a precision of 0.5 mag, caused by limited S/N and crowding. Supernovae searches reach as deep as the FSVS, but have a much lower time-resolution (e.g. Perlmutter et al., 1999).

9.7 Reduction and Analysis Methods

To obtain variability information on all the objects detected in our observations we use the technique of differential aperture photometry. We have written a pipe-line reduction package, consisting of IRAF taks, Fortran programs and at its core the SExtractor program by Bertin (1997). Every object in every observation is analysed and the results are stored in a master-table that lists the essential information (described below in detail) for each object. If a photometric calibration is available, the colours of each object are determined and written to the master-table. Below we outline the data flow through our pipe-line reduction, starting with the raw data as it comes from the telescope.

9.7.1 Bias subtraction

A constant fit to the overscan region of each observation is used to subtract the overall bias level. After this the 2-D pattern, determined from bias observations taken at the start of the night is subtracted.

9.7.2 Linearization of the data

A non-linearity in the read-out electronics causes all data taken with the INT WFC to be non-linear up to a level of $\sim$5%. The magnitude of this non-linearity as function of exposure level is determined by the Cambridge WFS group[3] and is posted in tabular and analytic form. These corrections are applied after bias-subtraction. The number of counts in each pixel is evaluated and adjusted accordingly.

9.7.3 Flatfielding

From twilight skyflats taken during the complete observing run a master flatfield is made for each passband, which is used for all the observations taken in that particular band during the observing run. For the I-band observations, which suffer from fringing at the 8% level, we obtained night time flats just after evening- and before morning-twilight. The fringe pattern appears to be stable throughout the nights and this allowed for fringing to be removed to the 2.5% level.

[3]see: http://www.ast.cam.ac.uk/ mike/casu/WFCsur/WFCsur.html for details on the WFC

9.7.4 Source detection

The bias-subtracted, linearized and flatfielded data are fed to the SExtractor program. This program detects sources and measures their instrumental magnitude in a number of different ways, as set by the user. Source detection is done by requiring that three neighbouring pixels are more than two sigma above the sky-background. Visual inspection shows that this threshold value is capable of detecting virtually all objects that can be identified by eye. Some contamination from trailed cosmic rays is present, but these are effectively removed after source extraction by a selection against full-widths at half-maxima that are smaller than the average ofoint-source objects. Apart from finding the sources and determining their instrumental magnitudes (see next Section), for each source the SExtractor program determines various other parameters such as its position, size, extent, ellipticity and orientiation.

9.7.5 Instrumental magnitudes

From the objects detected in the central 1k$\times$1k pixels of each chip the seeing is determined from the mean of the 2-D Gaussian fits of those objects that have an aspect ratio of unity. This seeing parameter is used in the determination of the instrumental magnitude which is done in five different ways: an isophotal magnitude and four aperture magnitudes. The aperture magnitudes are calculated with aperture radii of 0.5, 1.0, 1.5 and 2.0 times the seeing. Errors are calculated from the photon counting statistics.
The various object parameters and instrumental magnitudes measurements are written to a file, which contains the timing and field information in its name.

9.7.6 Field matching

Different observations taken of the same field are automatically matched using the OFFSET program, supplied with the DOPHOT package (Schechter, Mateo and Saha; 1993). This uses the 100 brightest, non-saturated stars, which are not located near the edges of the chips. Matching is done by triangle pattern recognition in the two images. This matching allows for scaling, rotation and translation of the different images. Output is given as the elements of a rotation-translation matrix. All images are transformed to one of the images that is taken as a reference image (typically the one with the best seeing).

9.7.7 Local reference star selection

In order to obtain differential magnitudes, a set of local reference stars has to be selected. The average magnitude of these stars is used to compare all instrumental magnitudes. In the selection of these local reference stars it is important to use the brightest stars that are not saturated. Using the brightest stars is essential because the error on the differential

magnitude of any object consists of the error that is obtained from counting statistics, and the error on the average of the reference stars. If a set of moderately bright stars is taken as local reference stars, then the error on the differential magnitude of any star *brighter* than the average value of the local reference stars will be dominated by the error on the average reference value and not by its own counting statistics. This causes possible small-amplitude variability, that should have been detected on the basis of counting statistics, to become undetectable. Currently, per chip, a set of at least five local standards are selected by requiring that their variation with respect to the average is less than five millimagnitudes. If this requirement is set more stringent not enough standards are found. In the North Galactic Pole (NGP) observations of May 1999 (which were taken as a reference field, see Paper II) the selection criterium had therefore to be relaxed to ten millimagnitudes in order to find a suitable number of stars. This is, of course, due to the limited number of stars in the NGP direction. As explained above, this selection criterium naturally sets the minimum amplitude of variation that can be found.

9.7.8 Differential magnitudes

For every object the differential magnitude is calculated against the average of the set of local reference stars. The error on the instrumental magnitude is propagated to the differential magnitude, taking the error on the average of the set of reference stars into account. The differential magnitude is calculated for all five instrumental magnitudes as described in Sect. 9.7.5. All differential magnitudes for each object are listed in one table. If an object is not encountered in a previous observation it is added to the catalogue of objects and its magnitude in the previous observations is set to a predefined, flagged value. The same is done, when an object, that has been detected previously, is not detected in subsequent observations.

9.7.9 Limiting magnitudes

Limiting magnitudes of each observation are calculated on the basis of the signal-to-noise (S/N) ratios of the brightest, non-saturated stars after photometric calibration. Using their calibrated magnitudes and detected number of photons, the limiting magnitude in each image is calculated, taking into account the sky brightness, the read-out-noise and the detector gain. We have taken the magnitude corresponding to a S/N-ratio of 5 to be the limiting magnitude in an image.

9.7.10 Variability

Variability of an object is determined on the basis of the differential magnitudes discussed above. A constant fit is made to the differential light curve. This constant fit returns a χ^2-value, the magnitude of which is taken as a measure of the object's variability. In case an

object is not detected in a particular observation, that observation's limiting magnitude is taken as an upper limit to the brightness of the object.

9.7.11 Astrometric and photometric calibration

We determine an astrometic calibration for all detected objects, by matching 20-30 stars in the central 10x10 arcminutes on the best seeing frame of each field with entries in the USNO 2-A catalogue. This is done automatically through the WCSTOOLS package[4] (Mink 1999). We then fit a second order polynomial in x and y to map all the pixels in the frame into world coordinates, which is done within the IRAF package GEOMAP. The r.m.s. of the fit ranged from $0\farcs19$ to $1\farcs28$ in R.A. and from $0\farcs16$ to $0\farcs67$ in DEC.
A photometric solution for all fields is obtained from observations of Selected Areas from Landolt's (1992) catalogue. Zero-point accuracies are of the order of 0.04 mags for B-band and V-band and 0.07 mag for I-band observations. These are sufficient for our needs. These accuracies are dominated by the error (0.02 mag) in the assumed extinction coefficients for the different filters. These extinction coefficients were determined from previous observations and time-variability is not accounted for.

9.7.12 Astrometric data-analysis and search for Kuiper Belt Objects

The data-analysis for the astrometry program, mainly targeted at finding Kuiper Belt Objects, will be discussed in a separate paper by Davis et al. (1999).

9.8 Final products

As final products the pipe-line reduction programs produce a number of files:

- The debiased and flatfielded images, stored by field.
- Data tables per chip and per field, containing the following information per detected object: an idenitifier, RA and Dec (Equinox J2000); X and Y position in one of the observations that was taken as a reference image; V-magnitude in the calibration image; $B-V$ plus error; $V-I$ plus error; the χ^2 value, taken as measure of the variability; and per observation, the differential magnitude, scaled on the apparent magnitude scale using the zero-points from the photometric calibration, the error on the differential magnitude (not including the error on the photometric calibration), the stellarity parameter, which measures the elongation of the object's profile; average FWHM of the Gaussian fits to the profile and a flag value returned by the Sextractor program (see Bertin et al. 1997, for an extensive discussion of this flag value).

[4] http://tdc-www.harvard.edu/software/wcstools/

- A table with the Heliocentric date of the observations. The first entry is the reference image, discussed above.
- A table with limiting magnitudes per observation.

9.9 Availability of the data

All reduced images are available upon request from the ING-WFS archive in Cambridge. All data-tables, containing the information described above, are retrievable three months after they are made in their final format from the FSVS-website[5].

9.10 First year observations

An extensive discussion of the results from first year of observations is given in Paper II. Observing conditions in the first two runs of the FSVS have been good and data are now available for a total of 30 fields ($8\overset{\square}{.}7$). As will be discussed in Paper II, using the above described pipe-line reduction, point source light curves have been obtained with variations as small as a few mmag for the brightest (V$\sim$17) sources. At 24th magnitude the 1-σ errors on the differential photometry is still in the 0.1-0.15 mag range.

9.11 Conclusions

The FSVS offers the unique possibility of studying the behaviour of variable objects in the magnitude range of $17 < V < 24$ with precisions ranging from 5 mmag (at V=17) to 0.15 mag (at V$\simeq$24). Observations in the first year show that the FSVS is producing promising results. To determine the nature of the variable objects that have been found, follow-up spectroscopy is scheduled for the fall of 1999. In the first year the FSVS has observed $\sim$20% of the minimum area it is aiming for, and observations for the second year have been approved.
Besides the study of variable objects, the FSVS offers a large dataset that can serve as the basis for many research topics (e.g. YSO's, gravitational lenses, galaxy counts, quasar searches). The FSVS-collaboration encourages the use of the data set for purposes other than the ones mentioned here.

Acknowledgements
PJG, PMV and the Faint Sky Variability Survey are supported by NWO Spinoza grant 08-0 to E.P.J.van den Heuvel.

[5]http://www.astro.uva.nl/$\sim$fsvs

References

Alcock, C., et al., 1997, ApJ 486, 697

Beaulieu, J.P., et al., 1995, A&A 303, 137

Davis, D.R., et al., 2000, *in preparation*

Engels, D., Cordis, L., Köhler, T., 1994, in *IAU Symp. 161*, eds. H.T. MacGillivray et al. (Kluwer, Dordrecht), p. 317

Everett, M., et al., 1999, MNRAS this issue (Paper II)

Fukugita, M. et al., 1996, AJ 111, 1748

Green, R.F., Schmidt, M. and Liebert, J., 1986, ApJS, 61, 305

Griest, K., 1991, ApJ 336, 412

Howell, S.B., Rappaport, S. and Politano, M.R., 1997, MNRAS 287, 929

Kolb, U., 1993, A&A 271, 149

Ibata, R.A., et al., 1999, ApJL, *submitted*, astro-ph 9908270

Mink, D.J., 1999, in *Astronomical Data Analysis Software and Systems VIII*, ASP Conference Series, Vol. 172. Ed. David M. Mehringer, Raymond L. Plante, and Douglas A. Roberts, p. 498

Katz, J.I, Piran, T. and Sari, R., 1998, Phys. Review Letters, 80, 1580

Kulkarni, S.R., et al., 1998, Nature 393, 35

Kulkarni, S.R., et al., 1999, Nature 398, 389

Perlmutter, S., et al., 1999, ApJ 517, 565

Piran, T., 1999, Physics Reports, *in press*

Schechter, P.L., Mateo, M. and Saha, A., 1993, PASP 105,1342

Stobie, R.S., Morgan, D.H., Bhathia, R.K., Kilkenny, D. and O'Donoghue, D., 1988, in *The Second Conference on Faint Blue Stars*, IAU Colloq. 95, eds. D. Philip et al., David Press, Schenectady, NY, p. 43

Van Paradijs, J., Kouveliotou, Ch. and Wijers, R.A.M.J., 2000, ARA&A *in preparation*

Vreeswijk, P.M. et al., 2000, *in preparation*

Warner, B., 1995, *Cataclysmic Variables*, Cambridge Astrophysics Series 28, CUP, Cambridge, UK

Williams, R., et al., 1996, AJ 112, 1335

Wisotzki, L., Köhler, T., Groote, D and Reimers, D., 1996, A&AS 115, 227

10

Nederlandse Samenvatting

10.1 γ uitbarstingen

10.1.1 Ver weg of dichtbij?

De ontdekking van γ uitbarstingen is een bijprodukt van de Koude Oorlog. De eerste γ uitbarstingen werden ontdekt door de Amerikaanse Vela satellieten die in de ruimte waren gebracht om de controle uit te voeren op een kernwapenverdrag tussen de Verenigde Staten en de Sovjet Unie waarin o.a. was afgesproken om geen kernproeven buiten de atmosfeer te houden. Bij een kernexplosie wordt veel gammastraling geproduceerd. Gammastraling is de meest energetische vorm van electromagnetische straling die wij kennen. Röntgenstraling, ultraviolet, licht, infrarood, microgolven en radiostraling zijn de minder energetische varianten van electromagnetische straling. Doordat gammastraling zo veel energie bevat is het juist deze straling die kernafval gevaarlijk maakt, omdat bij het verval van kernafval gammastraling vrijkomt.

De Amerikaanse Vela satellieten detecteerden tussen 1967 en 1973 zestien uitbarstingen van gammastraling waarvan met zekerheid vastgesteld kon worden dat deze niet van de Aarde, noch van de Zon, afkomstig waren. Hiermee werd de vraag geopperd, die nu, dertig jaar later, nog altijd niet is opgelost: wat is de oorzaak van deze γ uitbarstingen?
In de afgelopen twee jaar zijn we heel veel te weten gekomen over de afstand tot γ uitbarstingen en de omgeving waarin zij voorkomen. Dit is gekomen doordat deze uitbarstingen in 1997 voor het eerst ook in de andere delen van het electromagnetische spectrum zijn waargenomen. Het is duidelijk geworden dat, na de uitbarsting, de omgeving van de explosie nog enige tijd blijft nagloeien. Aan de hand van dit nagloeien konden niet alleen voor het eerst de posities van γ uitbarstingen zeer nauwkeurig aan de hemel bepaald worden, maar daarmee ook de afstanden tot deze uitbarstingen.

Deze afstandsbepaling was jarenlang een van de belangrijkste vragen binnen het onderzoek aan γ uitbarstingen. Als we namelijk willen weten wat de oorzaak van de uitbarstingen is, dan moeten we weten hoe groot de uitbarsting is geweest, of in andere woorden, wat de totale hoeveelheid energie was die bij de uitbarsting vrij kwam. Om dat te kunnen bepalen, is het nodig om de afstand te kennen. De hoeveelheid licht die wij van een luci-

fer op een meter afstand en van een vreugdevuur op een kilometer afstand ontvangen, is even groot. Pas als we weten hoe ver de lucifer en het vreugdevuur staan, kunnen we iets zeggen over de hoeveelheid hout die nodig is geweest om dat vuurt te maken.

De vraag hoever γ uitbarstingen van ons verwijderd zijn, was dus een zeer belangrijk kwestie binnen het γ uitbarstingen onderzoek en tot twee jaar geleden waren er twee goede mogelijkheden.

10.1.2 Om de hoek in ons eigen Melkwegstelsel

De eerste mogelijkheid was een ontstaan in ons eigen Melkwegstelsel, en zelfs relatief dichtbij de Zon op een afstand van hooguit een paar honderd lichtjaar[1]. Sinds de lancering van de eerste satellieten met röntgen detectoren aan boord, was het bekend geworden dat veel van de helderste röntgenbronnen aan de hemel te maken hebben met zogeheten 'compacte' objecten (zie ook paragraaf 10.2). Deze compacte objecten zijn witte dwergen, neutronensterren of zwarte gaten: de overblijfselen van een overleden ster. Zij worden gekenmerkt door een zeer hoge dichtheid. In een witte dwerg is de massa van de Zon[2] samengeperst in een volume zo groot als de Aarde. In een neutronenster is de massa van de Zon samengeperst in een bolletje zo groot als de stad Amsterdam, en in een zwart gat wordt de massa van van de Zon opeengepakt in bol die kleiner is dan drie kilometer. Doordat de verhouding van de hoeveelheid massa ten opzichte van de grootte van het object zo extreem is, kunnen compacte objecten veel energie opwekken als er gas op valt. En deze hoge energiëen waren nodig om, analoog aan de straling die we van röntgen dubbelsterren detecteren, de hoog-energetische gammastraling op te wekken die wij in een γ uitbarsting zien. Neutronensterren in ons eigen Melkwegstelsel waren daarom jarenlang de favoriete objecten om, op nog nader te bepalen manier, γ uitbarstingen te veroorzaken.

10.1.3 Ver weg, tot aan de rand van het bekende Heelal

De tweede mogelijkheid was dat de uitbarstingen zich helemaal niet 'om de hoek' voordeden, maar op veel grotere afstanden van miljarden lichtjaren. Hierbij zou in een enkele uitbarsting, die niet langer dan een paar minuten duurt, meer energie opgewekt moeten worden dan de Zon in zijn hele leven zal uitstralen. Om deze hoeveelheid energie op te wekken waren vele modellen bedacht, onder andere het botsen van twee neutronensterren.

Tot aan het begin van de jaren negentig had het galactische model, waarin de uitbarstingen in ons eigen Melkwegstelsel voorkomen, een duidelijke voorkeur in de sterrenkundige gemeenschap.

---

[1] Een lichtjaar is de afstand die het licht (met de lichtsnelheid; 300 000 km/s) aflegt en is gelijk aan 9 461 000 000 000 000 meter.

[2] De Zon heeft een massa van bijna 2×10^{30} kg. Dat is 332 000 keer de massa van de Aarde, die toch ook al een kleine 6 000 000 000 000 000 000 000 000 (10^{24}) kg aan massa heeft.

10.1.4 Gelijk verdeeld in plaats, maar niet in sterkte

In 1991 werd de Amerikaanse *Compton Gamma-Ray Observatory* satelliet gelanceerd, met aan boord BATSE, het *Burst and Transient Source Experiment.* BATSE is speciaal ontworpen voor het waarnemen van γ uitbarstingen en neemt gemiddeld één keer per dag een uitbarsting waar. De gevoeligheid van BATSE is vele malen groter dan die van eerdere detectoren voor γ uitbarstingen. De algemene verwachting was dat de posities van de uitbarstingen aan de hemel een duidelijke concentratie zouden vertonen naar het vlak van ons Melkwegstelsel (aan de hemel te zien als de Melkweg). Het bleek echter al snel (zie ook Fig. 10.1) dat de verdeling van posities over de hemel geheel gelijkmatig is. Er is geen concentratie naar een bepaald punt of vlak. De kans dat een γ uitbarsting aan een bepaald punt aan de hemel afgaat is voor elk punt even groot.

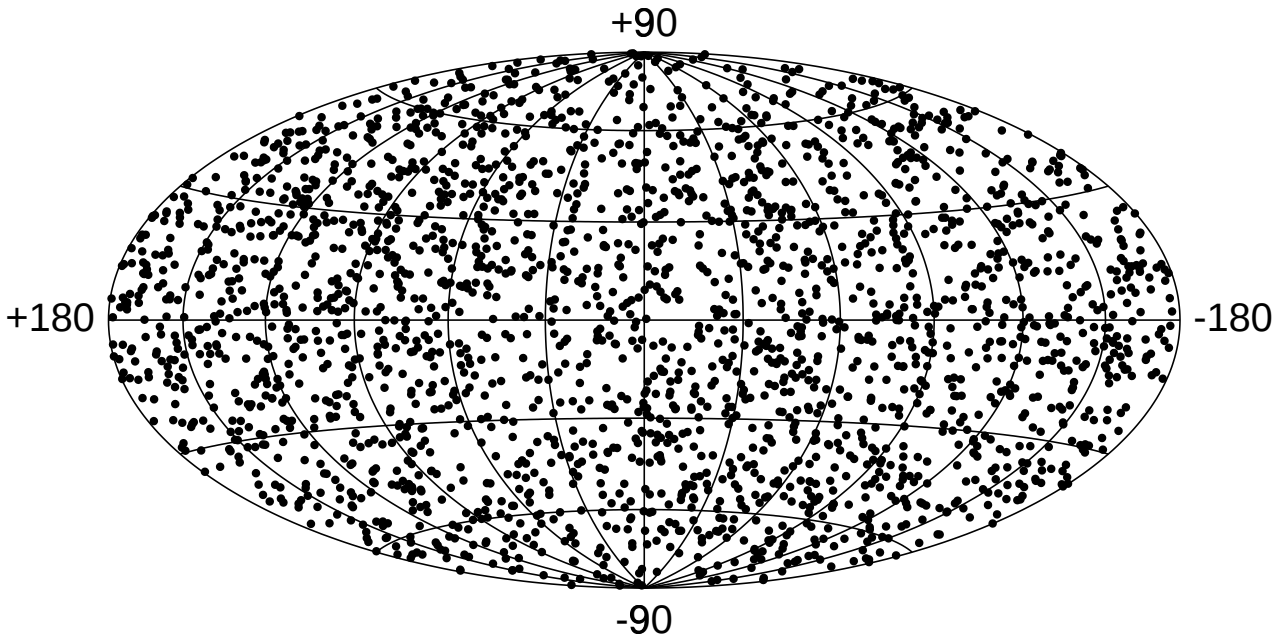

Figuur 10.1. De verdeling aan de hemel van 2408 γ uitbarstingen die tot augustus 1999 door BATSE zijn gedetecteerd. De projectie is zo gemaakt dat het vlak van ons Melkwegstelsel langs de evenaar loopt en de galactische noord- en zuidpool zich boven en onder aan de figuur bevinden. Deze verdeling laat zien dat de posities van γ uitbarstingen volkomen willekeurig over de hemel verdeeld zijn. Van linksonder tot rechtsboven loopt een band waarin iets minder γ uitbarstingen zijn waargenomen. Dit komt echter omdat dit deel van de hemel minder door de BATSE detectoren wordt gezien, omdat de Aarde hierbij in beeld staat.

Tegelijkertijd werd echter duidelijk dat de uitbarstingen niet evenredig in helderheid waren verdeeld. Als alle uitbarstingen even helder en uniform verdeeld in de ruimte zouden

zijn dan verwachten we dat als we N uitbarstingen van helderheid L zien, we N^3 uitbarstingen van helderheid L^{-2} zullen zien: het volume van de ruimte neemt als de derde macht van de afstand toe, maar de helderheid van de bronnen neemt als het kwadraat van de afstand af. Het bleek echter dat we te weinig zwakke uitbarstingen zien. Dit is te verklaren doordat er zich ergens een rand aan de ruimteverdeling is. Van verder dan een bepaalde afstand zien wij geen uitbarstingen op ons afkomen.

10.1.5 Wat van ver komt is lekker

Dit laatste resultaat was met het galactische model goed te verklaren, want ons Melkwegstelsel neemt slechts een beperkt volume in de ruimte in en als γ uitbarstingen iets met ons Melkwegstelsel te maken hebben, dan zullen ook zij een beperkt volume innemen. Het eerste resultaat was echter totaal onverwacht. Niet alleen omdat er geen concentratie naar de Melkweg werd gezien, maar vooral omdat er *totaal geen enkele* concentratie te zien was. Het had nog gekund dat de uitbarstingen zich in een grote bol rond ons Melkwegstelsel zouden bevinden, maar dan moest die bol zo groot zijn, dat het effect dat de Zon niet in het midden van het Melkwegstelsel staat, niet te zien is. Aan de andere kant kon de bol ook weer niet te groot zijn, want dan zouden we verwachten dat hij zou overlappen met een soortgelijke bol rond ons buurstelsel: de Andromeda Nevel, en daarmee een verhoogde waarschijnlijkheid zou geven om in de richting van de Andromeda Nevel een γ uitbarsting te zien.

Een kosmologische oorsprong voor γ uitbarstingen is echter goed te rijmen met de waarnemingen. Het Heelal ziet er op zeer grote afstanden namelijk overal hetzelfde uit. Dit verklaart de gelijkmatige verdeling aan de hemel. Het gebrek aan zwakke uitbarstingen kan verklaard worden door de kosmologische roodverschuiving. Deze zorgt ervoor dat het tempo waarmee GRB worden geproduceerd op grote afstand vermindert lijkt door de kosmologishe roodverschuiving. Bovendien is de energie per foton in de burst en het tempo waarmee we ze in een burst aan zien komen ook met de kosmologische roodverschuiving verzwakt. Dit maakt dat de waargenomen γ uitbarstingen zwakker zijn dan op grond van hun grote afstand alleen zou worden verwacht.

10.1.6 Gammastraling maakt kippig

Een voorkeur is echter nog geen bewijs. Uit de waarnemingen van de γ uitbarsting zelf kan de afstand tot de bron niet bepaald worden. Daarvoor is het nodig om hetzelfde fenomeen waar te nemen bij lagere energiëen of de bron te associëren met een object waarvan we de afstand kennen of kunnen bepalen. Voor het galactische model zou dat een ster kunnen zijn en voor het kosmologische model een sterrenstelsel. Voor zowel de identificatie van een laag-energetische tegenhanger als voor de associatie met een bekend object was het fundamentele probleem dat de posities van γ uitbarstingen slechts met

grote fouten kunnen worden bepaald. Een positie met een nauwkeurigheid aan de hemel die beter was dan de grootte van een volle maan was uitzondering. In een gebied aan de hemel zo groot als de volle maan staan in een diepe opname echter vele duizenden sterren en sterrenstelsels en een zoektocht naar dat ene sterretje of sterrenstelsel dat ten tijde van de uitbarsting ongebruikelijk gedrag vertoonde, is als het zoeken van een naald in een astronomische hooiberg.

10.1.7 Een heldere kijk op de hemel

Een eerste vereiste voor het bepalen van de afstand was dus een betere positiebepaling van de γ uitbarsting zelf. Deze verbetering kwam met de lancering van de Italiaans-Nederlandse *BeppoSAX* satelliet, een röntgensatelliet met aan boord twee groothoekcamera's, die samen ongeveer 8 procent van de gehele hemel continu in de gaten houden. Omdat γ uitbarstingen op willekeurige tijden en plaatsen aan de hemel afgaan, zal het voorkomen dat er af en toe een γ uitbarsting afgaat in het blikveld van de groothoekcamera's. Als de γ uitbarsting helder genoeg is bij de röntgenenergiëen waar de camera's gevoelig voor zijn, zal de uitbarsting gedetecteerd worden. De positie van de uitbarsting is dan te bepalen met een onnauwkeurigheid die, in oppervlak, nog slechts 1/25ste is van de grootte van de volle maan. Een enorme vooruitgang, vooral ook omdat de posities relatief snel (binnen een paar uur) bekend zijn. Deze ontwikkeling maakte het mogelijk om de tegenhangers van γ uitbarstingen in andere delen van het electromagnetische spectrum te identificeren.

10.1.8 Licht aan de horizon

De eerste van deze detecties met de groothoekcamera's op de *BeppoSAX* satelliet vond plaats op 20 juli 1996, toen de satelliet zich nog in de testfase bevond. De tweede detectie was op 11 januari 1997, maar, ondanks zoektochten in het optisch en in het radio, werd er geen laag-energetische tegenhanger gevonden. In de ochtenduren van 28 februari 1997 detecteerde een van de groothoekcamera's op *BeppoSAX* voor de derde maal een γ uitbarsting en de positie kon snel bepaald worden. Diezelfde avond had de Amsterdamse groep waarneemtijd op de 4.2 meter William Herschel spiegeltelescoop op La Palma. Vlak voor de positie van GRB 970228 onder de horizon zou verdwijnen, kon met de William Herschel telescoop een tweetal opnamen van dit gebied aan de hemel worden gemaakt: sneller en dieper dan ooit tevoren. Vergelijking van deze opnamen met opnamen die een aantal dagen later van hetzelfde stuk aan de hemel werden gemaakt, liet één ster-achtig object zien dat in de tussentijd was verdwenen (zie Fig. 10.2) en ook samenviel met een zwakker wordende röntgenbron. Een latere, nog diepere, opname van de positie van deze verdwijnende bron liet zien dat deze samenviel met een zeer zwak en klein sterrenstelsel. Dit was de associatie die nodig was om de afstand van γ uitbarstingen te bepalen: γ uitbarstingen komen voor in ver weg staande sterrenstelsels en zijn daarom kosmologisch in

oorsprong. Hoofdstuk 2 beschrijft de waarnemingen die tot deze conclusie leiden.

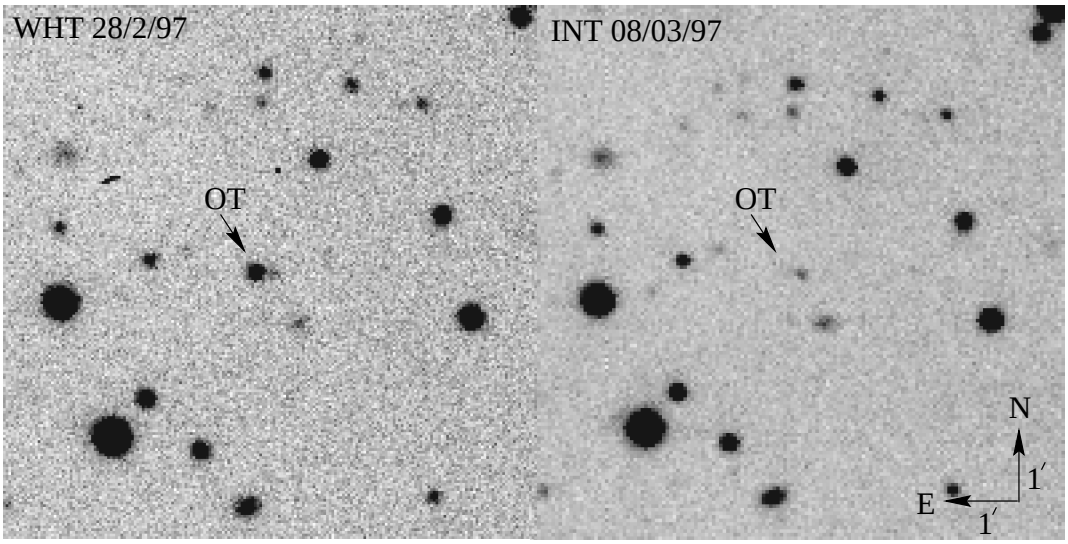

Figuur 10.2. Het eerste nagloeien van een γ uitbarsting gedetecteerd in de optisch golfband. De figuur links is genomen met de William Herschel Telescoop op 28 februari 1997 en de figuur rechts met de Isaac Newton Telescoop op 8 maart 1997. Duidelijk zichtbaar is dat de, met de pijl aangeduide, bron die zichtbaar is in het linkerplaatje, acht dagen later volkomen verdwenen is. Een latere, nog diepere opname, laat zien dat op de plaats van de bron nog wel een klein zwak sterrenstelsel is te zien, wat een zeer sterke aanwijzing leverde dat γ uitbarstingen op kosmologische afstanden staan. Het bewijs hiervoor werd geleverd bij een uitbarsting die op 8 mei 1997 afging en waarvoor een Amerikaanse groep onder leiding van dr. Mark Metzger de roodverschuiving kon bepalen.

10.1.9 Over schapen en dammen

Na deze eerste detectie van het nagloeien van een γ uitbarsting in de optische golfband volgden er snel meer. Het bewijs voor de kosmologische oorsprong werd geleverd door het bepalen van de roodverschuiving uit het spectrum van de uitbarsting die op 8 mei 1997 afging. Sinds februari 1997 zijn er een dozijn van deze 'optische counterparts' gevonden, onder andere beschreven in hoofdstuk 4. Niet elke 'jacht' was echter succesvol. In hoofdstuk 3 beschrijven we de pogingen om een optische counterpart te vinden die niet zijn gelukt, ondanks het feit dat de positie van de bron snel en diep is bekeken. Een mogelijke verklaring voor deze non-detecties kan zijn dat er zich tussen ons en de uitbarsting te veel stof bevindt, waardoor de bron niet meer zichtbaar is, of dat de uitbarsting zich heeft voortgedaan in een gebied met heel weinig gas, zodat er niet genoeg materiaal was om op te lichten en een nagloeien te produceren, of dat we er niet snel genoeg bij waren.

10.1.10 Nieuwe inzichten en oude vragen

Door de detectie van het nagloeien van γ uitbarstingen in alle delen van het electromagnetische spectrum is onze kennis over γ uitbarstingen enorm vergroot. We weten nu dat ze op kosmologische afstanden staan. We hebben kunnen bevestigen dat de modellen die vooraf waren bedacht over het nagloeien in veel gevallen kloppen. De associatie van γ uitbarstingen met sterrenstelsels is vrij zeker. De hoeveelheid energie die bij de uitbarsting vrijkomt, kan goed worden geschat en dat levert meteen ook één van de meest dringende, maar nog steeds onbeantwoorde vragen op: wat is de oorzaak van γ uitbarstingen?

Het lijkt er op dat een 'beaming'-effect, analoog aan de roeicoach met zijn toeter, er voor zorgt dat er bij de uitbarsting minder energie wordt opwekt dan wij nu, met de veronderstelling dat de explosie naar alle kanten toe even helder is, afleiden. Maar ook met deze extra factor in aanmerking genomen is een γ uitbarsting nog steeds het meest energetische fenomeen in het Heelal. Een associatie met een zeldzaam soort supernova is voorgesteld, maar of dit op alle γ uitbarstingen toepasbaar is, is nog onduidelijk. De sleutel die het raadsel van de γ uitbarstingen zal doen ontsluiten is nog niet gevonden.

10.2 Accretie

10.2.1 De Energiecentrale van het Heelal

Accretie is een belangrijke energie-centrale van het Heelal[3]. In de paragrafen over de γ uitbarstingen is al aan de orde gekomen dat dit verschijnsel waarschijnlijk met neutronensterren en zwarte gaten te maken heeft, maar het zou precieser zijn om te zeggen dat γ uitbarstingen met accretie te maken hebben. De hoeveelheid energie die in een γ uitbarsting wordt vrijgemaakt kan alleen maar door accretie opgewekt worden. Wat is accretie?

Accretie is de naam die wordt gegeven aan het proces van energie opwekking door materie in een zwaartekrachtsput te laten vallen. Accretie is de omzetting van potentiele energie naar kinetische energie. Als een object, bijvoorbeeld een komeet, van buiten het

[3]We kunnen het belang van accretie als energie-opwekker afschatten door te berekenen hoeveel energie er per seconde in ons Melkwegstelsel wordt opgewekt door accretie en dit te vergelijken met hoeveel energie er per seconde door kernfusie wordt opgewekt. Als we per sterrenstelsel uitgaan van 50 röntgendubbelsterren die 1 miljoen jaar lang op hun maximale helderheid stralen plus elke 100 jaar een supernova, plus elke miljoen jaar een γ uitbarsting, en dat afwegen tegen de typische energie die door de sterren wordt opgewekt, dan blijkt dat kernfusie het op dit moment als energie-opwekker wint als er meer dan 100 miljoen sterren in ons Melkwegstelsel zijn. Dit is het geval, want er zijn namelijk ongeveer 10 miljard sterren in ons Melkwegstelsel. Over de leeftijd van het Heelal genomen, zal accretie echter winnen omdat de quasars die zich in het jonge Heelal bevonden ook door accretie werden aangedreven en bovendien de hoeveelheid energie die door kernfusie wordt opgewekt steeds meer afneemt als het heelal ouder wordt

Zonnestelsel op ons af komt, dan wordt de aantrekkingskracht van de Zon op deze komeet steeds groter en de komeet zal een steeds grotere snelheid in de richting van de Zon krijgen: de potentiele energie van de komeet wordt omgezet in kinetische energie en het kan zijn dat hij de aantrekkingskracht van de Zon niet kan ontwijken en op de Zon zal storten.

Tijdens dit neerstorten wordt alle kinetische energie van de komeet omgezet in warmte en straling. Een mooi voorbeeld hiervan hebben we kunnen zien bij de inslag van de komeet Shoemaker-Levy 9 op de planeet Jupiter in 1994. Bij de inslag kwam een grote hoeveelheid straling vrij en de atmosfeer van Jupiter werd lokaal sterk verhit. Dit is accretie aan het werk.

De hoeveelheid energie die hierbij vrij kan komen, hangt af van hoe zwaar het object is dat de aantrekkingskracht uitoefent, en hoe diep het aanstormende object in de zwaartekrachtsput kan duiken: hoe zwaar en hoe groot het aantrekkende object dus is. De Zon is vrij inefficient bij het opwekken van accretie-energie. De Zon is eigenlijk te groot en te licht om dit efficient te doen. Als we de hoeveelheid licht die de Zon per jaar uitstraalt zouden willen opwekken door er materie op te laten vallen, dan hebben we per jaar een drie-honderdste van een miljoenste (3×10^{-8}) van de massa van de Zon nodig. Na 300 miljoen jaar zou de Zon dan al twee keer zo zwaar zijn geworden. De kernfusie processen in het binnenste van de Zon hebben jaarlijks niet meer dan een honderste van een miljardste (10^{-11}) van de massa van de Zon nodig om hem te laten schijnen[4].

Als we echter de verhouding van massa over straal opschroeven, dan wordt accretie snel efficient. In een witte dwerg, een uitgebrande sterkern met een massa van ongeveer een zonsmassa, maar een straal gelijk aan die van de Aarde, is accretie al 100 keer efficienter dan bij de Zon. Bij neutronensterren en zwarte gaten, met een massa van meer dan een zonsmassa en een straal kleiner dan 10 kilometer, is accretie bijna 20 keer efficienter in het opwekken van energie dan kernfusie. Deze objecten noemen we ‘compacte objecten’.

10.2.2 Vuurwerk aan de röntgenhemel

Na de lancering van de eerste röntgensatellieten in het begin van de jaren zeventig bleek al snel dat sommige heldere röntgenbronnen geassocieerd konden worden met dubbelstersystemen waarin een compact object en een normale ster om elkaar draaien. In deze systemen draait een zware en heldere ster rond een compact object, en valt er door de sterrenwind van de zware ster materiaal op het compacte object. Bij sommige van de helderste (onder andere de allerhelderste) röntgenbronnen kon dat echter niet snel bewezen worden. Pas in 1976 kon van de helderste röntgenbron aan de hemel (Sco X-1) bewezen worden dat ook deze zich in een dubbelstersysteem bevindt. Hier is de begeleider een heel licht, zwak sterretje. In de loop van hun evolutie zijn de beleider en het compacte object

[4]De Zon ‘verslindt’ voor zijn kernfusie nog altijd een slordige 600 miljoen ton per seconde!

zo dicht bij elkaar gekomen dat de begeleider het maximaal beschikbare volume vult. Dit volume, de Roche-lobe, wordt bepaald door de aantrekkingskracht tussen de begeleider en het compacte object. Op een lijn tussen de middelpunten van de sterren bevindt zich een punt waarin de aantrekkingskracht van het compacte object en de begeleider elkaar opheffen: het eerste Lagrange punt. Als gas in de buitenste gedeelten van de begeleider bij dit Lagrange punt komt, kan het, door de eigen beweging van de atomen, van de begeleider naar het compacte object overstromen.

Uiteindelijk zal dit gas op het compacte object vallen (dit noemen we het accreteren van massa) en de energie die hierbij vrijkomt wordt voornamelijk als röntgenstraling uitgezonden. Deze dubbelsterren behoren tot de sterkste röntgenbronnen aan de hemel. Ook de meeste andere hoog-energetische fenomenen, zoals supernovae, γ uitbarstingen, quasars en actieve kernen van Melkwegstelsels, worden van energie voorzien door accretie van materiaal op compacte objecten.

10.2.3 Accretieschijven

Het gas dat in een röntgendubbelster van de begeleider op het compacte object valt, doet dit niet rechtstreeks. Doordat de twee sterren om elkaar heen draaien, zal het gas dat de begeleider verlaat niet rechtstreeks op het compacte object vallen, maar afgebogen worden omuiteindelijk om het compacte object heen te cirkelen. Dit is te vergelijken met het proberen recht naar het midden te lopen op een rondraaiende schijf.

Als de deeltjes in de gasstroom geen onderlinge contacten hebben, dan zullen ze uiteindelijk in een ring rond het compacte object terecht komen, en nooit op het compacte object accreteren. Als we de massa uiteindelijk op het compacte object willen hebben, dan moeten de deeltjes hun hoeveelheid draaiing (het impulsmoment) verliezen, bijvoorbeeld door botsingen, die tussen de deeltjes in de ring op zullen treden. De meeste deeltjes zullen impulsmoment verliezen en naar binnen toe bewegen. Sommige echter, zullen impulsmoment winnen en naar buiten toe bewegen. We zien dat de cirkel van deeltjes uit zal spreiden tot een schijf: een accretieschijf.

De preciese werking van deze accretieschijven is een van de belangrijke onopgeloste vragen in de astrofysica. Het probleem is dat de vereiste hoeveelheid stroperigheid (viscositeit) tussen de deeltjes in een accretieschijf veel groter moet zijn dan we op basis van laboratoriumproeven kunnen meten, hoewel een instabiliteit in het magneetveld van de accretieschijf de benodigde hoeveelheid viscositeit kan leveren.

Om de natuurkunde van accretieschijven te begrijpen is het niet alleen nodig om deze schijven theoretisch te berekenen, maar ook observationeel te bestuderen om aan de hand van waarnemingen te kunnen achterhalen hoe ze in elkaar zitten. Het grote probleem bij dit observationele onderzoek is dat geen enkele accretieschijf rond een compact object met de huidige telescopen opgelost kan worden. We zien dus altijd slechts één lichtpuntje

en nooit een klein schijfje. Het is dus niet mogelijk om direct de verdeling van het licht over de schijf waar te nemen en daaruit conclusies te trekken over het temperatuur- en dichtheidsverloop over de schijf.

10.2.4 Over Kaarten en Eclipsen

Een oplossing voor dit probleem is gevonden door te kijken hoe de hoeveelheid licht, die we van een dubbelstersysteem ontvangen, varieert in de tijd. De objecten die we hiervoor gebruiken heten 'Cataclysmische Variabelen (CV)'. Deze bestaan uit een gewone, zonachtige ster, die massa overdraagt aan een witte dwerg, de uitgebrande sintel van een zon-achtige ster. De massa die van de normale ster, de begeleider, naar de witte dwerg overvloeit, doet dit via een accretieschijf (zie Fig. 10.3 voor een grafische voorstelling van een CV). CVs zijn ideale systemen voor het bestuderen van accretieschijven omdat de begeleider een heel licht sterretje is dat zelf niet veel licht uitstraalt, en omdat de witte dwerg in het systeem niet compact genoeg is om voldoende röntgenstraling op te kunnen wekken om de structuur van de schijf te verstoren. Bovendien staan ze relatief dichtbij (typisch op een paar honderd lichtjaar afstand) en zijn daardoor vrij helder aan de hemel.

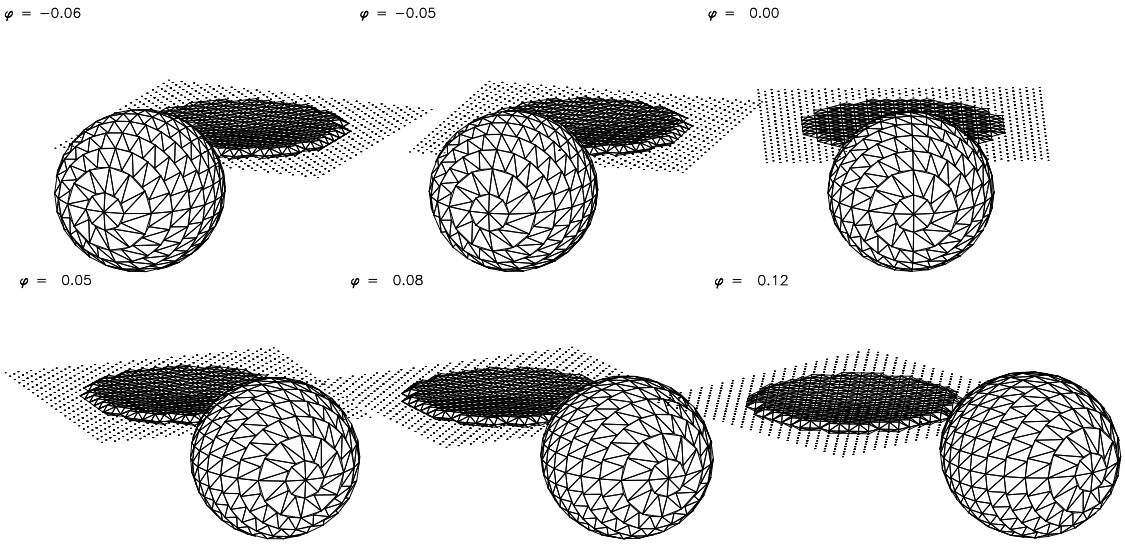

Figuur 10.3. Een grafische voorstelling van een eclipserende CV die we op verschillende momenten in zijn baan zien. De begeleider (de ronde ster vooraan) bedekt tijdens de baanbeweging een gedeelte van de accretieschijf (de platte pannenkoek achteraan), die de witte dwerg (op deze schaal niet te zien) omringt. Door de hoeveelheid licht tijdens een eclips te meten kunnen we de lichtverdeling over de schijf reconstrueren.

Het vlak waarin de twee sterren om elkaar heen draaien heet het baanvlak en dit baanvlak kan elke orientatie hebben ten opzicht van onze gezichtslijn. In sommige systemen kijken we van bovenaf op de accretieschijf, die als een dunne pannenkoek in het baanvlak

ligt, en bij sommige systemen kijken we (bijna) precies tegen de zijkant van de accretieschijf aan. In deze laatste systemen zal één keer per baanperiode de donkere begeleider precies voor de heldere accretieschijf langs trekken. De hoeveelheid licht die wij dan op Aarde van dit systeem ontvangen, gaat tijdens deze eclips hard omlaag en komt na de eclips weer snel terug. Sinds 11 augustus hebben velen van u dit effect 'live' mee kunnen maken, toen de maan de zon volledig eclipseerde. In Fig. 10.4 laten we een zogeheten lichtkromme van een CV zien. Hierin staat de hoeveelheid licht uitgezet tegen de tijd (of in dit geval de baanperiode van de CV). We zien dat tijdens de eclips de hoeveelheid licht snel afneemt, een minimum bereikt en daarna weer snel toeneemt. Omdat de bodem van de lichtkromme niet vlak loopt, is dit een gedeeltelijke eclips (zoals de zonsverduistering vanuit Nederland). Als de bodem wel even vlak loopt, hebben we een totale eclips (zoals de zonsverduistering gezien vanuit Noord-Frankrijk, Duitsland of Hongarije).

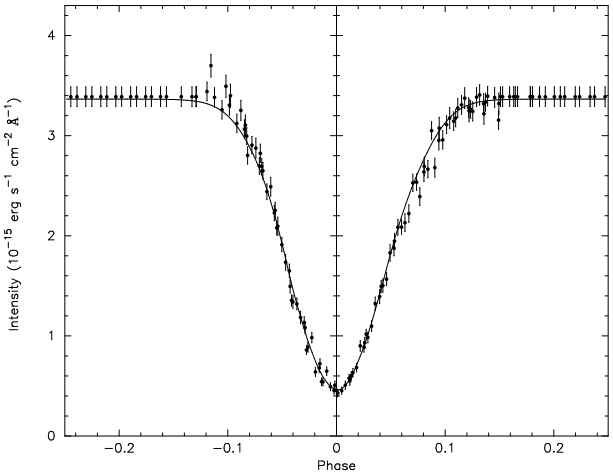

Figuur 10.4. De lichtkromme van een CV. De hoeveelheid licht is constant buiten de eclips, neemt snel af als de ster voor de accretieschijf langs trekt, bereikt een minimum als de ster de schijf maximaal afdekt, en neemt dan weer toe tot het niveau buiten eclips.

De vorm van de eclips lichtkromme kan gezien worden als een afscannen van de accretieschijf. Tussen twee punten tijdens de eclips verdwijnt er voor onze gezichtslijn een strook van de schijf, die een bepaalde helderheid had. Na mid-eclips komt er een andere strook licht, die een hoek maakt ten opzichte van de eerste, weer te voorschijn. Hiermee kunnen we dus een reconstructie maken van waar op de schijf licht uitgestraald wordt. Dit is de basis van de techniek van 'eclipse mappen', die in Hoofdstuk 6, 8 en 7 wordt toegepast. In deze hoofdstukken hebben we voor drie verschillende CVs de hoeveelheid licht die de accretieschijf uitzendt, als functie van de kleur van het licht, gereconstrueerd. Uit deze reconstructie hebben we in SW Sex[5] het temperatuursverloop over de schijf kun-

[5]De naamgeving van variabele sterren geschiedt door letters toe te voegen aan de naam van het sterrenbeeld. Men begint met een enkele letter en bij de R. De eerste variabele in het sterrenbeeld Sextans (de

nen reconstrueren en kunnen concluderen dat deze niet in overeenstemming is met wat op basis van de theorie van accretieschijven verwacht zou worden. De reden hiervoor is waarschijnlijk een schok die zich in de schijf bevindt. De accretiestroom van de begeleider naar de witte dwerg botst op de accretieschijf en in SW Sex zien we, dat er zich in het verlengde van het traject van de accretiestroom, maar *in* de schijf een schok bevindt, die heter is dan de rest van de schijf en bovendien de plaats is waar een wind ontstaat die de structuur van de schijf verstoort.

Een groep van cataclysmische variabelen waartoe SW Sex behoort wordt over het algemeen onderverdeeld in twee subgroepen; die van de SW Sex systemen en die van de UX UMa systemen. Ze worden onderscheiden aan de hand van hun spectroscopische gedrag. In Hoofdstuk 7 passen we de eclipse mapping techniek toe op het systeem RW Tri, dat tot de UX UMa subgroep behoort. We zien echter dat dit systeem in onze waarnemingen erg veel lijkt op een systeem uit de SW Sex subgroep. We concluderen daaruit dat het spectroscopische gedrag van deze cataclysmische variabelen kan veranderen, waardoor ze zowel tot de ene groep als tot de andere kunnen behoren. Omdat hierdoor het onderscheid tussen de twee subgroepen vervalt, stellen we voor om de typering slechts te gebruiken voor het aanduiden van het spectroscopische gedrag van een cataclysmische variabele op een bepaald moment. Een fysisch onderscheid tussen de twee subgroepen kan niet gemaakt worden.

In het systeem IP Peg (Hoofdstuk 8) is het reconstrueren van de accretieschijf niet zo gemakkelijk als in SW Sex. De lichtkromme van IP Peg (zie Fig. 10.5) laat zien dat er behalve een eclips ook nog een duidelijke 'bochel' op de lichtkromme zit, die net voor de eclips maar liefst twee keer zo helder is als de rest van de schijf samen. Deze 'bochels' zijn een bekend fenomeen, en het tijdstip waarop ze te zien zijn, valt samen met het tijdstip waarop onze gezichtslijn precies de plek ziet waar de accretiestroom en de accretieschijf op elkaar botsen. Op deze plek wordt de schijf dus lokaal extra verhit en zal meer licht uitstralen. Omdat we de bochel slechts onder bepaalde hoeken kunnen zien, weten we dat we te maken hebben met een schijf met een duidelijke drie-dimensionale structuur. Dat wil zeggen dat we de schijf niet kunnen beschouwen als een twee-dimensionaal oppervlak (zoals een flinterdun papiertje), dat precies in het baanvlak ligt. Om de hoeveelheid licht op de accretieschijf te kunnen reconstrueren, moeten we daarom eerst definieren hoe wij denken dat de schijf er uit zal zien. Deze experimentele techniek hebben we voor het eerst op IP Peg toegepast en in Hoofdstuk 8 beschrijven we hoe we aan de hand van de helderheid van de bochel (de '*bright spot*') de geometrie van de accretieschijf hebben kunnen bepalen. Met gebruik making van deze geometrie en de drie-dimensionale

sextant) is dan ook R Sex, de tweede S Sex etc. Na de Z begint men met dubbele letters, weer bij de R, waarbij de tweede letter nooit eerder is dan de eerste. Dus RR Sex, RS Sex, etc, RZ Sex, SS Sex, ST Sex, etc. Na ZZ Sex komt AA Sex, AB Sex etc, tot QZ Sex, waarna overgestapt wordt naar een aanduiding met V en dan een nummer. Omdat er al 334 sterren met een letter zijn aangeduid is de eerste V335 Sex, etc. SW Sex is dus de 23ste variabele in het sterrenbeeld Sextans.

eclipse-mapping methode hebben we kunnen bepalen dat de buitenkant van de schijf in IP Peg koud genoeg is om moleculen te laten ontstaan.

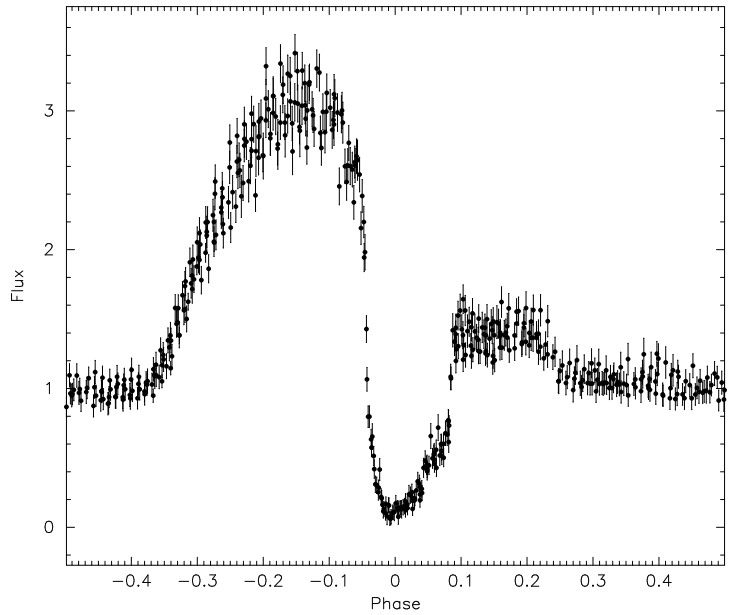

Figuur 10.5. De lichtkromme van de CV IP Peg. De bochel op de lichtkromme die zichtbaar is bij fase –0.15 is het gevolg van de accretiestroom die op de accretieschijf botst. Omdat deze bochel niet gedurende de hele baan zichtbaar is, weten we dat de structuur van de schijf in IP Peg duidelijk drie-dimensionaal is.

In de laatste jaren is gebleken dat de snelheid waarmee de begeleider massa overdraagt aan de witte dwerg niet altijd even groot is. Deze variaties gebeuren op tijdschalen van dagen tot jaren en zijn over het algemeen slecht bekend. De oorzaak van deze variaties is ook nog onbekend. Als de hoeveelheid massa, die de begeleider overdraagt, varieert dan zal de accretieschijf rond de witte dwerg hier op reageren door kleiner of groter te worden. Normaal gesproken is dit slecht waar te nemen, maar in eclipserende systemen kunnen we dit effect wel zien, omdat de begeleider zelf niet van grootte verandert en de schaduw van de begeleider op de accretieschijf dus altijd even groot is. In het systeem GS Pav (Hoofdstuk 5) hebben we in kaart kunnen brengen hoe de accretieschijf varieert doordat de schijf in dit systeem soms geheel in de schaduw van de begeleider valt en soms maar gedeeltelijk. De eclips is dus soms totaal en soms gedeeltelijk. Door de maximale hoeveelheid licht die verdwijnt in verband te brengen met de helderheid van het systeem buiten eclips hebben we niet alleen vast kunnen stellen dat de grootte van de schijf in het systeem verandert, maar dat dit ook op een systematische manier gebeurt. Over een periode van 2,5 jaar verandert de schijf op een unieke wijze van grootte. De oorzaak van deze verandering is waarschijnlijk dat de snelheid waarmee de begeleider massa overdraagt varieert, maar verder onderzoek zal dat uit moeten wijzen.

10.3 Zwak en Variabel

De ontdekking van optische tegenhangers van γ uitbarstingen laat zien dat de bestudering van zeer zwakke sterachtige bronnen aan de hemel onverwachte, maar zeer belangrijke resultaten op kan leveren. Het gedrag van zwakke sterren (met een helderheid V>20,[6]) is zeer slecht bekend. Voor het nauwkeurig meten van het gedrag van deze sterren zijn gevoelige detectoren, relatief grote telescopen en veel waarneemtijd nodig. Pas sinds kort zijn deze belemmerende factoren weggenomen en kan een detailstudie van de zwakke hemel uitgevoerd worden. Twee van de typen objecten waar wij in geïnteresseerd zijn en die hiermee gevonden kunnen worden zijn γ uitbarstingen die niet in gammastraling, maar wel in het optische licht gezien worden, en zeer oude CVs waarbij de overdracht van de begeleider naar de witte dwerg nog maar zeer langzaam gaat.

De 'optische γ uitbarstingen' worden verwacht opo grond van de theorie dat een γ uitbarsting niet even helder in elke richting hoeft te zijn, maar dat straling wordt gebundeld in een bepaalde richting. De verwachting is dan dat deze bundeling in gammastraling veel sterker zal zijn dan in het optisch. Het kan dus voorkomen dat de bundel gammastraling naast de Aarde is gericht en wij dus niets zien, maar dat de optische bundel de Aarde wel bestrijkt. Het detecteren van deze optische γ uitbarstingen kan vertellen of, en hoe sterk, de γ uitbarstingen gebundeld zijn. Dit is weer van belang voor de hoeveelheid energie die nodig is om een γ uitbarsting te veroorzaken en dus voor een verklaring van de oorzaak van γ uitbarstingen.

De CVs waarvan de baanperioden nu bekend zijn laten een duidelijke voorkeur zien voor systemen waarin de baanperiode langer is dan drie uur. Theoretische berekeningen van de evolutie van CVs laten echter zien dat deze lang-periodieke systemen niet meer dan 1% aan het totale aantal CVs bijdragen. We zien hier het effect van een 'waarneemvoordeel'. De CVs met lange perioden zijn helderder, heter en daardoor makkelijker te vinden. De overgrote meerderheid van de CVs zou baanperioden van minder dan twee uur moeten hebben, en intrinsiek vrij zwak moeten zijn. Bovendien is de verwachting dat de accretieschijf in deze systemen niet zo heel heet is en dus ook niet de kleur van het systeem zal overheersen. Als we dus op zoek gaan naar blauwe (want hete) objecten, dan zal de meerderheid van de CVs daar niet in gevonden worden.

Alle CVs vertonen echter een variatie in de hoeveelheid licht die ze uitstralen. Deze variaties worden veroorzaakt doordat de hoeveelheid massa die op de accretieschijf valt niet altijd even groot is (op een tijdschaal van minuten), of omdat de vervorming van de

[6]Het astrofysische magnitudestelsel kent aan de waargenomen helderheid van sterren een getal toe, dat oploopt naarmate de ster zwakker wordt. Sirius, de helderste ster aan de hemel heeft een magnitude –1.46, en Wega, de helderste ster in de Lier heeft een magnitude 0, en is daarmee het ijkpunt van de magnitude schaal: Wega heeft altijd magnitude 0, ongeacht de kleur of spectrale band waarin hij wordt waargenomen. Alle andere sterren worden dus geschaald aan de helderheid van Wega, en een ster die 100 keer zwakker is dan Wega heeft een magnitude 5, één die 10 000 keer zwakker een magnitude 10, etc.

begeleider er voor zorgt dat deze niet van onder alle hoeken gezien even helder is, of omdat de begeleider eens per baanperiode voor de accretieschijf langstrekt en we dus een eclips zien. Een studie van de hemel op zoek naar deze zwakke, variabele sterren zou dus het overgrote deel van de CV aan het licht kunnen brengen.

Het vinden van optische γ uitbarstingen en het volledig in kaart brengen van de CV populatie, zijn twee van de belangrijkste drijfveren achter een groot onderzoeksproject dat in 1998 is gestart met behulp van een groothoekcamera achter de 2.5m Isaac Newton Telescoop op de Brits/Nederlandse sterrenwacht op La Palma. De groothoekcamera bestaat uit vier CCD detectoren en kan in één keer een gebied aan de hemel bekijken dat even groot is als het oppervlak van de volle maan. Door de grootte van de spiegel en de donkere hemel boven La Palma kunnen daarmee in een opname van tien minuten sterren gedetecteerd worden van 25ste magnitude[7]. Hiermee zal in vijf jaar een gebied aan de hemel in kaart worden gebracht ter grootte van 200 volle manen. In Hoofdstuk 9 beschrijven we de doelen en de data-reductie van deze belangrijke nieuwe stap in het onderzoek naar γ uitbarstingen en cataclysmische variabelen.

[7]Dat is 19 magnituden, of een factor 40 miljoen, zwakker dan met het blote oog op de donkerste nacht gezien kan worden.

Publications

Refereed Journals

• Vreeswijk, P.M., Galama, T.J.,et al., P.J. Groot, 1999, ApJ *submitted*
The X-ray, Infrared and Optical counterpart to GRB 980703

• Galama, T.J., Vreeswijk, P.M., Van Paradijs J., et al., Groot, P.J., et al., 1999, A&AS, 138, 465
On the possible association of SN 1998bw and GRB 980425

• Galama, T.J., Wijers, R.A.M.J., Vreeswijk, P.M., Groot, P.J., et al., 1999, A&AS 138, 451
Physical parameters of GRB 970508 from its afterglow synchroton emission

• Smith, I.A., Tilanus, R.P.J., Van Paradijs, J., Galama, T.J., Groot, P.J., Vreeswijk, P.M., Kouveliotou, C., Wijers, R.A.M.J. and Tnavir, N., 1999, A&A 347, 92 *SCUBA sub-millimeter observations of gamma-ray bursters I: GRB 970508, 971214, 980326, 980329, 980519, 980703, 981220, 981226*

• Magnier, E.A., Waters, L.B.F.M., Groot, P.J., Van den Ancker, M.E., Kuan Y-J. and Martín, E.L., 1999, A&A, 346, 441
The circumstellar environment of IRAS 05327+3404

• Fruchter, A.S., Pian, E., Thorsett, S.E., et al., P.J. Groot, et al., 1999, ApJ 516, 683
The Fading Optical Counterpart of GRB 970228, 6 Months and 1 Year Later

• Groot, P.J., Augusteijn, T., Barziv, O. and Van Paradijs, J., 1998, A&A Letters 340, L31; Chapter 5
The eclipsing Cataclysmic Variable GS Pavonis: Evidence for disk radius changes

• Galama, T.J., Vreeswijk, P.M., Van Paradijs, J. et al., P.J. Groot, et al., 1998, Nature, 395, 670
An unusual supernova in the error box of the γ-ray burst of April 25, 1998

• Palazzi, E., Pian, E., Masetti, N, Nicastro., L., Vreeswijk, P., Galama, T.J., Groot, P. et al., 1998, A&A 336, L95
Optical and near-infrared follow-up observations of GRB 980329

• Groot, P.J., Galama, T.J., Vreeswijk, et al., 1998, ApJ 502, L123; Chapter 4

The Rapid Decay of the Optical Emission from GRB 980326 and Its Possible Implications

• Galama, T.J., Wijers, R.A.M.J., Bremer, M., Groot, P.J., et al., 1998, ApJ 500, L101
The 1.4 GHz Light Curve of GRB 970508

• Galama, T.J., Wijers, R.A.M.J., Bremer, M., Groot, P.J., Strom, R.G., Kouveliotou, C. and Van Paradijs, J., 1998, ApJ 500, L97
The Radio-to-X-Ray Spectrum of GRB 970508 on 1997 May 21.0 UT

• Galama, T.J., Groot, P.J., Van Paradijs, J., et al., 1998, ApJ 497, L13
Optical Follow-up of GRB 970508

• Groot, P.J., Galama, T.J., Van Paradijs, J., Kouveliotou, C., Wijers, R.A.M.J., Bloom, J., Tanvir, T., Vanderspek, R., et al., 1998, ApJ 493, L27; Chapter 3
A Search for Optical Afterglow from GRB 970828

• Sahu, K.C., Livio, M., Petro, L., Bond, H., Macchetto, F.D., Galama, T.J., Groot, P.J., Van Paradijs, J., Kouveliotou, C., 1997, ApJ 489, L127 *Observations of GRB 970228 and GRB 970508 and the Neutron Star Merger Model*

• Barziv, O., Kuulkers, E., Méndez, M., Van der Hooft, F., Groot, P.J, et al. 1997, A&A 325, 1035
Optical photometry of Sco X-2

• Natarajan, P., Bloom, J.S., Sigurdsson, S., Johnson, R.A., Tanvir, N.R., Groot, P.J., Galama, T.J., Van Paradijs, J., Kouveliotou, C., 1997, New Astro 2, 471
The host to gamma-ray burst 970508: a distant dwarf galaxy?

• Galama, T.J., Groot, P.J., Strom, R.G., Van Paradijs, J., et al., 1997, ApJ 486, L5
Radio and Optical Follow-up observations and improved interplanetary network position of GRB 970111

• Galama, T.J., Groot, P.J., Van Paradijs, J., et al., 1997, Nature 387, 479
The decay of optical emission from the gamma-ray burst GRB 970228

• Sahu, K.C., Livio, M., et al., Groot, P.J., Galama, T.J, 1997, Nature 387, 476
The optical counterpart to gamma-ray burst GRB 970228 observed using the Hubble Space Telescope

• Galama, T.J., De Bruyn, A.G., Van Paradijs, J., Hanlon, L., Groot, P.J. et al., 1997, A&A 321, 229
Two variable radio sources near the position of GRB 940301

• Van der Hooft, F., Groot, P.J., Shahbaz, T., et al., 1997, MNRAS 286, L43
The black hole transient Nova Scorpii 1994 (= GRO J1655–40): orbital ephemeris and optical light curve

• Van Paradijs, J., Groot, P.J., Galama, T.J., et al., 1997, Nature 386, 686; Chapter 2
Discovery of transient optical emission from the error box of the GRB of February 28, 1997

• Van Paradijs, J., Waters, L.B.F.M., Groot, P.J., et al., 1996, A&A 314, 146
Infrared observations of Soft Gamma-ray Repeaters

• Piters, A.J.M., Groot, P.J. and Van Paradijs, J., 1996, A&AS 118, 529
A Combined Fourier-Bessel transformation method to derive accurate rotational velocities

• Groot, P.J., Piters, A.J.M. and Van Paradijs, J., 1996, A&AS 118, 545
Rotational velocities of F dwarfs; application of the Fourier-Bessel transformation method

Forthcoming

• Hanlon, L., Metcalfe, L., Delaney, M., et al., Groot P., et al., 1998, A&A, *submitted*
Infrared Space Observatory Imaging of the GRB 970805 Optical Transient

• Groot, P.J., Rutten, R.G.M. and Van Paradijs, J., 1999, A&A, *submitted*; Chapter 6
SW Sextantis in an excited, low state

• Groot, P.J., Rutten, R.G.M. and Van Paradijs, J., 2000, A&A, *submitted*; Chapter 7
Spectral Eclipse Mapping of RW Tri

• Groot, P.J., Vreeswijk, P.M., Howell, S.B. et al., 2000, MNRAS, *submitted*; Chapter 9
The Faint Sky Variability Survey; Overview

• Everett, M., Groot, P.J., Howell, S.B., et al., 2000, MNRAS, *submitted*
The Faint Sky Variability Survey; Observations

• Shahbaz,T., Groot, P.J., Philipps, S.N. et al., 1999, MNRAS, *submitted*
Irradiation of the secondary star in X-ray Nova Scorpii 1994 (=GRO J1655–40)

• McGowan, K., Charles, P., et al., P.J. Groot, et al., 2000, MNRAS, *submitted*
Multiwavelength observations of LMC X-2

IAU Circulars and GCN Notes

• Groot, P.J., Galama, T. et al., 1997, IAUC 6574
GRB 970111 and GRB 970228

• Groot, P.J., Galama, T., et al., 1997, IAUC 6584
GRB 970228

• Groot, P.J., Galama, T., et al., 1997, IAUC 6588
GRB 970228

• Groot, P.J., Galama, T., et al., 1997, IAUC 6616
GRB 970402

• Galama, T.J., Groot, P.J., Van Paradijs, J., Kouveliotou, C. et al., 1997, IAUC 6665
GRB 970508

• Groot, P.J., Galama, T.J., Van Paradijs, J., Kouveliotou, C. et al., 1997, IAUC 6660
GRB 970508

• Donahue, M., Sahu, K.C., Livio, M., et al., Groot, P., 1997, IAUC 6666
GRB 970508

• Groot, P.J., Galama, T.J., Hurley, K., Kouveliotou, C. et al., 1997, IAUC 6723
GRB 970616

• Groot, P.J., Galama, T.J., Hurley, K., Kouveliotou, C. et al., 1997, IAUC 6723
GRB 970815

• Greiner, J., Schwarz, R., Groot, P.J., Galama, T.J., 1997, IAUC 6757
GRB 970828

• Castro-Tirado, A.J., Gorosabel, J., Galama, T., Groot, P., Van Paradijs J., and Kouveliotou, C., 1998, IAUC 6848
GRB 970508

• Groot, P.J., Vreeswijk, P.M., Pian, E. et al., 1998, IAUC 6852
GRB 980326

• Groot, P.J., Galama, T., Van Paradijs, J. et al., 1997, GCN #17
GRB 971227

• Groot, P.J., Galama, T., Van Paradijs, J. et al., 1997, GCN #21
GRB 971227

• Groot, P.J., Galama, T., Van Paradijs, J. et al., 1997, GCN #26
GRB 971227

• Groot, P.J., Vreeswijk, P.M., Galama, T.J., et al., 1998, GCN #32
GRB 980326

• Palazzi, E., Masetti, N., Pian, E., et al., Groot, P., 1998, GCN #48
GRB 980329

• Galama, T.J., Vreeswijk, P.M., Groot, P.J. et al., 1998, GCN #60
GRB 980425

• Galama, T.J., Vreeswijk, P.M., Groot, P.J. et al., 1998, GCN #62
GRB 980425

• Vreeswijk, P.M., Galama, T.J., Groot, P.J. et al., 1998, GCN #65
GRB 980425

Conference Proceedings

• Piters, A.M., Groot, P.J. and Van Paradijs, J., 1994, in *Cool stars, stellar systems and the Sun*, ASP Conf. Ser. 64, J.P. Caillaut ed., BookCrafters Inc.
Rotational velocities of F dwarfs

• Groot, P.J., Van der Klis, M., Van Paradijs, J., Augusteijn, T., Berger, M., 1996, in *Cataclysmic Variables and Related Objects*, eds. Evans and Wood, Ap&SS Library 208, p. 367, Kluwer Academic Pub, Dordrecht, The Netherlands
The optical counterpart of the LMXB GX13+1

• Sahu, K.C., Livio, M., et al., Groot, P.J., Galama, T., 1997, BAAS 190, 5305
HST observations of GRB 970228

• Groot, P.J., Galama, T.J., Van Paradijs, J., Kouveliotou, C. et al., 1998, Proceedings of the 4th Huntsville GRB Symposium
A Search for optical Afterglow from GRB 970828

• Groot, P.J., Galama, T.J., Van Paradijs, J., Kouveliotou, C. et al., 1998, Proceedings of the 4th Huntsville GRB Symposium
Ground-based optical photometry of GRB 970508

• Galama, T.J., Groot, P.J., Van Paradijs, J., Kouveliotou, C. et al., 1998, Proceedings of the 4th Huntsville GRB Symposium
A Revised analysis of the optical lightcurve from GRB 970228

• Livio, M., Sahu, K., Petro, L. et al., Groot, P.J., 1998, Proceedings of the Fourth Huntsville Gamma-Ray Burst Symposium
The Gamma Ray Bursts GRB 970228 and GRB 970508: What Have We Learnt?

• Groot, P.J., Rutten, R.G.M., and Van Paradijs, J., 1999, New Astronomy Reviews, in *Brian Warner Symposium on Cataclysmic Variables*, ed. P. Charles and A.R. King
The hot-spot environment in SW Sex

Public Outreach Publications

• Groot, P.J., Galama, T.J., Van Paradijs, J., Kouveliotou, C., 1997, Spectrum 14, 8
The first ever optical counterpart of a Gamma-ray Burst: GRB 970228

• Galama, T.J. and Groot, P.J., 1998, NTvN 64/4, 87 (in Dutch)
The first optical identification of a GRB: Bruno Rossi prize for the BeppoSAX-team and J. van Paradijs.

• Groot, P.J. and Galama, T.J., 1998, Yearbook University of Amsterdam (in Dutch),
Internationalisation on a Cosmic Scale

Dankwoord

Bedankt!

Dag Allemaal